RATIONAL DESIGN OF ELECTRICALLY CONDUCTIVE

POLYMER COMPOSITES FOR

ELECTRONIC PACKAGING

A Dissertation
Presented to
The Academic Faculty

by

Zhuo Li

In Partial Fulfillment
of the Requirements for the Degree
Ph.D. in the
School of Materials Science and Engineering

Georgia Institute of Technology
May, 2014

RATIONAL DESIGN OF ELECTRICALLY CONDUCTIVE

POLYMER COMPOSITES FOR

ELECTRONIC PACKAGING

Approved by:

Dr. C.P.Wong, Advisor
School of Materials Science and
Engineering
Georgia Institute of Technology

Dr. Donggang Yao
School of Materials Science and
Engineering
Georgia Institute of Technology

Dr. Meilin Liu
School of Materials Science and
Engineering
Georgia Institute of Technology

Dr. Z. John Zhang
School of Chemistry and Biochemistry
Georgia Institute of Technology

Dr. Gleb Yushin
School of Materials Science and
Engineering
Georgia Institute of Technology

Date Approved: March 31, 2014

To my dear husband Fengshou Zhang, for his love and support.

ACKNOWLEDGEMENTS

TABLE OF CONTENTS

LIST OF TABLES

LIST OF FIGURES

xviii

xxiii

SUMMARY

Electrically conductive polymer composites are polymer composites filled with conductive fillers. While most polymers are insulating by nature, the addition of conductive fillers, such as metals, carbon materials, and conductive polymers can make the composites display a wide range of conductivity for various applications in electronic packaging.

This dissertation discusses two important types of electrically conductive composite, namely the silver-based electrically conductive adhesives (ECAs) and carbon-based composites.

In the first part (Chapters 2-6), two problems are addressed for silver-based ECAs.

The first one is how to improve the electrical conductivity of ECAs through surface modification of silver. ECAs are proposed as environmentally-friendly alternatives of Sn/Pb solders, but their limited electrical conductivity restrict their applications. However, the electrical conductivity of most conventional ECAs is still one to two orders of magnitude lower than that of pure metals even at filler loadings as high as 80-90 wt.%. The relatively low conductivity mainly results from the contact resistance between neighboring fillers. Most commercial silver fillers are coated with a thin layer of silver fatty acid lubricant, which facilitates the processing of ECAs but simultaneously inhibits electrical conduction. In this work, based on the understanding of the surface chemistry of the silver flakes, we are able to chemically reduce the insulating lubricant on the flakes to silver nanoparticles during the curing process of polymer matrices; this was achieved by either adding a small amount of reducing agent, or by modifying the polymer

matrices with functional groups with reducing capability. Furthermore, it is found that these nanoparticles can sinter with each other and form metallurgical bonds during the curing of the polymer matrix, further increasing the conductivity. The findings in this work can enhance the electrical conductivity of silver flake-based ECAs by one order of magnitude (10^5 S/cm) without sacrificing their processibility.

The second problem is how to develop stretchable ECAs that have both high conductivity and high elasticity to meet the requirement of future flexible/stretchable electronics. In this part, I am mainly focused on replacing the rigid conventional epoxy matrix with flexible polyurethane (PU) and silicone rubber matrices. The chain length of prepolymers, structures of curing agents, and catalysts concentrations *etc.* are carefully optimized to achieve a good balance between electrical conductivity and mechanical flexibility.

The findings in first part provide a better understanding of the relationship between electrical conductivity of silver-based ECAs and the surface chemistry of silver flakes. It will guide the production of ECAs with improved conductivity. The development of PU-and silicone-ECAs will fill the gap between the fast-developing flexible/stretchable electronics and conventional rigid ECAs materials and will be a useful building block for future flexible/stretchable electronics.

The second part of this dissertation discusses the feasibility of using carbon black (CB) or carbon nanotubes (CNTs)/polymer composites as sensors to diagnose the aging conditions of polymer-based insulation components in nuclear power plants. The conductive composites are "variable resistors" whose resistance decreases as the insulation (matrix of the sensor) shrinks and densifies during thermal aging. A change in

resistance can identify the aging situation and predict the remaining lifetime of the monitored insulation parts. We not only demonstrate the feasibility of carbon/polymer composites as aging sensors but also solve three practical problems occurred during the preparation of carbon/polymer composites. These problems are the decreased thermal stability of silicone composites induced by the cobalt catalyst residues in CNTs, the curing inhibition of silicone rubber by functionalized CNTs, and the quantification of dispersion of carbon fillers in polymers. The aging sensor study helps the launching of commercial product AgeAlert® sensors, and the fundamental studies of the three problems can guide the future work in carbon-based composites preparation. The program developed to quantify the dispersion of fillers in composites can be applied to any composite systems and therefore facilitate the processing of composites.

CHAPTER 1 INTRODUCTION

1.1 Brief overview of electronic packaging

Electronic packaging is one major branch of electronic engineering. It refers as the bridge to interconnect integrated circuit (IC) and other components into a system-level board to form electronic products. Generally, it provides four functions: 1) distribute signals, 2) distribute power, 3) thermal management (cooling), and 4) protection of components and interconnections.

Electronic packaging is typically divided into four levels (Figure 1.1), including:

1) Level 0: semiconductor chip level (IC level)

2) Level 1: an IC die is assembled into a package carrier (substrate or lead frame) by different interconnection techniques (wire bonding, tape automated bonding, or flip chip assembly). The IC die is protected by either a lid or encapsulated with molding compound.

3) Level 2: the packaged IC die is mounted to a printed circuit board (PCB) or other substrates.

4) Level 3: board to board interconnects.
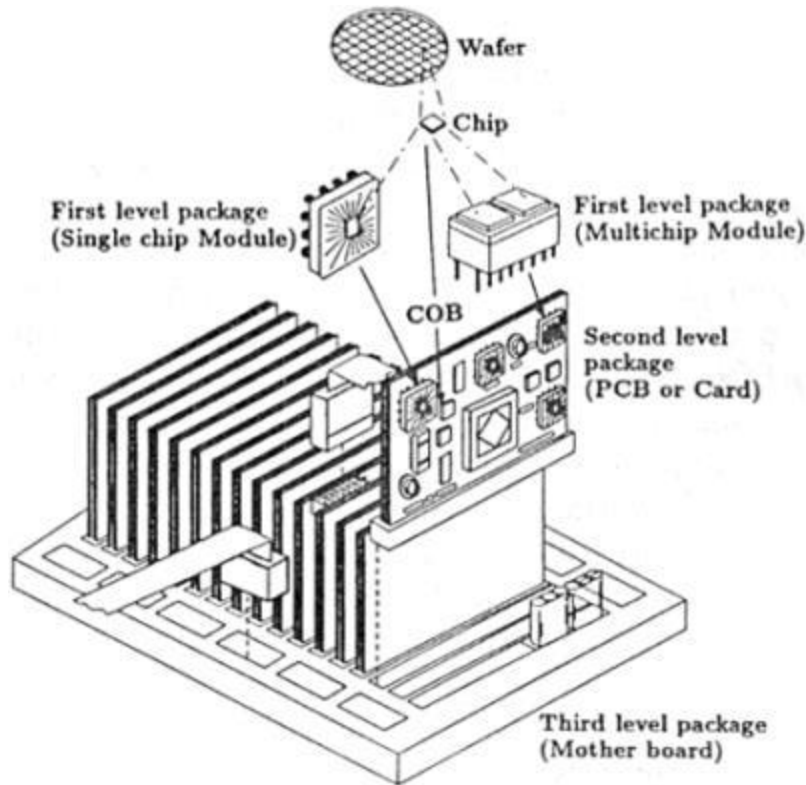
Figure 1.1 Different levels of electronic packaging [1].

Packaging governs the size, weight and shape of the electronic products and it also determines the functional diversification via package designs. With the fast evolution of electronics today, electronic packaging becomes either the enabling factor or limiting factor. Very often, packaging materials become the top priority in a package design, because they can contribute significantly to the device performance, functionality, reliability and cost of the final product. Yet, the emerging package types, such as 3D packaging, die and wafer stacking, wafer level packaging, system in package, and new device types including Microelectromechanical systems (MEMS), optoelectronics, Radio-frequency devices (RF), sensors, and flexible/stretchable devices, pose more stringent requirements for materials. For example, the 3D stacking of chips and silicon-in-packaging structures needs materials with improved thermal dissipation capability;

2

increased input/output (I/O) density needs materials with excellent conductivity and current carrying capability; flexible/stretchable devices needs components with high mechanical compliance; and ever shrinking geometries of electronics needs better fabrication and processing methods.

The present dissertation is focused on electrically conductive polymer composites used in electronic packaging. In the following section, we will review the recent findings and applications in electronic packaging of silver filled conductive adhesives and carbon based conductive composites, respectively.

1.2 Silver-based electrically conductive adhesives

1.2.1 Introduction

Electrically conductive polymer composites are polymer composites filled with conductive fillers. The polymer matrices can be thermoplastics, thermosets, or elastomers. The conductive fillers can be any conductive elements, including metals, carbon materials and conductive polymers. The conductive fillers provide the electrical properties and the polymeric matrices provide the mechanical properties.

In this section, we will mainly discuss silver filled electrically conductive composites, also known as electrically conductive adhesives (ECAs).

ECAs can be categorized with respect to conductive filler loading level into isotropically conductive adhesives (ICAs), anisotropically conductive adhesives (ACAs) and non-conductive adhesives (NCAs) (Figure 1.2). For ICAs, the loading level of conductive fillers exceeds the percolation threshold, providing electrical conductivity in all directions. For ACA, the loading level of conductive fillers is below the percolation threshold, and they only provide a unidirectional electrical conductivity in the vertical

3

direction when pressure is applied with heat treatment. For NCAs, although the name sounds like a paradox, they are used to provide electrical interconnects by creating mechanical tension between opposing conductors.
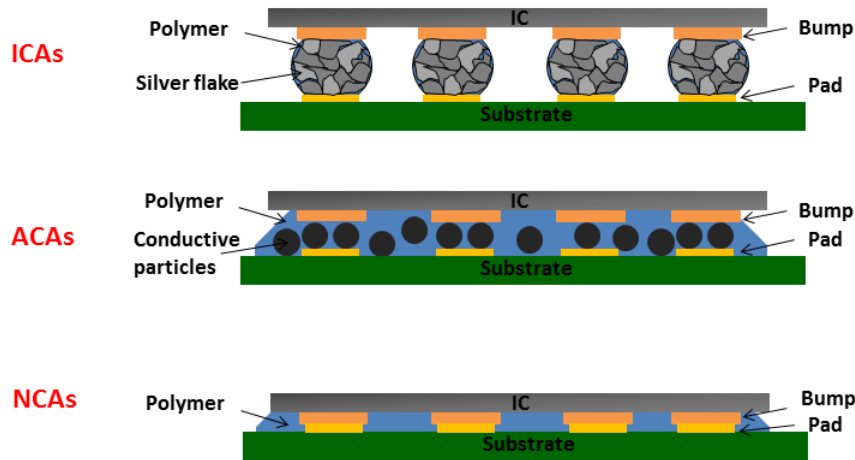
Figure 1.2 Schematic illustration of ICAs, ACAs and NCAs.

1.2.2 Isotropic conductive adhesives and their applications

ICAs, also called as "polymer solders", have almost identical electrical conductivity in all directions due a large filler loading. Both thermosets and thermoplastics are used as the polymer matrix in ICAs. Although thermoplastic ICAs have "reworkability", the degradation of adhesion at high temperature and porosity caused by trapped solvents limit their wide use. Most of commercial ICAs are based on thermosetting resins. Thermoset epoxies are by far the most common binders due to the combination of good adhesive strength, chemical and corrosion resistances and low cost. With the development of flexible electronics and to solve the problem of high rigidity of epoxy-based ICAs, rubbers such as polyurethane [2, 3], silicone [4-6], polyurethane modified epoxy [7, 8], and nitrile rubber [9] are studied as polymer matrices recently. For the conductive fillers, while silver, gold, nickel, copper and carbon are all used in ICAs,

4

silver are the most commonly used conductive fillers because of the highest conductivity, the lower cost than gold, and better oxidation resistance than copper and nickel. Also in contrast of most metal oxide that are insulating, silver oxide is conductive.

The most common application of ICAs is die attach material where bare silicon die are adhered to lead frames in level 1 packaging. ICAs can also be used in flip-chip interconnection and surface mount technology (SMT). Compared to solders, ICAs offer many advantages such as lower stresses on IC die due to low material moduli, low curing temperature, ease of use in a manufacturing environment, and environmental-friendliness [10, 11]. However, the electrical conductivity, thermal conductivity, current carrying capability needs to be improved.

1.2.3 **Anisotropic conductive adhesives and their applications**

ACAs, sometimes also called anisotropic conductive films (ACFs) provide uni-directional electrical conductivity in the vertical or Z-axis. This directional conductivity is achieved by using a relatively low volume loading of conductive filler (5–20 vol.%). The low filler loading is not sufficient to form conductive network throughout the polymer matrix. Therefore, ACAs are insulating in the X-Y direction. The conductivity in Z-direction is achieved either by applying heat and pressure simultaneously in the Z-direction until the particles bridge the two conductor surfaces or by alignment of magnetic fillers under magnetic field.

Because ACAs are insulating in X-Y direction, they are well-suited for very fine pitch interconnection and for interconnection in flat panel displays. ACAs have been widely used in various packaging technologies for flat panel display such as tape carrier package (TCP), chip on flex (COF) and chip on glass (COG) to achieve smaller, lighter

5

and thinner displays. Besides displays, it also finds applications in flex circuits and SMT

for chip-scale package (CSP)[12], and flip–chip attachment [13, 14].

1.2.4 **Improve the conductivity of ECAs**

One concern to replace solders with ECAs is the limited electrical conductivity.

Therefore, many studies are focused on improving the electrical conductivity of ECAs.

Generally, there are three strategies; namely decreasing the inter-particle distance,

removing the surfactants on conductive fillers, and nanoparticles sintering.

1.2.4.1 <u>Decreasing the inter-particle distance</u>

ECAs are basically composites with insulating matrix and conductive filler. The

resistance of a conductive composite usually consists of two main components: the

resistance from conductive fillers, and the contact resistance between two neighboring

particles [15], where the latter one is much larger than the former one [16]. For contact

resistance, tunneling is the main mechanism for conduction. According to the tunneling

model by Simmons [17-20], the composite resistance is given by

$$R_c = \frac{M}{N} \frac{8\pi h s}{3a^2 \gamma e^2} exp(\gamma s), \quad \gamma = \frac{4\pi}{h} \sqrt{2m\varphi} \qquad (1)$$

where M is the number of conducting particles per path, N is the number of

conduction paths, m and e are the mass and charge of an electron, respectively, h is

Planck's constant, φ, s and α are the height of the potential barrier, the tunneling

distance and the effective cross-section area where tunneling occurs, respectively. From

this equation, it is clear that tunneling distance is one dominating factor for the

conductivity of ECAs. Therefore, several reports are focused on reducing the interparticle

distance by compressing the fillers.

6

Mechanical compression by heat pressing has been widely reported as an effective way to compact the metal fillers after the pattern are printed. Chen et al, Leung and Lam, both report an increase in conductivity after heating pressing [21, 22]. Lu et al found that the shrinkage of thermoset matrix during curing can be another driving force to compact the fillers. During curing, the resin shrinks and draws the conductive fillers closer to each other. The decrease in inter-filler distance helps to reduce the contact resistance of ECAs [23]. As a result, during formulating of ECAs, selecting resins with higher cross-linking density and higher shrinkage after curing is favored to improve the electrical conductivity [24].

1.2.4.2   Removing the surfactants on silver fillers

Silver flakes used in ECAs are also often coated with a layer of surfactants. These surfactants play an important role in facilitating dispersion in ECA matrix and decrease the viscosity of the ECA [25-27]. Considering the high filler loading level of ECAs, the dispersion and rheology control is indispensable for the performance and printing process of ECAs. However, the insulating surfactants become undesirable for electron conduction; they form a large energy barrier for the electron tunneling between neighboring flakes. Therefore, to improve conductivity, the surfactant layer should be removed during the curing of ECA. For silver flakes, long chain fatty acids are usually used to treat the surface and they form a silver salt complex [25-27]. Lu et al [27] studied thermal stability of these silver salt complex. Thermal oxidation of these surfactants during high-temperature curing can improve the electrical conductivity of ECAs [28]. But the high curing temperature may not be compatible with some plastic substrates. Li et al [29-31] studied replacing the long chain fatty acid salt with a short chain dicarboxylic

7

acid because of the strong affinity of carboxylic functional group (–COOH) to silver and stronger acidity of such short chain dicarboxylic acids. The short chain acid can reduce the inter-particle distance and thus easier electronic tunneling/transportation between Ag flakes in ECAs.

1.2.4.3 <u>Sintering of fillers</u>

As shown in Equation (1), the contact resistance can be reduced by cutting down the contact spots and increasing the contact area. One approach to reduce the contact resistance is incorporating some nanoparticles into the ECAs and sintering these nanoarpticles [32-37]. These metal nanoparticles can be accommodated into the small spaces between neighboring flakes and get sintered. The sintering forms some metallurgical joints between neighboring particles, thus a significantly higher conductivity of 10^5 S/cm can be observed [28, 35, 37].

Similar to silver flakes, nanoparticles are stabilized by surfactants, which act as insulators between particles. Therefore, the resistance before sintering is very high. Sintering under a high temperature can remove the capping agents and form metallurgy joints between particles, but the temperature is still too high compared with the glass transition and decomposition temperatures of most polymers. Therefore, substantial efforts have been devoted to trigger sintering through methods other than heat treatment.

One of them is to introduce other energy sources, such as microwave, laser irradiation, plasma and electrical sintering. Various light sources, including laser [38] [39, 40], xenon flash lamp or even incandescent lamps [41-43] have been used to trigger the sintering of nanoparticles. The emission spectrum can be tuned to selectively couple with nanoparticles without directly affecting the substrate. Besides photonic sintering,

8

electro-magnetic heating is another efficient power source for sintering. Mark et al. reported sintering by applying DC or AC voltage[44]. Perelaer et al. utilized the fact that only the conductive particles rather than the polymer substrates absorb microwaves to selectively sinter the nanoparticle filled ECA inks by microwave [45, 46]. The advantage of microwave sintering is the ultrafast process but the disadvantage is the difficulty to accurately control the temperature of the sintering. Reinhold et al. discussed using low pressure Argon plasma for sintering of silver nanoparticles as the high energy plasma species was reported to enhanced grain boundary diffusion [47]. Yet, plasma sintering has the limitation to be applied for printing layers with greater thicknesses than the penetration depth of the plasma species.

In addition to providing energy source, another route to triggering sintering of silver nanoparticles is chemically destabilizing the polymers or surfactants wrapping the nanoparticles. The destabilization can be achieved by 1) dissolution/desorption in solvents or substrates. Wakuda et al showed that the destabilization process can be achieved by dipping the nanoparticles into alcohol solvents where the dodecylamine dispersant can be dissolved and removed [48, 49]. Mark et al found thatcommercial photo paper coated with silanol groups could promote sintering by dissolving or detaching the stabilizing ligands in silver nanoparticle-based ECAs [50]. 2) Oxidation. Coutts et al. found that the thiol ligands protecting gold nanoparticles are easy to get oxidized to lose part of the affinity of nanoparticles. Moreover, the exothermic oxidation reaction would provide energy for sintering[51]. 3) Introducing destabilization electrolytes. Grouchko et al. reported silver nanoparticles stabilized by polyacrylic acid sodium salt (PAA Na) started to sinter after adding halides that induced detachment of

9

the carboxylate group of PAA Na from the Ag surface [52]. Long et al. observed that benzoquinone stabilized silver nanoparticles also started sintering after introducing cations [53]. Magdassi neutralized the poly(acrylic acid) stabilized silver nanoparticles with oppositely charged polymers, and thus triggered the sintering of nanoparticles [54]. Sintering by chemically destabilizing the surfactants is promising for low-cost, large-scale, low-temperature sintering of nanoparticles.

The methods discussed above are mainly applicable to silver nano-ink, or ECAs with silver nanoparticles as the major fillers. For ECAs filled with flakes, which is a more common form of interconnection in electronic packaging, silver nanoparticles are added to assist the bonding between flakes [36]. The presence of polymer matrix, additives, and large size flakes make many of these sintering methods difficult to take effects. For example, silver flakes may prevent the absorption of light by the silver nanoparticles in sintering. And the destabilization electrolytes to facilitate sintering may not be compatible to the polymer matrix of ECA.

Moreover, dispersion of nanoparticles in the silver flakes-filled ECA is always a problem and not all of the metal nanoparticles participate in forming metallurgical joints between flakes. An alternative way is in-situ generation of metallic nanoparticles from the surfactant on metallic fillers during the curing process of ECAs. Metallic fillers usually contain a thin layer of surfactant as stabilizers. For example, the most commonly used metallic filler, silver are generally wrapped with a thin layer of silver salts of fatty acids [55-57]. Using the surfactant layer as the source of silver nanoparticle generation achieves the goals of surfactant layer removal and nanoparticle generation/sintering. Reducing agents including sodium borohydride [58], aldehyde [59], polyethylene glycol

10

[60] or epoxy resin with reducing groups [61] were demonstrated to be very effective to sinter the flakes and increase the electrical conductivity.

1.2.4.4 Surface modification of metallic fillers

Another approach for improving electrical conductivity is to incorporate transient liquid-phase metallic fillers in ECA formulations. The filler used is a mixture of a high-melting-point metal powder (such as Cu) and a low-melting-point alloy powder (such as Sn–Pb or Sn–In). The low-melting-alloy filler melts when its melting point is achieved during the cure of the polymer matrix. The liquid phase dissolves the high melting point particles. The liquid exists only for a short period of time and then forms an alloy and solidifies. The electrical conduction is established through a plurality of metallurgical connections in situ formed from these two powders in a polymer binder. The polymer binder with acid functional ingredient fluxes both the metal powders and the metals to be joined and facilitates the transient liquid bonding of the powders to form a stable metallurgical network for electrical conduction, and also forms an interpenetrating polymer network providing adhesion. High electrical conductivity can be achieved using this method [52] and [53]. One critical limitation of this technology is the numbers of combinations of low melting and high melting fillers. Only certain combinations of two metallic fillers which are mutually soluble exist to form this type of metallurgical interconnections.

Yang et al. studied iodination treatment of silver flakes in ECAs [62]. After iodination, nonstoichiometric silver/silver iodide nanoislands form on the silver filler surface. These nanoislands are more easily oxidized than the bare silver surface and may activate the silver filler surface.

11

1.3 Carbon-based electrically conductive composites

Although the electrical conductivity of carbon-based composites cannot be compared with silver-based ECAs, the unique combination of high-aspect ratio, low density, mechanical robustness, high surface area, high thermal conductivity make carbon-based composites, especially CNT or graphene based-composites find wide application in electronics. For example, the combination of high electrical conductivity, low density and high aspect ratio find carbon-based composites suitable to work as electromagnetic interference (EMI) shielding materials. The nanoscale dimension and high conductivity make CNT or graphene-based composites good candidate for transparent conductive electrodes for displays, solar-cells and organic light-emitting diodes (OLEDs). The combination of electrical and mechanical properties allows carbon composites to serve as sensors and actuators. Also carbon composites are widely used as flexible/stretchable conductors for flexible/stretchable electronics. In the following section, we will discuss the various applications of carbon-based composites in electronics, and how to adjust the structure of carbon-based composites to meet the requirements in each application.

1.3.1 Electromagnetic interference shielding materials

The large demand of high-speed communication leads to the fast development of high-frequency electronics. However, the electromagnetic waves produced from one device may have an adverse effect on the performance of other high-frequency devices. This effect, called EMI, has become a serious concern in modern society. EMI shielding materials are therefore developed to protect the devices as well as the radiation sources [63].

12

EMI shielding can be achieved through three ways, namely reflection, absorption and multiple-reflection of EM waves [64]. For reflection of the radiation, the shield must have mobile charge carriers to interact with the electromagnetic fields in the radiation. That is the shield needs to be electrically conducting. For absorption of the radiation by the shield, the shield should have electric and/or magnetic dipoles which interact with the electromagnetic fields in the radiation. For multiple reflections, the EMI materials need to contain large surface area or interface area to have reflections at various surfaces or interfaces.

Electrically conducting polymer composites have received enormous attention recently compared to conventional metal-based EMI shielding materials, because of their light weight, resistance to corrosion, flexibility and processing advantages (such as moldability) [63].

The EMI shielding efficiency of a composite material depends on many factors, including the intrinsic electrical conductivity of fillers, dielectric constant, and aspect ratio [63]. Although various forms of carbon particles, such as graphite [65], CB [66], and carbon fibers [67] have been used as fillers in the EMI shielding composites, more recently, CNT-based and graphene-based composites stand out as more attracting candidates. The intrinsic high conductivity, high aspect ratio of CNTs and graphene allow a better connectivity at lower filler loading. Therefore, their composites have higher SE and smaller skin depth. Also the low filler loading leads to better processibility, mechanical compliance and better adhesion when used as EMI coating. Moreover, the exceptional mechanical properties make CNTs and graphene strong reinforcement for the composites. [68].

13

Various CNT/polymer composites have been reported as EMI shielding materials, including single-walled carbon nanotube (SWNT)/epoxy composites [69, 70], SWNT/PU composites [71], multi-walled carbon nanotube (MWNT)/polystyrene (PS) foam composites [72], MWNT/ poly(methyl methacrylate) (PMMA) composites [73, 74], MWNT/PU composites [75], MWNT/polypropylene (PP), MWNT/polyaniline (PANI) composites [76], MWNT/polypyrrole composites (PPY) [76], MWNT/siloxane/poly-(urea urethane) composites [77]. The influences of wall defects [69], aspect ratio [69], and alignment of CNTs on the EMI shielding have been investigated.

Graphene also has the high aspect ratio and thus good connectivity as in the case of CNTs, therefore, more recently, graphene based composites have also been reported as effective EMI materials. These include graphene/epoxy composites [78], graphene/PMMA foam [79], graphene/polyvinylidene fluoride (PVDF) foam [80], graphene/PS foam [81], graphene/poly(ethylene oxide) (PEO)[82], and graphene/PANI[83].

1.3.2 Transparent conductive electrodes

The second application of carbon/polymer composites is transparent conductive electrodes. Thin, transparent, conducting films are widely used in liquid crystal displays, flat panel displays, plasma displays, touch panels, OLEDs, and solar cells. Currently, indium tin oxide (ITO) is the major player in these areas. However, the high cost and scarcity of indium as well as the mechanical brittleness of ITO leads to intensive studies of alternatives [84].

To meet minimum industry standards, such a material should have a sheet resistance, Rs $\leq$ 100 $\Omega/\square$, coupled with an optical transparency of T $\geq$ 90% (550 nm)

14

[85]. CNT films and thin graphene films are found to be a good candidate for transparent conductivity electrodes due to the nanometer dimension and high conductivity [86]. While most of the studies are focused on pure carbon, pure nanotube films tend to have significant surface roughness [87, 88] that can be undesirable to certain electrode applications. Therefore, CNT/polymer or graphene/polymer composite films are studied as electrodes.

Most of the studies are using conducting polymers as matrices. While composites prepared with small-ion-doped conducting polymers are unsuitable for use in applications such as OLEDs (the presence of residual mobile counter-ions can poison the emissive layer), composites prepared from conducting polymers doped with large, immobile counter-ions, such as poly(3,4-ethylenedioxythiophene) doped with poly(styrenesulfonate) (PEDOT:PSS) does not have this problem. PEDOT has been combined with carbon nanotubes to produce composites with conductivities of up to 7×104 S/m [89-94].

At the same time, polymer composites with non-conducting polymer matrices are also reported. These include CNT/PS composites with high CNT concentration [95] and CNT/polyimide composites[96].

1.3.3 **Sensors and actuator**

Carbon/polymer composites have also been reported as various sensors. The polymer matrix may swell when absorb solvents. By utilizing the changes in electrical resistivity of the composite due to polymer swelling, the CNT/polymer composites can be used as vapor sensors [97-99]. In addition, carbon fiber/polymer composites[100-103] and CNT/polymer composites [104-106] are also investigated as potential strain sensors.

15

From the resistance change, it is expected to diagnose the mechanical change of the monitored structure.

In addition to sensors, the electromechanical behavior of nanotubes/polymer composites can be used as actuators for MEMS and switches. Although most actuator research has focused on the carbon materials such as bucky-papers in liquid electrolyte, there has been an increasing interest in utilizing CNT-reinforced composites as potential actuator materials both in liquid and solid electrolyte.

In these CNT/polymer composites-based actuators, CNTs can enhance the actuator performances through two ways: 1) When the polymer used in the composites is electroactive itself, carbon nanotubes can maintain the higher strains in electroactive polymer actuators as reinforcement and can increase the electrochemical efficiency in the actuation by providing high electrical conductivity [107-110]. 2) CNTs can also be added to common polymer matrices and serve as the active actuating part [111-113].

1.3.4 Other applications

In addition to the exceptional electrical properties, the massive thermal conductivity and negative thermal expansion co-efficiency have helped the carbon materials find their applications in thermal management and CTE control [114] in electronic packaging. SWNTs [115, 116], MWNTs [117], graphene [118], graphite nanoplatelets [119] were all investigated as effective fillers to improve the thermal conductivity of polymer composites. The alignment of CNTs [117], the purity [120], filler dispersion [121], and carbon-polymer interface [122] were found to affect the final thermal conductivity of the composites.

Another important application of carbon/polymer composites for electronic packaging is power storage. Due to the large surface area and electrical conductivity, carbon materials, such as activated carbon, carbon aerogel, CNTs and graphene have been extensively studied as electrodes for supercapacitors or lithium ion batteries. Their composites with conductive polymers are also promising electrode materials. The progress of CNT/conductive polymer composites and graphene/conductive polymer composites as energy storage materials can be found in the recent reviews [123] and [124], respectively.

1.4 Research objectives and organization of the dissertation

The present dissertation aims at enhancing the properties of electrically conductive composites through the filler composition, filler surface treatment, polymer structure modification, and understanding of the polymer curing behavior to meet the requirements for different applications. These can be various properties, including the electrical conductivity, mechanical flexibility/stretchability, sensitivity as sensors, thermal stability, and dispersion of fillers. Chapters 2-6 are focused on silver-based ECAs and Chapters 7-10 are focused on carbon-based conductive composites.

Chapter 2 and Chapter 3 aim to enhance of the electrical conductivity by understanding the surface chemistry of silver flakes in epoxy-ICAs and magnetically aligned ACAs, respectively. Chapter 4 proposes to use PU-ICAs to replace conventional epoxy-ICAs in order to achieve both high electrical conductivity and good mechanical compliance. Chapter 5 and Chapter 6 focus on the conduction development mechanism of silicone-ICAs and use silicone-ICAs as stretchable conductors in radio-frequency devices.

17

Chapter 7 focuses on developing carbon/polymer composites-based sensors to diagnose the aging conditions of polymers. Chapter 8, 9,and 10 aim at solving three problems of CNT/silicone composites, namely the decreased thermal stability of silicone composites induced by the cobalt catalyst residues in CNTs, the curing inhibition of silicone rubber by functionalized CNTs, and the dispersion problem of carbon fillers in polymers.

Chapter 11 suggests several areas for future work.

CHAPTER 2 HIGH PERFORMANCE ISOTROPIC CONDUCTIVE ADHESIVES WITH ENHANCED CONDUCTIVITY

2.1 Background

ECAs based on silver filled polymers have attracted tremendous attention. They can achieve electrical resistivity of 10^{-3}-10^{-4} Ω.cm, which is orders of magnitude lower than that of conductive polymers while maintaining the properties of polymers such as adhesion, flowability and compliance [125, 126]. However, the electrical resistivity of most conventional conductive composites is still two orders of magnitude higher than that of pure metals despite a filler loading as high as 80-90 wt.%. According to previous researches, the high resistivity mainly results from the contact resistance between neighboring metallic fillers. The conduction mechanism is mostly based on physical contacts (or electrical tunneling) rather than metallurgical joints between neighboring particles [15, 127, 128].

One effective way to enhance the electrical conductivity is to incorporate metallic nanoparticles into the ECAs [32-37]. These metal nanoparticles can be sintered at much lower temperatures than bulk metal (~250 ^{o}C for silver nanoparticles vs. ~ 960 ^{o}C for bulk silver) due to the large area of active surface [16, 37, 129]. The sintering forms some metallurgical joints between neighboring particles, thus a significantly lower resistivity of 10^{-5} Ω.cm can be observed [35]. However, there are several challenges associated with the introduction of nanoparticles: 1) these metallic nanoparticles are difficult to be dispersed homogeneously within the polymer matrix. The high surface area renders them great tendency to aggregate during mixing; 2) Not all of the metal nanoparticles are

19

participated in forming metallurgical joints; and 3) the cost of metallic nanoparticles is still high.

To avoid the concerns of high cost and poor dispersion of externally introduced metallic nanoparticles and to improve the efficiency of sintering, here we introduce an approach for in-situ generation of metallic nanoparticles by chemically reducing the surfactant on metallic fillers during the curing process of ECAs. Silver flakes filled epoxy composites are used as an example.

The in-situ reduction of the surfactant layer to silver nanoparticles is able to substantially reduce the contact resistance from several aspects: 1) the removal of organic surfactant layer decreases the electrical tunneling resistance [17-20]; 2) since the silver salts are on the surface of silver, the generated silver nanoparticles only exist around each silver filler, thus, all the generated nanoparticles can take effect to bridge neighboring fillers by sintering; and 3) the removal of the surfactant layer also reduces the energy barrier of sintering and thus enables the sintering at even lower temperatures [130]. In addition to the reduced electrical resistance, this approach also has many other advantages. The in-situ synthesis avoids mixing of nanoparticles in the polymer as well as the high cost of purchasing these nanoparticles. Since this method introduces only a small amount of reducing agents, it facilitates scaling-up processing.

This chapter includes six parts, namely 1) studying of the surface chemistry of silver flakes and elucidates the chemical structure of the surfactants; 2) choosing the best reducing agents; 3) Optimizing the reduction process; 4) mechanistic study of the reduction of surface layer and generation of nanoparticles; 5) possible reaction

mechanism of the chemical reduction of silver lubricant; and 6) possible side-effect of reducing agents.

2.2 Materials and methods

2.2.1 Materials

The ECA in the present project uses epoxy as resin and silver flakes as conductive filler. Epoxy resin used is a bisphenol-F type resin, cured with anhydride. Imidazole is used as catalyst for epoxy curing. Two silver flakes, Ag-A and Ag-B, and untreated silver particles S-7000 are obtained from Ferro. Inc. Reducing agent R-1, R-2, R-3, R-4 are obtained from Sigma-Aldrich. All chemicals are used as received.

2.2.2 Preparation of ECAs

Epoxy resin is mixed with anhydride curing agent with a weight ratio of 1:0.85, then 1 wt.% catalyst was added to the mixture. In a typical ECA formulation, 80 wt.% silver flakes (Ag-A and Ag-B with a mass ratio of 1:1), 20 wt.% of the epoxy mixture and appropriate amount of reducing agents are mixed together by Vertex. To measure the electrical resistivity, two strips of a Kapton tape (Dupont) are applied onto a pre-cleaned glass slide and the formulated ECA paste is printed on the glass slide. Then the pastes are thermally cured in an air-circulating oven.
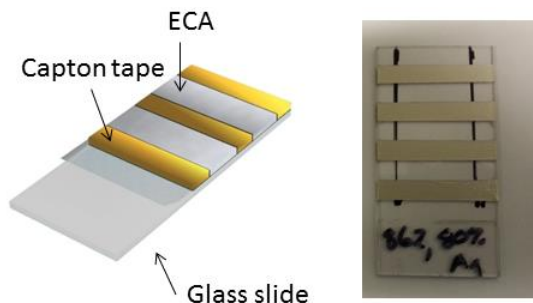
Figure 2.1 Test coupons for electrical conductivity measurement.

2.2.3 Characterization of silver flakes

Weight loss of silver flakes during heating in air is studied using thermogravimetric analyzer (TGA, TA Instruments, model Q5000). The heating rate is 10 ^{o}C /min.

Morphologies of the untreated and treated silver flakes are observed by field emission scanning electron microscopy (SEM, LEO 1530).

Decomposition of the lubricants on the surface of silver flakes is studied by differential scanning calorimetry (DSC, TA Instruments, Q2000). The heating rate was 10 ^{o}C/min.

Raman spectra of silver flakes are obtained by using a LabRAM ARAMIS Raman confocal microscope (HORIBA Jobin Yvon) equipped with a 532 nm diode pumped solid state laser. Si wafer is used as a substrate for Raman measurements.

The nanoparticle generated by reacting silver stearate and reducing agents were dispersed in toluene and dried in a copper grid before characterized by transmission electron microscopy (TEM, JEOL 100CX). The nanoparticle colloidal in toluene was also characterized by UV-VIS spectroscopy (Shimadzu UV-2450). Powder X-ray diffraction (XRD) analysis was carried out with a Philips X-pert alpha-1 diffractometer, using Cu K_{α} radiation (45 Kv and 40 mA).

2.2.4 Characterization of ECAs

Bulk resistances (R) of cured ECA strips are measured by a Keithley 2000 multimeter according to a typical four-probe method. The widths and lengths of the specimens were measured by digital caliber (VWR). The thickness of the specimen is measured by Heidenhain (thickness measuring equipment, ND 281B, Germany). Bulk

22

resistivity, ρ, is calculated using $\rho = Rtw/l$, where l, w, t are the length, width and thickness of the sample, respectively.

The curing of ECA or epoxy resin and the glass transition temperature of cured resin are performed by DSC (TA Instruments, Q2000). The heating rate was 10 $^\circ$C/min.

Fourier-Transform Infrared Spectroscope (FT-IR, Nicolet, Magna IR 560) with an in-situ heating apparatus is used to investigate the reaction between reducing agents and silver stearate and the reaction between reducing agents and epoxy resin. The in-situ heating program is ramping from 40 °C to 170 °C by 10 °C/min. The spectra are collected during heating. A resolution of 2 cm^{-1} was used over 64 scans. Background spectra were obtained before the first analysis of each sample with only KBr pellets to ensure that there is no contamination.

Three point bending tests are performed on the cured epoxy resins with different concentrations of reducing agents. A rectangular shape epoxy samples are prepared by casting and curing in a Teflon mold. The span length is 20mm and compression speed is 5mm/min.

2.3   Results and discussion

2.3.1   Characterization of the silver flake surfaces

The resistance of ECA usually consists of two main components: the resistance from conductive fillers and the contact resistance between two neighboring particles [15]. According to our previous studies, the contact resistance is much larger than the intrinsic resistance of conductive fillers, usually because of the insulation layer on the surface of conductive fillers [16] (Figure 2.2). For most of the commercial silver flakes, this insulation layer is a surfactant that protects the flakes from oxidation and also lubricates

23

the silver flakes to lower down the viscosity when they are mixed with a resin [55-57]. This layer is beneficial for the processibility and stability of the ECAs. But it forms an insulation barrier to obstacle the electrical conduction, which can be one of major contributors to the high contact resistance.
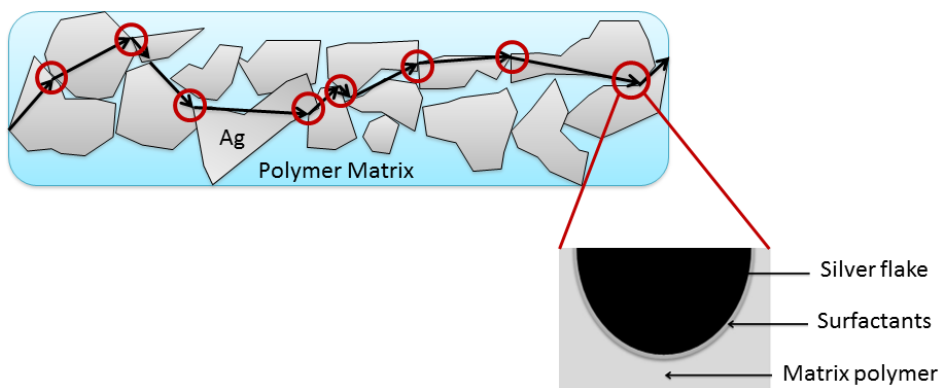
Figure 2.2 The contact resistance between silver flakes are much larger than the intrinsic resistance of silver itself.

To remove these surfactants, it is important to understand the chemical structure of these surfactants.

Figure 2.3 shows Raman spectra of the silver flakes Ag-A and Ag-B, respectively. For Ag-B, the presence of carboxylate groups on the surface of silver flakes is verified by the symmetric ($v_s(COO^-)$) stretching at 1393 cm^{-1} and asymmetric ($v_{as}(COO^-)$) stretching at 1565 cm^{-1} [131]. The strong intensity of these peaks indicates that the surfactants are acids bonded to the surface as anions. The peak at 927 cm^{-1} is assigned to the C–COO$^-$ stretching [131]. The peaks at 1092 and 1149 cm^{-1} are from the C-C backbones [132]. The peaks at 1286 and 1431 cm^{-1} are attributed to the twist and scissor of methylene groups [132]. The Surface Enhanced Raman (SERS) peaks of C–H stretching of the lubricant on Ag are well resolved in the region of 2800-2950 cm^{-1} [61]. Ag-A shows peaks also corresponding to carboxylate groups, C-C backbones and methylene groups in

24

similar positions with Ag-B. The Raman spectra indicate that both flakes are covered with a long chain fatty acid surfactant and the fatty acid already forms a silver salt with the silver flakes.
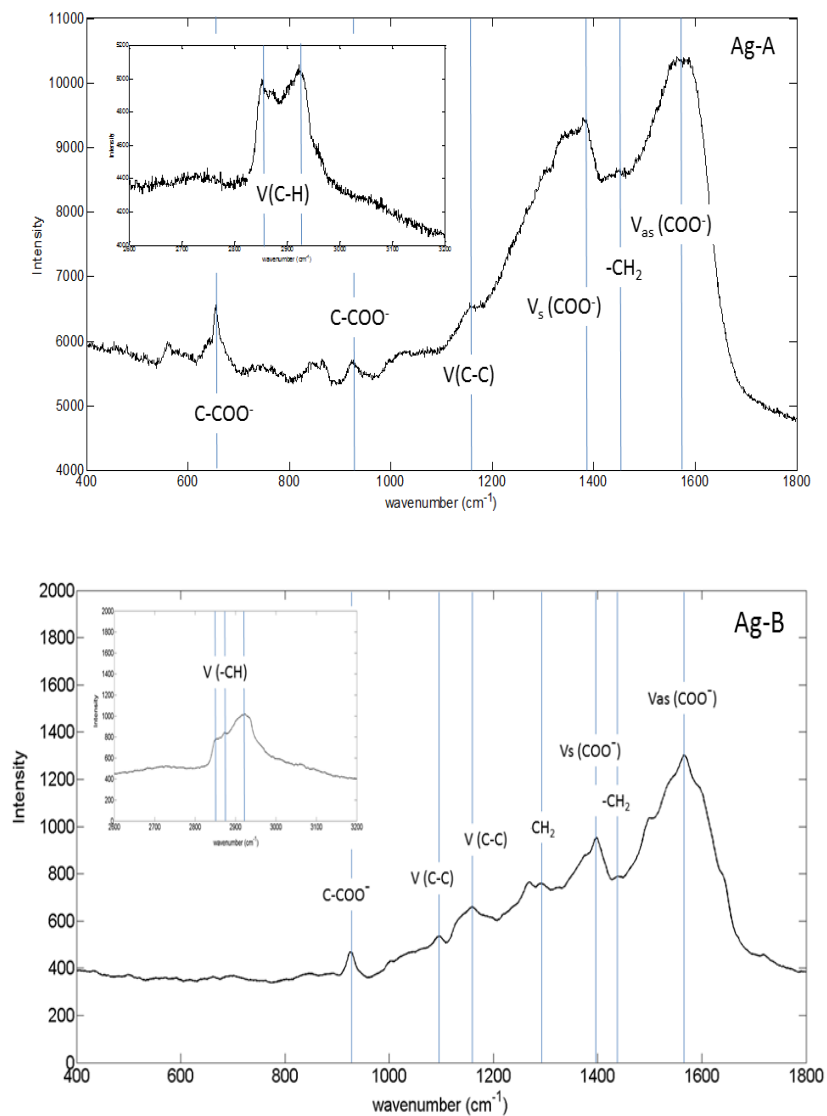
Figure 2.3 The Raman spectra of Ag-A and Ag-B. The flakes are characterized as received.

Figure 2.4 shows TGA results of the silver flakes. Ag-B and Ag-A show significant weight losses at 215.5 $^{\circ}$C and 190.31 $^{\circ}$C, respectively (Figure 2.4, inset). The weight loss of both flakes is attributed to the thermal decomposition of the surfactants on

25

the flakes. The different decomposition temperatures of Ag-A and Ag-B indicates that the two flakes are treated with different fatty acids and it is possible that the chain length of fatty acid on Ag-B is longer than the one on Ag-A. At 450 ^{o}C, the weight losses of Ag-B and Ag-A are 0.21% and 0.06%, respectively. That is, Ag-B has a thicker layer of surfactants than Ag-A. The thermal decomposition of the surfactants on silver flakes is confirmed by DSC measurements of the two flakes. Both Ag-B and Ag-A show endothermic peaks at 243.59 ^{o}C and 228.73 ^{o}C, respectively (Figure 2.5). These exothermic DSC peaks result from the oxidation of the lubricant layer. Lu et al. found that silver flakes lubricated with fatty acids of a longer chain showed exothermic DSC peaks at higher temperatures [55-57]. Therefore, it is possible that the lubricant on the surface of Ag-B may have a longer chain than that on Ag-A, which is consistent with TGA results.
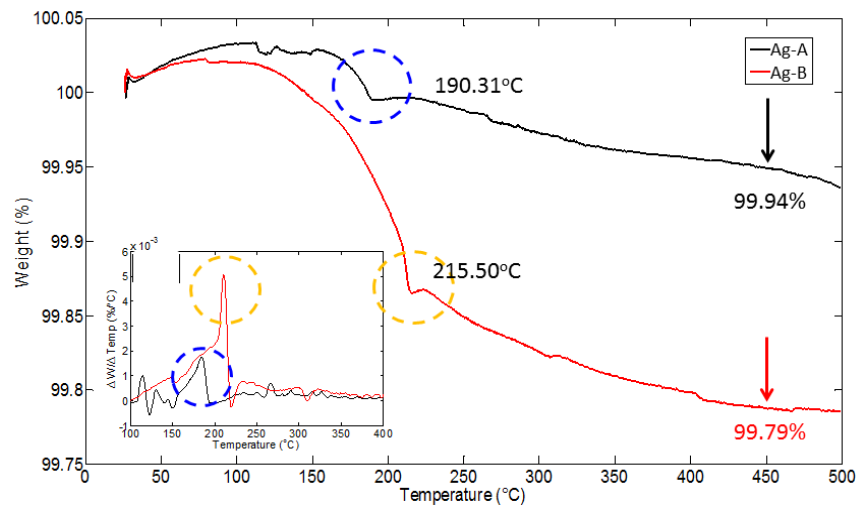
Figure 2.4 TGA of Ag-A and Ag-B. Inset is the first derivative of weight loss with temperature.
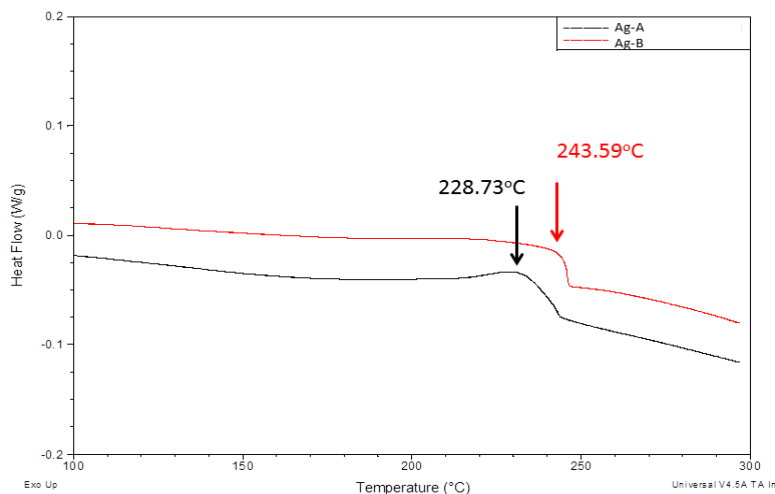
Figure 2.5 DSC of Ag-A and Ag-B.

In sum, the two commercial silver flakes Ag-B and Ag-A are coated with a thin layer of surfactants, as demonstrated by TGA, DSC and Raman spectra. The composition of the surfactants is silver salts of fatty acids for both flakes. Ag-B has a thicker layer of surfactants than Ag-A, and the chain length of the fatty acid on Ag-B is probably longer than that on Ag-A.

2.3.2 Searching for reducing agents

The next step is to find some proper reducing agents to reduce these salts to silver nanoparticles. Although seldom efforts have been paid to reduce the silver surfactants on the flakes in ECA systems, extensive studies have been published on synthesis of silver nanoparticles from silver salts by chemical reduction. Many reducing agents have been demonstrated to effectively reduce silver salts to silver nanoparticles at mild conditions.

We select four types of reducing agents in the present study. To compare the effectiveness and select the best reducing agents, we keep the basic ECA formulation (80 wt.% silver flakes, 20 wt.% resin mixture and 1wt.% reducing agent) and curing profile

27

(150 $^{\circ}$C for 1 hour) the same while only change the reducing agents. The bulk resistivity

of the ECAs with various reducing agents and the control ECA sample (sample without

any reducing agents) are shown in the Figure 2.6. The control sample yield a bulk

resistivity of 4.44×10^{-4} Ω.cm. All the reducing agents show clear effects to reduce the

resistivity. The bulk resistivity after adding R-1, R-2, R-3 and R-4 decrease to 2.50×10^{-4}

Ω.cm, 1.41×10^{-4} Ω.cm, 2.37×10^{-4} Ω.cm, 2.73×10^{-4} Ω.cm, respectively. It is interesting to

find that the R-2 has a slightly stronger effect than other reducing agents.
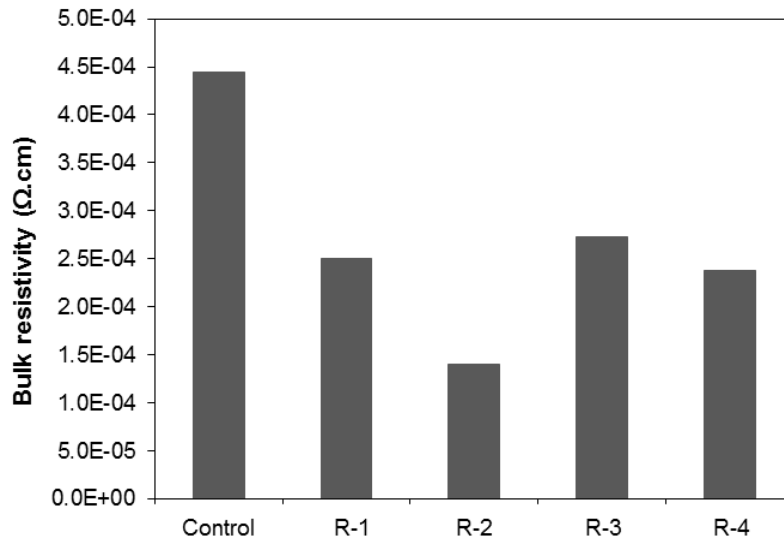
Figure 2.6 Bulk resistivity of ECAs without reducing agents and with 1 wt.% different
reducing agents.

Therefore, R-2 was selected as the best reducing agents and the optimization and

reducing mechanism study was focused on R-2.

2.3.3 **Optimization of the reduction process**

The optimization process includes the tuning of the concentration of R-2 and the

curing temperature. Figure 2.7 shows the bulk resistivity of ECAs at different

concentration of R-2. All the samples are cured at 180 $^{\circ}$C. Generally 180 $^{\circ}$C can yield a

smaller resistivity than the samples cured at 150 $^{\circ}$C. This is because higher temperature

helps with the sintering process of the formed silver nanoparticles. The resistivity

increases slightly with the concentration of R-2 from 0.5 wt.% to 4 wt%. When reaching

5 wt.%, however, the resistivity drops to $8.7 \times 10^{-5}\Omega$.cm. When further increasing the

concentration of R-2, the resistivity increases again. Therefore, in terms of electrical

resistivity, the optimal concentration of R-2 is found to be 5 wt.%. Then ECAs with 5

wt.% R-2 are cured at different temperatures from 150 $^{\circ}$C to 180 $^{\circ}$C for 1 hour (

      Figure 2.8). The resistivity decreases with the curing temperature as expected,

because the higher temperature promotes the sintering process of the generated

nanoparticles. When reaching 170 $^{\circ}$C, the resistivity gets to a plateau and raising the

temperature further does not decrease the resistivity any more. The optimal curing

temperature was thus set to be 170 $^{\circ}$C.
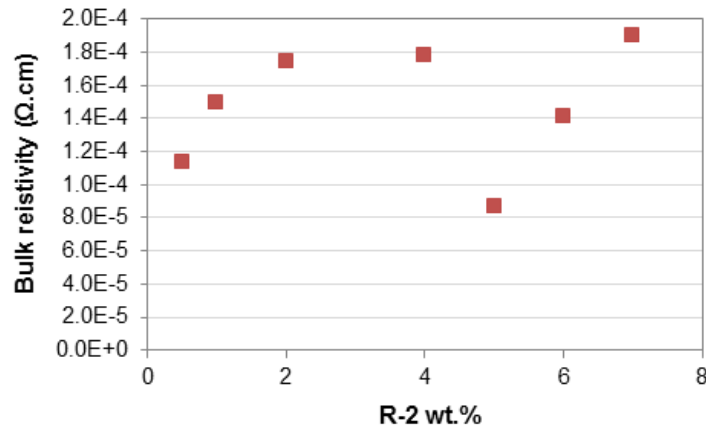
Figure 2.7 Bulk resistivity of ECAs with different concentrations of R-2. All the samples
are cured at 180 $^{\circ}$C for 1 hour.

29
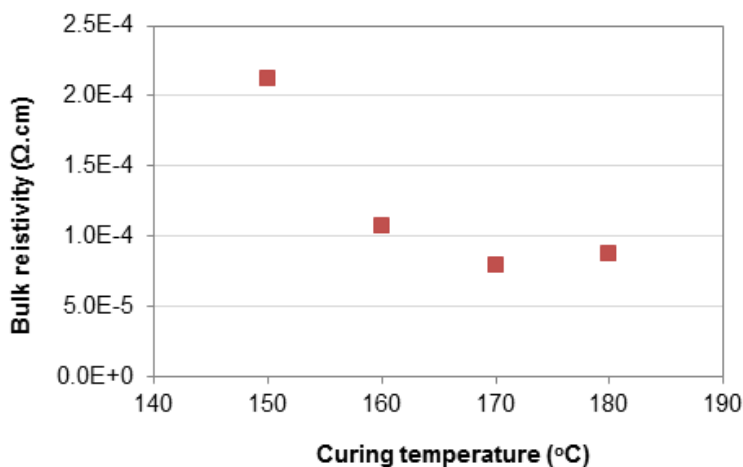
Figure 2.8 Bulk resistivity of ECAs with 5 wt.% of R-2 cured at different temperatures for 1 hour.

2.3.4 **Mechanism study**

Now the addition of reducing agent R-2 into the ECA formulation has been demonstrated to be very effective to reduce the electrical resistivity of ECAs. However, it is not clear that the reduction in resistivity follows the same mechanism as we proposed. In this part, we investigate the interaction between silver and R-2 in order to understand the chemical details of the reduced resistivity. Specifically, we aim at answering three questions:

1. Are the surfactants on silver fillers removed after adding R-2?

2. Are the surfactants chemically reduced to silver nanoparticles?

3. Do the silver nanoparticles sinter with each other and form neckings/bridges between silver flakes?

To answer the first question, the difficulty lies in that although the surfactants on silver flakes are characterized as silver salts of long-chain fatty acids, the specific type (such as the chain length, if it is saturated or unsaturated, the configuration, *etc.*) remains unknown and varies from on type of flake to the other. Therefore, we use stearic acid as

the representative of all the long-chain fatty acids that are used to treat silver flakes. Here we start with untreated silver particles and treat them with stearic acid. Then the treated silver particles are immersed in reducing agent R-2. In this way, it is expected that the particle surface can be characterized by TGA while the structure evolution of R-2 can be detected by FT-IR (Figure 2.9).
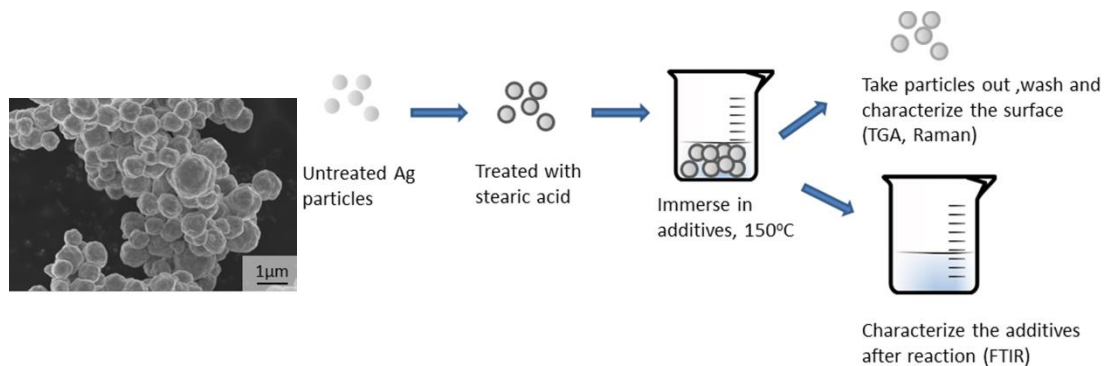
Figure 2.9 Treatment and reduction of silver particles.

To answer the second question, the difficulty is that the amount of surfactant on silver flakes (usually < 0.4wt.% of the flakes, as shown in Figure 2.4) is too small to be extracted and analyzed. Therefore, in the second step, we directly use silver stearate to immerse in R-2 and reacts with it directly. Although the silver stearate salts and the silver stearate coordinated on the surface of silver flakes may be in different geometry and state, the chemical pathway of reacting with additives may stay similar. As shown in Figure 2.10, starting with silver stearate rather than surface treated silver can provide large amount of reactants for structure evolution analysis. Moreover, if reduction reaction occurs, the obtained nanoparticle colloidal will be a solid support to the proposed mechanism.
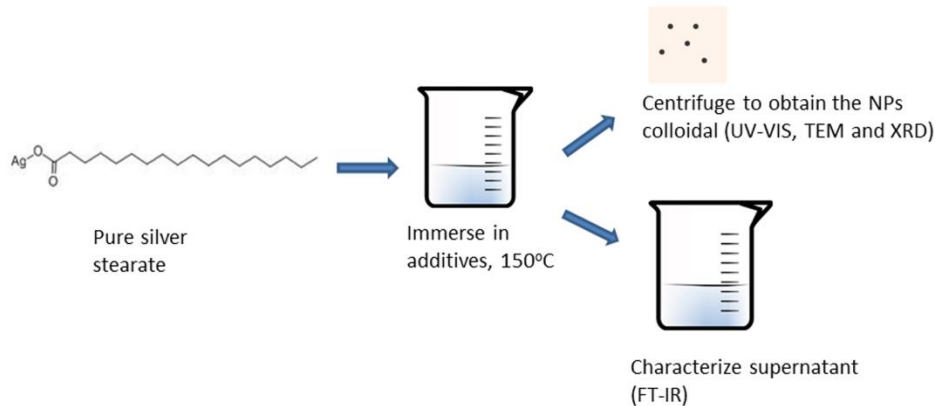
Figure 2.10 Reduction of silver stearate.

To observe the nanoparticle sintering, we will observe the surface morphology changes of silver flakes after isothermal treatment with and without R-2. But considering flakes possess different shapes and sizes, it is not convincing enough if the neckings between flakes are formed during sintering processes or it is the original shape of the flakes. Therefore, we also use fatty acid treated silver coated glass slide as the starting materials. These glass slides have flatter surfaces and it would be obvious if nanoparticles are generated (Figure 2.11).
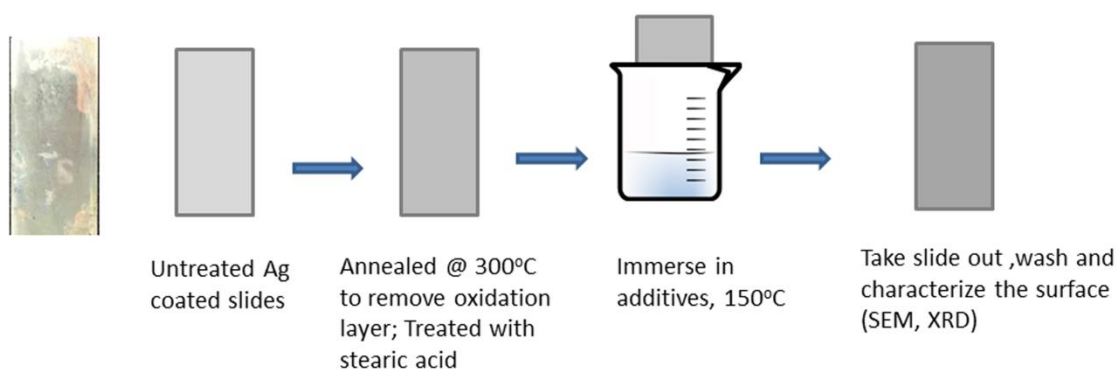
Figure 2.11 Treatment of silver coated glass slide.

2.3.4.1 R-2 react with stearic acid treated silver particles

We first treated the pristine silver particle S7000 with stearic acid according to prior study [25-27]. The treated silver particles were mixed with R-2 and put in oven at

32

150°C. As shown in Figure 2.12, at the initial stage of mixing, silver particles are floating on R-2. Although silver has a much large density than R-2, the huge surface energy support these particles floating on the liquid. R-2 has a surface tension of 47.3 mN·m^{-1} at 25 $^{\circ}$C [133] while stearic acid has a surface tension of 22.7 mN·m^{-1}[134] (Note that the existence of silver stearate won't change the surface tension of stearic acid significantly [134]). Even after 5 minutes, almost all the silver particles are floating on the liquid surface. From 10 minutes, these silver particles begin to segregate into plates while some particles settle down to the bottom of the vial. The plates become larger and moreover, more particles settle down as heating time increases. This indicates that the stearic acid surfactant has been gradually removed during the reaction with R-2, so the surface becomes less hydrophobic and thus more compatible with R-2.
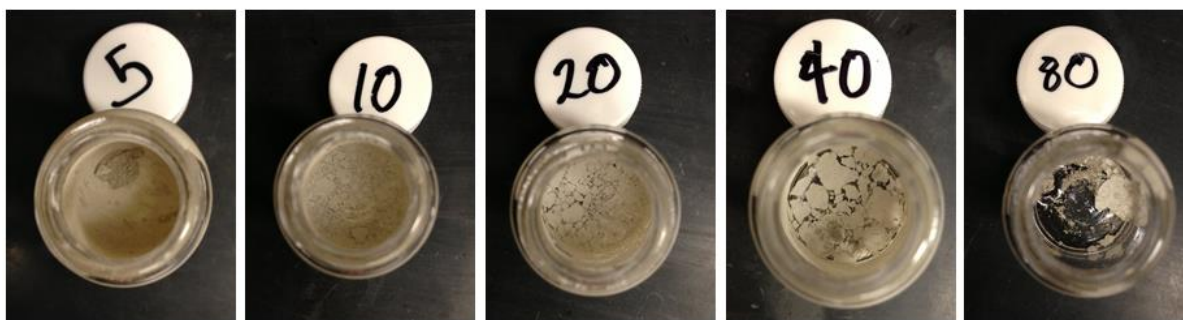
Figure 2.12 The surface tension change of stearic acid treated silver spheres after R-2 treatment. The treatment time is shown on the cap with a unit of minutes.

The removal of surfactants with R-2 is confirmed by TGA results (Figure 2.13). The stearic acid treated particles contain 0.44 wt.% surfactant. This amount decreases significantly to 0.205 wt.% after 5 minutes' treatment. The amount further decreases with treatment time; there is only approximately 0.1 wt.% after 80 minutes' treatment. Also, the maximum weight loss occurs at 200°C for untreated particles. After 5 minutes, this

33

peak moves to 215°C. After 10 minutes, this peak diminished, which is consistent with the observation in Figure 2.12.

In sum, the results of this set of experiment proves that R-2 does interact with stearic acid (more accurately silver stearate) and helps to remove this lubricant layer, as least as a fluxing agent.
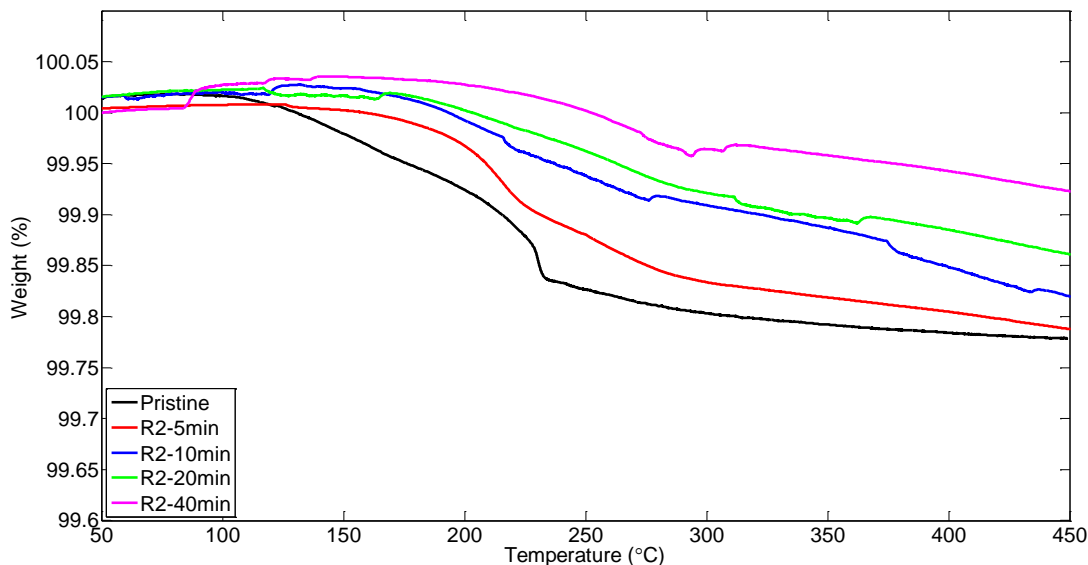
Figure 2.13 TGA of R-2 treated lubricated silver particles.

2.3.4.2 R-2 reacted with stearic acid treated silver particles

The second step is reacting the silver stearate with R-2 directly. After reaction, a white color waxy part was formed, which is similar to the products in silver stearate thermal decomposition reaction [135]. After the reaction, methanol was used to dissolve the waxy part and dark brown color nanoparticles were precipitated after centrifuging at 5000 rpm for 15 minutes. The supernatant was dried on a KBr plate and FT-IR was performed to investigate the chemical structure. As shown in Figure 2.14, a peak at 1720 cm^{-1} appears, which is assigned to the carbonyl group for free acid [136]. This indicates

that the silver stearate was reduced to form silver nanoparticles while the stearate part does not get reduced. It gets a proton and forms fatty acid again.
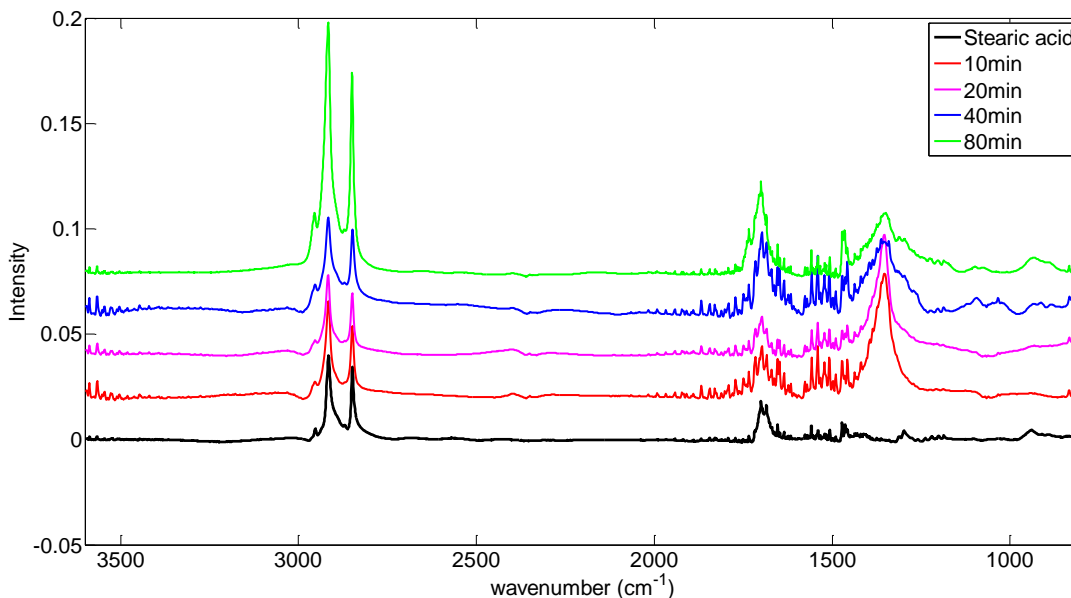
Figure 2.14 FT-IR spectra of R-2 after reacted with stearic acid treated silver particles.

The nanoparticles after centrifuge was washed and re-dispersed in toluene. UV-visible spectra were taken on the toluene solution. As shown in Figure 2.15, there is no plasmonic peak from Ag nanoparticles before 10 minutes, meaning no nanoparticles generated before 10 minutes. Starting from 20 minutes' reaction, a peak around 420-440 nm arises due to the generation of Ag nanoparticles. The peak maximum shifted from 442.5 nm to 426.5 and 423.5 nm after 20, 40 and 80 minutes' reaction, respectively. The blue shift may suggest either a decrease in particle size, or the gradual desorption of stearic acid. Stearic acid chemically adsorption on silver surface is demonstrated to red shift the resonance peak and decrease the UV peak intensity, because the adsorption changes the free electron density of silver nanoparticles and thus changes the surface

35

plasmon band of silver particles (pure silver ~390nm) [137]. Therefore, the blue shift

may indicate the desorption of stearic acid.
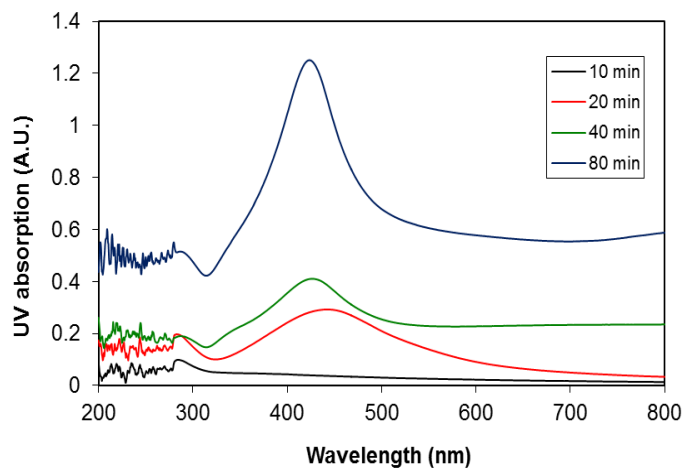
Figure 2.15 UV-Vis spectra of nanoparticles dispersed in toluene.

The nanoparticles dispersed in toluene were also observed by TEM (Figure 2.16)

and the particle size distribution was analyzed (Figure 2.17). For the sample obtained by

reacting silver stearate with R-2 for 20 minutes, since it is the initial stage of Ag

nanoparticle formation, some nanoparticles were wrapped inside surfactants. Increasing

the reaction time, it is obvious that the particle size distribution become wider and some

nanoparticles coarsen to form larger ones. The increasing in size excludes the possibility

that the blue shift in UV-visible spectra is from the decrease in nanoparticles sizes.

Therefore, the blue shift in UV-VIS probably results from the desorption of stearic acid

with time. It is also consistent with the TEM results shown here. As the surfactant shell is

very obvious in 20 minutes reaction sample, while no more shell in 40 minutes and 80

minutes samples.

36
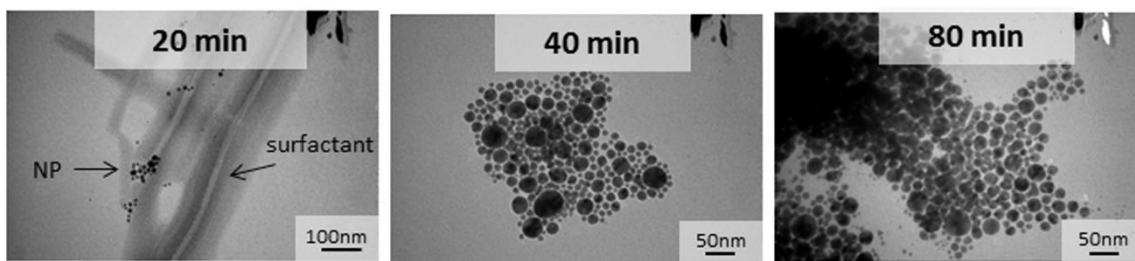
Figure 2.16 TEM images of Ag nanoparticles generated by reducing silver stearate with R-2 at different time.
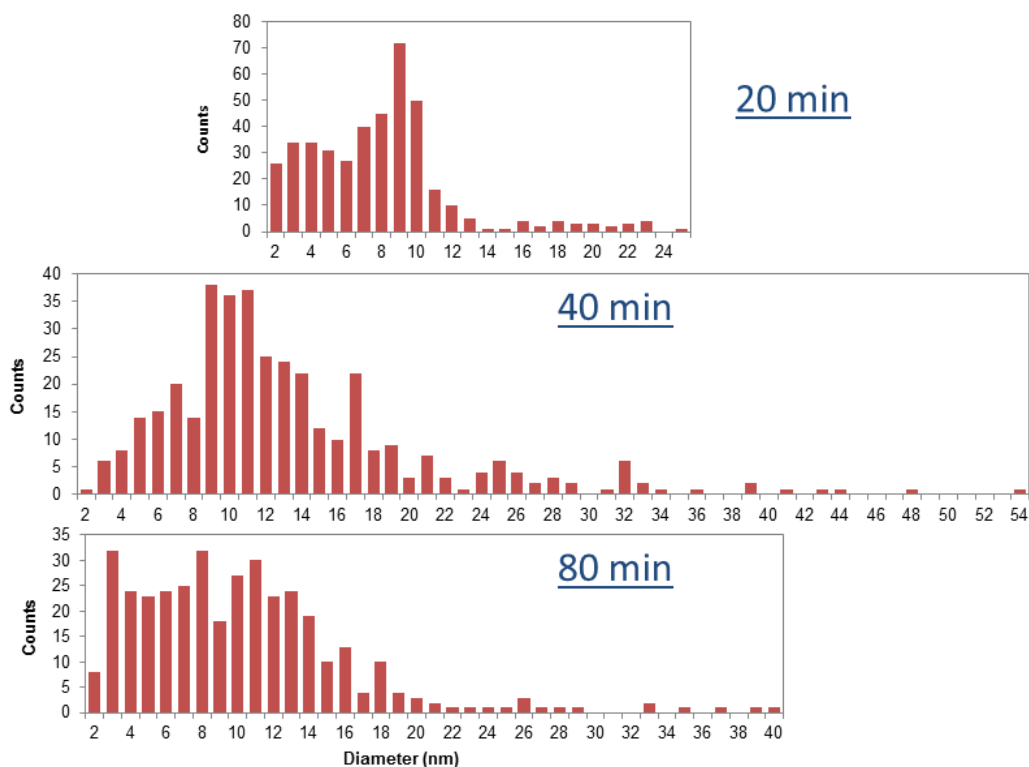
Figure 2.17 Size distribution of nanoparticles obtained from Figure 2.16.

Powder XRD was also performed to confirm the formation and particle sizes of nanoparticles. The peak at 38.2 and 44.2 resulted from (111) and (200) face of silver, respectively. This confirmed the nanoparticles are silver nanoparticles instead of silver oxide. For 20 minutes reaction, the peaks are broad and shallow, indicating really small crystalline size. While after 40 minutes reaction, the peak becomes sharp, indicating the growth of crystal size with longer reaction time. Moreover, the peak width at half

maximum keeps constant after 40 minutes, indicating that the crystalline size does not change with time after grow to 20 nm according to the Scherrer equation.
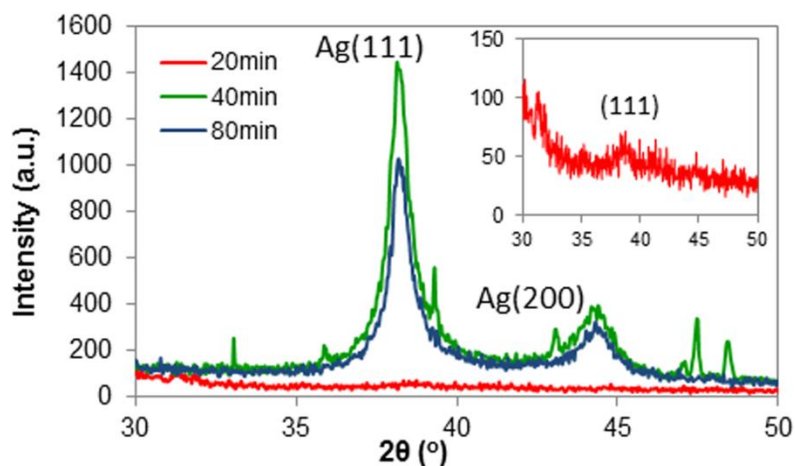
Figure 2.18 XRD of nanoparticles obtained at different reaction time.

This step answers the second question of the mechanism study that the silver stearate salt on the surface is not simply removed by the reaction with R-2; it could be chemically reduced to silver nanoparticles.

2.3.4.3   Nanoparticle sintering and growth

The sintering process was first observed in the case of silver flakes. Ag-B was treated with R-2 at 150°C. Figure 2.19 shows the surface morphology changes of silver flakes after isothermal treatment with and without R-2. The original flakes show quite smooth surfaces. After thermal treated at 150°C for 30 min, the surface of silver flakes remained relatively smooth, yet some submicron roughness can be seen on the surface. On the contrary, silver flakes immersed in R-2 during thermal treatment show very clearly the growth of silver nano/submicron-sized particles on their surfaces and at their edges. The relatively rough surface was the result of the reduction of silver carboxylate and the formation of highly surface reactive silver nano/submicron-sized particles. These

38

particles then sintered with the silver flakes to form the neckings between silver flakes.

The sintering bridges the flakes together and thus decreases the contact resistance.
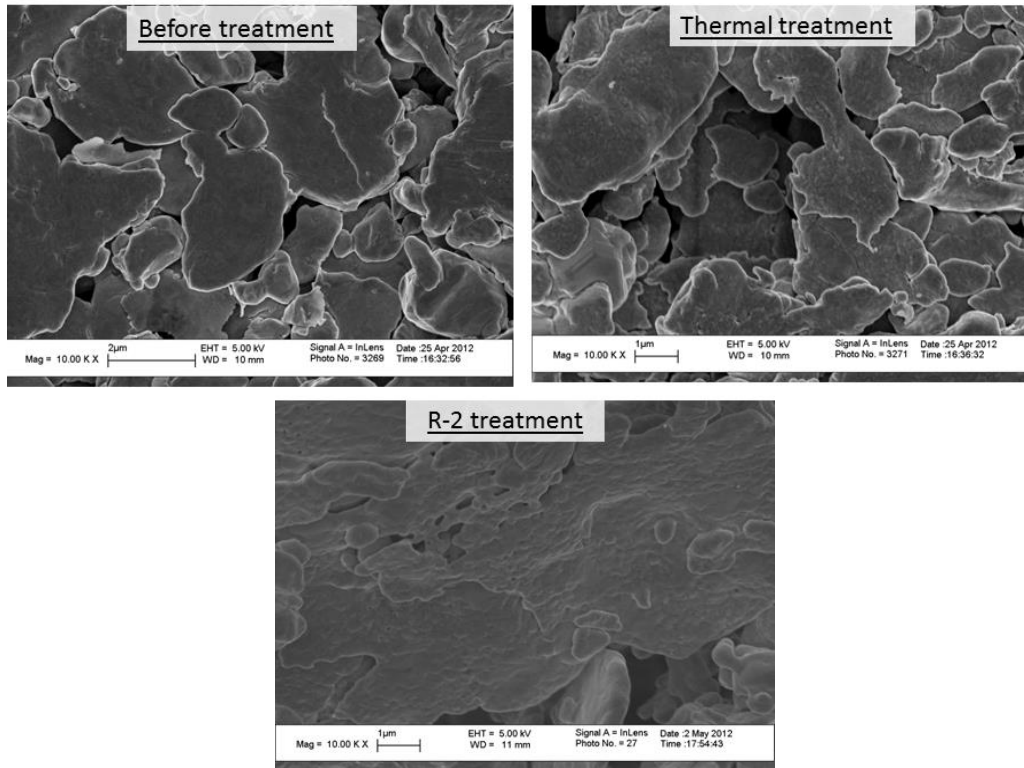
Figure 2.19 SEM images of Ag-B (a) without any treatment Ag-B, (b) after heating at 150℃ for 30 minutes, and (c) Ag-B immersed in R-2 and heated at 150 ℃ for 30 minutes.

We also performed the SEM for silver coated glass slides at different reaction time (Figure 2.20). Nanoparticles with size of tens of nanometers were generated after immersing the slide in R-2 for 10 minutes. Both the amount of particles and their sizes grow with reaction time, which confirms the possibility of nanoparticle generation and sintering in ECA as well.
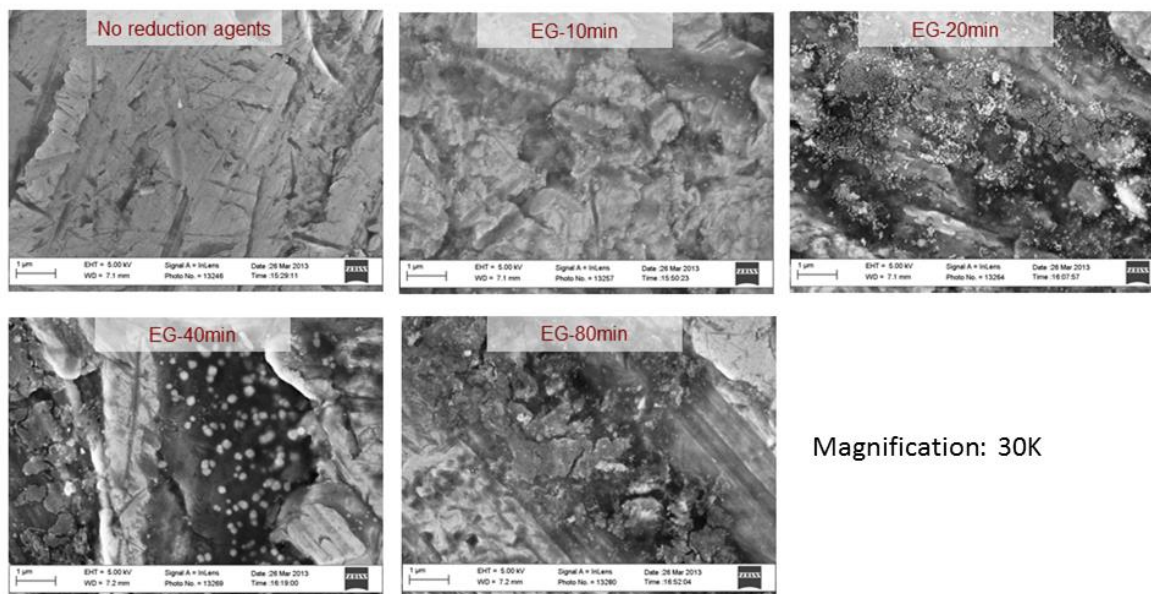
Figure 2.20 SEM images of silver coated glass after reduced by R-2 at 150°C for different time. Silver was pretreated with stearic acid for 24 hours. The magnification is 30k.

Therefore, R-2 plays a positive role to reduce the surfactants on the silver flakes and transform them into silver nanoparticles, which sinter with each other during high temperature curing. The addition of R-2 is favored to promote the sintering process and decrease the resistivity.

2.3.5 Possible reaction mechanism

There are several mechanisms proposed to explain the generation of Ag nanoparticles from silver stearate either by thermal decomposition or chemical reduction. In one scheme, the primary products are carbon dioxide, the corresponding paraffins of the fatty acid and metallic silver (scheme 1) [138]. In one study of metal acetate decomposition, Ag nanoparticles, acetic acid, carbon dioxide and hydrogen and carbon were observed as the products (scheme 2) [139]. Similar phenomenon was observed in the thermal decomposition of silver stearate in the air, where hydrocarbon chain were oxidized into gas [140]. While most of studies observed the generation of Ag

40

nanoparticles directly, Uvarov found that stearate showed phase transitions at 397 and 426 K in air. The former transition was claimed to be irreversible leading to decreased conductivity while the latter, accompanied by the thermal decomposition, resulted in increased conductivity. They attributed the first transition as hydrolysis of the silver carboxylate in humid air and silver oxide instead of silver nanoparticles were generated (scheme 3) [141]. During chemical reduction of silver stearate, Rao et al proposed that the silver stearate was reduced to Ag nanoparticles and stearate acid, while the reducing agents such as DMF and aldehyde were oxidized (scheme 4) [142].

$$CH_3(CH_2)_nCOOAg \rightarrow Ag + CO_2 + CH_3(CH_2)_nCH_3 \ (n = 0, 2, 4) \ (1)$$

$$2CH_3COOAg \rightarrow 2Ag + CH_3CO_2H + CO_2 + H_2 + C \ (2)$$

$$(CH_3(CH_2)_nCOOAg)_2 + H_2O \rightarrow 2CH_3(CH_2)_nCO_2H + Ag_2O \ (3)$$

$$2Ag^+(RCOO^-) + HCHO + H_2O \rightarrow 2(Ag^0 - RCOOH) + HCOOH \ (4)$$
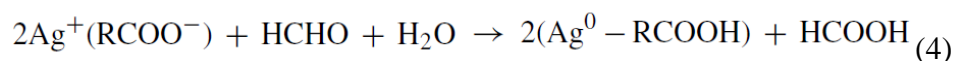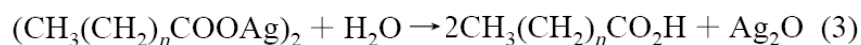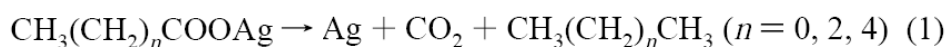
From our results, XRD, UV-VIS and TEM confirm that Ag nanoparticles can be generated by reducing silver stearate; we did not observe any generation of gas during the reaction and the FT-IR result demonstrates that the silver stearate was transformed to stearate acid after the reaction. Stearic acid would further serve as surfactants for the newly formed nanoparticles until they are also consumed as silver salt source for NP generation. Generally, the reaction mechanism could be similar with Scheme 4, although the exact oxidation product of R-2 is not clear yet.

2.3.6 Possible side effects

The possibilities of R-2 reacting with epoxy prepolymer and anhydride curing agents are studied by running DSC. For mixture of R-2 and epoxy prepolymer, no

exothermic peak is observed, only one endothermic peak at around 203 ^{o}C, which

corresponds to the evaporation of R-2. Therefore, R-2 does not react with the

prepolymer. When anhydride is mixed with R-2, an exothermic peak is observed at 133

^{o}C, which indicates the reaction between anhydride and R-2.
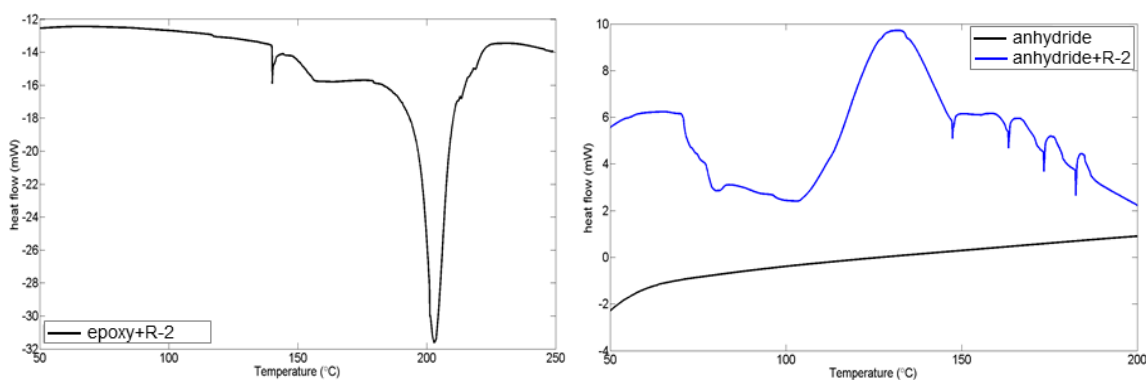
Figure 2.21 DSC of the mixture of epoxy prepolymer and R-2 (left) and the mixture of
anhydride curing agents and R-2 (right).

In order to get the details of the reaction between R-2 and anhydride, in-situ IR is

used to track the structure change of R-2/anhydride mixture during heating up process.

Figure 2.22 shows the IR spectra of the R-2/anhydride mixture at different temperature.

The gradual disappearance of the two peaks at 1860 and 1780 cm^{-1} with temperature

indicates the consumption of anhydride groups of anhydride. The peak at 1735 cm^{-1}

corresponds to the ester groups. Therefore, we assume that the R-2 open the anhydride

ring and form one acid group and an ester group [143, 144]. The formed acid group can

further react with epoxide groups in epoxy prepolymer and form another ester bonding

and secondary hydroxyl group. The secondary hydroxyl group may again react with

anhydride and epoxide group. That is, R-2 itself becomes a catalyst for epoxy curing. But

it is not clear how it will affect the overall cross-linking density of the epoxy matrix.

Then we conduct the curing profile tests, glass transition measurements and three point bending tests to detect the cross-linking density change of epoxy resin after adding R-2.
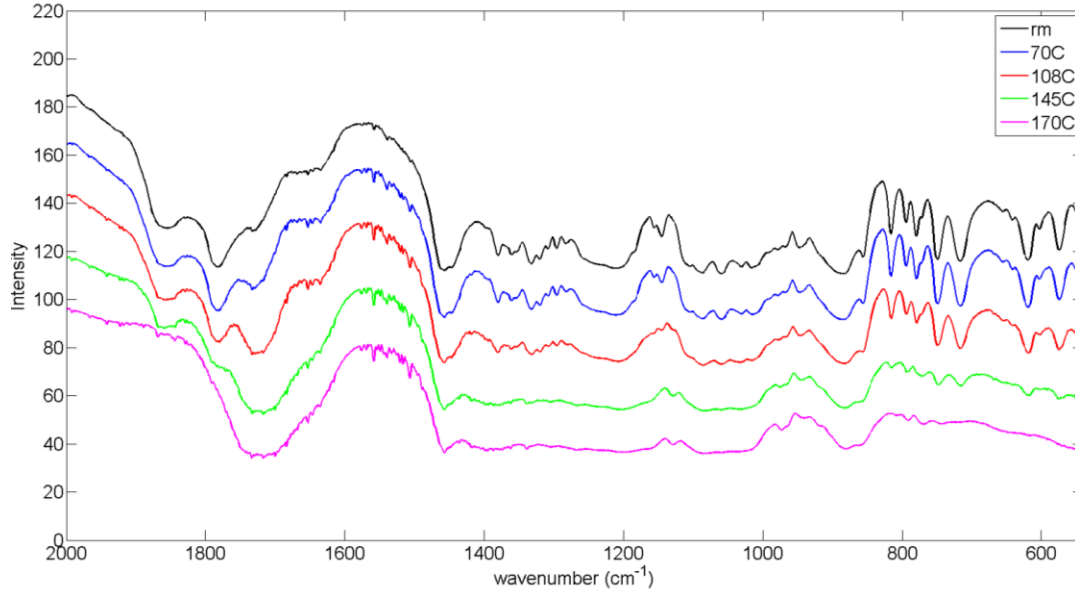
Figure 2.22 FT-IR spectra of R-2/anhydride mixture at different temperatures.

Figure 2.23 shows the curing peaks of the ECAs with different concentrations of R-2. The exothermic heat results from the curing reaction between epoxy prepolymer and anhydride. The peak intensity decreases with R-2 concentration, indicating incomplete crosslinking reaction. The glass transition temperature (T_g) of cured epoxy matrix is also measured with DSC. The control sample have a T_g of 118 ^{o}C, while after adding 0.7% and 1% R-2, the T_g decreases to 85 and 70 ^{o}C, respectively. It is demonstrated that T_g is proportional to the cross-linking density of epoxy [145]. The decrease in T_g suggests a reduced cross-linking density after adding R-2. Figure 2.24 shows the three point bending tests of control epoxy resin and resins with different concentrations of R-2. The bending modulus does not show an obvious trend with R-2 concentration but the strain at break

43

decreases dramatically with the addition of R-2. The brittleness brought by R-2 addition

also indicates a decreased cross-linking density.
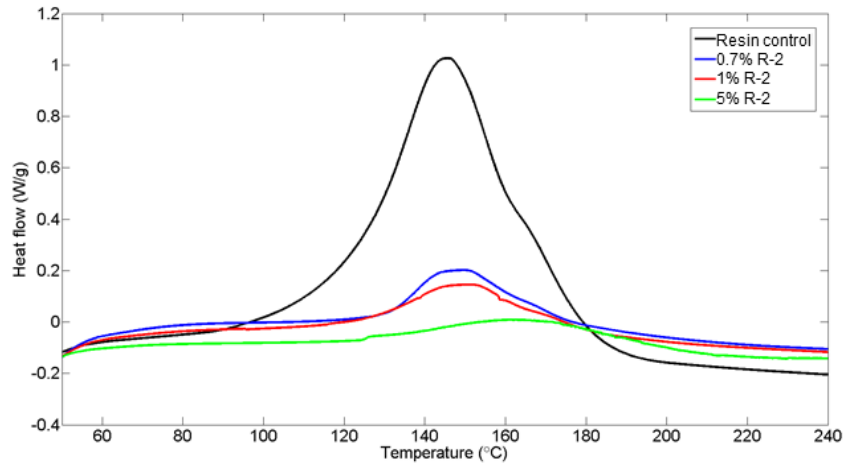
Figure 2.23 The curing peak of control ECA and ECAs with different concentrations of R-2, measured by DSC.
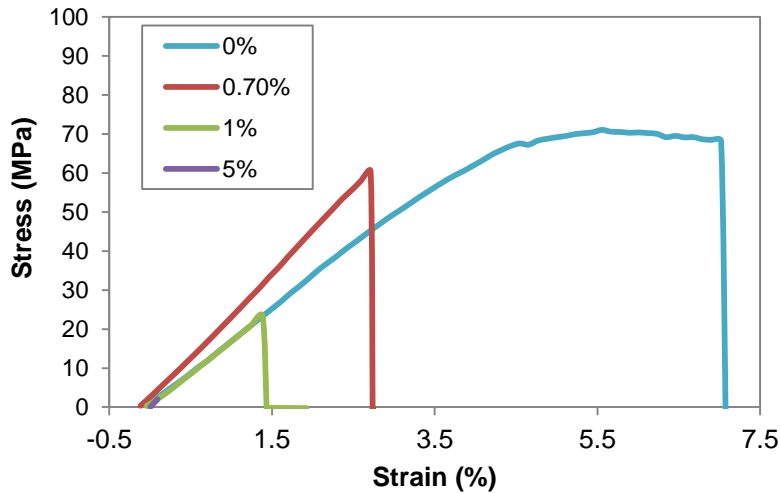
Figure 2.24 The stress-strain curve of control epoxy and epoxy resins with different concentration of R-2.

In sum, R-2 plays a double-role in the epoxy based ECA system. On the one hand, it decreases the resistivity by reducing the surfactants on silver flakes and generating nanoparticles for sintering; on the other hand, it reacts with anhydride and reduced the

cross-linking density of epoxy, rending a higher resistivity of ECAs. 5 wt.% of R-2 is the sweet spot balancing the above two effects.

2.4   Conclusion

In this work, we have demonstrated that commercial silver flakes are coated with a thin layer of surfactants, and the composition is silver salts of fatty acid. Mild reducing agents can decrease the resistivity of the composites by reducing the surfactants on silver flakes to silver nanoparticles, which are sintered together during curing. R-2 shows the best result in decreasing the resistivity. However, R-2 can adversely affect the cross-linking between epoxy prepolymer and anhydride curing agents and thus the conductivity. 5 wt.% of R-2 is the sweet spot in terms of conductivity between the two above effects.

CHAPTER 3 ANISOTROPIC ELECTRICALLY CONDUCTIVE ADHESIVES BY MAGNETIC ALIGNMENT

3.1 Introduction

The modern electronic industry is striving for reduced form-factor and increased functionality, which requires higher density of interconnection and finer pitch. The reduction in the pitch of components decreases the solder volume considerably. Smaller solder joints will have a larger portion of inter-metallics between the solder, bump and substrate metallization. The inherent brittleness of intermetallics makes these microjoints more vulnerable to the mechanical stress in reliability tests [146]. As an alternative to Sn/Pb solder, ECAs not only provide environment benefits, but also enable fine pitch interconnection without having the above-mentioned issue.

As mentioned in Chapter 1, ECAs can be classified into three categories according to the filler loading and physical properties, namely ICAs, ACAs and NCAs. ICAs provide electrical conductivity in all directions, to achieve accurate electrical interconnection in a fine pitch application, ICAs need to be precisely printed, which could be quite challenging.

ACAs only offer electrical conductivity in between the component termination and the pad (Z-direction) while maintain insulating in X,Y-directions. Therefore, ACAs can be applied over the entire footprint of the device, making the material application much easier than ICAs for fine pitch components [125]. Combined with the environmental-friendliness and low processing temperature, ACAs have demonstrated their application in LCD panel packaging [147, 148], flip-chip interconnection [149], chip-on-flex packaging [150], and chip-on-glass packaging [151].

46

Conventionally, the directional conductivity in Z-direction of ACAs is achieved by using a relatively low loading of conductive filler (5–20 vol.%) [125]. The low volume loading is insufficient for inter-particle contact and prevents conductivity in the X–Y plane of the adhesive. The Z-direction conductivity is achieved by simultaneous application of heat and pressure in Z-direction until the particles bridge the two conductor surfaces. But this process requires specialized tolling and may have the coplanarity issues because of the surface variations in the component and pad during pressure application.

Therefore, an alternative way to make ACAs was proposed, that is, using magnetic particles as fillers and enhancing the anisotropic conductivity by field alignment (Figure 3.1). The idea has been demonstrated in AT&T bell lab in 1990s [152-154]. More recently, this magnetic aligned ACAs have been applied as chip-to-chip interconnection in microwave applications, RF System-in-Package applications and wireless biomedical sensor applications [155-157], and as surface-mount interconnection in PCB level assembly[158].

However, no previous report has systematically study the approach to enhance the conductivity in Z-direction while maintain the insulation in X-,Y-directions. In this study, silver coated nickel core-shell particles are used as fillers to achieve magnetic alignment. Nickel is chosen as the magnetic core because it is ferromagnetic, the curie temperature is $355^{o}C$, much higher than the processing temperatures of ECAs, and its own resistivity is 6.93×10^{-6} $\Omega\cdot$cm, higher than iron and cobalt. The silver shell enable us to extend the interface study results from ICA (chapter 6) to lubricate and reduce the surface of silver coated nickel, and hence achieve a high conductivity and processibility at the same time.

47
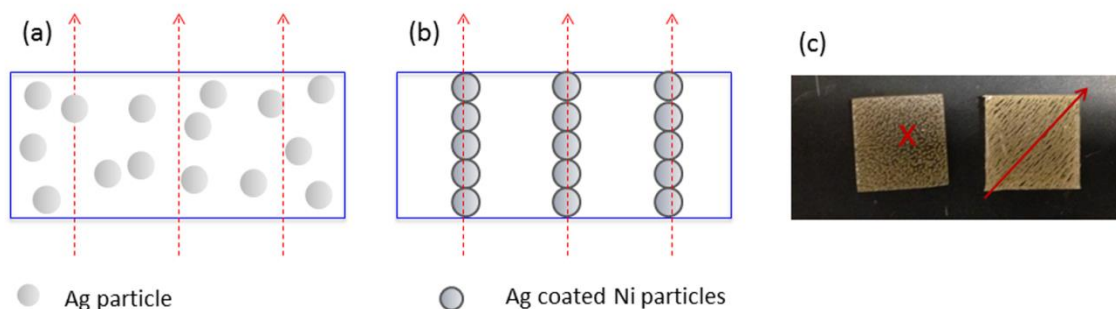
Figure 3.1 Schematic illustration of ECAs filled with (a) silver particles and (b) silver coated nickel particles in a magnetic field. (c) The conduction direction of the anisotropic ECAs can be tuned by changing the direction of applied magnetic field.

3.2 Experimental

3.2.1 Materials

The ECA here uses epoxy as resin and silver coated nickel as conductive filler. Epoxy resin used is a bisphenol-F type resin, cured with anhydride. Imidazole is used as catalyst for epoxy curing. Silver coated nickel particles Conduct-O-Fill® type 147-71 and type 147-061 were obtained from Potters industries Inc. Stearic acid, iodine was obtained from Sigma-Aldrich and used as received.

3.2.2 Preparation of silver flakes and ECAs samples

The lubrication treatment of silver coated nickel particle was performed by adding these particles into stearic acid (5:1 by weight ratio) ethanol solution at room temperature for 24 hrs.

The iodination treatment was performed by dispersing the lubricated filler particles in the ethanol solution of iodine ($0.5\mu mol\ L^{-1}$ for silver flakes and smaller

concentration of silver coated nickel particles as shown in the context) for surface modification. The reaction times were varied by 10 min ~ 72 hrs. Then a simple filtration was performed to wash out remaining iodine and the flakes were dried in a vacuum oven [62].

To prepare the ECA sample, epoxy prepolymer is mixed with anhydride with a weight ratio of 1: 0.85, then 1wt.% catalyst was added to the mixture. In a typical ECA formulation, silver coated nickel particles were mixed with the mixture by vertex and then put into a 1cm×1cm×1.2mm Teflon mode. The ECA pastes were thermally cured at 150 ^{o}C for 1 hr. A plate type, N48 rare-earth Neodymium magnet (1 inch in diameter, 1/8 inch thick) was placed under the Teflon mode to provide the magnetic field.

3.2.3 **Characterization**

The Z-direction resistance was measured by sandwiching the sample between two 1.5cm×1.5cm×1mm copper plates and measured the conductivity from top plate to the bottom plate. The bulk resistance (R) of the cured ECA was measured with four-wire method by a Keithley 2000 multimeter. The thickness of the specimen was measured by Heidenhain (thickness measuring equipment, ND 281B, Germany). Bulk resistivity, ρ, was calculated using $\rho = Rtw/l$ where l, w, t are the length, width and thickness of the sample, respectively.

Weight gain resulted from oxidation of silver coated nickel particles during heating was studied using TGA (TA instrument, model 2050) with the heating rate of 5 ^{o}C/min to 1000°C and kept in 1000°C isothermally for 600 minutes.

Morphologies of the silver coated nickel particles were studied by field emission scanning electron microcopy (SEM, LEO 1530) and element analysis was performed by the energy dispersive X-ray spectroscopy (EDS).

XRD analysis was carried out with a Philips X-pert alpha-1 diffractometer, using Cu K_α radiation (45 Kv and 40 mA).

The thermal diffusivity (α) of anisotropic ECAs was measured by the laser flash method using a LFA 471 (Netzsch). The thermal conductivity was calculated by $\kappa = \alpha C_p \rho$, in which ρ and C_p are the density and heat capacity of mhBN–epoxy composite. The C_p was measured using DSC (Q-600 TA Instruments). All thermal measurements were carried out at room temperature.

3.3 Results and discussion

3.3.1 Tuning the magnetic field

In the present study, the magnetic field is provided by a magnet. During the alignment process, the magnetic force needs to be balanced with other resistance forces, including the gravimetric force, the dragging force resulted from the viscosity matrix, and the surface tension from the interface between polymer and air. The magnetic field needs to be carefully tuned to reach such a balance. Because the magnetic field near a magnet is inversely proportional to the square of the distance from a pole of the magnet, the magnetic field is controlled by changing the distance between the sample and the magnet pole. As shown in Figure 3.2, when sample is too close to the magnet (12.45mm), the magnetic force is too strong, the magnetic aligning force overwhelms the surface tension force at the top surface of the ECA, and the columns continue to grow into dendritic structure above the surface. Therefore, the top surface is very rough. On the other hand, if

50

the magnetic field is not strong enough (14.85 mm), many columns fail to reach to the top

surface of the ECA. As a result, some of the conductive fillers are wasted and the column

density is thus decreased. Both cases of are undesirable and a proper magnetic field

strength is a key factor for optimized alignment. Here an optimized field is achieved

when the sample is placed 13.65mm away from the magnetic pole.
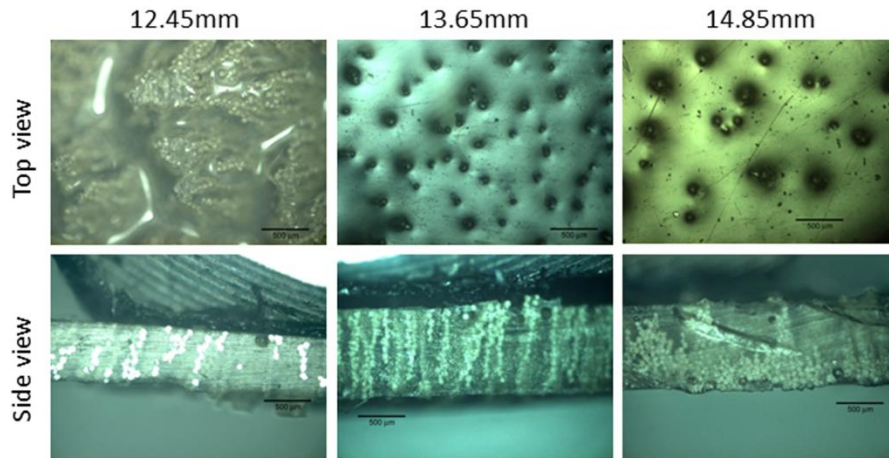
Figure 3.2 Cross-section (upper row) and top-down views (lower row) of Ag-coated
spheres (70 µm diameter, 5vol.%) in epoxy resin after magnetic alignment. The effect of
alignment is strongly affected by the magnetic field strength, which is controlled by the
distance from the magnet here.

3.3.2 **Effect of filler loading**

After optimizing the magnetic field, we tested the ECAs with different

concentration of Ag coated Ni fillers (Figure 3.3). The particles used are 70µm size

particles. For all the samples, the particles form vertical columns under magnetic field.

The columns are well-separated from each other with a fixed distance, which is attributed

to the repulsion force from neighboring columns of the same magnetic polarity. With

increasing the filler concentration, the column density per unit area increases and the

inter-column distance decreases, indicating more conduction pathways are formed. But

thanks to the repulsion force between columns, the dispersion of columns is relatively

homogeneous.
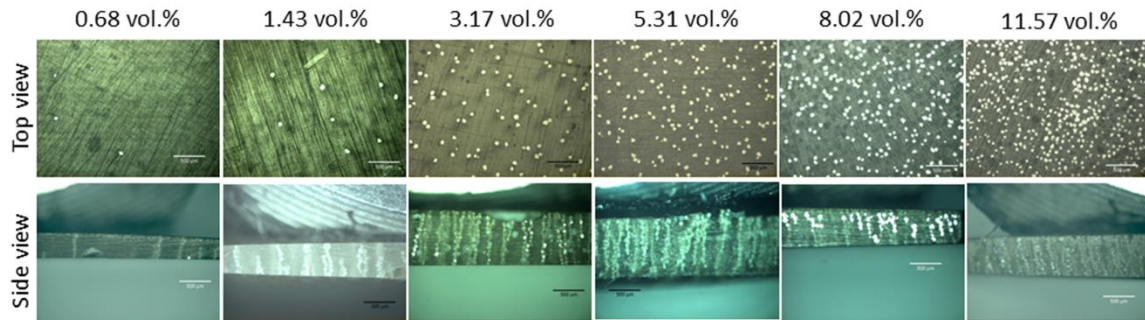
Figure 3.3 Cross-section (upper row) and top-down views (lower row) of Ag-coated spheres (70 μm diameter) with different filler loading in epoxy resin after magnetic alignment.

For all the above samples, they are all insulating horizontally and electrically

conductive vertically. We calculated the electrical conductivity in the Z-direction and

compared it with the isotropic conductivity of the randomly dispersed samples (i.e.

without magnetic field). As can be seen in Figure 3.4 (a), the randomly dispersed samples

become conductive at a high loading of 22.07vol.%. For the aligned samples, however, it

is still conductive even when the filler loading is 0.68vol.%. In addition, the conductivity

of aligned ECAs is much higher than that of randomly dispersed samples at each filler

loading. That is, we dramatically reduced the necessary filler loading for achieving the

same conductivity by filler alignment. Similarly, it is also found that the thermal

conductivity at Z-direction of the aligned samples is higher than that of the randomly

dispersed samples (Figure 3.4b). While there is an obvious percolation threshold hold for

the randomly dispersed samples, the electrical and thermal conductivity of aligned

samples follow a linear incremental trend.
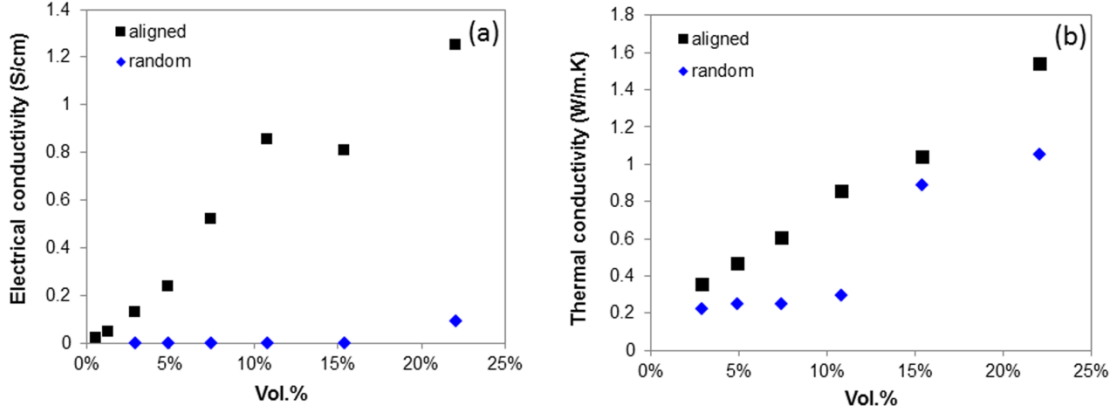
Figure 3.4 (a) Electrical conductivity and (b) thermal conductivity of Ag coated Ni filled epoxy composites with different filler loading. The blue data points represent samples with random filler distribution while the blue data points represent the samples after magnetic alignment (Z-direction resistivity).

Since the columns are well-separated with a certain distance, the inter-column distance Y and column density per unit area N_d can be calculated according to

$$\frac{\frac{\pi D^3}{6} \times \frac{t}{D} \times N_d}{t} = vol\%$$ (1)

Therefore,

$$N_d = \frac{6\ vol.\%}{\pi D^2}$$ (2)

$$Y \approx \frac{1}{\sqrt{N_d}} = \frac{D}{1.382\sqrt{vol\%}}$$ (3)

where N_d: particle column density (# of columns/ mm^2);

Y: inter-column distance (μm);

vol%: volume fraction of particles;

D: diameter of particle (μm);

t: thickness of composite (mm).

53
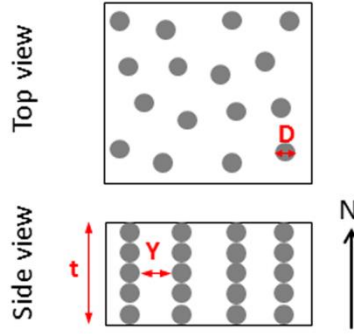
Figure 3.5 Schematic illustration of samples after alignment.

The column density and inter-column distance can also be measured from the images shown in Figure 3.3. The results are shown in Figure 3.6. The measured value and the calculated value from Equations 2 and 3 are quite consistent when the filler loading is moderate. When the loading is too low, there are very small amount of columns formed. Because the magnetic field is formed by placing the sample above a magnet, it is not homogeneous. The field is stronger at border and weaker at the center. The columns are thus more concentrated in the borders, leading to the observed deviation from the prediction. For highly loaded samples, the sterical hindrance overcomes the magnetic repulsion force, leading to some local aggregation. Therefore, there are more columns formed than predicted.
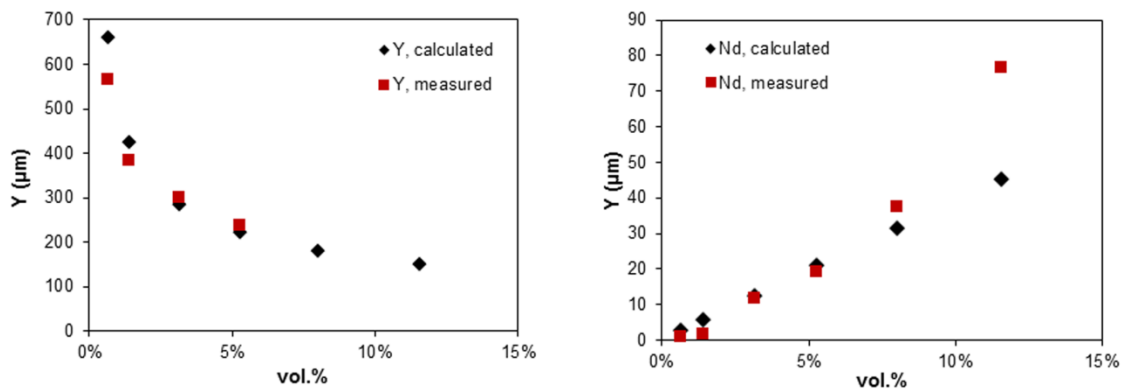
Figure 3.6 The intercolumn distance Y (left) and column density N_d (right) obtained from model predication and microscopic observation.

It is well known that the resistance of the ECA consists of the particle resistance R_p and the contact resistance between particles R_c. The current ECA can be considered as a big resistor composed of small parallel resistors with the same resistance. Each column is a small resistor. The resistance of each column is $t/D\times(R_c+R_p)$ and the total resistance can be calculated as

$$R = \frac{(M-1)R_c+MR_p}{N_d\times100} \approx \frac{M(R_c+R_p)}{N_d\times100} = \frac{\frac{t}{D}(R_c+R_p)}{N_d}\times10 = \frac{5t\pi D(R_c+R_p)}{3\ vol.\%}$$

$$R = \frac{(M-1)R_c+MR_p}{N_d\times100} \approx \frac{M(R_c+R_p)}{N_d\times100} = \frac{\frac{t}{D}(R_c+R_p)}{N_d}\times10 = \frac{5t\pi D(R_c+R_p)}{3\ vol.\%} \qquad (4)$$

Or the total conductivity of ECA samples is $\sigma = \frac{3\ vol.\%}{5\pi D\ (R_c+R_p)}$

$$\sigma = \frac{3\ vol.\%}{5\pi D\ (R_c+R_p)} \qquad\qquad (5)$$

where Rc: contact resistance of particles;

Rp: resistance of particles;

Nd: particle column density (# of columns/ mm2);

M: particles number per column;

D: diameter of particle (μm);

t: thickness of composite (mm).

From Eq.5, it is understandable why the electrical conductivity is linearly proportional to the volume percentage of filler loading. Also we are able to calculate the sum of individual particle resistance and contact resistance R_c+R_p. For the ECA sample prepared with 70 μm particles, this value is around 46.1 with a standard deviation of 19.3

.

3.3.3 **Effect of particle size**

We also tested the alignment and resistivity when using Ag coated Ni particles with smaller sizes. The SEM images of the two particles are shown in Figure 3.7.
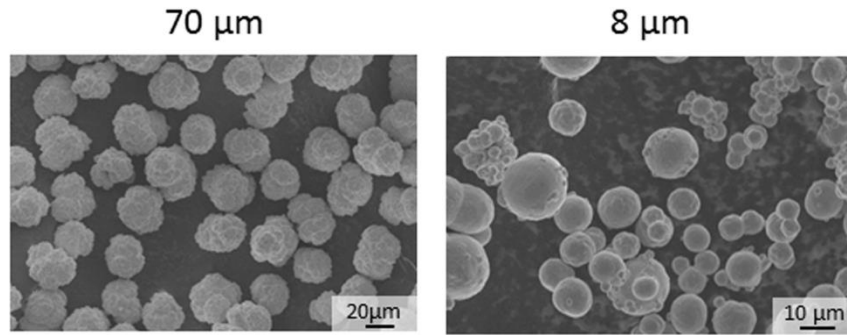
Figure 3.7 SEM images of silver coated nickel with a diameter of 70µm (left) and 8µm (right).

As shown in Figure 3.8, the smaller particles are also well-aligned under magnetic field. Three concentrations were tested, 1.43 vol.%, 3.17 vol.%, and 5.31 vol.%. The decreased particle size enables more columns to form at the same concentration of fillers, i.e. more conduction paths to decrease the total resistance. However, smaller particle size also means more particles in each column, and therefore a larger contact resistance for each column.
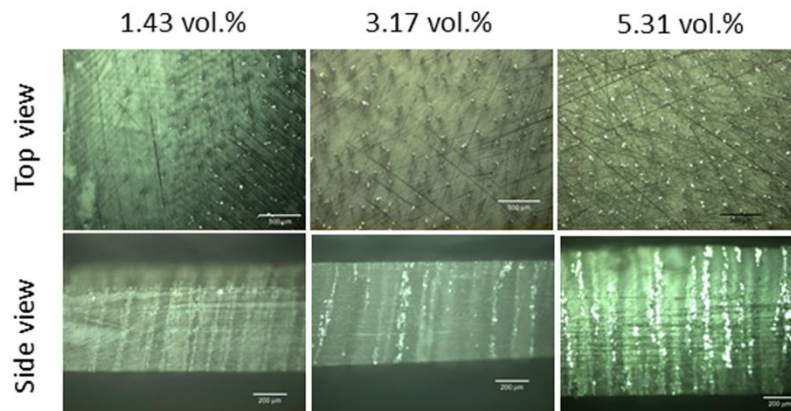
Figure 3.8 Cross-section (upper row) and top-down views (lower row) of Ag-coated spheres (8 µm diameter) with different filler loading in epoxy resin after magnetic alignment.

Figure 3.9 shows the inter-column distance Y and column density N_d at different filler concentration when using 8 μm and 70 μm particles. The inter-column distance decrease to 1/8 when using smaller particles and the column density increased around 80 times. However, when we measure the electrical conductivity, it is one order of magnitude smaller than that of the ECAs prepared with 70 μm particles. We calculated the sum of contact resistance and the particle resistance (R_c+R_p) according to Eq. 5, the sum of these two is around $2 \times 10^4 \Omega$.cm. This explains the higher resistance of the ECA with smaller particle fillers. That is the contact resistance effect to increase the total resistance exceeds the trend to reduce the resistance by forming more columns. Therefore, a larger size of particle is preferred in the current system.
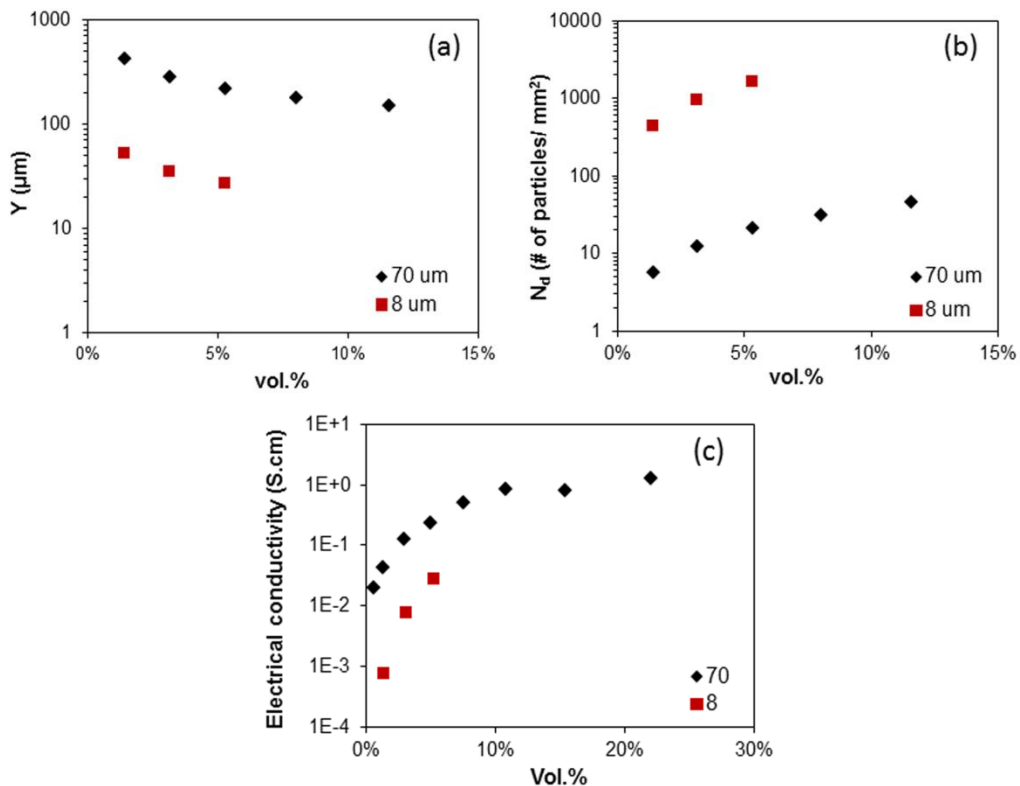
Figure 3.9 The intercolumn distance Y (left) and column density Nd (right) with different filler size. The data were obtained from model predication.

3.3.4 **Effect of silver layer thickness**

From Eq.5, it is clear that to enhance the electrical conductivity, we need to decrease the particle resistance R_p or to decrease the contact resistance R_c. The particle resistance R_p can be reduced by adding thicker layer of silver while the contact resistance can be reduced by interface treatment such as iodination as in our previous work in isotropic conductive ECAs.

To investigate the effect of silver shell thickness, 1.5g of the original Ag/Ni core shell particles are immersed in 20ml commercial Ag plating solution with stirring for 5 min at 65 ^{o}C. The particles with thicker layer were then characterized by SEM and TGA. The silver coating is quite homogeneous from the SEM images. In the TGA tests, silver is thermally stable while nickel can be oxidized to nickel oxide at elevated temperatures. As shown in Figure 3.11, the pure nickel will have a weight gain of 24.6 wt.% because of the oxidation. The original Ag coated Ni and the particles after a second coating shows a weight gain of 13.5% and 5.7%, respectively, which indicates a much thicker coating of silver after plating.
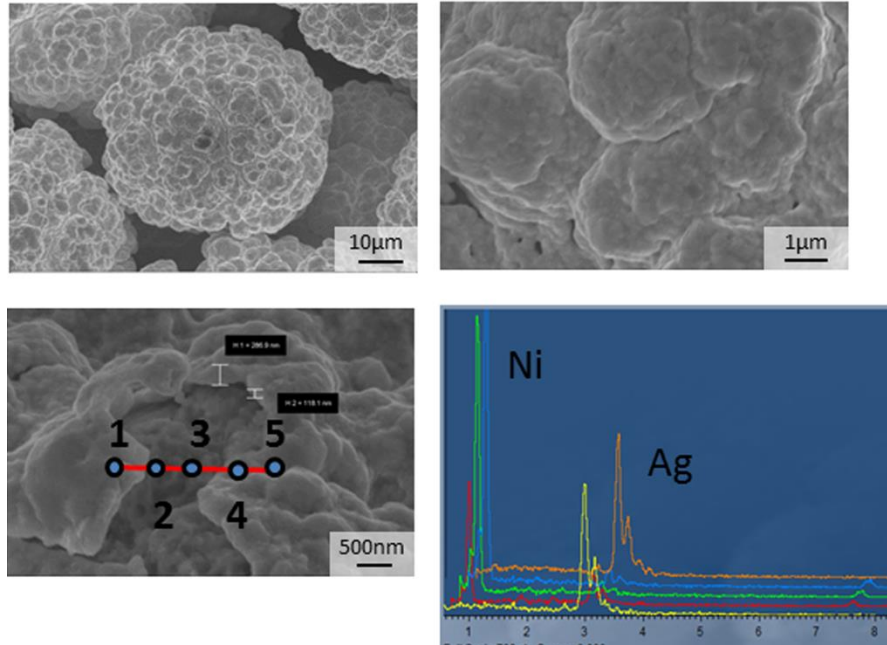
Figure 3.10 SEM of pure silver and nickel flakes (left) and silver coated nickel particles with different silver shell thickness (right).
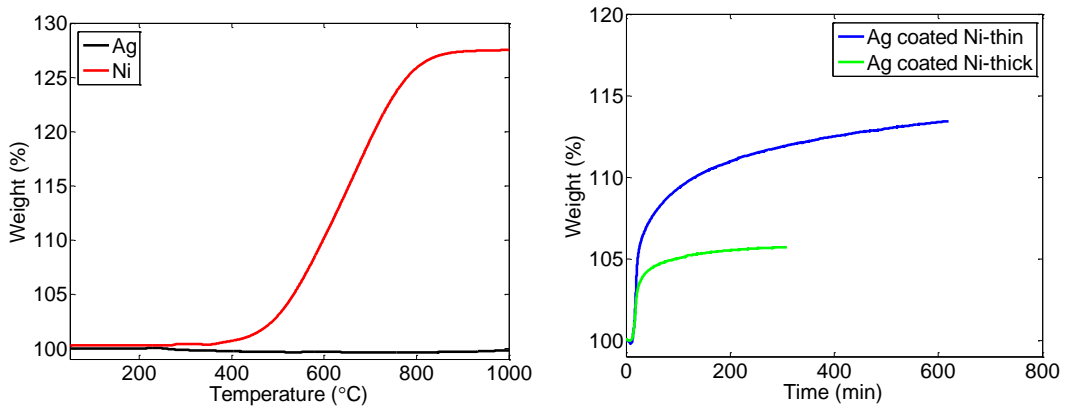
Figure 3.11 TGA of pure silver and nickel flakes (left) and silver coated nickel particles with different silver shell thickness (right).

The electrical conductivity and thermal conductivity in Z-direction of the original particle filled epoxy composites and particles with thicker silver coating were then measured. As shown in Figure 3.12, the electrical conductivity increases linearly with filler loading for both samples. This is consistent with previous prediction (Eq.5). By putting a thicker layer of silver, we can decrease the particle resistance and therefore the

total resistance. As shown in Figure 3.12, the totally conductivity increased by approximately two times when adding a thicker layer of silver. We reverse calculated the sum of average contact resistance and particle resistance (R_c+R_p) from Equation 5 and this value deceased from 46.1 Ω to 15.7Ω.
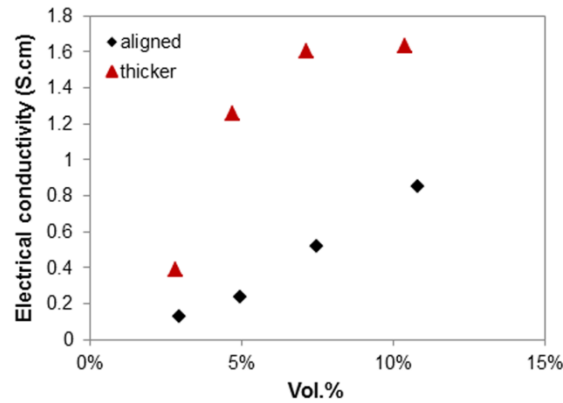
Figure 3.12 Electrical conductivity in the Z-direction of original particles and particles with thicker Ag layers filled epoxy composites.

Similarly, the thicker layer of silver also enhances the thermal conductivity. As shown in Figure 3.13, the thermal conductivity of composites also increased linearly with volume percentage of particles. The increasing rate increased 50% when we have thicker layer of silver.
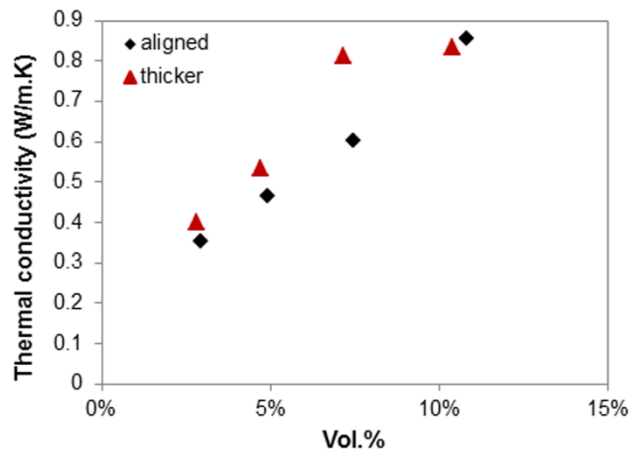
Figure 3.13 Thermal conductivity in the Z-direction of original particles and particles with thicker Ag layers filled epoxy composites.

3.3.5 **Effect of iodination treatment**

The iodination treatment of silver flakes have been demonstrated a very effective way to reduce the contact resistance in ECAs [62]. To reduce the contact resistance R_c here, the iodination treatment of the silver shell in the Ag/Ni particles was studied. The iodination process for silver coated nickel particles is much faster than that for silver flakes. After immersion in iodine ethanol solution (0.5μmol/l) for only 1 minute, the white color powder immediately turned into yellow (bulk AgI is also yellow) (Figure 3.14). From the SEM images (Figure 3.15), we found that nanoparticles formed on the surface of Ag coated Ni particles even after 1minute reaction. In contrast, the flake surfaces are relatively smooth even after iodination process, and no obvious nanoparticle formation can be observed (Figure 3.15). It is possible that the plated silver is formed from coalescence of silver nanoparticles and they may have higher surface energy and larger tendency to get oxidized by iodine. To confirm the composition of these formed nanoparticles, a series of XRD was performed (Figure 3.16). For silver flakes, after iodination treated for 3 hours, although a significant enhancement in electrical conductivity was observed for the flakes-filled ECA, the silver flakes themselves contains very small amount of AgI. As shown in XRD result, the AgI peaks cannot be detected. For the silver coated nickel particles, as expected, we observed peaks from Ag FCC structure and Ni FCC structures. For silver coated nickel particles treated with iodine solution for only 1 minute, obvious peaks formed at $2\theta = 21^{o}$, 23°, 39°, and 43°, representing the (100), (002), (110), (013) planes of β-AgI, respectively.

Figure 3.14 Pictures of Ag coated Ni particles before (left) and after iodination for 1 minute (right).
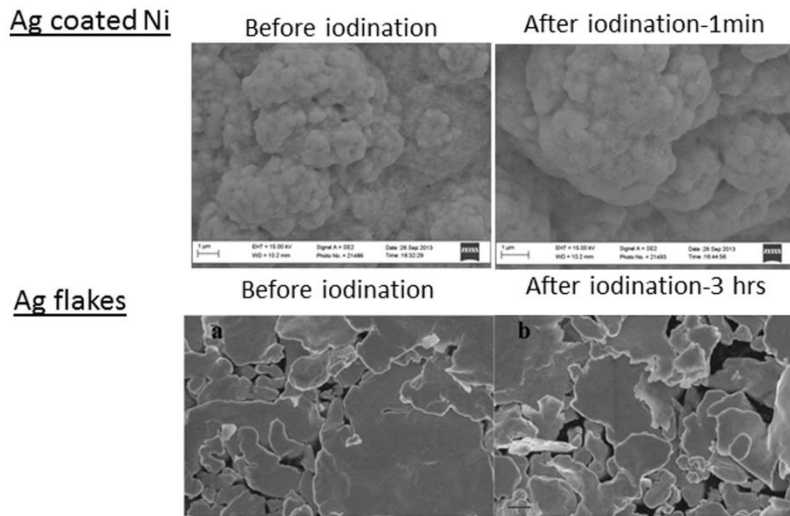
Figure 3.15 SEM of Ag coated Ni particles and Ag flakes before and after iodination. The iodine concentration is 0.5µmol/l and the treatment time is 1 minute for the particles and 3 hours for flakes.
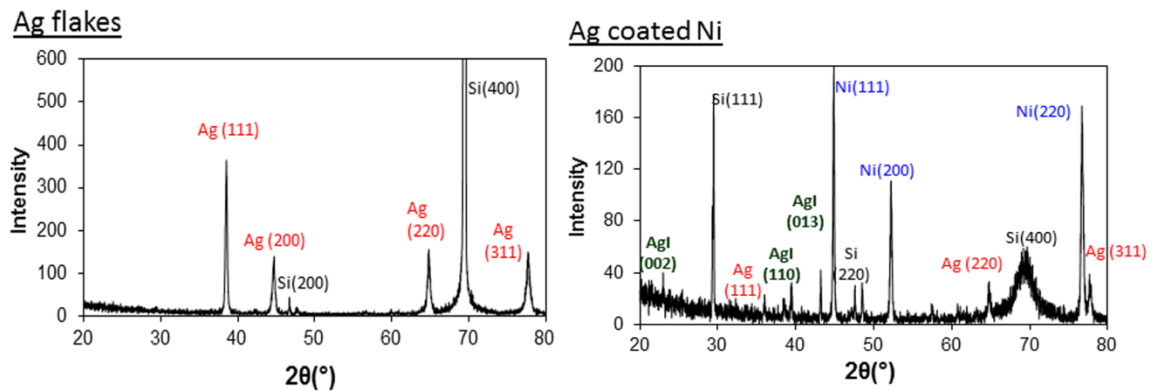
Figure 3.16 XRD of silver flakes 26 iodinated for 3 hours and silver coated nickel particles iodinated for 1 minute. The iodine solution concentration is 0.5µmol/l in both cases.

62

Previous study showed mild iodination treatment (short treatment time and low concentration of iodine) would enhance the electrical conductivity whereas overtreatment with iodine would decrease the conductivity [62]. One possible reason is that small amount of AgI on the Ag flake surface can be in-situ decomposed to generate Ag nanoparticles while too many insulating AgI will obstacle the electrical conduction.

Because the iodination treatment time is already reduced to 1 minute, to avoid over-treatment, the iodine concentration is reduced from 0.5µmol/l for flake treatment to below 50nmol/l for Ag coated Ni. The Ag coated Ni particles are treated with stearic acid/ethanol solution for 24 hours to get a lubricant layer. Then the particles are treated with iodine/ethanol solution at different concentrations before mixing into epoxy resin. The effect of iodine concentration during iodination treatment is investigated.

Figure 3.17 shows the electrical conductivity at Z direction of the Ag coated Ni filled ECAs. Similar to the situation for silver flakes, only lubrication with fatty acid would reduce the electrical conductivity because they form an insulating layer on the surface of Ag coated Ni. But after iodination treatment, the electrical conductivity gets improved compared with just lubricated particles. To be noticed that the concentration of iodine used here is less than 50 nmol/l, which is 1/10 of the concentration used to treat silver flakes. The improvement by iodination is more significant when the particle loading is larger. At 10.82vol.% loading, the conductivity can be enhanced by 4 times after treated with 50 nmol/l iodine solution. This is possibly because more contacts are formed at higher loading and iodination facilitates reducing contact resistance. There is no obvious trend that which concentration of iodine works best.
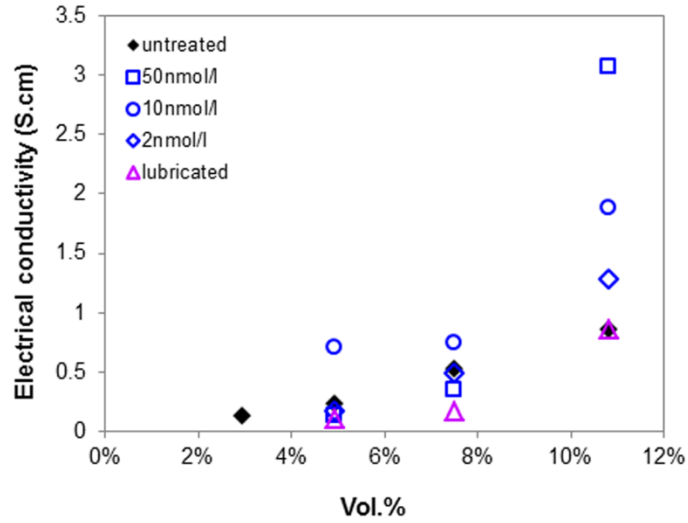
Figure 3.17 Electrical conductivity of ECAs filled with Ag coated Ni particles with iodination treatment at different concentration of iodine.

Lubrication of the particles will increase the contact resistance, and thus increase R_c+R_p (Figure 3.18). The iodination treatment can reduce the contact resistance R_c, therefore the R_c+R_p can be reduced to below 20Ω. Moreover, this value decreases with loading because the reduction of R_c by iodination is more significant at higher loading. At 10.82 vol.%, the R_c+R_p value can be reduced below 10 Ω.
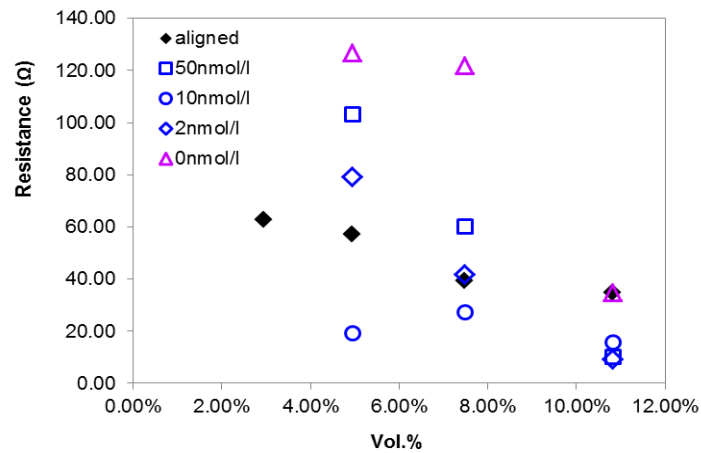
Figure 3.18 Rc+Rp value of ECAs filled with Ag coated Ni particles with iodination treatment at different concentration of iodine.

We also measured the thermal conductivity of the iodinated particles, as shown in Figure 3.19. The iodination process may improve the thermal conductivity slightly, probably due to the silver nanoparticle formation from AgI decomposition. Moreover, for thermal conductivity, there is an obvious trend that at lower concentration of iodination, the thermal conductivity is higher. This trend is observed at all the filler loading tested. At a loading of 10.82 vol.%, the thermal conductivity can be improved from 0.85 W/m.K to 0.98 W/m.K after treatment with 2 nmol/l iodine solution.
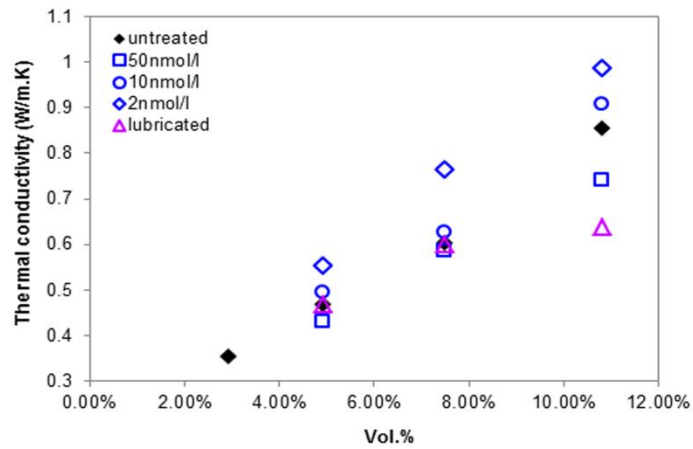
Figure 3.19 Thermal conductivity of ECAs filled with Ag coated Ni particles with iodination treatment at different concentration of iodine.

3.3.6 Effect of iodination treatment and silver shell thickness

It has been demonstrated that a thicker silver shell can reduce Rp while iodination treatment can reduce Rc. The current step is to combine the iodination treatment and deposition of a thicker silver shell to further enhance the electrical and thermal conductivity. Figure 3.20 shows the electrical conductivity of ECAs filled with silver coated nickel particles with thicker silver shell and treated with iodine (red) in comparison with ECAs filled with particles with thicker Ag shell without iodination treatment (black), and ECAs filled with particles with iodination treatment but without thicker shell (blue). It can be seen that the combination of thicker shell and iodination

65

treatment yields a better conductivity than that of single step treatment. But this effect is

more obvious at higher loadings (7.2 vol.%).
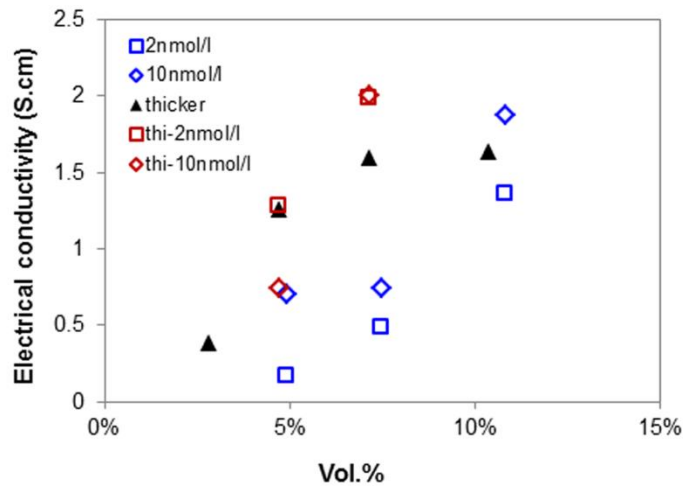
Figure 3.20 The electrical conductivity of ECAs filled with Ag coated Ni particles treated with iodine at two different concentration (blue), Ag coated Ni particles with thicker Ag shell (black), and Ag coated Ni particles with thicker Ag shell and treated with iodine (red).

Besides the electrical conductivity, the thermal conductivity was also investigated

(Figure 3.21). The effect of iodination treatment of Ag coated Ni particles with thicker

Ag shell on thermal conductivity is not very significant though.
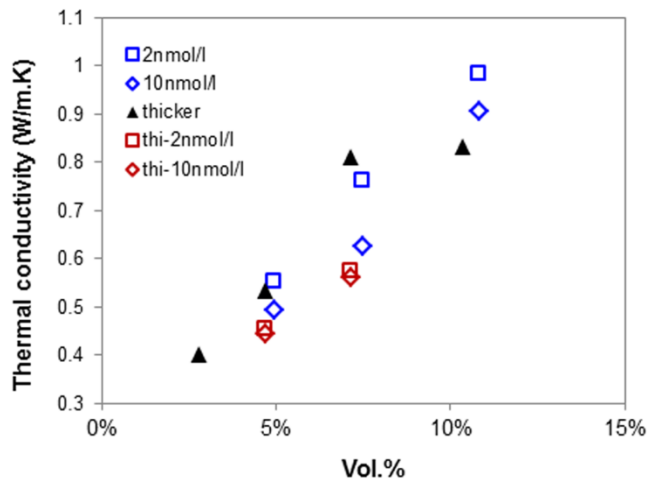
Figure 3.21 The thermal conductivity of ECAs filled with Ag coated Ni particles treated with iodine at two different concentration (blue), Ag coated Ni particles with thicker Ag shell (black), and Ag coated Ni particles with thicker Ag shell and treated with iodine (red).

66

3.4 Summary and future work

Anisotropic ECAs are successfully prepared with silver coated nickel particles as fillers and aligning these fillers in a magnetic field. Anisotropic ECAs have higher electrical and thermal conductivity at Z-direction compared with that of isotropic ECAs, while maintain electrically insulating at X-,Y-directions. To achieve higher conductivity at Z-direction, larger particle size, thicker Ag shell and iodination treatment at very low concentration of iodine are preferred.

Future work include using Ag coated Ni flakes or wires as fillers to further reduce the filler loading, or using Ni nanoparticle decorated Ag flakes as fillers.

CHAPTER 4 HIGHLY CONDUCTIVE, FLEXIBLE POLYURETHANE-BASED ADHESIVES FOR FLEXIBLE AND PRINTED ELECTRONICS

4.1 Introduction

Modern consumer electronics are striving for increased functionality. Mechanical flexibility becomes an important trend for electronics because of the natural integration and increased functionality impossible within the confines of rigid, planar substrates. For example, flexible electronics enable applications where circuits are wrapped conformal around complex shapes or rolled up for storage, such as flexible displays [159, 160], flexible and conformal antennas [161], thin film transistors [162, 163], sensors arrays [164], electronic solar cell arrays [165, 166], and flexible energy storage devices [167, 168]. However, flexible electronics impose stringent requirements for interconnect materials [169-172]. In addition to the conventional functions of providing sufficient power, ground and signal transmission, interconnects for flexible electronics are required to maintain excellent mechanical robustness and electrical interconnectivity during mechanical deformation.

While metal wires with elegantly designed structures [171, 173-178] or ink-jet printed metal patterns [161, 179-181] have been demonstrated to wire-bond chips to flexible substrates, there are considerably fewer reports on the adhesive materials to support the flip-chip interconnects or SMT for flexible electronics. Sn-based eutectic solders cannot be used in flexible electronics, because the high process temperature will damage flexible, low cost substrates such as paper and poly(ethylene terephthalate) (PET). Conventional epoxy-based ECAs suffer from the rigidity while silicone-based

68

ECAs usually have limited conductivity (resistivity $> 2.0 \times 10^{-4}$ $\Omega \cdot$cm) [4, 182].

Therefore, ECAs with high electrical conductivity, low process temperature, good

mechanical compliance and strong adhesion are needed to enable SMT and flip-chip

interconnection on flexible and low-cost substrates in flexible electronics.

In this chapter, we describe a novel approach to develop PU-based flexible ECA

that can meet all of the above requirements. By selecting the appropriate resin, the PU-

ECA exhibits excellent electrical conductivity (resistivity $\sim 1.0 \times 10^{-5}$ $\Omega \cdot$cm) and the

resistivity does not change when bending at a 2.64 % flexural strain, rolling at a radius of

8 mm or pressing under 250 kPa. Additionally, the adhesion strength is much better than

that of a commercial ECA (Abletherm® 3188) and pure PU resin. The PU-ECA in this

study demonstrates many other advantages, including a low curing temperature (150 $^{\circ}$C),

which enables printing and curing on low-cost flexible substrates; simple and cost-

effective processing, by eliminating the use of any expensive silver nanoparticles [28, 35]

or additives [9, 183] to achieve high electrical conductivity; and environmental-

friendliness. These excellent material properties will be very promising for the exiting

conductive adhesive interconnection and emerging flexible electronics.

4.2 Experimental

4.2.1 Synthesis of PU-ECA

Polyethylene glycol (PEG, Sigma-Aldrich) was put into a vacuum pump for 6

hours before mixing with hexamethylene diisocyanate (HDI, Bayer AG) and various

amounts of silver flakes (Ferro Corp.). The two flakes with different sizes were added

with a ratio of 1:1. The mixture was homogenized with for 5 minutes. Then the paste was

kept in the vacuum oven for 12 hours to evaporate the solvents in the HDI prepolymer.

69

The PEG chain length was optimized for a low modulus, high electrical conductivity and low glass transition temperature. The Young's modulus was measured by tensile test with extension rate of 50 mm/min (Instron Microtester 5548). The glass transition temperature and crystallization temperature were measured by DSC (TA Instrument Q2000). The bulk resistivity measurement is detailed in the following characterization section.

4.2.2 **Characterization**

To measure the electrical resistivity, the paste was cast in a Teflon mold (22 mm $\times$ 7 mm $\times$ 0.5 mm). After cure at $150^{o}C$ for 1 hour, the bulk resistance of the film was measured by four-wire method with a Keithley 2000 multimeter. The thickness was measured by a profilometer (Heidenhain ND 281, Germany). Bulk resistivity ρ was then calculated by

$$\rho = R\frac{wt}{l}$$

where l, w, and t are the length, width and thickness of the film, respectively.

Raman spectra of silver flakes were obtained by a LabRAM ARAMIS Raman confocal microscope (HORIBA Jobin Yvon) equipped with a 532 nm diode pumped solid state (DPSS) laser. Si wafer was used as a substrate.

The dimensional change of PU-ECA paste during thermal cure was measured by a thermomechanical analyzer using the macroexpansion mode (TMA, TA instruments, Q400) [23]. A small amount of the paste was sandwiched between two microscope cover glasses. The sample was cured in the TMA and dimensional changes during cure were recorded. The static force of the probe was kept at 0.02 N to ensure that the adhesive paste was not squeezed out during heating. The heating rate was 5 °C per minute.

70

Decomposition of the lubricants on the surface of silver flakes with and without PEG was studied by a modulated DSC (TA Instruments, Q2000). The heating rate was $1°C$ min^{-1}.

PEG treated silver flakes were prepared by immersing silver flakes in PEG at 150^oC for 30 minutes. Silver flakes lost their luster after being treated. Then PEG and surfactant reduction products were removed by adding acetone and centrifuging for five cycles. Finally, the silver flakes were dried in vacuum before SEM observation and TGA tests. Morphologies of untreated silver flakes and silver flakes treated with PEG were observed by field emission SEM (LEO 1530). Weight loss of untreated and PEG-treated silver flakes during heating was studied using TGA (TA Instruments, Q50) with a heating rate of 5 °C/min.

The storage modulus of a PU-ECA film was measured with a dynamic mechanical analyzer (DMA, TA Instruments, 2980), in tension mode. The sample is heated from 0^oC to 100^oC at 5^oC/min with a constant frequency of 10Hz.

The lap shear test was performed according to ASTM D1002. To eliminate the effects of the thickness of adhesives on the adhesion strength [184], 0.5 wt.% of glass beads with uniform diameter of 75 µm were added to the adhesives to serve as "spacers". When applying compression force during the curing of the adhesives, the thickness of all the samples were kept around 75 µm.

A DC power supply (Hewlett-Packard 6553A) was used to power the LED chips (Lite-On, 160-1458-1-ND).

71

The simulation of antenna performance was conducted by high frequency structural simulator (HFSS,Ansys Inc.). The S11 parameter was measured by a vector network analyzer (VNA, Agilent, 85052D).

4.3   Results and Discussion

4.3.1   Optimization of PU-ECA Formulation

The PU-ECA is prepared by a facile process. The PU resin used is methylethylketoxime (MEKO) blocked HDI cured by PEG. Two silver flakes with different sizes (0.8-2 µm and 1.9-5.5 µm, respectively) are used because the bimodal size of fillers is reported to enhance the packing efficiency and thus decrease the viscosity of the paste [5, 28, 61]. The optimal chain length of PEG is found based on three aspects; the low bulk resistivity of the PU-ECA, low Young's modulus and low glass transition temperature (T_g) of the PU cured with PEG.

The bulk resistivity of PU-ECA prepared with PEG of different lengths is shown in Figure 4.1(a). The resistivity increases with the PEG chain length at the same filler loading, especially with a molecular weight up to 1000.

The Young's moduli decrease with the increase of PEG molecular weight from 200 to 600 (Figure 4.1(b)). PEG forms the soft segment of the PU resin and the increase of soft segment usually leads to a lower Young's modulus. However, the Young's modulus shows a sudden increase when the molecular weight reaches 1000. This is because the long PEG segments forms crystalline structures, and the melting point of the crystalline for PEG with molecular weight of 1000 is around 37^oC (Figure 4.1(c)). At room temperature, the partially-crystallized PU thus has a much higher modulus than other formulations with amorphous structures do.

72

The DSC results of cured PU with different PEG chain lengths are shown in Figure 4.1(c). PEG with molecular weights of 200 and 400 do not form crystalline while PEG 400 has a lower Tg (-25°C) than that PEG 200 (6 °C). The lower Tg renders a consistent mechanical properties in a larger temperature window. Therefore, PEG 400 is selected in an optimized formulation for PU-ECA.
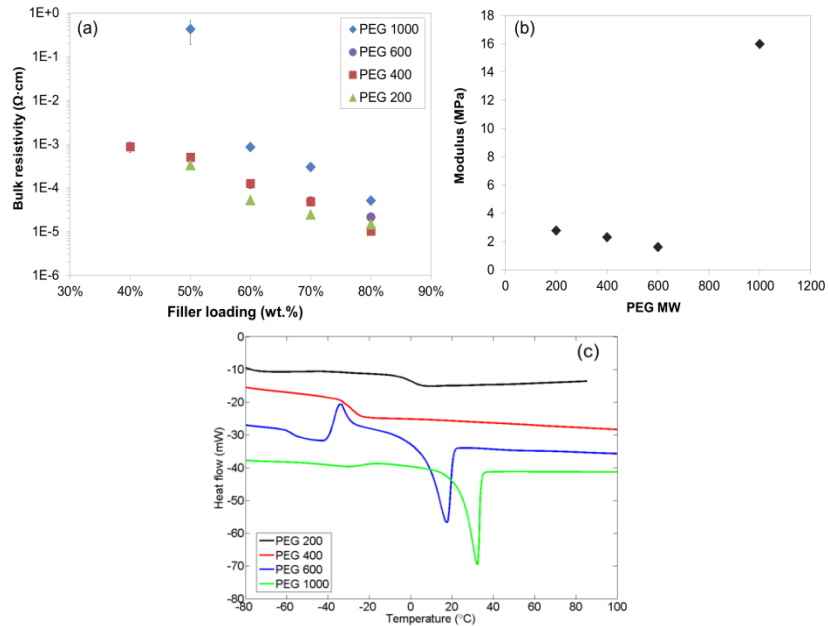
Figure 4.1 (a) Bulk resistivity of PU ECAs as a function of silver loading for PU resin prepared with PEG of different molecular weights. (b) Young's modulus of PU resin prepared with PEG of different molecular weights. (c) DSC results of PU resin prepared with PEG of different molecular weights.

4.3.2 **Properties of PU-ECA**

4.3.2.1 Bulk resistivity and the conduction mechanism

The bulk resistivity as a function of curing temperature is shown in Figure 4.2(a) and the obtained resistivity can be as low as 1.0×10^{-5} Ω·cm at 80 wt.% silver loading when cured at 150°C or above. The resistivity of PU-ECA (1.0×10^{-5} Ω·cm) is one order of magnitude smaller than that of silver/polydimethylsiloxane (PDMS) [5] and

silver/MWNT/PDMS composites [183], 2/3 less than that of silver-MWNT/nitrile butadiene rubber (NBR) composites [9] and 1/2 less than that of epoxy ECA at the same process-temperature [28, 61]. It is also even lower than the reported resistivity of some printed silver-ink [161, 179]. It is noted that in prior studies these high electrical conductivities are usually obtained by introducing silver nanoparticles [28, 35] or silver nanoparticle-decorated CNTs [9, 183], because these nanoparticles can be sintered at relatively low temperatures (~250°C or below) to decrease the contact resistance [35]. However, the dispersion of metallic nanoparticles into the polymer matrix is quite challenging and the cost of nanoparticles is still high. In the case of PU-ECA, the ultrahigh electrical conductivity can be achieved simply by optimizing the formulation of the PU resin, instead of the use of expensive nanoparticles or complex preparation methods. Two possible factors contribute to the high conductivity of PU-ECA. The first factor is the significant shrinkage during curing of PU-ECA, which leads to an increased volume percentage of silver after curing. As shown in the TMA result (Figure 4.2(b)), the PU-ECA experiences significant volume shrinkage from 35°C to 110°C. Volume shrinkage during curing was also observed for epoxy-based ECA in previous reports while silicone-based ECA does not show obvious shrinkage (Figure 5.1). According to previous studies [23, 185], such shrinkage can generate a compressive force to draw the silver flakes together and decrease the bulk resistivity. Here, the shrinkage of PU matrix reduces the bulk resistivity of PU-ECA from the upper limit of the measurement at 20°C to as low as 10 Ω at 110°C. After reaching 110°C, thermal expansion exceeds the curing shrinkage while the resistance continues to drop at around 140°C, indicating that factors other than the matrix shrinkage contribute to the improved conductivity at temperatures

74

over 110°C. The second possible factor is that the hydroxyl groups in the polyether chains can in-situ reduce the silver salts on the surface silver flakes to produce silver nanoparticles, which can be sintered during the curing of PU-ECA to form metallic bridges between neighboring flakes. As demonstrated by the Raman spectra (Figure 2.3), the commercial silver flakes in use are coated with a thin layer of silver salts of fatty acids. This insulating layer helps to improve the processability but dramatically increases the contact resistance between silver fillers inside ECAs [26, 27, 127]. Polymers with hydroxyl groups such as PEG [186] and polyvinyl alcohol [187] have been extensively reported to reduce silver salts to silver nanoparticles effectively at mild conditions. PEG used as a curing agent in this study can also serve as a reducing agent to reduce the silver carboxylate and generate silver nanoparticles during curing at 150 $^{\circ}$C. Indeed, the DSC results (Figure 4.2(c)) of pure silver flake shows a small peak at 201 $^{\circ}$C, corresponding to the thermal decomposition of silver carboxylate [61]. When adding PEG to silver, the peak at at 201 $^{\circ}$C in the DSC curve disappears; instead, an exothermic peak is observed at 130 $^{\circ}$C, indicating the reduction reaction of silver carboxylate by PEG. In the TGA tests (Figure 4.2(d)), the untreated silver flakes shows a weight loss of 0.20% when heated to 450°C in a dynamic run due to the decomposition of surfactants on the silver flakes while the PEG treated silver flakes shows a significantly smaller weight loss of 0.10%, implying partially removal of surfactants by PEG. The formation of nanoparticles by reduction reaction is confirmed by SEM. The untreated flakes show smooth surfaces, while after heating at 150°C with PEG for 30 minutes, the silver flakes clearly show some roughness owing to the growth of silver nano/submicron-sized particles on their surfaces and edges (Figure 4.2(e)). Moreover, these grown submicron/nano particles on the silver

75

flake surfaces are sintered forming neckings between silver flakes. These neckings metallically bridge the neighboring flakes and thus significantly reduce the contact resistance between silver flakes, which corresponds to the resistance drop at 140°C in Figure 4.2(b). While the reduction of the silver carboxylate on the silver flakes by PEG acts similarly to the introduction of silver nanoparticles or silver nanoparticles decorated CNT, the silver carboxylate reduction process is more cost effective and efficient to improve the electrical conductivity.
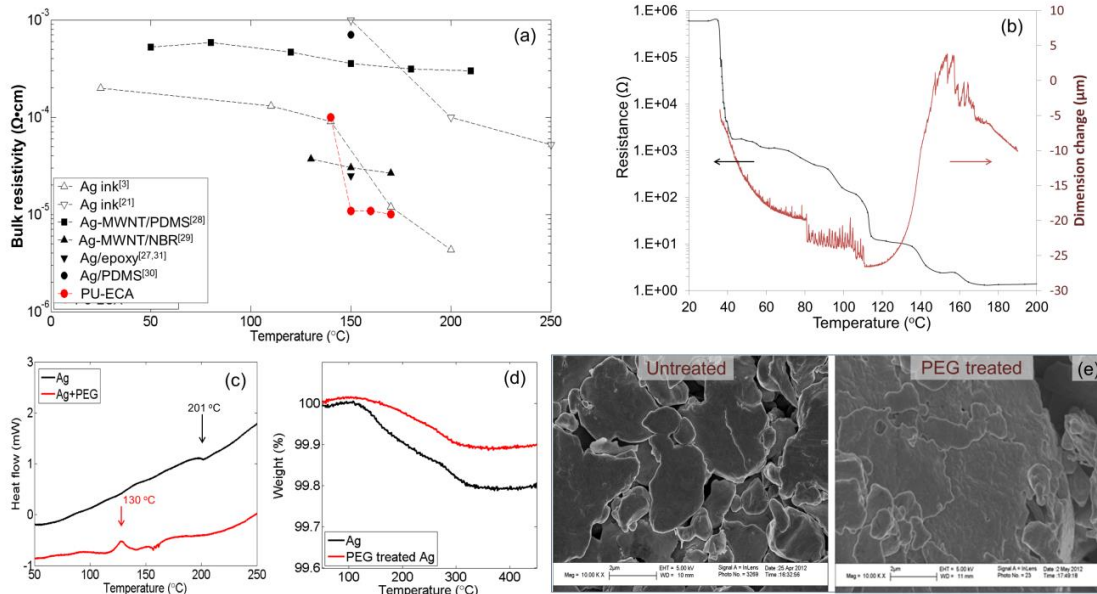
Figure 4.2 (a) The bulk resistivity of PU-ECA compared with other interconnect materials for flexible electronics. (b) The bulk resistance and dimension change of PU based ECA as a function of temperature. (c) DSC results of silver flakes and silver flakes with PEG. (d) The weight loss of untreated and PEG treated silver flakes. (e) SEM images of untreated and PEG treated silver flakes.

4.3.2.2   Conductivity under mechanical deformation

In addition to high electrical conductivity at static state, ECAs for flexible electronics need to maintain their conductivity under mechanical deformation. The storage modulus of a PU-ECA film at 25°C is 1098 MPa as measured by DMA, indicating a flexible structure. Figure 4.3 shows the electrical conductivity change of

76

PU-ECA film under various forms of mechanical deformations. First, the bending deformation of a free-standing PU-ECA film is made by three-point bending fixture. The resistance change is less than 10% when bending at flexural strain up to 2.64%. Moreover, the resistance stays constant even after 1,000 cycles of bending. The same sample is also tested by rolling at different radii in a setup similar to a previous report [9]. The resistance does not change significantly when the radius is larger than 7 mm, though the resistivity does increase to 3.3×10^{-5}, 4.2×10^{-5} and 6.8×10^{-5} $\Omega \cdot$cm when rolling at 7.5, 5 and 3.5 mm respectively. The rough surfaces of silver flakes and the neckings between neighboring flakes from PEG treatment (Figure 4.2(d)) help to maintain the contacts between fillers and thus the resistivity during moderate deformation. When the deformation increases to a certain level, the resistivity increases due to the loss of contacts. The increased resistivity in the rolling test, however, is still lower than that of most silver based composites reported [179, 183]. A further cycling test shows that the resistivity is invariant after rolling at 8 mm for 1,000 times. The normal pressure test on the PU-ECA film up to 250 kPa exhibits no change in resistivity. It should be noted that the thickness of PU-ECA film tested here is around 360 μm, which is much larger than some previously-reported bendable conductive materials (60 μm [9] and 20 μm [161]). In addition, the PU-ECA samples tested here are free-standing films while the samples tested in [161] and [9] are printed on a flexible substrate. Since the bending stiffness of a thin sheet is proportional to the cube of its thickness [188], the PU-ECA could have the potential to exhibit even better flexibility and electrical properties under deformation than the results shown in Figure 4.3 if the thickness of the samples is decreased.
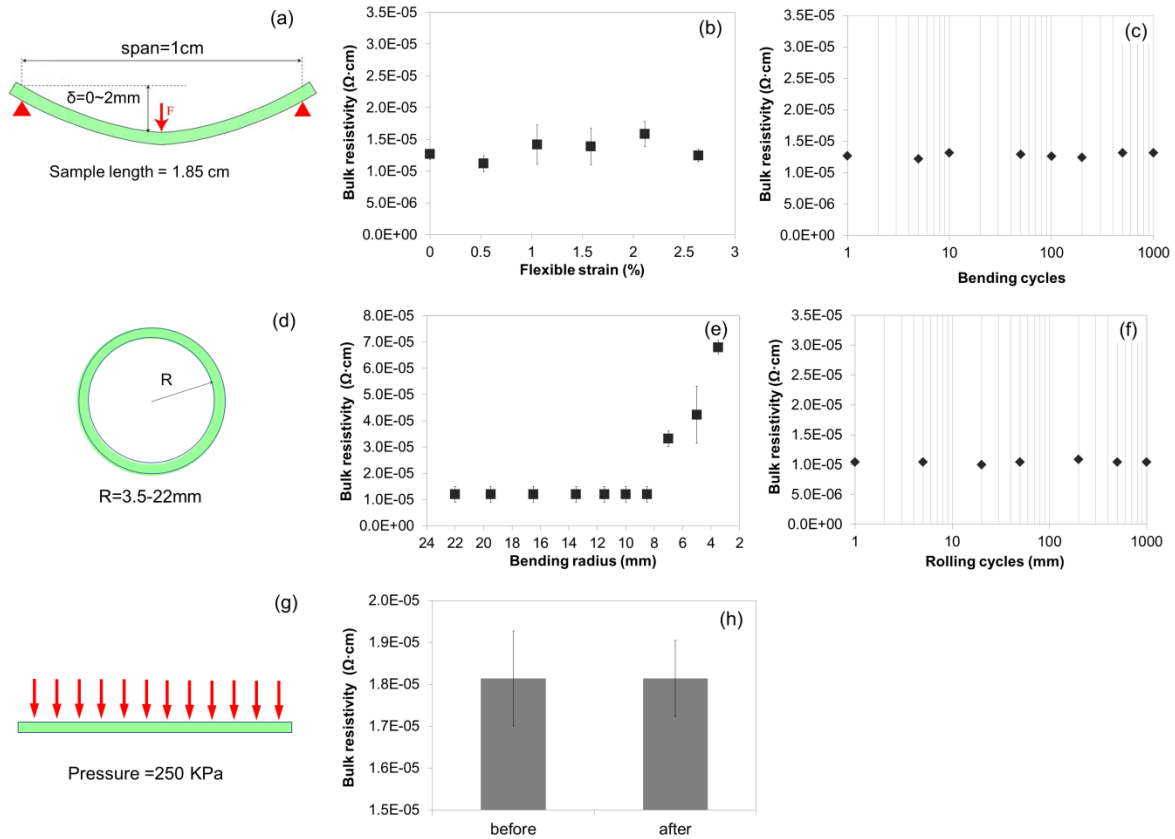
Figure 4.3 (a) The schematic illustration of three point bending test of the PU-ECA film. (b) The electrical resistivity as a functional of flexural strain. (c) The electrical resistivity as a function of bending cycles at a flexural strain of 2.64%. (d) The schematic illustration of rolling test of the PU-ECA film. (e) The electrical resistivity as a functional of rolling radius. (f) The electrical resistivity as a function of rolling cycles at a radius of 8mm. (g) The schematic illustration of high pressure test of the PU-ECA film. (h) The electrical resistivity before and after high-pressure test.

4.3.2.3   Adhesion strength

The adhesion of PU-ECA to a photo paper, poly ethylene terephthalte (PET) and polyimide (PI) substrates is measured by a standard tape test. No noticeable ECA materials are removed by the tape, indicating good adhesion of PU-ECA to these flexible substrates (Figure 4.4(a)). Moreover, a lap shear test is performed on two Cu strips bonded with PU of different silver loadings. Compared with pure PU, the adhesion strength increases from 0.12 kg mm^{-2} to 0.14 kg mm^{-2} when the silver loading increases

78

to 60 and 70 wt.% loading. This increase may result from the increased modulus that

helps with the interfacial strength. When the loading further increased to 80 wt.%, the

adhesion decreased to 0.125 kg mm^{-2} due to reduced flowability of the ECAs which

causes incomplete asperity filling on bonding surfaces and loss of contact area by

inorganic fillers. However, this value is still higher than that of either the pure PU resin or

the commercial PU based ECA (0.07 kg mm^{-2}, labeled 3188).
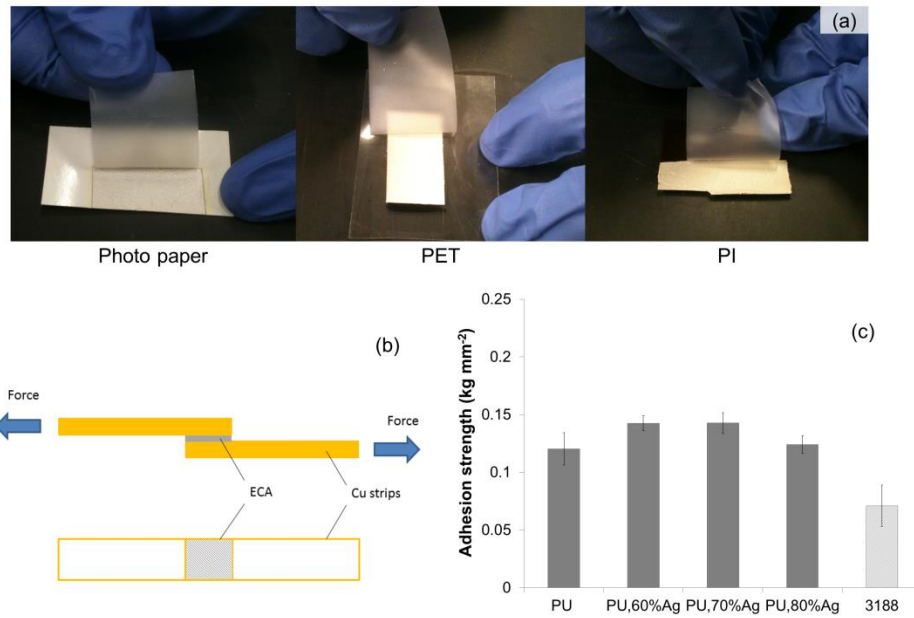
Figure 4.4 (a) The adhesion of PU-ECA to different flexible substrates is investigated using scotch tape. (b) Die shear test result of PU-ECA with different silver loading and commercial ECA Abletherm® 3188 as a benchmark material. (c) Lap shear test result of PU-ECA with different silver loading and 3188 (a commercial PU based adhesive).

4.3.3 Demonstration of PU-ECA in flexible electronics

The PU-ECA in this study meets the requirements of interconnect materials in

flexible electronics, such as high electrical conductivity, low process temperature, good

mechanical compliance, and strong adhesion, which enable PU-ECA to be applied in a

variety of flexible electronics.

79

4.3.3.1 PU-ECA as interconnection materials

PU-ECA can be used as die-attach materials for flexible electronics. LED chips are attached to a PU-ECA pattern on a photo paper substrate. The brightness of these LED chips is invariant for the flat (Figure 4.5(a)), and rolling state (Figure 4.5(b) and Figure 4.5(c), radius = 18.5 and 15 mm, respectively), indicating the excellent adhesion and power transmission of the PU-ECA.
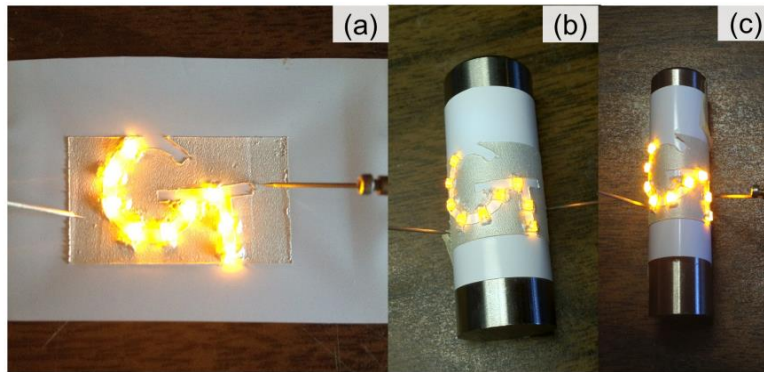
Figure 4.5 (a) LED chips are attached to photo paper substrate by PU-ECA. The brightness of the LED chips does not change when rolling at radius of 18.5 mm (b) and 15 mm (c).

Furthermore, the PU-ECA can increase the circuit integration density by providing multiple-layer structures. As shown in Figure 4.6(a), a three-layer structure is built by drilling Vias through the substrate and using PU-ECA as polymer bumps and via filling materials. Each layer powers two LED chips. With the 3-D structure, six LEDs in all three layers can be illuminated to provide a more intense light per area (Figure 4.6(b)). Additionally, this package can withstand large deformation while maintaining its electrical functionality (Figure 4.6(c)).

80
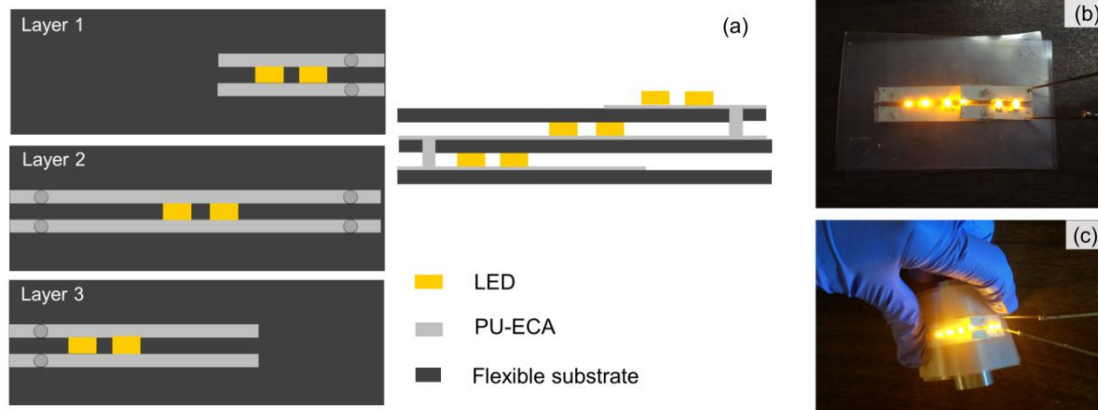
Figure 4.6 (a) Configuration and (b) photo of a three-layer structure built by drilling vias through each layer and using PU-ECA as Z-direction interconnects. Six LED chips are powered with two in each layer. (c) The brightness does not change when the three-layer package is bent.

4.3.3.2   Wearable antennas

The flexible PU-ECA may also be used as flexible RF-devices. A flexible antenna is fabricated by stencil printing PU-ECA on various substrates such as photo paper and bandage. As shown in Figure 4.7, PU-ECA printed on bandage can be bent and twisted without damaging the antenna pattern. From the simulation, within a range from 500 MHz to 5 GHz, the resonant frequency of the antenna is around 1.9 GHz. The resonant frequency of a free-standing antenna is measured to be 2.01 GHz, while when the antenna is wrapped around a human wrist, the resonant frequency shifts to 1.53 GHz. The shift in resonant frequency may result from the influence of the electromagnetic properties of the human body as well as the physical deformation. In both cases, the S11 parameter is below 10 db, indicating good performance of the printed flexible antenna.

81
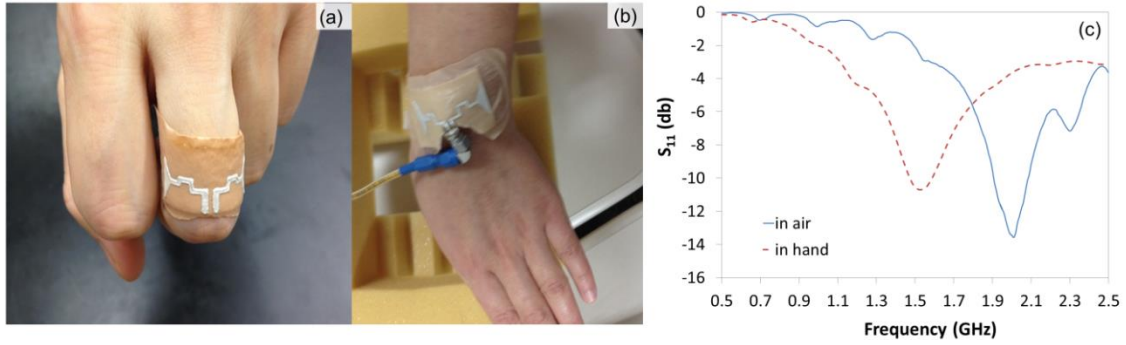
Figure 4.7 (a) Flexible antenna made of PU ECA can be printed on bandage and wrapped around a finger. (b) Testing the antenna on a wrist by a VNA. (c) The S11 parameter of the antenna in the frequency range of 0.5 to 2.5 GHz.

4.4   Conclusions

In summary, the PU-ECA in this study offers a high electrical conductivity achieved by the polymer shrinkage and in-situ formation of silver nanoparticles. The electrical resistivity reaches 1.0×10^{-5} $\Omega \cdot cm$ and remains stable when bending at 2.64 % flexural strain, rolling at a radius of 8 mm or pressing under 250 kPa. It also has good adhesion to various flexible substrates and Cu surfaces. The combination of these properties will make PU-ECA a very promising interconnect material for flexible and printed electronics.

CHAPTER 5 CONDUCTION DEVELOPMENT MECHANISM OF SILICONE-BASED ELECTRICALLY CONDUCTIVE ADHESIVES

5.1 Introduction

ECAs have been intensively studied as an alternative to solder in electronics. Compared with solder alloys, ECAs are more environmentally friendly, are easier to process, have lower processing temperatures, and allow for higher-resolution printing. ECAs are usually composed of a thermoset resin (usually epoxy, polyurethane, or polyimide) filled with metallic particles. With the rapid development of flexible/stretchable electronics, elastomers such as silicone-based ECAs (Silo-ECAs) have recently seen a tremendous growth in interest due to their unique combination of elasticity, biocompatibility [189], patternability [182, 190], and thermal stability [182]. Silo-ECAs have enabled exploration into various new applications, including microfluidic devices [191, 192], stretchable RF devices [193, 194], sensors [195], biomedical devices [196], flexible interconnects [5, 183], etc.

In spite of their excellent mechanical properties, the limited electrical performance of Silo-ECAs hinders wider use. The bulk resistivity of Silo-ECAs is usually above 2×10^{-4} $\Omega\cdot$cm with 80 wt.% silver [4, 5, 182, 191], while epoxy- and PU-based ECAs have been reported to achieve electrical resistivity of 2.5×10^{-5} $\Omega\cdot$ cm [37, 61] and 1×10^{-5} $\Omega\cdot$cm [60], respectively, at the same level of filler loading. Moreover, it has been found that even increasing the loading level cannot reduce the resistivity of Silo-ECAs below 2×10^{-4} $\Omega\cdot$cm [4].

This limited electrical conductivity deteriorates the performance of Silo-ECAs in flexible/printed electronics. For example, as device interconnects, a resistivity larger than

83

1×10^{-4} Ω·cm leads to severe resistive loss [197]; as printed signal transmission materials in radio frequency identification (RFID) antennas, a low conductivity decreases the quality factor as well as the reading distance [22]. Thus, enhanced electrical properties of Silo-ECA will expand its applications in a variety of flexible/printed electronics.

It is worth revisiting the conduction mechanisms of ECAs in order to explore the methods of enhancing the electrical conductivity of Silo-ECAs. In prior studies on epoxy- and PU-based ECAs, several conduction mechanisms have been proposed. In these studies, the correlation between resin shrinkage during curing and conductivity development is used to explain that the compaction of fillers by shrinkage provide a major driving force for conductivity development [23, 198, 199]; surface chemistry studies also discuss the decomposition of the surfactants on the silver flakes [35, 61, 200], as another reason for the conductivity development.

Compared to epoxy resins, silicone experiences much less curing shrinkage and has a lower elastic modulus. Therefore, the shrinking force in silicone is not as influential as in epoxy resin for filler compacting and it is questionable that Silo-ECAs would follow the conductivity development mechanisms proposed previously. In the present study, we discuss the conduction development mechanism of the Silo-ECAs based on newly-proposed chemical reactions on the silver flakes' surface and on the resulting silver flakes morphology changes, and present a novel way to a breakthrough of Silo-ECA conductivity.

84

5.2 Experimental

5.2.1 **Materials**

The silicone matrices for Silo-ECAs are a mixture of vinyl-poly(dimethyl) siloxane (Vinyl-PDMS) and hydride-terminated PDMS (H-PDMS). Mono hydroxy-terminated PDMS (OH-PDMS) is used as a reference for FT-IR. The details of these materials are listed in Table 5.1. Platinum(0)-1,3-divinyl-1,1,3,3-tetramethyldisiloxane complex (Sigma-Aldrich Co.) and PT88 (Wacker Chemie AG) are used as the catalyst and the curing inhibitor, respectively. Silver flakes are donated from Ferro Co.

Table 5.1 Silicones used in this study.

Abbreviation	Commercial name	Functional groups	Functional group%	MW
Vinyl-PDMS	Wacker® V1K	Vinyl	2.6%	18,000
H-PDMS-1	Sigma-Aldrich	Hydride	Chain-end	580
H-PDMS-2	Sigma-Aldrich	Hydride	Chain-end	24,000
H-PDMS-3	Gelest® H41	Hydride	Chain-end	63,000
OH-PDMS	Sigma-Aldrich	Hydroxide	Chain-end	4,670

5.2.2 **Preparation of ECAs**

Vinyl-PDMS and H-PDMS are mixed with a molar ratio of 1:1 and platinum catalyst is added to the mixture. In a typical ECA formulation, 80 wt.% silver and 20 wt.% of the above silicone mixture are homogenized for 5 minutes. The electrical conductivity measurement specimen is made by casting the ECA in a Teflon mold (22 mm×7 mm×0.5 mm) and then curing at 160 °C in an air-circulating oven (Thermal Scientific) for 1 hour.

5.2.3 Silver flake treatment and characterization

H-PDMS treated silver flakes are prepared by immersing silver flakes in H-PDMS-3 at 160 °C for 30 minutes. The treated silver flakes are washed with toluene in three centrifuge cycles in order to remove the remaining H-PDMS and with acetone in another three cycles to remove the products of the surfactant reduction reaction. Note that the surfactant on the silver flakes cannot be washed off by acetone or toluene during this process [25]. Finally, the silver flakes are dried in vacuum before characterization. The H-PDMS before and after treatment are studied by FT-IR (Nicolet, Magna IR 560).

Morphologies of untreated and treated silver flakes are observed by SEM (LEO 1530). Weight loss of untreated and treated silver flakes during heating is studied using TGA (TA Instruments Q50) with a heating rate of 5 °C/min. Raman spectra of silver flakes are obtained by using a LabRAM ARAMIS Raman confocal microscope (HORIBA Jobin Yvon) equipped with a 532 nm diode pumped solid state laser. Si wafer is used as a substrate for Raman measurements.

5.2.4 Characterization of ECAs

The dimensional change of the Silo-ECA paste during thermal curing is measured using a TMA in a macro-expansion mode (TA instruments, Q400) [23]. A small amount of the paste is sandwiched between two microscope cover slides and cured in the TMA. The dimensional changes during curing are recorded. The static force of the probe is kept at 0.02 N to ensure that the adhesive paste is not squeezed out during heating. The heating rate used is 5 °C min^{-1}.

For the in-situ resistance measurement during curing, two strips of polyimide tape are placed onto a glass slide with an 8 mm distance between them. The ECA paste is

86

spread between the gap by a doctor blade. Four Cu/Ni wires are bonded to the ECA as four electrodes. The specimen is then placed in an air-circulating oven. Electrical resistances during heating are recorded at 10 seconds intervals using a Keithley 2000 multimeter.

Bulk resistances of cured ECA strips are measured by a Keithley 2000 multimeter. The widths and lengths of the specimens are measured by a digital calliper (VWR). The thickness of the specimen is measured by Heidenhain (thickness measuring equipment, ND 281B, Germany). Bulk resistivity, ρ, is calculated using $\rho = Rtw/l$, where l, w, t are the length, width and thickness of the sample, respectively.

FT-IR (Nicolet, Magna IR 560) with an in-situ heating apparatus is used to investigate the curing of the PDMS matrix. A drop of the resin is sandwiched between two KBr pellets and heated from 40°C to 160°C at a ramping rate of 5°C/min. The spectra are collected during heating. A resolution of 2 cm^{-1} is used over 64 scans.

The Young's modulus is measured by tensile testing with an extension rate of 100 mm min^{-1} (Instron Microtester 5548). The curing temperatures are measured by DSC (TA Instrument Q2000) with a ramping rate of 5°C /min from 40°C to 250°C.

5.3 Hypothesis

5.3.1 **Shrinkage of polymers**

Curing shrinkage was found to be the prerequisite for achieving conductivity in epoxy-based ECAs [23]; the shrinkage leads to closer compaction of silver fillers, which can dramatically decrease the contact resistance according to the electron tunnelling theories [17-20]. Figure 5.1 shows the curing shrinkage of epoxy-, PU-, and silicone-based ECA (V-PDMS and H-PDMS-3 molar ratio 1:1, with 500 ppm platinum catalyst in

87

terms of silicone resin) as measured by TMA, and the in-situ electrical resistance change with temperature. It is clear from the TMA results that epoxy- and PU-based ECAs show an obvious dimension change of approximately 20-30 microns due to curing shrinkage. The conductivity development also synchronizes with this resin shrinkage. In the case of Silo-ECAs, an initial dimension decrease below 50 °C results from the spreading of Silo-ECAs. Above 50 °C, only thermal expansion is observed, corresponding well with the previous report that the curing shrinkage of silicone is around 0.5% [201], which can hardly be detected by TMA. It is doubtful that such a small shrinkage would produce effective compaction force for silver flakes, as in the case of epoxy- or PU-based ECAs.
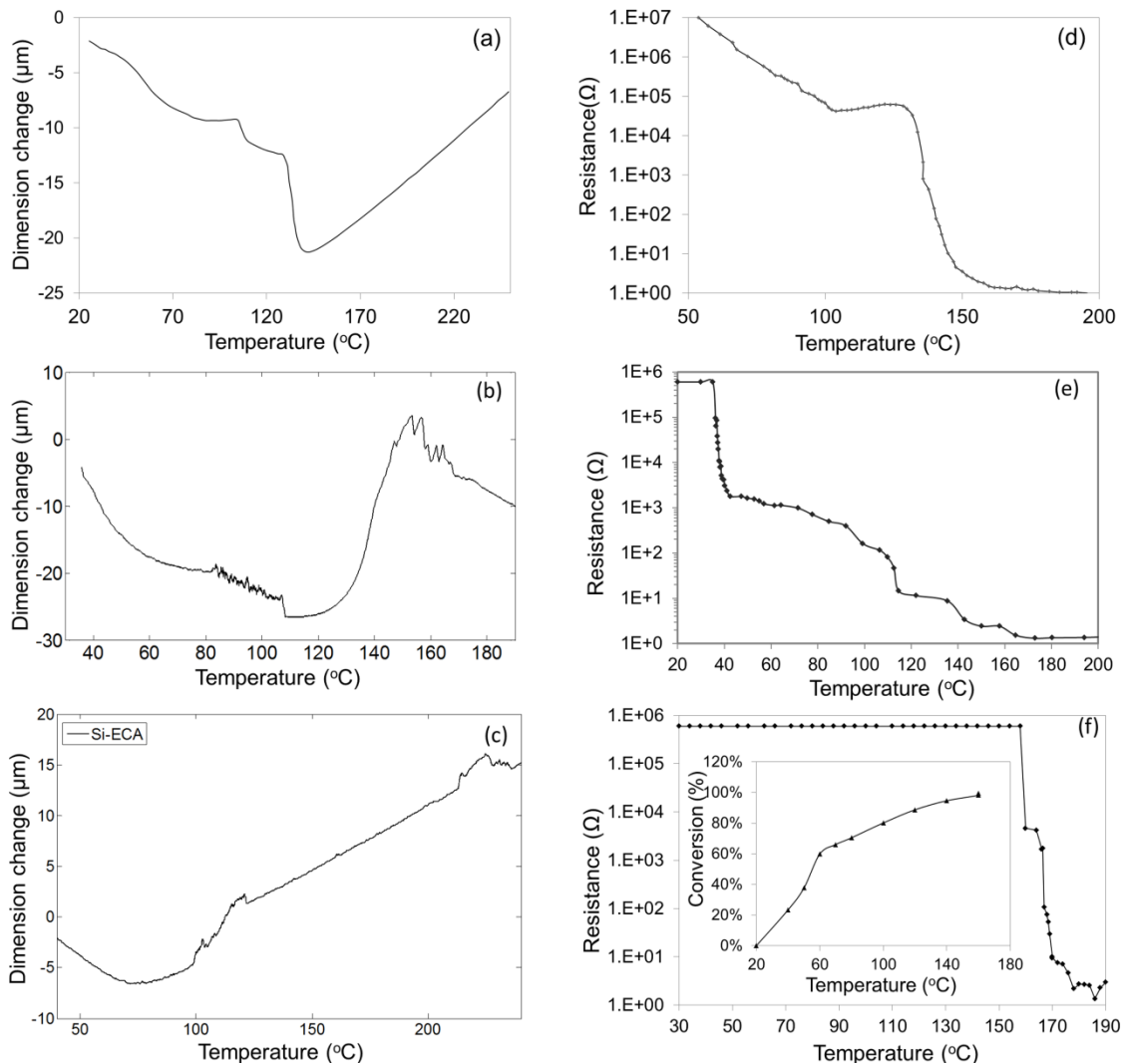
Figure 5.1 Left column: (a) curing shrinkage of epoxy-based [23], (b) PU-based [60], and (c) silicone-based ECAs as measured by TMA. Right column: (d) the resistance change as a function of temperature of epoxy-based [23], (e) PU-based [60] and (f) silicone-based ECAs (inset is the conversion of the silicone curing reaction calculated by the consumption of Si-H group in FT-IR spectra; details shown in section 5.4.1). (a), (b), (d), (e) are adapted from ref. [23] and [60] as a courtesy of the authors.

To further investigate the effect of the low curing shrinkage of silicone on the resistivity, the bulk resistivity of the same Silo-ECA formulation cured at 60 °C and 160 °C are compared (Table 5.2). Although both samples are completely cured and similar curing shrinkage is expected, they yield highly dissimilar conductivities: while the sample cured at 60 °C remained insulative, the one cured at 160 °C developed a

89

resistivity of 1.6×10^{-4} $\Omega \cdot$cm. Moreover, the same formulation without the curing agent

(such that it cannot be cured and no curing shrinkage can occur) achieved a resistivity of

2.9×10^{-5} $\Omega \cdot$cm after holding at 160 °C for the same time required for curing. Thus, it may

be seen that curing shrinkage is not a prerequisite for conductivity development in Silo-

ECAs unlike the case of PU- or epoxy-based ECAs.

Table 5.2 The bulk resistivity of Silo-ECA cured at different temperatures

Samples	Bulk resistivity ($\Omega \cdot$cm)
Cured at 60°C	insulative
Cured at 160°C	1.6×10^{-4}
160°C without catalyst (not cured)	2.9×10^{-5}

Interestingly, the Silo-ECA shows a sudden resistance drop during heating at

approximately 160°C (Figure 5.1(f)), which coincides with the temperature at which

curing is completed, as tracked by the in-situ FT-IR (Figure 5.1(f), inset). This abrupt

conductivity development differs from the gradual decrease of electrical resistance

observed during the curing of epoxy- and PU-based ECAs. This indicates that shrinkage

may not be a major cause of the conductivity development; instead there might be

another reason for the sudden change.

5.3.2 **Removal of silver surfactants**

The unusually high conductivity of Silo-ECAs heated at 160°C without curing

leads to the consideration of another possible conduction mechanism, such as the removal

of surfactants from the silver flakes. Most commercial silver flakes are lubricated with

long-chain fatty acid, whose carboxylic group coordinates with silver and forms a silver

carboxylate complex layer [25-27]. This surfactant layer helps to prevent oxidation and to

facilitate the dispersion of silver flakes in high filler-loading ECAs [25-27]. However, they are undesirable for electron conduction, as they form a large energy barrier for electron tunnelling between neighbouring flakes. Therefore, removing the surfactant layer during or after curing becomes one important way of making highly conductive ECAs. Various methods have been reported to efficiently remove these surfactants, including thermal oxidation during high-temperature curing [27, 28], replacement of the long-chain fatty acid salts with a shorter dicarboxylic acid [29-31], surface iodination of silver flakes [62], and addition of reducing agents to reduce the silver salts to metal nanoparticles [58, 60, 61]. This last method is especially effective, because it not only removes the surfactants, but also generates silver nanoparticles from silver-fatty acid complex that will later be sintered during curing to bridge between neighbouring flakes. Conventional reducing agents for silver nanoparticle synthesis, such as sodium boron tetrahydride, ethylene glycol, and poly(ethylene glycol) display the capability to reduce silver carboxylate surfactants and generate nanoparticles in epoxy- and PU-based ECAs [58, 60, 61]. Recently, H-PDMS, which is a silicone curing agent, has also been demonstrated to reduce silver salts to silver nanoparticles [192, 202]. Hence, it is possible that the reduction of silver surfactants is the main reason for conduction development.

To investigate this possibility, silver flakes are mixed with H-PDMS and heated at 160 °C for 30 minutes. Then H-PDMS treated silver flakes are compared with pristine silver flakes and the flakes thermally treated at 160 °C for 30 minutes in terms of TGA profiles, SEM morphologies, and Raman spectra.
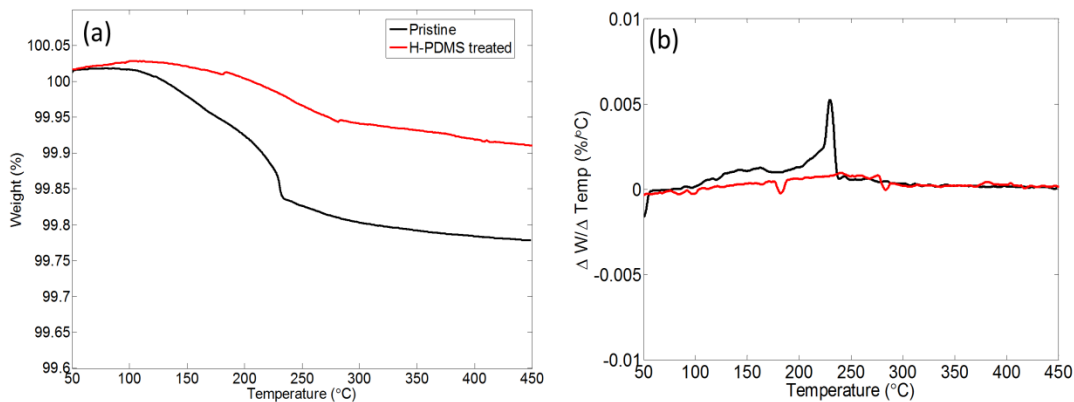
Figure 5.2 (a) Weight loss and (b) first derivative of weight loss over temperature of the untreated silver flakes (black line) and the H-PDMS treated silver flakes (red).

In the TGA results, the pristine flakes show an obvious weight loss at 220.92 °C (Figure 5.2 (b)), which is attributed to the decomposition of the surfactants.[13] The total weight loss of the pristine flakes is 0.22% when heated to 450°C in a dynamic run (Figure 5.2 (a)). In the case of the H-PDMS-treated silver flakes, the weight loss around 220°C almost disappears and a significantly smaller total weight loss of 0.09% is observed after reaching 450°C, implying partial removal of surfactants by H-PDMS.

92
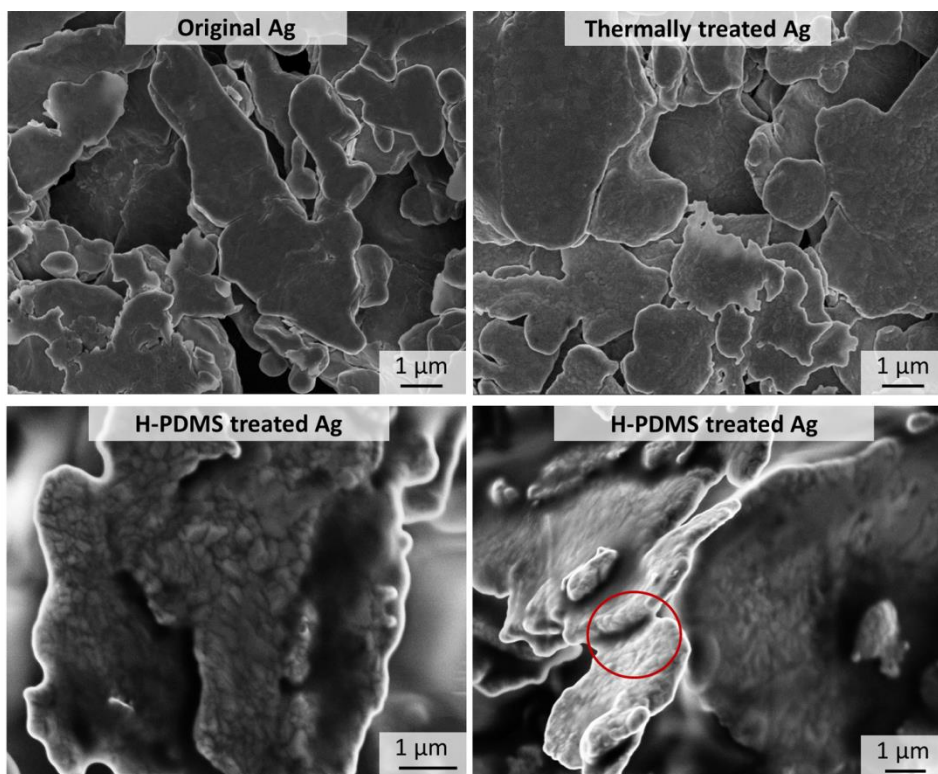
Figure 5.3 SEM images of original silver flakes, silver flakes treated at 160 °C for 30 minutes, and flakes treated with H-PDMS at 160 °C for 30 minutes.

SEM images are used to confirm the formation and sintering of silver nanoparticles by H-PDMS reduction. As shown in Figure 5.3, pristine and thermally-treated silver flakes show relatively smooth surfaces, while the H-PDMS-treated silver flakes clearly show in some degree roughness owing to the growth of nano- and sub-micrometer-sized silver particles on their surfaces and edges. Moreover, these grown sub-micrometer-, and nano-sized particles on the silver flake surfaces are sintered, forming necking between the silver flakes (highlighted by red circles in Figure 5.3).
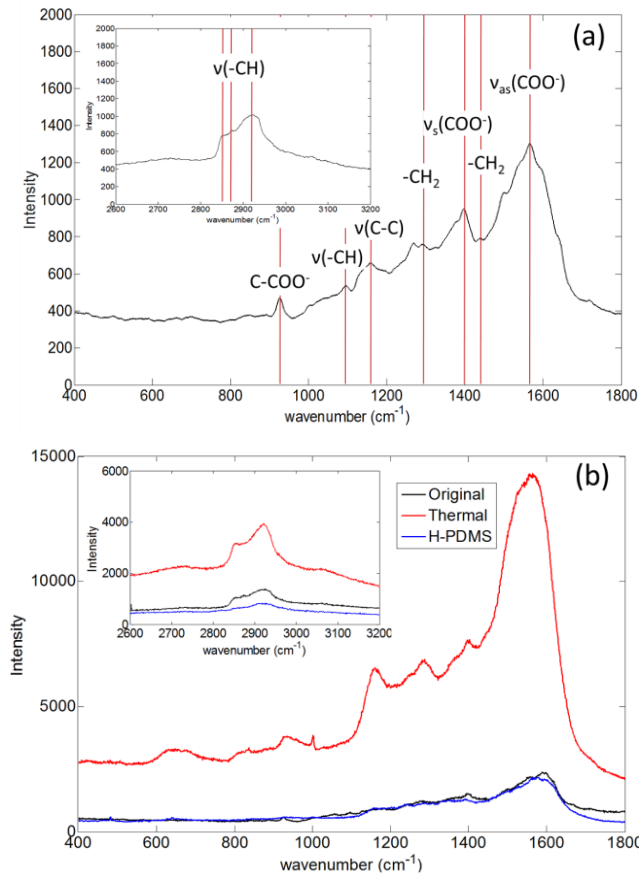
Figure 5.4 (a) Raman spectrum of the silver flakes without any treatment. (b) Raman spectra of the silver flakes with various treatments.

Figure 5.4(a) shows the Raman spectrum of the pristine silver flakes. The presence of silver carboxylate surfactants on the silver flakes is verified by the symmetric ($vs(COO^-)$) stretching at 1393 cm^{-1} and asymmetric ($vas(COO^-)$) stretching at 1565 cm^{-1}. The strong intensity of these peaks indicates that the surfactants are acids bonded to the surface as anions [131]. The peak at 927 cm^{-1} is assigned to the C–COO$^-$ stretching, those at 1092 and 1149 cm^{-1} are from the C-C backbones, and the peaks at 1286 and 1431 cm^{-1} are attributed to the twist and scissor of methylene groups [132]. The surface enhanced Raman scattering (SERS) peaks of C–H stretching of the surfactant on the silver are well resolved in the region of 2800-2950 cm^{-1}[61]. After thermal treatment, the appearance of sub-micron roughness (Figure 5.3) exhibits the SERS effect of an almost

94

twenty-fold increase in intensity. Interestingly, although more nanoparticles and sub-micron sized particles are generated, the intensity of H-PDMS-treated silver flakes is actually smaller than that of the original flakes (Figure 5.4 (b)). This indicates that the amount of the surfactant on the silver flake surfaces is dramatically reduced, so the total surfactant concentration is too small to be detected even by SERS effect. Therefore, it is confirmed that H-PDMS reduces the surfactants to nanoparticles during curing.

To further understand the chemical reaction between silver surfactant and H-PDMS, the chemical structure of H-PDMS before and after treatment are characterized by FTIR. H-PDMS-1 is chosen here because of its low viscosity, which allows the silver flakes to precipitate and form a free-standing film after treatment (Figure 5.5). The supernatant is thus extracted by a pipette and dried on the KBr pellet for FTIR analysis. As shown in Figure 5.5(d), after heating with silver flakes, H-PDMS-1 has seen a clear decrease in absorption of Si-H group (2130 cm^{-1} and 913 cm^{-1})[203] and correspondingly a growth in Si-OH group (3314 cm^{-1} and 863 cm^{-1}) [203], making the spectrum very close to that of OH-PDMS. The IR results indicate that during reducing the silver surfactant, the Si-H group is oxidized to Si-OH. Note that pure heat treatment of H-PDMS-1 (without silver flakes) does not show such obvious oxidation of Si-H, although some Si-H may get oxidized in open air by post-cure reaction [190]. This is consistent with previous studies observing that the Si-H groups can reduce the metal salts to metal nanoparticles while getting oxidized themselves [192, 202].
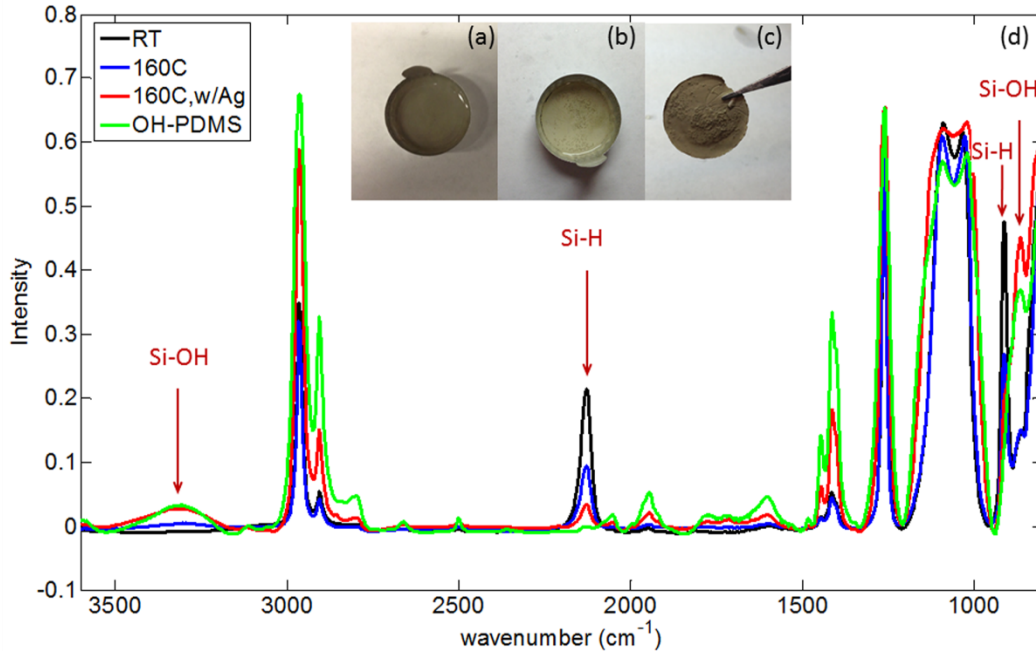
Figure 5.5 The mixture of silver flakes with H-PDMS-1 (a) before and (b) after thermal treatment; (c) the silver flakes form a free-standing film after treated with H-PDMS at 160°C. (d) The FTIR spectra of H-PDMS-1 at room temperature (black), after heating at 160°C for 30 minutes (blue), after heating at 160°C for 30 minutes with silver flakes (red), and hydroxide-terminated PDMS as a reference (green).

5.3.3 Hypothesis about the conduction mechanism of Silo-ECAs

Two conclusions can be drawn from the above observations: 1) In Silo-ECAs, the silver surfactant removal is the main contributor to the resistance drop during curing; 2) The electrical resistance drop occurs at the same point that the curing reaction finishes, indicating that it is likely that the shrinkage kinetically controls the conduction change. We combine these two factors and propose the hypothesis for the conduction development mechanism of Silo-ECAs.

The electrical resistance drop mainly results from the removal of the surfactants and sintering between neighbouring silver flakes, but this process can only occur before the curing process is completed. This results from the fact that when the curing finishes, the viscosity is so high that the transport of H-PDMS is prevented, or H-PDMS is

96

completely consumed. At the same time, the relatively small shrinkage of the silicone matrix "pulls" all of the flakes together, resulting in a dramatic drop in resistance; this resistance becomes the final resistance of the ECA.

5.4 Hypothesis demonstration and improvement

If the above hypothesis holds true, in order to improve the electrical conductivity of Silo-ECAs, the reduction and sintering processes need to take place completely before the cross-linking reaction causes an insurmountable increase in the viscosity. That is, we need to postpone the curing process without changing the curing temperature.

To validate the hypothesis, and also to improve the electrical conductivity, three approaches to "postpone" the curing of the silicone matrix are examined. These three approaches are: 1) using long chain H-PDMS; 2) using lower concentration of the platinum catalyst; and 3) adding curing inhibitors.

5.4.1 Using long chain H-PDMS

The rationale of this first approach is that the bulkier the molecule is, the slower the molecule can move to find the reaction sites. Here, the vinyl-PDMS is fixed and three H-PDMS with different chain lengths (Table 5.2) are used as curing agents. The platinum catalyst concentration is 500 ppm, and the curing profile is 5 °C /min to 160 °C, where it is held isothermally for 1 hour.
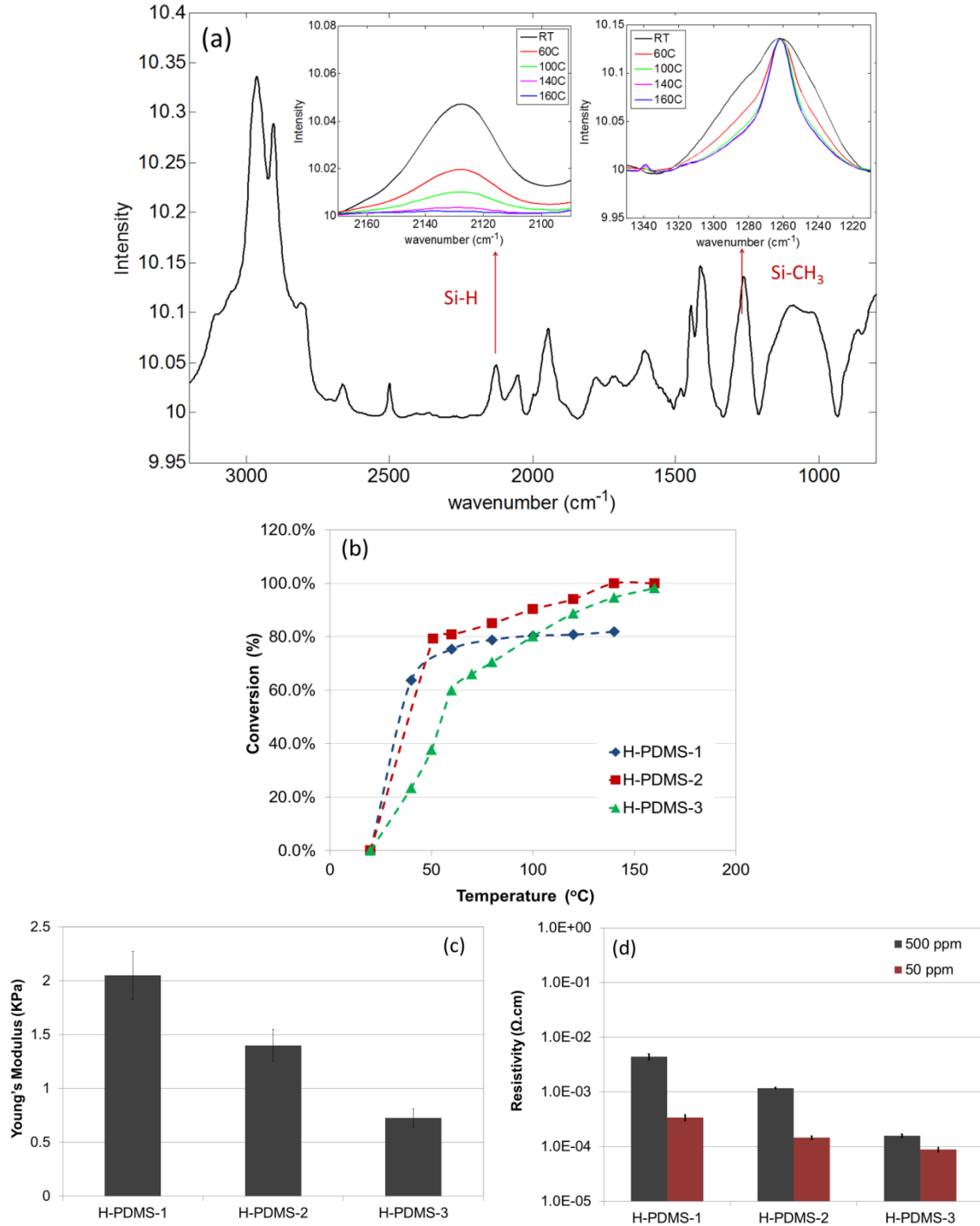
Figure 5.6 (a) FTIR spectra of the silicone matrix before curing; the consumption of H-PDMS-3 with temperature increases (inset); (b) The conversion percentage as a function of temperature of three different formulations; (c) The elastic moduli of cured silicone matrix with three different H-PDMS; (d) The bulk resistivity of Silo-ECA cured with H-PDMS of different chain lengths and different concentrations of platinum catalysts.

Figure 5.6(a) shows the curing kinetics of the three Silo-ECAs tracked by in-situ FTIR spectra. The peaks at 2130 cm^{-1} and 1261 cm^{-1} are attributed to the stretching of the Si-H group and the CH$_3$ symmetrical deformation of Si-CH$_3$, respectively [204]. The Si-H group is gradually consumed, while the peak intensity of Si-CH$_3$ remains level during curing. Therefore, the 1261 cm^{-1} peak is used as reference peak and the peak intensity ratio I (2130cm^{-1})/ I (1261cm^{-1}) is used to calculate the conversion of the curing reaction. As can be seen in Figure 5.6 (b), the initiation of the curing reaction is faster for shorter chain molecules. This means that, in the case of long-chain H-PDMS, it takes longer to cure, which allows a more complete sintering process.

As expected, the electrical resistivity decreases from 6×10^{-3} Ω•cm, to 1×10^{-3} Ω•cm, to 2×10^{-4} Ω•cm, as the H-PDMS molecular weight increases (Figure 5.6 (d)). Usually, the increased molecular weight means a decreased cross-linking density, which is also confirmed by the decreased Young's modulus shown in Figure 5.6 (c). If the conduction mechanism is purely the result of the shrinkage of the polymers, a decreased cross-linking density would lead to less shrinkage and a higher bulk resistivity [185]. However, here the opposite is observed, which confirms that shrinkage is not the main mechanism of conductivity development in the case of Silo-ECAs. Instead, the high electrical conductivity results mainly from the reduction of silver surfactant and subsequent sintering of the generated silver nanoparticles from the reduction reaction. That is why, in the case of H-PDMS-3, a longer time before complete cure allows for more sintering and improves the electrical conductivity.

99

5.4.2 **Using lower concentration of platinum catalysts**

According to previous reports, the concentration of platinum catalyst can influence the kinetics of PDMS curing; the larger the concentration of catalyst is, the faster the reaction speed will be [190]. Encouraged by this finding, the second strategy to improve the conductivity of Silo-ECA is to reduce the concentration of platinum catalyst to slow down the curing.
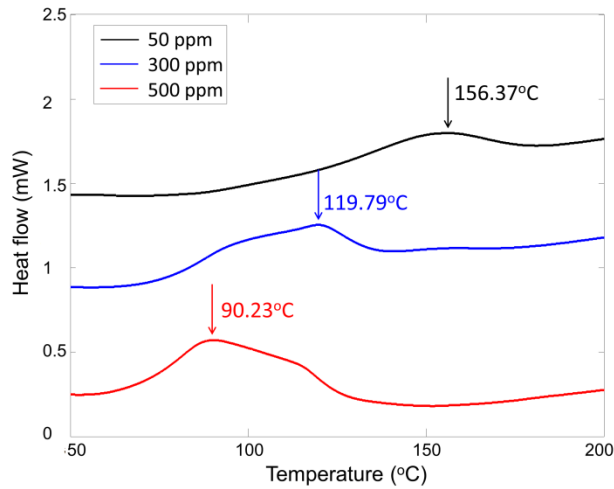
Figure 5.7 DSC of PDMS matrix cured by H-PDMS-3 with different concentrations of platinum catalysts.

Figure 5.7 shows the curing profile of a matrix cured by H-PDMS-3 with different catalyst concentrations. As expected, the peak curing temperature increases from 90.23°C, to 119.79°C, to 156.37°C, when the catalyst concentration decreases from 500ppm, to 300ppm, and further to 50ppm, respectively. At lower concentrations of catalyst, the slow curing allows a more complete reduction of silver surfactants and silver nanoparticle sintering, and thus results in a higher conductivity. Indeed, the resistivity of Silo-ECA (cured by H-PDMS-3) decreases from 1.59×10^{-4} Ω•cm to 8.82×10^{-5} Ω•cm when the catalyst concentration decreases from 500 ppm to 50 ppm. It should be noted that simply by adjusting the catalyst concentration, we are able to achieve a resistivity of

100

8.82×10^{-5} Ω•cm, 55% lower than the best value reported up to this point. The effect of the platinum catalyst on the conductivity of Silo-ECA is also clearly shown for other two formulations. Silo-ECAs prepared with H-PDMS-1 and H-PDMS-2 have much lower resistivity of 3.38×10^{-4} Ω•cm and 1.47×10^{-4} Ω•cm, respectively, when the concentration of catalyst drops from 500 ppm to 50 ppm. The effect of the platinum catalyst on Silo-ECA resistivity is more significant for H-PDMS-1 than for H-PDMS-2 and H-PDMS-3, which also indicates that this is a kinetically-controlled process.

5.4.3 Using curing inhibitors

Another approach to slow down the curing reaction is to add a small amount of inhibitor. Inhibitors can temporarily deactivate the platinum catalyst at room temperature. During thermal curing, the inhibitor evaporates at elevated temperatures, after which the silicone resin can be cured. Therefore, the curing rate of silicone can be easily controlled by adjusting the ratio of the inhibitor to the platinum catalyst [190].
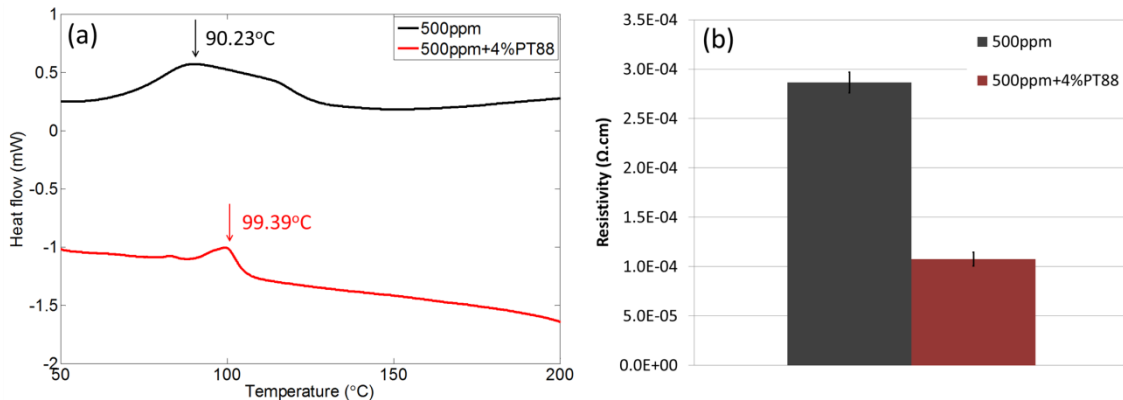
Figure 5.8 (a) DSC of PDMS matrix cured by H-PDMS-3 with and without the curing inhibitor PT88. (b) The electrical resistivity of PDMS-ECA cured with and without curing inhibitor.

Figure 5.8 shows the curing profile of silicone (prepared with H-PDMS-3) with and without the inhibitor PT88. In both cases, the platinum concentration is 500 ppm.

101

After 4% PT88 is added, the curing peak temperature moves from 90.23°C to 99.39°C. Correspondingly, the resistivity decreases from 2.86×10^{-4} Ω•cm to 1.08×10^{-4} Ω•cm, as a longer curing time enables a more thorough reduction reaction.

5.5 Conclusions

In summary, we propose a new conduction development mechanism for Silo-ECAs, which is different from the polymer shrinkage theory proposed for epoxy- and PU-based ECAs. The reduction of surfactants on silver flakes by H-PDMS and subsequent sintering of the silver nanoparticles generated is the driving force behind the increase in conductivity; however, the curing process kinetically controls the conductivity development, as the reduction and sintering cease when the curing is completed. Following this new mechanism, by prolonging the curing process of silicone, we can decrease the electrical resistivity of Silo-ECAs to $8.82 \times 10\text{-}5$ Ω•cm, which is 55% lower than the best value reported for Silo-ECAs so far.

CHAPTER 6 RATIONAL DESIGN OF PRINTABLE, HIGHLY CONDUCTIVE SILICONE-BASED ELECTRICALLY CONDUCTIVE ADHESIVE FOR STRETCHABLE RADIO-FREQUENCY ANTENNAE

6.1 Introduction

Research and development in modern electronics strives for increased functionality and reduced form factor. Stretchable radio-frequency (RF) electronics are gaining popularity as a result of the increased functionality they gain through their flexible nature, impossible within the confines of rigid, planar substrates. Stretchable RF electronics not only enable applications in which circuits can be wrapped conformally around complex curvilinear shapes or biological tissues, such as in body-worn wireless sensor nodes [205], and RFID [206], but also allow facile tuning of the resonance frequency by mechanical deformation[207]. However, the field of stretchable RF electronics is still in its infancy, and like other emerging electronics technologies, new materials and processing methods are the two driving forces for their continued development.

There are currently two general approaches to the fabrication of stretchable electronics. The first utilizes conventional rigid materials, but employs elegantly-designed wavy or arc-shaped structures that are capable of accommodating applied strains of 100% or more [171, 173-178]. The second approach is to maintain the conventional circuit layout, but embed stretchable or flowable conductive materials, such as conductive polymers [208, 209], conductive polymer composites[5, 194, 210], and liquid metal alloys [211, 212] as stretchable conduction lines. For antennae, this second approach is usually preferred

because of its relative simplicity in circuit design and fabrication. However, this approach imposes stringent requirements for the conductive materials, including 1) The material must have a very high electrical conductivity to achieve high-efficiency for the RF devices [213]; and 2) the material needs to be highly elastic to provide a tunable resonant frequency [212], and must maintain a similar electrical conductivity under applied strain. Conductive polymers and carbon-based conductive composites have conductivities at least three orders of magnitudes lower than those of metals, leading to an inferior efficiency [209]; while liquid metal alloys usually present the fundamental problems of a high melting temperature (limiting their usage in cold weather), thermal expansion coefficient mismatch with dielectric substrates, and a tendency towards leakage.

In this chapter, we report the use of stretchable silo-ECAs as conductor and pure silicone elastomers as substrate to fabricate stretchable antennae. Silicone rubbers have the unique combination of high elasticity, biocompatibility[189], patternability[182, 190], and low dielectric constant and low dissipation, making them an excellent candidate for stretchable antenna substrates. The silicone substrate selected in the present study, Elastosil® M 4642, has an elongation of break of 787%, suitable patternability by soft-lithography, and a low dielectric constant ca. 3 and dissipation factor <0.01 for 10MHz-1GHz (Figure 6.1). More importantly, the silo-ECA conductors can be rationally designed to achieve 1) a high conductivity at both static state and stretching state for a high radiation efficiency; 2) a proper viscosity to enable stencil printing or soft-lithography for high-resolution and large scale fabrication; and 3) cross-linking with the silicone substrate to eliminate delamination and leaking issues. We use these materials to fabricate a quarter-wavelength bow-tie antenna that can be tuned from 3.45GHz to

104

2.42GHz by simple mechanical stretching to 60% strain, while maintaining a high reflection power below -15dB.
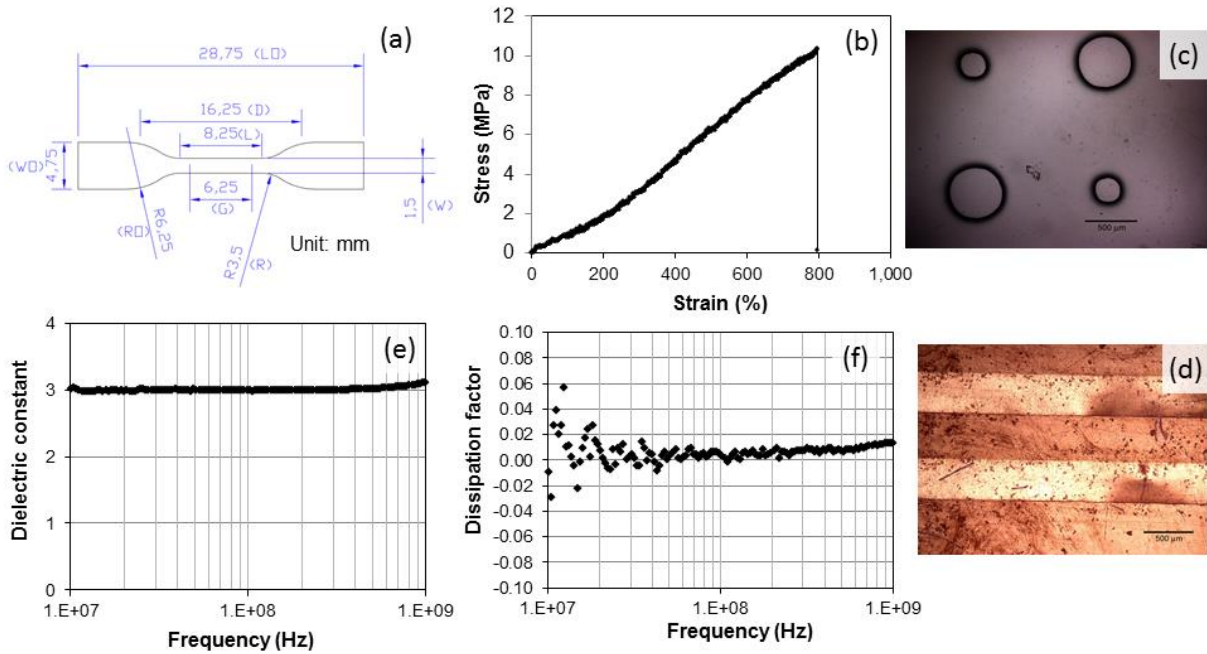
Figure 6.1(a) The dumbbell shape for the tensile test of silicone substrate Elastosil® M 4642. (b) The tensile test result of the silicone substrate. (c) The circle pattern and (d) the line pattern formed by soft-lithography on silicone substrate. (e) The dielectric constant and (f) dissipation factor of the silicone substrate from 10MHz to 1GHz.

6.2 Experimental

6.2.1 Synthesis of silo-ECA

The silicone matrix for the silo-ECAs is prepared by mixing vinyl-modified PDMS (Wacker® V1K) and hydride-terminated PDMS (Gelest® H41) with a molar ratio of 1:1 and 50 ppm platinum(0)-1,3-divinyl-1,1,3,3-tetramethyldisiloxane complex (Sigma-Aldrich Co.) as catalyst. The iodination treatment of silver flakes was performed by dispersing the flakes (Silflake® 144) in an ethanol solution of iodine (0.5µmol L^{-1}) for 1 hr. Then a simple filtration was performed to wash out remaining iodine, and the flakes were dried in a vacuum oven for 24 hr [62]. In a typical ECA formulation, 80 wt.%

treated silver flake and 20 wt.% of the above silicone mixture were homogenized for 5 mins.

6.2.2 **Characterization**

The mechanical properties of the silicone substrate were tested in a typical tensile test setup (Instron microtester 5548). Samples were cut into a dumbbell shape (Figure S1a) and tested at a rate of 10 mm/min. The dielectric properties were measured by an RF impedance analyzer (Agilent E4991A).

To measure the electrical conductivity, the paste was cast in a Teflon mold (22 mm × 7 mm × 0.5 mm). After curing at 160°C for 1 hour, the bulk resistance of the film was measured by the four-wire method with a Keithley 2000 multimeter. The thickness was measured by a profilometer (Heidenhain ND 281, Germany). Electrical conductivity σ was then calculated by

$$\sigma = \frac{l}{Rwt}$$

Where R is the bulk resistance and l, w, and t are the length, width and thickness of the film, respectively.

Raman spectra of silver flakes were obtained by a LabRAM ARAMIS Raman confocal microscope (HORIBA Jobin Yvon) equipped with a 532 nm diode pumped solid state (DPSS) laser. Si wafer was used as a substrate.

Decomposition of the lubricants on the surface of silver flakes was studied by TGA (TA Instruments, Q50) with a heating rate of $5°C$ min^{-1} in nitrogen.

The nanoparticles generated by reacting silver stearate and hydride-terminated PDMS were dispersed in toluene and dried in a copper grid before being characterized by TEM (JEOL 100CX). The nanoparticle colloidal in toluene was also characterized by UV-VIS

spectroscopy (Shimadzu UV-2450). Powder XRD analysis was carried out with a Philips X-pert alpha-1 diffractometer, using Cu K_α radiation (45 Kv and 40 mA).

The complex viscosity of uncured silo-ECA was measured using a discovery hybrid rheometer (TA Instruments, HR2).

The dimension change of the fabricated quarter-wavelength antenna during stretching was simulated using COMSOL multiphysics®. A rectangular substrate (35mm×30mm×0.7mm) was stretched in the simulation, with the assumption that silicone substrate has a Poisson's ratio of 0.49 [214].

The simulation of antenna performance was conducted by high frequency structural simulator (HFSS, Ansys Inc.). The S11 parameter was measured by a VNA (Agilent, 85052D).

6.3 Results and discussion

6.3.1 Enhancement of the electrical conductivity

High conductivity is one of the most critical requirements for the silo-ECAs to be used in stretchable antennae, because it will affect the conduction loss and thus the radiation efficiency. The conductors in conventional antennae are built with copper, which has a conductivity of 5.96×10^5 S/cm. Elastomers filled with conductive polymers or carbon materials can be easily stretched but they can hardly achieve the same level of conductivity even at static state [209, 215-224], which inevitably leads to a reduced radiation efficiency[209]. Therefore, silver-filled silo-ECAs are used here as the conductor. ECAs, especially epoxy-based ECAs, have gained widespread popularity as an environmentally friendly alternative for Sn/Pb solders due to their satisfactory conductivity [126]. Although the silicone matrix cannot provide sufficient curing

107

shrinkage to pack the silver fillers more tightly and enhance the electrical conductivity as in the case of conventional epoxy-based ECAs [23], the conductivity can still be improved through surface modification of the silver fillers. The first modification is the introduction of long-chain hydride-terminated polydimenthyl siloxane (H-PDMS) to the silo-ECA matrix, which we have extensively studied in Chapter 5. The high molecular weight of long-chain H-PDMS not only provides a high elasticity due to its low cross-linking density, but also allows for a slower curing of the silicone matrix, providing more time for the generation and sintering of silver nanoparticles before the completion of curing [6]. The second modification made to the filler particles is the iodination of the silver flakes before mixing with the silicone matrix. It was found that nonstoichiometric Ag/AgI nanoislands sparsely form on the silver flake surface after immersion of the flakes in dilute iodine/ethanol solution. The continuous decomposition of AgI and oxidation of Ag initiate the reconstruction of the silver flakes surface [62]. The exposure of fresh silver at the flake surface further facilitates the sintering between silver flakes during curing. After combination of these two surface modification methods, the silo-ECA can provide an initial conductivity of 1.51×10^4 S/cm filled with 80 wt.% silver flakes, which is comparable with conventional epoxy-based ECAs and in the same order of magnitude with as many metals [28, 37, 61].

6.3.2 Maintaining the conductivity during stretching

The more challenging part lies in maintaining a high conductivity of silo-ECA during stretching. Polymer composites loaded with conductive fillers usually experience significant conductivity decrease under mechanical strain. This response, called the piezoresistive effect, results from the displacement of fillers within the matrix. Analytical

models of the piezoresistance of polymer composites filled with carbon black [225, 226], CNTs [15, 227], and metal spheres [228] have been extensively studied and the conductivity after stretching is given by

$$\sigma_1 \approx \sigma_0 exp\left[\frac{4\pi\sqrt{2m\varphi}}{h}(s_0 - s_1)\right] \tag{1}$$

where, σ_0 and σ_1 are the conductivity before and after stretching, h is Plank's constant, φ is the height of the tunneling potential barrier, m is the mass of an electron, and s_0 and s_1 are the average interparticle distance between fillers before and after stretching, respectively. According to this equation, in order to maintain the conductivity after mechanical deformation, either the tunneling potential barrier φ should be reduced or the interparticle distance s_1 during stretching should be minimized. The surface modification methods mentioned above remove the insulating lubricant on the silver flake surfaces and thus reduce the tunneling potential barrier φ between the silver flakes only benefiting the initial conductivity but also mitigating the conductivity change upon stretching.

To minimize the interparticle distance s_1, the shape and morphology of the silver fillers used in silo-ECA are carefully engineered. To maintain the interparticle distance, fillers with a high aspect ratio are usually preferred and previous studies have mostly focused on 1-D high aspect ratio fillers, such as CNTs and silver nanowires [9, 176, 183, 195, 215, 216, 218-220, 222, 223]. However, in the case of aligned fillers, such as ultra-long SWNTs [215, 216], the conductivity is maintained only if the applied stress is in the longitudinal direction of the fillers, whereas extension in other directions only causes the conductivity to deteriorate. In the case of the randomly dispersed 1-D fillers, though they begin with a random network, they will become aligned under the applied stress during stretching. The contacts will be maintained in the stretching direction, but the loss of a

number of the conduction paths in the other two directions may decrease the overall conductivity of the composite [229]. Therefore, 2-D silver flakes are selected as fillers in this study. Silver flakes are stacked on each other parallel by the shear force in the printing process, as shown in Figure 6.2(a). As a result, even after stretching the 2-D stacking allows silver flakes to keep the tunneling distance almost unaltered within a certain strain, because the sliding between parallel flakes in the X-Y direction does not alter the distance between these flakes. As such, the resistance in the X-Y direction can be kept similar at a certain range of tensile strain. In addition to the shape design, secondary textures due to the *in situ* formation of silver nanoparticles from chemically reduction of the lubricant are another important factor to reduce the interparticle distance. As illustrated in Figure 6.2(b), these secondary textures could reduce the tunneling distance without changing the filler loading. This texture not only enhances the electrical conductivity of ECAs in the static state but also shortens the interparticle distance in the stretched state.
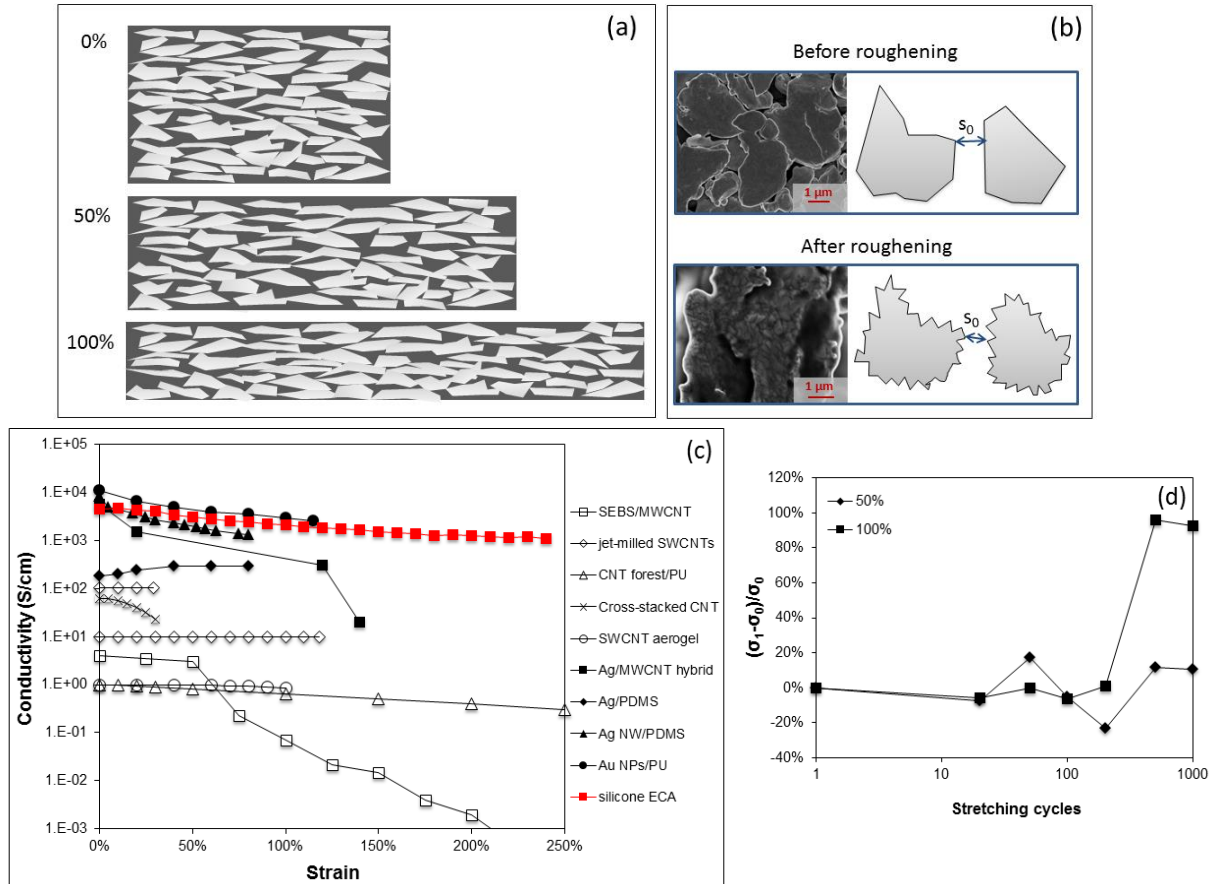
Figure 6.2 (a) A cartoon illustrates the silver flake displacement during stretching at different strain. (b) Scanning electron microscopic (SEM) images and schematic drawing showing the roughening process of the silver flakes can decrease the interparticle distance between neighboring flakes. (c) Conductivity change of the silo-ECA as a functional of tensile strain, as compared with the values from previous studies. (d) The conductivity of silo-ECA after cycling at 50% strain and 100% strain.

To measure the conductivity during stretching, a stripe of silo-ECA is printed on silicone substrate and cut into a dumbbell shape, as shown in Figure 6.3. The sample is then mounted on a tensile tester (Instron microtester 5548). Real-time electrical resistance change is measured by a typical four-wire method with all the wires "soldered" to the silo-ECA stripe with additional silo-ECA and the applied strain is simultaneously recorded by the tensile tester. The conductivity of the silo-ECA drops to 5030 S/cm after embedding in the substrate, yet it is still higher than most previously reported stretchable

conductors. Figure 6.2(c) shows the conductivity change as a function of applied tensile strain of the silo-ECA as compared with previously reported stretchable conductors. A general trend is visible where in the metal-filled conductive composites [183, 191, 195, 230] have significantly higher conductivity than carbon-filled conductive composites [215-220], while some CNT-based composites can maintain a high conductivity at larger elongation due to their high-aspect ratio [218]. The conductivity of the silo-ECA is two orders of magnitude higher than conventional silver/PDMS composites [191] due to the surface treatments mentioned above, and is comparable with gold nanoparticle/polyurethane composites [230]. More importantly, silo-ECA has better elasticity than previously reported metal/polymer composites and can maintain high conductivity at large deformations. For example, even at a strain of 240%, the conductivity is still as high as 1107 S/cm, indicating that the external stress only leads to sliding between overlapping flakes and does not change the tunneling distance significantly. In addition, the conductivity change is within 25% after 1000 cycles of stretching at 50% applied strain (Figure 6.2(d)). When we increase the tensile strain to 100%, the conductivity remains almost invariant over the first 500 cycles, and then even increases to double its previous value. The increase in conductivity may result from the further alignment of flakes in X,Y-direction by the mechanical stretching, giving rise to a better conductivity in the X,Y-direction. Maintaining the resistance at a very large strain is essential to have an impedance match for the antenna in the stretching state. Apparently, with a relatively slight change of resistance at large strains, these silo-ECAs are highly suitable for building stretchable antennae.
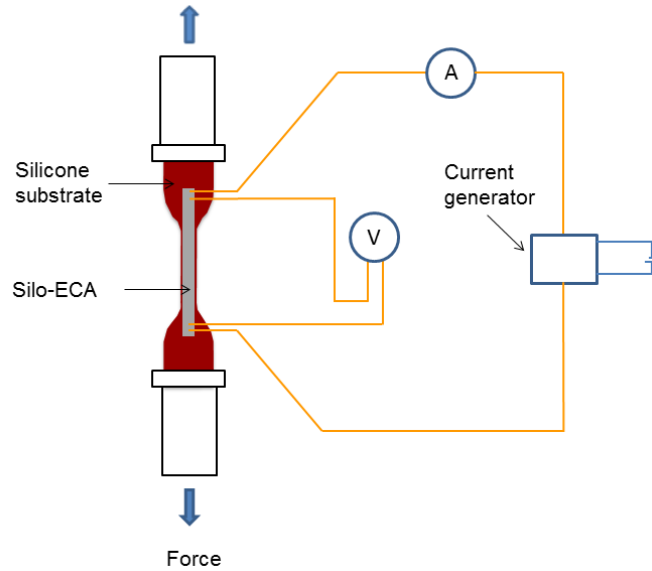
Figure 6.3 The illustration of the setup to measure conductivity change during stretching.

6.3.3 **Fabrication of stretchable antennae**

Another advantage of the current silo-ECA is the printability of the material as fine patterns, which is critical for the fabrication of stretchable antenna. For liquid-metal-based antennae, the antenna pattern is formed by injecting liquid metal into pre-patterned PDMS substrate with micro-fluid channels [212], a method by which it is difficult to fabricate complex patterns and has leakage concerns. CNT paste can be printed by screen printing, but the weak adhesion to PDMS substrate may limit the resolution of the printed patterns [216]. With a suitable viscosity of ca.366 Pa.s at room temperature and potential chemical bonding to the silicone substrate during cross-linking, the silo-ECA is eligible for high-definition stencil-printing as well as soft lithography to fabricate stretchable antennae. Figure 6.4(a) and (b) illustrate the two processes to fabricate the antenna pattern. In the stencil printing process, ECA is stencil-printed on a PTFE board and is half-cured. Then the silicone substrate is applied to cover the ECA pattern. After curing the ECA and silicone substrate, the silicone substrate and ECA are both peeled off from

113

the PTFE board as one piece and form the stretchable antenna. It should be noted that during the curing process, cross-linking occurs at the interface between ECA and silicone substrate, eliminating the delamination issues. In the soft-lithography process, a master mold is fabricated by patterning a silicon wafer via photolithography. Then silicon wafer is treated with 1H,1H,2H,2H-perfluorododecyltrichlorosilane to make it hydrophobic and to facilitate the peeling of the silicone substrate from the silicon wafer. Silicone prepolymer is poured onto the master mold and is cured to form an elastomeric mold. After peeling off the silicone elastomeric mold, the silo-ECA is dispensed into the cavity of the silicone substrate to form the conductive pattern. Figure 6.4(c)-(f) shows the printed lines and circles created by the two methods. Patterns on the scale of hundreds of microns can be accurately replicated through both methods, though the soft-lithography process can duplicate shapes with clearer definition and more uniform thickness.
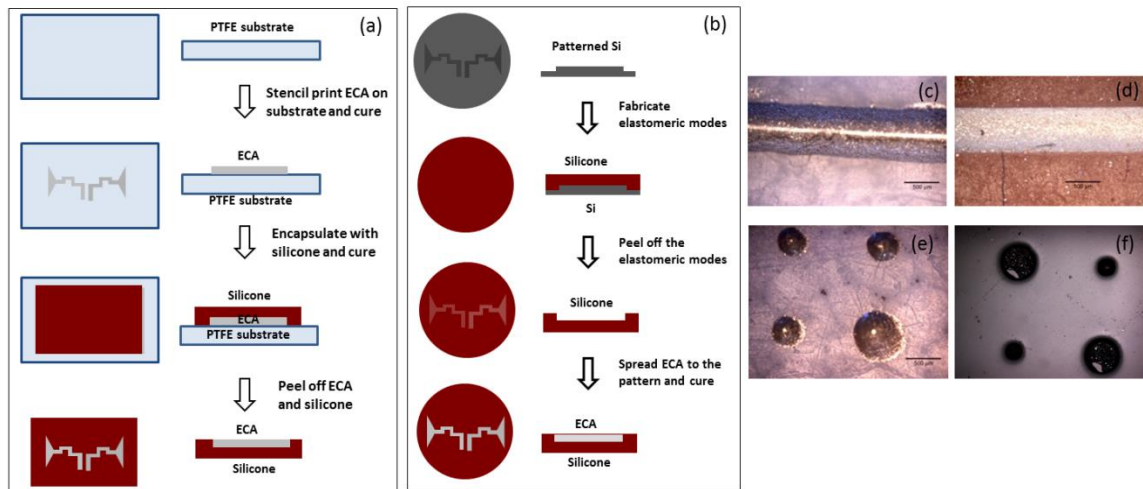
Figure 6.4 (a) Stencil printing process to fabricate a stretchable antenna. (b) Soft-lithography process to fabricate a stretchable antenna. Lines printed by (c) stencil printing and (d) soft-lithography. Circles printed by (e) stencil printing and (f) soft-lithography.

6.3.4 **Performance of the stretchable antennae**

High conductivity and elasticity, as well as facile fabrication, make our silo-ECA a promising building block for stretchable RF devices. As a demonstration, one half-wavelength bow-tie antenna (Figure 6.5(a)) and one quarter-wavelength bow-tie antenna (Figure 6.5(b)) are fabricated through the soft-lithography process (Figure 6.5(c) and (d)). It is clear that the fabricated antenna samples have a high fidelity to the original design. The reflected EM power of these two antennae are measured by a VNA and compared with the simulated data. If the antenna radiates efficiently, the majority of incident EM power is radiated into space with little reflected power. For the half-wavelength antenna shown in Figure 6.5e, the measured resonance frequency locates at 1.75GHz at the range of 50MHz-3GHz, slightly lower than the simulated value of 1.85GHz. The reflected power, also known as |S11|, is -18.5dB, which is higher than the simulated value of -13.1dB, indicating a high radiation efficiency of more than 99%. The band width of the actual antenna is larger than that of the simulated data, which may result from environment interference and the conductivity loss. For the quarter-wavelength antenna (Figure 6.5(f)), the measured resonance frequency lies in 3.50GHz at the range of 50MHz-4GHz, very close to the simulated value of 3.45 GHz. The |S11| of the real antenna is -17.7dB, also slightly higher than the simulated value of -16.9dB, indicating a better radiation efficiency than the simulation value. Similar to the half-wavelength antenna, the actual bandwidth of the fabricated quarter-wavelength antenna is larger than the simulated result.
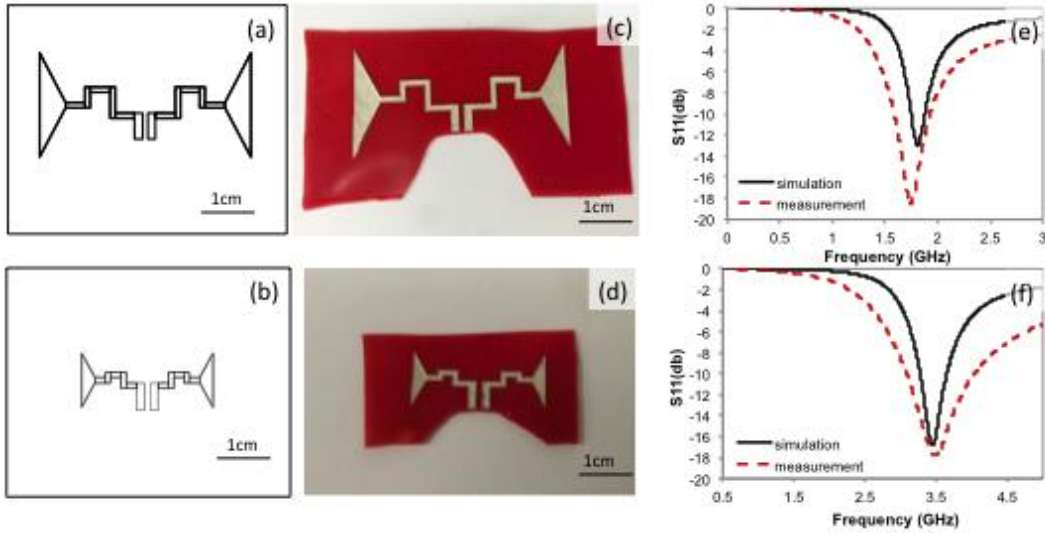
Figure 6.5 (a,b) The design of bow-tie antenna with two different sizes; (c,d) Bow-tie antenna fabricated by soft-lithography process; (e,f) The measured and simulated reflected EM power as a function of frequency. The upper row shows the results of half-wavelength antenna and the lower row shows the results of quarter-wavelength antenna.

Figure 6.6 illustrates the performance of the quarter-wavelength antenna under different tensile strain. The dimension change of the antenna is simulated by finite element analysis and then loaded into the HFSS to predict the reflected power of the deformed antenna. In order to determine the actual antenna performance under strain, the prepared quarter-wavelength antenna is mounted on the tensile tester and its reflected power is measured by the VNA during stretching. As shown in Figure 6.6(a), the resonance frequency decreases monotonically from 3.45 to 2.42GHz as it is stretched to 60% strain, demonstrating the tunability of the fabricated antenna over a wide range of frequency by simple mechanical modulation. The consistent agreement between measurement and simulation suggests the frequency tuning can be well-predicted. Figure 6.6(b) shows that the reflected power of the antenna is kept below -15dB when the antenna is stretched by up to 60%, indicating that the high-quality radiation efficiency is maintained during stretching. After releasing the strain, the resonance frequency returns to 3.45 GHz. It

116

should be noted that the antenna could be stretched to a strain larger than 60%, but the connections with the SMA become weak and the antenna pattern is severely deformed, making the performance unpredictable.
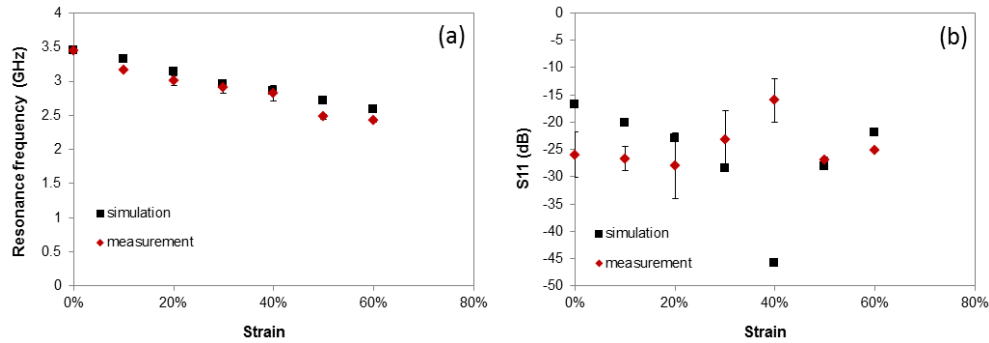
Figure 6.6 (a) The simulated and measured resonance frequency of the quarter-wavelength antenna as a function of tensile strain; (b) The simulated and measured reflected power of the quarter-wavelength antenna as a function of tensile strain.

6.4 Conclusion

In conclusion, we have developed silo-ECA materials that have a conductivity of 1.51×10^4 S/cm and can maintain conductivity above 1.11×10^3 S/cm, even at a large stain of 240%. By using the stretchable silo-ECAs as conductor and pure silicone elastomers as substrate, stretchable antennae can be fabricated by stencil printing or soft-lithography. The resulting antenna's resonance frequency is tunable over a wide range by mechanical modulation. This fabrication method is low-cost, can support large-scale production, has high reliability over a wide temperature range, and eliminates the concerns of leaking or delamination between conductor and substrate experienced in previously reported micro-fluidic antennae.

117

CHAPTER 7 CARBON /POLYMER NANOCOMPOSITES: SENSING THE THERMAL AGING CONDITIONS OF ELECTRICAL INSULATION COMPONENTS

7.1   Introduction

Insulation failure represents a significant contribution to the reliability issues of electrical components, including motors, aircraft, electrical generators, and cables. According to the Electric Power Research Institute, 37% of motor failures result from winding failures, which are frequently tied with insulation systems failures [231]. Although strict materials qualification tests are required before insulation materials are put to use, common operational conditions are more complex than standard aging tests. These polymer-based insulation materials are exposed to various deteriorative environmental stressors in operation, including elevated temperature, radiation (seen in nuclear power plants), humidity, and corrosive chemical environments. Moreover, unforeseen conditions and accidents such as excessive mechanical/electrical loads, reduced/blocked component cooling situations and high humidity conditions due to water or steam leaks or reduced ventilation may further increase the temperature and humidity. Therefore, a diagnostic condition monitoring (CM) method is currently in great demand.

CM is a technique that utilizes the changes and trends of the monitored characteristics to predict the need for maintenance before serious deterioration or breakdown occurs. The commonly monitored characteristics include 1) Ultimate tensile elongation, which has been widely accepted as an industry standard to predict remaining lifetime [232, 233]; 2) Cross-linking density of polymers, which can be measured by indenter modulus measurements [234, 235], swelling test [236], or the NMR relaxation

118

time T_2 measurements [237, 238]; 3) Density: the density of most cable materials will increase with aging due to volume shrinkage, which can provide an indication of the aging process [239]; 4) Oxidation induction time (OIT) and oxygen induction temperature (OITP) testing, which evaluates the resistance of polymers to oxidative thermal degradation according to DSC results [240]; 5) Chemical structure evolution: Fourier transform infrared spectroscopy (FTIR) has been employed to monitor the increasing amount of carbonyl groups (~ 1730 cm^{-1}) present in a polymer material due to oxidative degradation [236]. Table 7.1 summarizes the pros and cons of the traditional CM methods in terms of sensitivity, wide applicability, the amount of samples needed for testing, whether or not the method is destructive, cost of measurements (i.e. if any specific instrument or expertise is needed). As can be seen from Table 7.1, these conventional methods suffer from many problems. Indenter modulus, NMR, OIT and FTIR measurements need expensive testing equipment and trained personnel. Cross-linking density measurements cannot be applied to highly crystalline polymers while OIT/OITP tests are mainly applicable to polyolefin type polymers. Density tests may have the low signal to noise ratio as some polymers do not experience significant density change after aging. Moreover, all methods except indenter modulus profiling are destructive and none of them can achieve in-situ monitoring. Therefore, a non-destructive, facile and in-situ CM method is highly demanded to monitor the aging of insulation systems.

119

Table 7.1 Comparison of developed CM methods

	Sensitivity	Wide applicability	Amount of sample	Destructive	Cost
Elongation	High	Yes	Large	Yes	Low
Indenter Modulus	High	No	None	No	High
NMR	High	No	Small	Yes	High
Swelling	High	No	Large	Yes	Low
Density	Low	No	Small	Yes	Low
OIT/OITP	High[1]	No	Small	Yes	High
FTIR	High	No	Small	Yes	High

1. OIT/OITP tests become insensitive at the late stage of aging.

In our previous report [241, 242], we developed aging sensors based on carbon black (CB)/polymer composites. The electrical resistivity change of aging sensors can provide real-time signals and realize non-destructive monitoring. Also, the substantial electrical resistivity change of sensors gives a much higher sensitivity than conventional CM methods. However, the sensor signals cannot be used to predict the remaining lifetime because a direct relationship between the electrical resistivity of the sensors and the aging time of the monitored insulation system is lacking. Therefore, in this report, we investigate the kinetics of thermal aging obtained from sensor signals and correlate that with the kinetics obtained from typical tensile tests, which allows quantitative prediction of the remaining lifetime with sensor signals.

7.2 Experimental

7.2.1 Materials

Three polymers, ethylene propylene diene monomer rubber (EPDM), silicone rubber (SR) and epoxy were used as composite matrices for the aging sensors. EPDM, SR and peroxide cross-linking initiator were all provided by RSCC Wire & Cable LLC. The EPDM and SR are currently used as cable jackets. Antioxidant was removed from

the original EPDM resin and SR resin to eliminate the incubation period of aging. Epoxy is often used as encapsulates for motors, transforms and stators etc. Here a diglycidyl ether of bisphenol A (DGEBA, E500, Elantas PDG Inc.) is used as epoxy resin and a cyclic anhydride (C25, Elantas PDG Inc.) is used as curing agent. The molar ratio of epoxy resin and curing agent ratio is 1:0.84. Carbon black (CB) XC-72 was obtained from Cabot Corp, USA. The specific surface area and structure are 143 m^2/g and 174 cm^3/100 g based on an adsorption number of dibutyl phthalate (DBP). Multi-wall carbon nanotubes (MWNTs) of 10-20 μm in length and 10-20 nm in diameter are obtained from Chengdu Organic Chemicals Co.

7.2.2 **Methods**

7.2.2.1   Composite preparation

The fillers and polymer matrices are mixed in a three-roll mill. The optimal number of roll milling cycle is 100 for the best filler dispersion [243]. The obtained homogenous mixture is transferred to a Teflon mold and cured by heat pressing at 150°C for 1 hour for EPDM-based and SR-based composites, and 150 ^{o}C for 1 hour and 180 ^{o}C for 8 hours for epoxy-based composites. The sample thickness is kept around 300 μm to mitigate the diffusion limited oxidation effect (DLO) [235, 244] (Detailed calculation of thickness to eliminate DLO is available in Appendix A).

7.2.2.2   Thermal aging

Thermal aging is carried out in a commercial air-circulating oven with a temperature variance less than 1°C. For EPDM-based sensors, isothermal aging at 136°C, 150°C, and 170°C are performed respectively. For SR-based sensors, isothermal aging at

121

180°C, 190°C, and 210°C are performed respectively. For epoxy-based sensors, isothermal aging at 190°C, 210°C, and 230°C are performed respectively.

7.2.2.3 Electrical Resistivity measurement

The sensors are prepared by casting into a Teflon mold with dimensions of 3.25 mm × 1.7 mm × 0.3 mm before curing. Two electrode wires (0.16 mm in diameter, Ni plated Cu wires) are embedded in each sample, as shown in Figure 7.1. Then the sensors are encapsulated with pure epoxy resin. Electrical resistance of the sensor is tested by a multimeter (Fluke 289). The values are taken from an average of ten specimens.
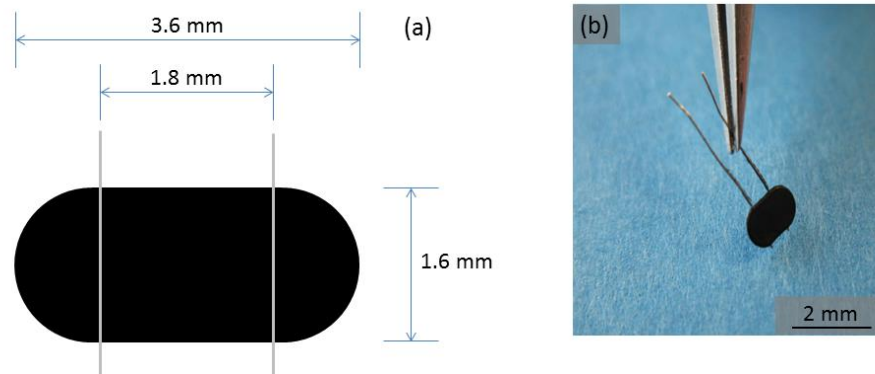
Figure 7.1 (a) The schematic illustration and (b) image of an aging sensor.

7.2.2.4 Mechanical properties measurement

The samples for mechanical measurements are without electrodes. Tensile tests are performed to the EPDM and SR composite samples, according to International Standard IEC 62582-3. They are cut into a dumbbell shape (Figure 7.2) and tested in a typical tensile test setup (Instron microtester 5548). The testing speed is 10 mm/min. The epoxy composite samples are rigid, especially after aging. Thus flexural properties are measured using a three point bending fixture according to ASTM D790-10. The samples

122

are made into a rectangular shape by casting into a Teflon mold with dimensions of 34 mm × 8 mm × 0.3 mm. The values are taken from an average of five specimens.
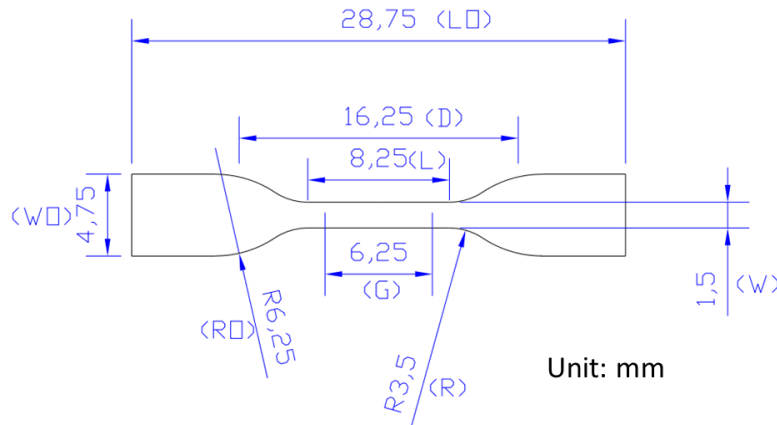
Figure 7.2 The dimensions of the dumbbell shape samples for tensile tests.

7.3 Results and discussion

7.3.1 Working principle of the aging sensors

The aging sensors are conductive composites made of the same polymer as the insulation component and placed in close proximity to the component under monitoring, so that they age in the same manner under exactly the same environment as the monitored insulation component. The sensing mechanism of the aging sensor in this study is based on the so-called "percolation" effect of conductive composites. Near the percolation threshold (PT) point an extremely large change (several orders of magnitude) in resistivity can occur by very small variation (several percentage points) of volume fraction of the conductive filler [245]. During aging, the polymer matrix shrinks and densifies as a result of several mechanisms including polymer chain cross-linking, chain scission, and loss of light volatile fractions while the conductive particles remain intact [246]. The shrinkage of the polymer during aging results in an increase in volume fraction of the conductive particles and hence a dramatic decrease in resistivity of the

123

conductive composite. Therefore, the resistivity change can be correlated with the polymer shrinkage and thus the equivalent aging time of the insulation system.

7.3.2 **Formulation of sensors**

The percolation behavior of the all the composite is investigated first. Figure 7.3 shows the percolation behavior of all the composite and the percolation threshold calculated by the scaling law [247]. For all three resins, the percolation threshold of CNT composites are much lower than their corresponding CB based composite, due to the high aspect ratio of CNTs. This is beneficial in sensor fabrication because the reduced filler concentration can lead to a better ductility of sensors, especially approaching the end of lifetime. In sensor manufacturing, we want to keep the initial resistance of the sensors in the range of 1-10 $M\Omega$, so that it is lower than the upper measuring limit of most commercial multi-meters. The real concentration of fillers in sensor fabrication are also listed in Figure 7.3.
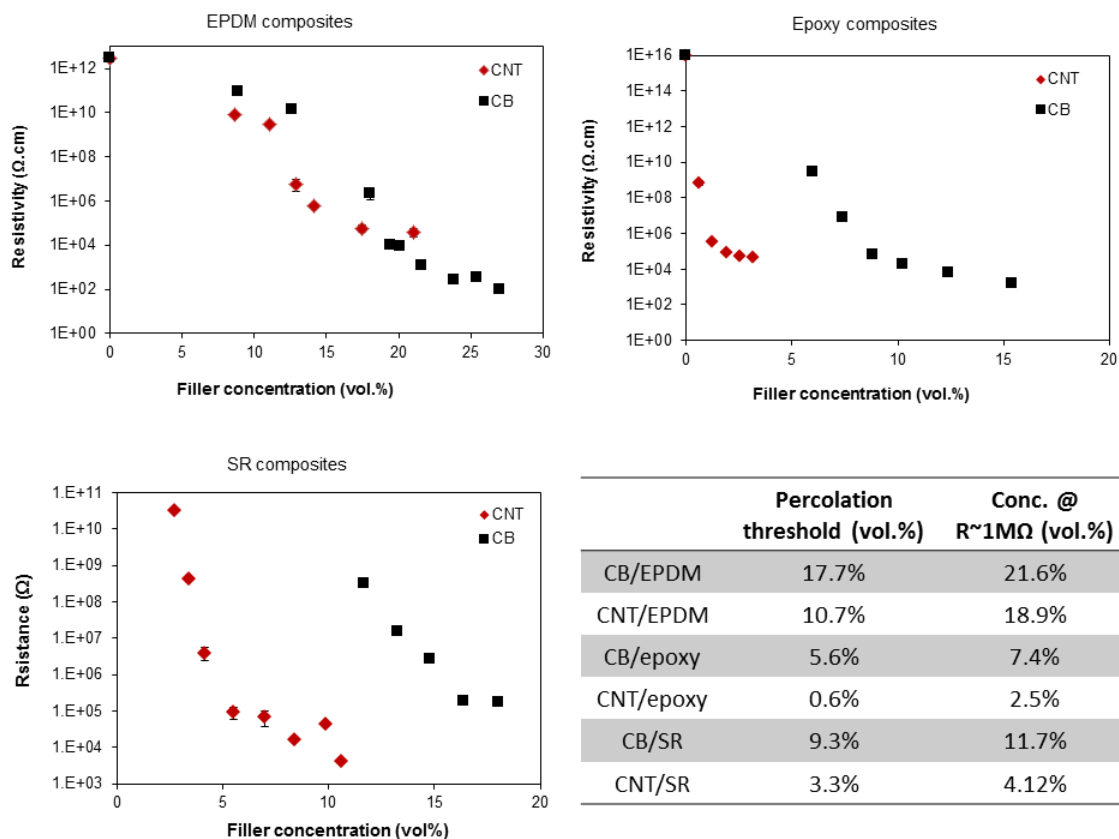
Figure 7.3 The percolation curve of EPDM, epoxy and SR composites.

	Percolation threshold (vol.%)	Conc. @ R~1MΩ (vol.%)
CB/EPDM	17.7%	21.6%
CNT/EPDM	10.7%	18.9%
CB/epoxy	5.6%	7.4%
CNT/epoxy	0.6%	2.5%
CB/SR	9.3%	11.7%
CNT/SR	3.3%	4.12%

7.3.3 **Resistivity versus aging time**

Figure 7.4 shows the resistivity change of EPDM composite-based aging sensors as a function of aging time at different temperatures. To accelerate the thermal aging, elevated temperatures are used. The overall aging time is twice of the lifetime of pure EPDM resin. The composites display a continuous resistivity drop with aging time at all temperatures. The entire resistivity drop is dramatic- more than four orders of magnitude for the CB/EPDMS sensors and five orders of magnitude for CNT/EPDM. This resistivity change is very fast at the initial stage, and gradually slows down. The large drop in resistivity during aging provides a more sensitive signal than any other CM technique, including elongation change [232, 233], density change [239] and OIT change

125

[240]. In addition, the resistivity change obeys general Arrhenius trends of aging reactions; that is, at higher temperatures, the aging is faster, and thus the resistivity drops more quickly.
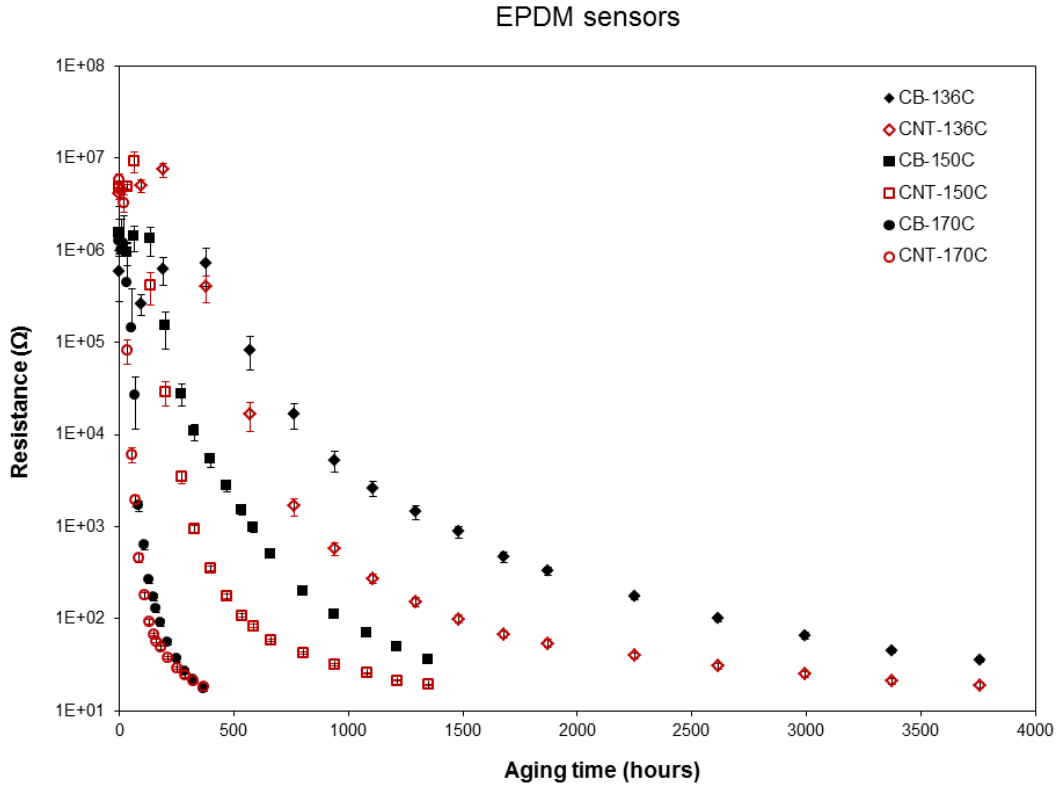
Figure 7.4 The electrical resistivity of CNT/EPDM composite-based sensors as a function of aging time.

The epoxy composite-based samples shows similar trend with the EPDM composite-based samples (Figure 7.5). The resistance drop is more than two orders of magnitude during the lifetime of epoxy while the resistance change becomes mild after that. The CB/epoxy sample shows a slightly more significant resistance drop than CNT/epoxy samples, probably due to the better antioxidant capability of CNTs [248].

126
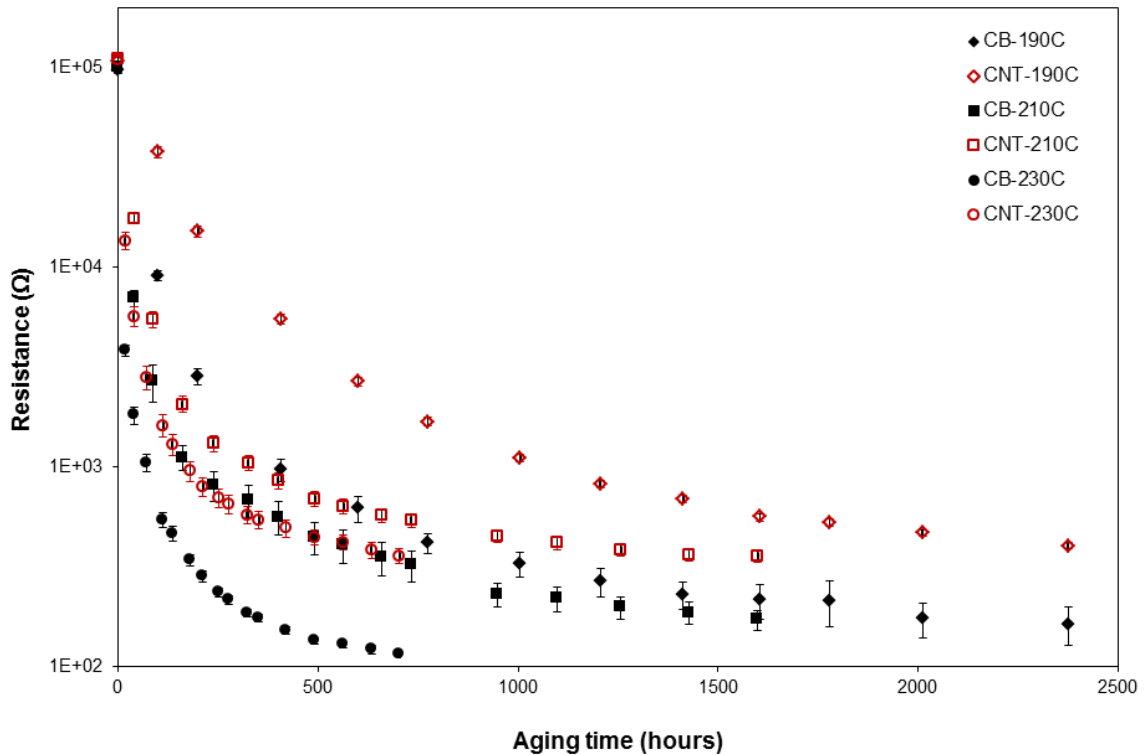
Figure 7.5 The electrical resistance of epoxy composite based sensors as a function of aging time.

The resistance change of SR based composites shows very different trends with the other sensors (Figure 7.6). Within the lifetime of SR, the resistance drop shows a similar trend with EPDM and epoxy sensors- the resistance decreases monotonically and the change is faster at the beginning and slows down. However, after the lifetime, the resistance suddenly increase for both CB and CNT based samples at all temperatures. It is possible that the degradation mechanism changed after the lifetime, some other reactions replace the dominating reaction within the lifetime.
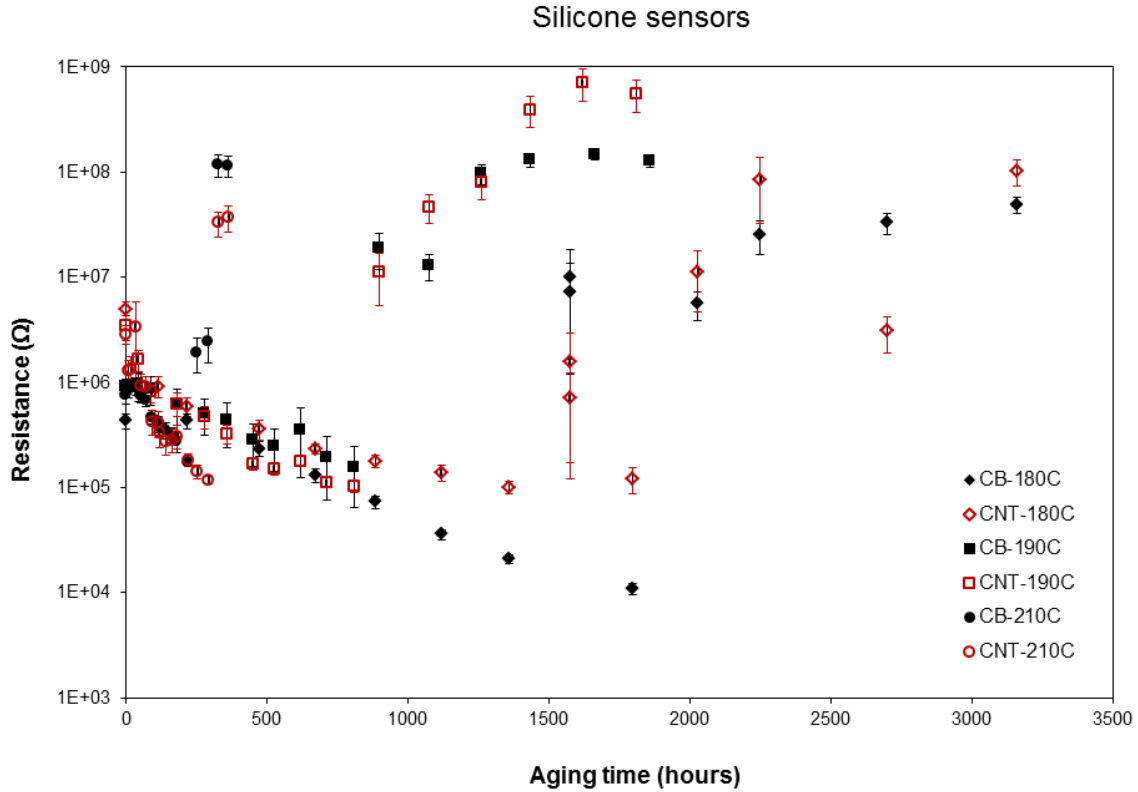
Figure 7.6 The electrical resistance of SR composite based sensors as a function of aging time.

Arrhenius analysis is employed to predict the rate of aging and remaining lifetime. The basic idea underlying the Arrhenius approach is that the thermal oxidative aging reactions can be accelerated by raising the temperature. In the Arrhenius equation, the rate constant k of the degradation reactions is dependent on the absolute temperature T given by

$$k = A\exp(-\frac{E_a}{RT})$$

where

E_a = activation energy

A = pre-exponential factor

R = ideal gas constant

128

Traditional Arrhenius analysis usually picks out the time corresponding to a certain amount of degradation (for example, 50% elongation in the tensile tests) and plots the log of these values versus inverse absolute temperature. However, using a single data point at each temperature will waste most of the obtained data. Therefore, the "time-temperature superposition method", which uses all of the experimental data at each temperature, is adopted for the Arrhenius analysis of the electrical resistivity results [249]. The "time-temperature superposition method" has been successfully utilized to diagnose the aging conditions in the elongation measurements [249]. Its rational is that if the same degradation reaction occurs at two different temperatures, the degradation curves at these two temperatures should have the same shape and should be related by multiplication with a constant (a_T).

We performed the "time-temperature superposition" on the data shown in Figure 7.4 to Figure 7.6 by considering the lowest temperature as the reference temperature condition and shifting the data at each higher temperature horizontally by the constant multiplicative factor that gives the best overall superposition with the reference curve (a_T = 1 for the reference temperature). Figure 7.7 to Figure 7.9 shows the time-temperature superposition of the data. It is clear that the resistivity change curves at different temperatures do have the same shape and show an excellent superposition. Once the empirically determined shift factors are determined, they can be tested with the Arrhenius equation. The Arrhenius equation shown above is transformed as below.

$$\ln a_T = \frac{E_a}{R}(\frac{1}{T_{ref}} - \frac{1}{T})$$

The slope of log (a_T) versus inverse absolute temperature yields a linear curve with the slope representing the activation energy (right column of Figure 7.7 to Figure

129

7.9). The Arrhenius behavior is confirmed for all sensors within the temperature range of

the present study.
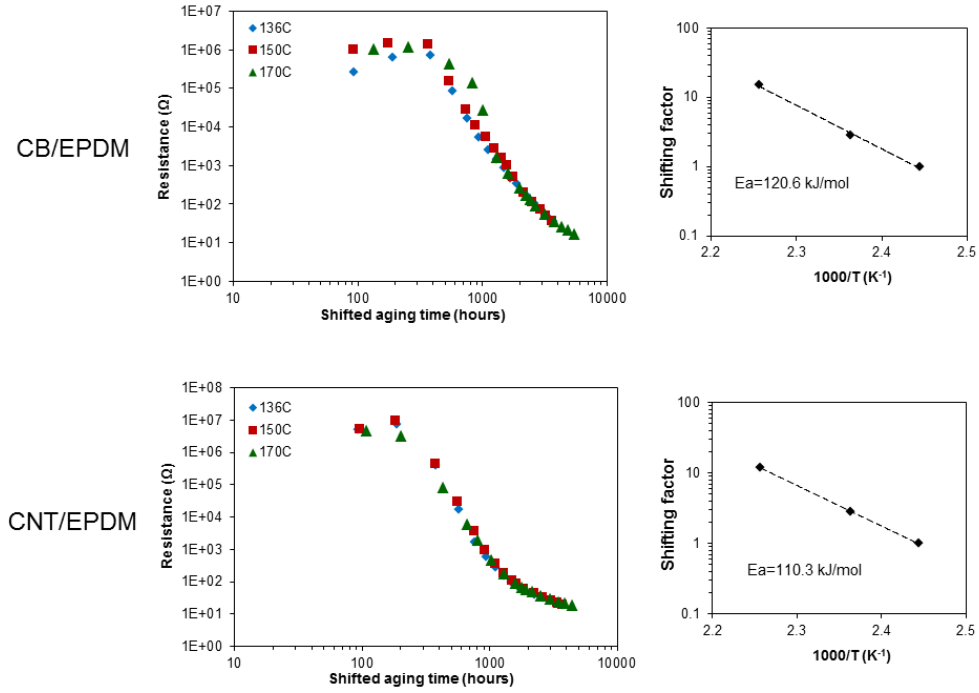
Figure 7.7 Time-temperature superposed resistance results for EPDM composites based
sensors from Figure 7.4 at a reference temperature of 136°C (left column). Arrhenius plot
of the shifting factors (right column).
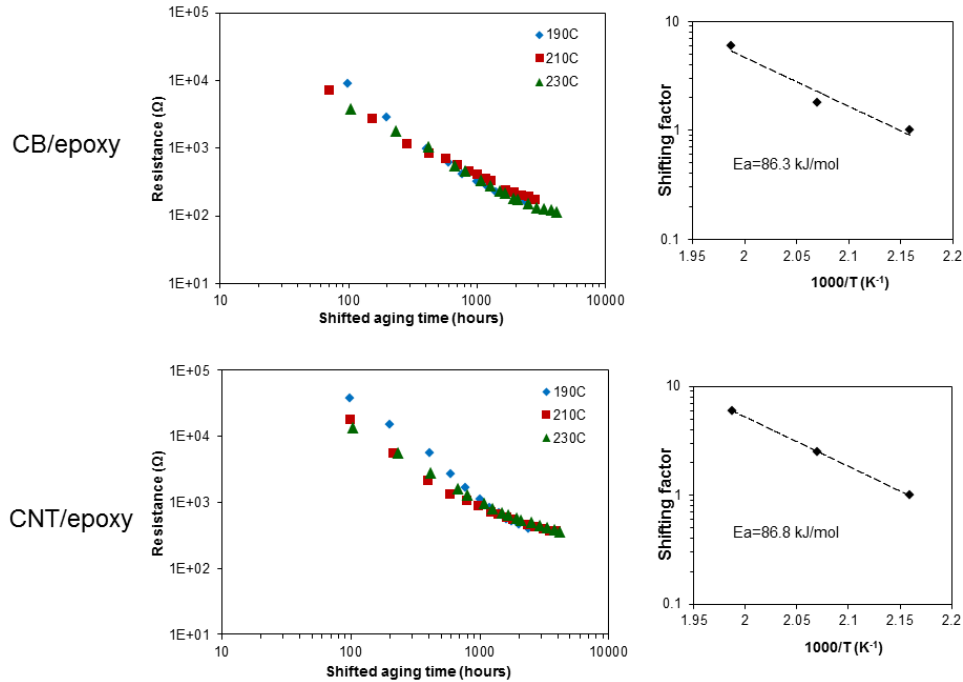
Figure 7.8 Time-temperature superposed resistance results for epoxy composites based sensors from Figure 7.5 at a reference temperature of 190°C (left column). Arrhenius plot of the shifting factors (right column).
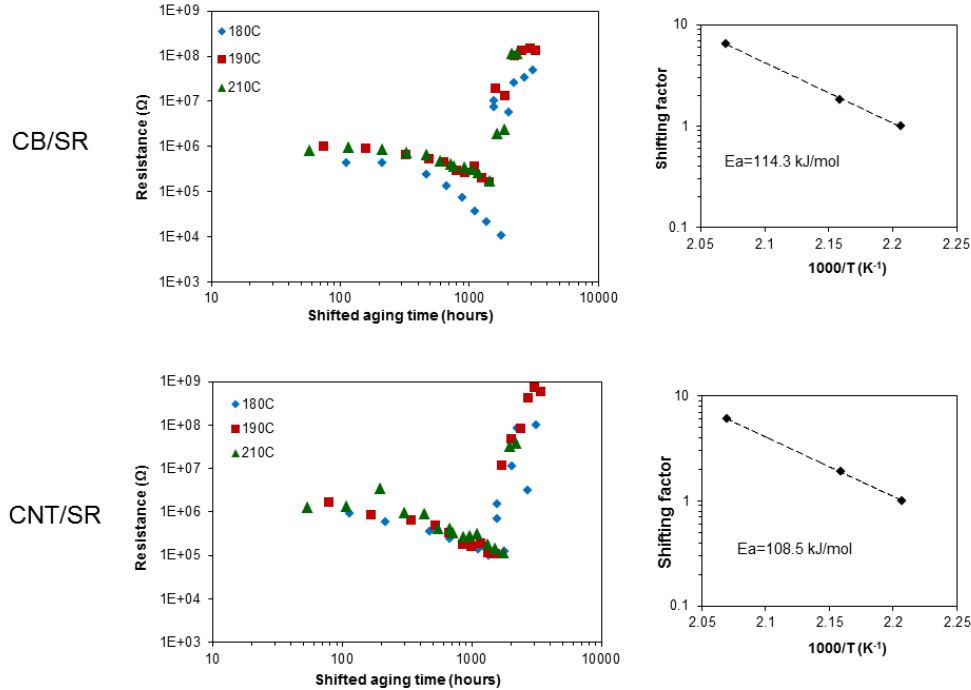
Figure 7.9 Time-temperature superposed resistance results for SR composites based sensors from Figure 7.6 at a reference temperature of 180°C (left column). Arrhenius plot of the shifting factors (right column).

131

7.3.4 **Elongation versus aging time**

The traditional method of elongation measurements is used to verify the results obtained by the resistance change of the composite-based sensors.

Figure 7.10 shows the elongation at break from the tensile tests of EPDM composites aged for different time. The elongation at break decreased with the aging time for all samples with a faster rate at the beginning of the aging process and gradually slows down after the lifetime. Also, the degradation rate increases with aging temperature. For EPDM composites aged at the same temperature, CNT composites aged faster and the degradation of mechanical properties is also faster. This is because the specific CNT used here have a slight acceleration effect on the degradation of EPDM, as demonstrated by the thermal gravimetric results shown in Figure 7.11. The acceleration effect may result from the metallic nanoparticles that were used for CNT growth but not completely removed during the CNT purification [250].
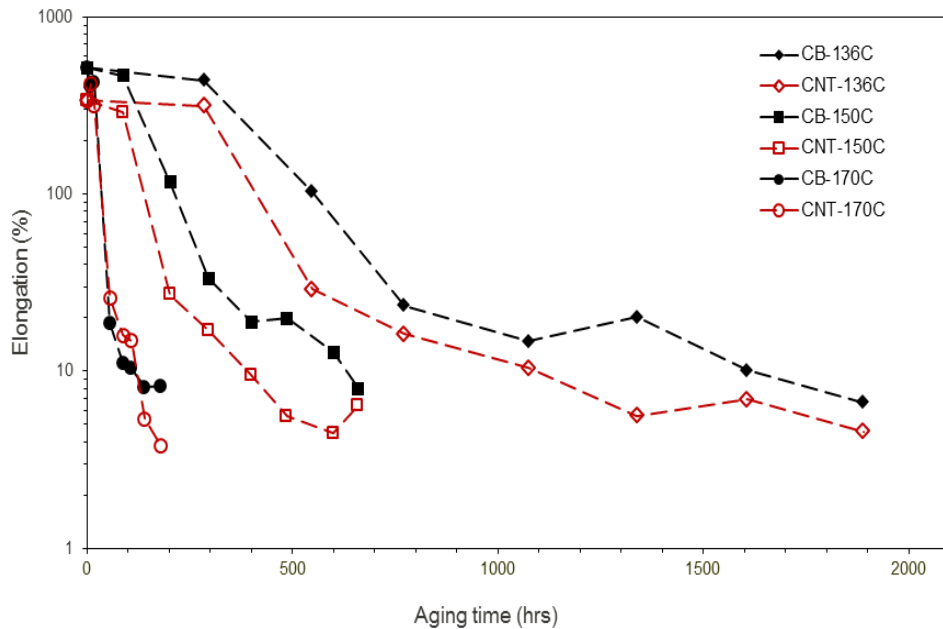
Figure 7.10 The elongation at break of CB/EPDM and CNT/EPDM composites aged for different time at three different aging temperatures.
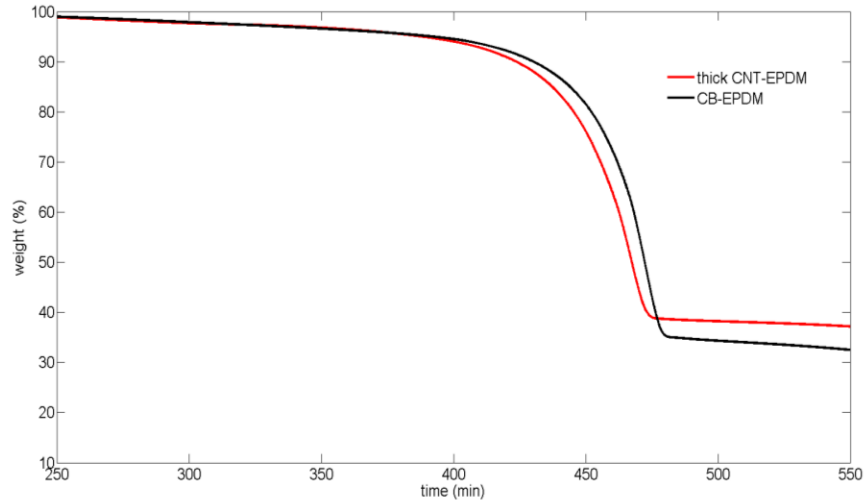
Figure 7.11 TGA results of the CNT/EPDM and CB/EPDM composites. CNT/EPDM shows a lower thermal stability than the CB/EPDM, which will lead to faster degradation.

Figure 7.12 and Figure 7.13 show the bending strain and elongation at break of epoxy composites and silicone composites respectively. All the composites show the same trends; the mechanical properties degrade with aging time and the degradation is faster at higher temperatures. The filler loading required for CNT-based composites to achieve the same resistance is much smaller than that of the CB composites, therefore, the elasticity of CNT-based composites are better than the corresponding CB composites throughout the aging process at various temperatures.

133
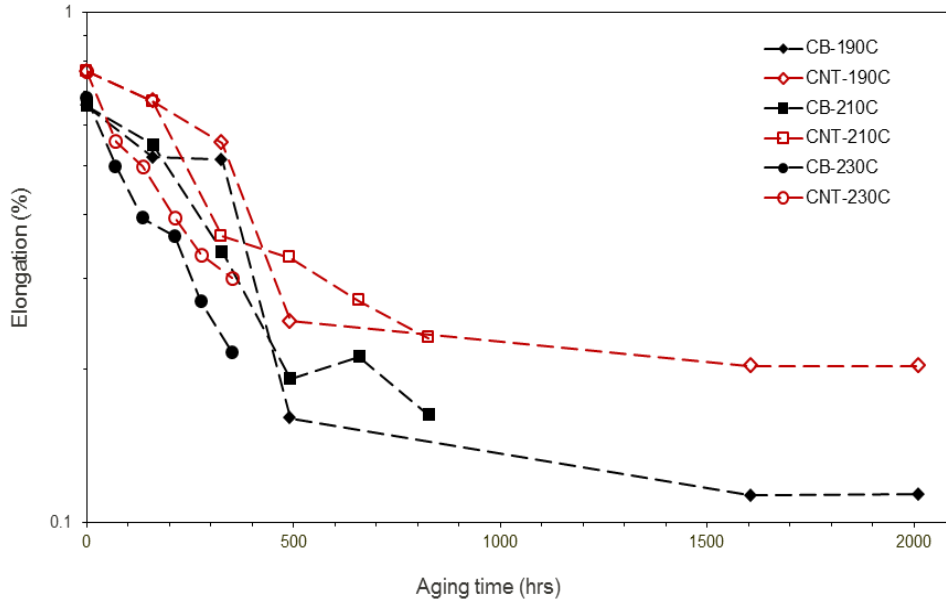
Figure 7.12 The elongation at break of CB/epoxy and CNT/epoxy composites aged for different time at three different aging temperatures.
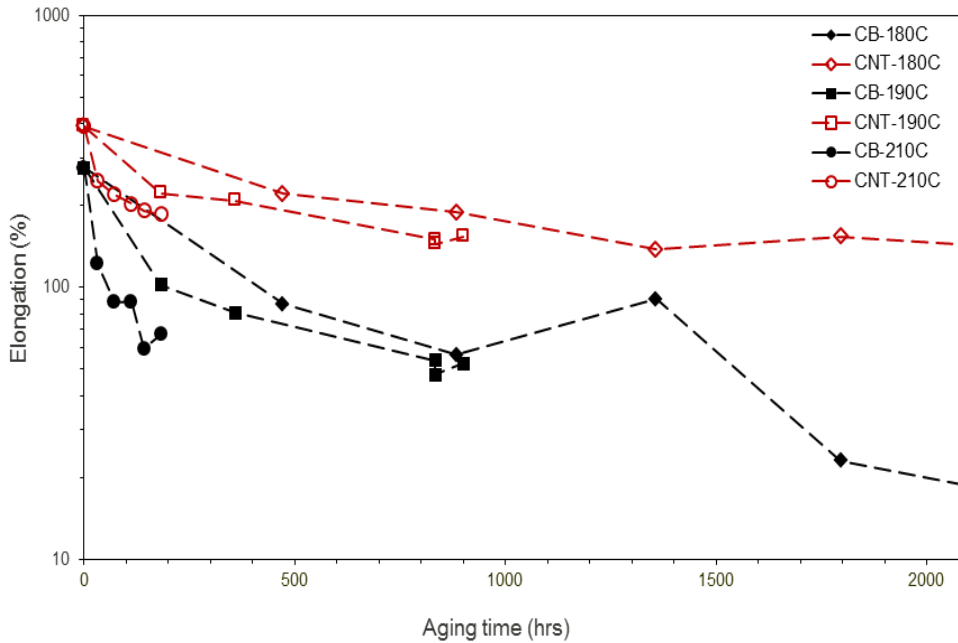
Figure 7.13 The elongation at break of CB/silicone and CNT/silicone composites aged for different time at three different aging temperatures.

The elongations of the composite materials are also recorded to correlate with the resistance change of the corresponding aging sensors. Again, to make full use of the data

in the aging tests, the "time-temperature superposition" method is employed to obtain the

activation energy, as shown from Figure 7.14 to

Figure 7.16. The mechanical test data also confirms the Arrhenius behavior of all

three composites.
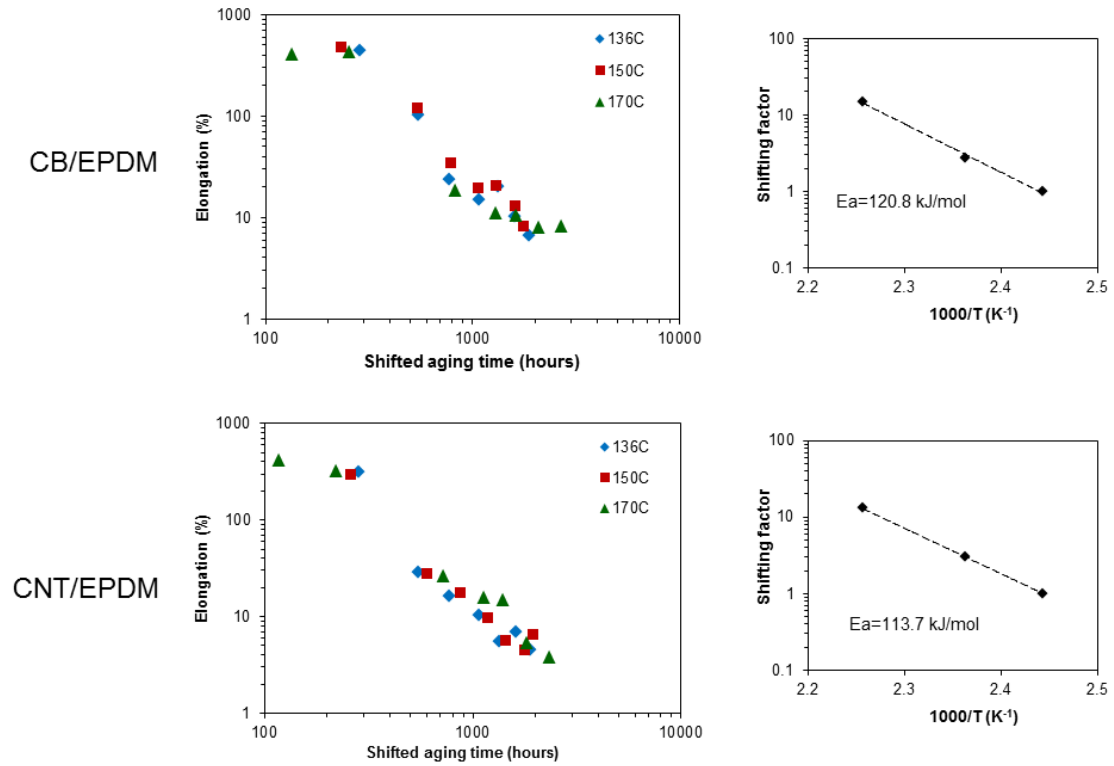
Figure 7.14 Time-temperature superposed elongation results for EPDM composites based sensors at a reference temperature of 136°C (left column). Arrhenius plot of the shifting factors (right column).
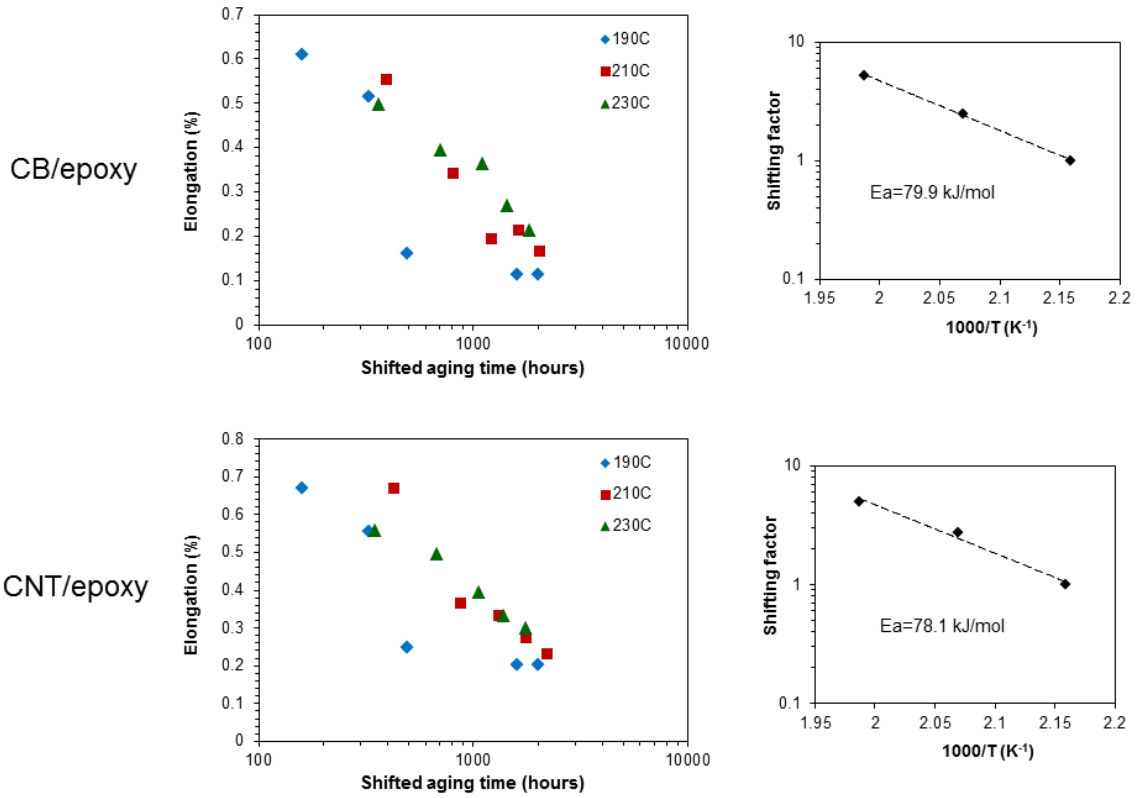
Figure 7.15 Time-temperature superposed elongation results for epoxy composites based sensors at a reference temperature of 190°C (left column). Arrhenius plot of the shifting factors (right column).

136
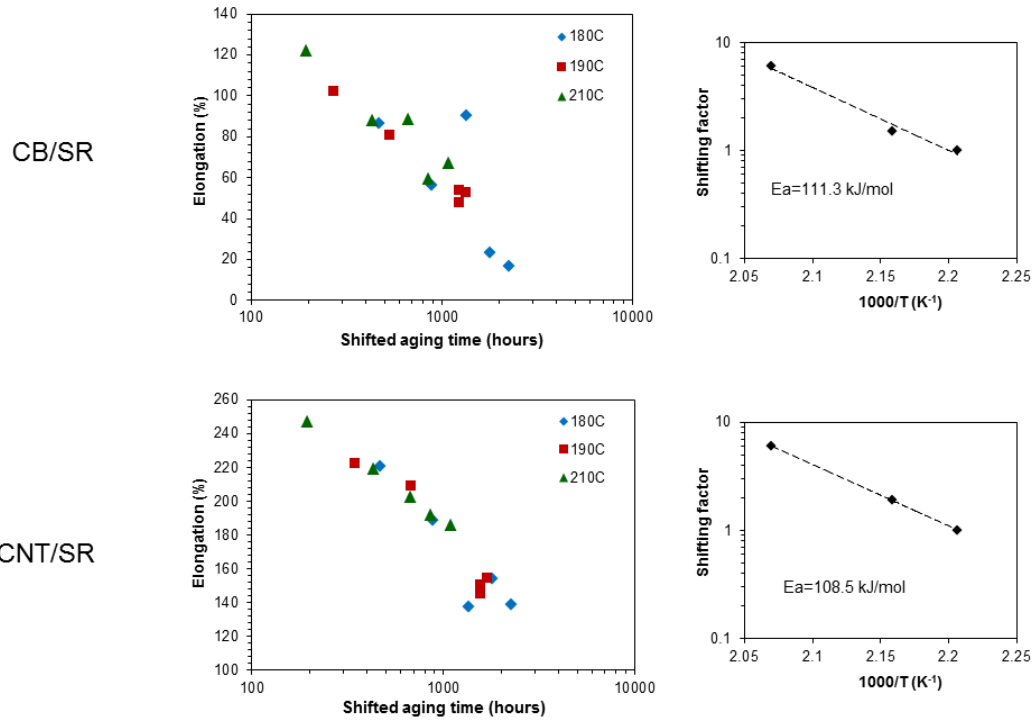
Figure 7.16 Time-temperature superposed elongation results for SR composites based sensors at a reference temperature of 180°C (left column). Arrhenius plot of the shifting factors (right column).

7.3.5 **Correlation between elongation and resistance**

The activation energy represents the minimum energy needed for the aging reactions to occur. By obtaining the activation energy from the accelerated aging tests and assuming the aging reaction remains the same at lower temperatures, the lifetime can be predicted for the low-temperature, long-term aging conditions. The activation energy values obtained from the electrical resistance and the elongation test are listed in Table 7.2. For EPDM, the lifetime of pure EPDM at different aging temperatures is 116.6±6.2 kJ/mol measured by the manufacturer according to IEEE standard [251]. For the CNT/EPDM composites, the activation energy obtained from sensors and elongation tests are 110.3 kJ/mol and 113.7 kJ/mol, respectively, which has 5% and 2% variance from manufacturer's data sheet. Similarly, the CB/EPDM composites have an activation

energy of 120.6 and 120.8 kJ/mol from the resistance measurements elongation tests, which are only 3% higher than the manufacturer's data. The similar values of activation energy obtained from different methods indicate that the resistance change can be correlated with the aging time of the insulation system under monitoring.

Table 7.2 Activation energy obtained from different measures

	Ea, Resistance (kJ/mol)	Ea, Elongation (kJ/mol)	Ea, Data sheet (kJ/mol)
CB/EPDM	120.6	120.8	116.6±6.2
CNT/EPDM	110.3	113.7	116.6±6.2
CB/epoxy	86.3	79.9	84.2±0.9
CNT/epoxy	86.8	78.2	84.2±0.9
CB/SR	114.3	111.3	
CNT/SR	108.5	108.5	

Indeed, Figure 7.17 shows the relationship between the resistance and aging time of CNT/EPDM composite-based sensors as an example. The designed lifetime for the EPDM insulation material is 1,873 hours, 675 hours and 175 hours at 136°C, 150°C and 170°C, respectively. No matter which temperature they are aged at, all the sensors have the same resistance of 55Ω when the end of lifetime is reached. Similarly, the half lifetime remaining and 75% lifetime remaining correspond to 600 Ω and 80kΩ of the sensors, respectively. By obtaining a curve shown in Figure 7.17, we can track the "age" of the insulation system at every single moment by reading the resistance of the aging sensors, regardless of the aging temperatures. Therefore, the electrical resistance signals

138

from the sensor can be used to accurately predict the remaining lifetime of the monitored
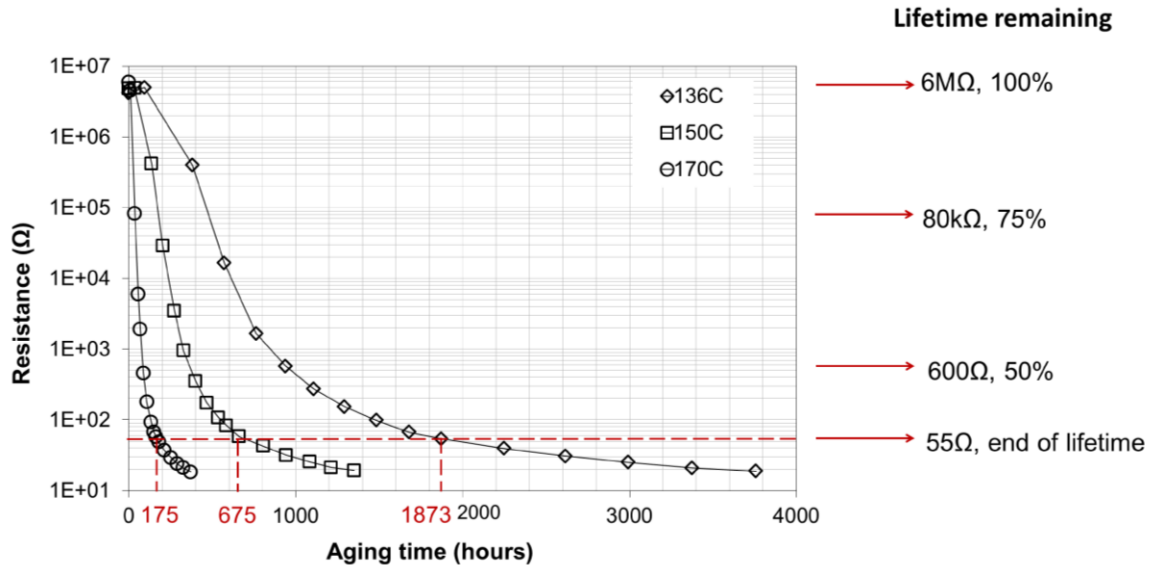
insulation system.

Figure 7.17 Sensors' response, i.e. resistance can be related to different aging time and
be used to predict remaining lifetime of the insulation system.

Similarly, for epoxy, the activation energy from the manufacturer's data sheet is

84.2±0.9 kJ/mol. For CNT/epoxy sensors, and the activation energy obtained from the

resistance measurements and mechanical tests are 86.8 kJ/mol and 78.2 kJ/mol,

respectively. For CB/epoxy sensors, the activation energy obtained is 86.3 and 79.9

kJ/mol. Because the activation energy derived from the aging sensor signals is within 5%

variance of that derived from lifetime tests, the sensor signals can effectively represent

the aging time at each stage of aging. The lifetime for the epoxy insulation material is

2,000 hours, 850 hours and 400 hours at 190°C, 210°C and 230°C, respectively (Figure

7.18). For the CNT/epoxy-based sensors, the lifetime corresponds to a resistance of

450Ω. Similarly, the 50% lifetime remaining and 75% lifetime remaining correspond to

950Ω and 3500Ω, respectively.
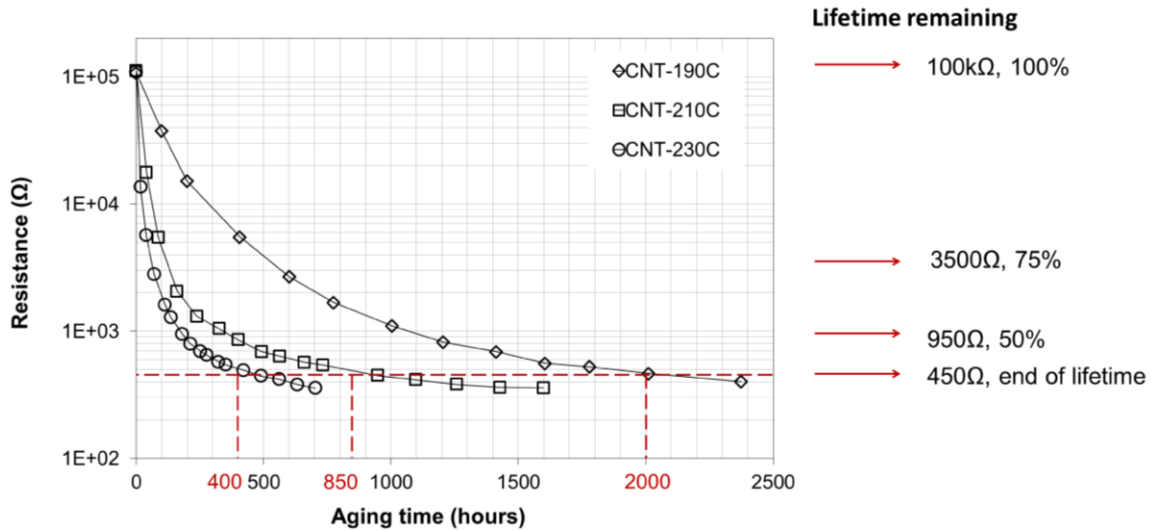
Figure 7.18 The resistance value of CNT/epoxy sensors can be related to different aging time of epoxy insulation system.

For the SR-based sensors, because the degradation mechanism changes during aging, as shown in the abrupt increase of resistance during aging (Figure 7.6), the resistance data from sensors cannot be used to predict the lifetime remaining of this SR cables.

7.3.6 **Limitations of the current aging sensors and future work**

The sensor mechanism is based on the assumption that the composite has similar degradation kinetics with the monitored insulation polymer. This explains why the same polymer as the monitored insulation system is used as composite matrix, and only a small amount of CNTs is added. However, in some cases, CNTs can retard the thermal degradation of polymer materials due to their anti-oxidation effect [248], or may accelerate the thermal degradation of polymers due to the catalytic effect of metal nanoparticle residues (details in next chapter) [250]. The composite-based sensors could

have different degradation kinetics from the pure polymer in the insulation system, and thus would no longer represent the aging situations of the insulation system. At this moment, composites with different conductive fillers that will not affect the thermal degradation kinetics need to be considered in the formulation of the aging sensors.

The future work of current research also includes the attaching of passive RFID devices to the aging sensors, which allows the wireless monitoring and control.

7.4 Conclusion

The carbon/polymer conductive composite-based aging sensors in this study are "variable resistors" whose resistance decreases as the polymer matrix of the sensor shrinks and densifies during thermal aging. Since the sensor is made of the same polymer matrix as the monitored insulation system, the thermal degradation kinetics obtained from the sensors is very close to the degradation kinetics of the insulation system. We demonstrated that in the two illustrated polymers, a change in resistance can identify the aging situation and predict the remaining lifetime of the monitored insulation parts. These sensors have many advantages over conventional monitoring techniques, including a lack of damage to the insulation system, real-time monitoring of the insulation system, facile operation without complex equipment or specialized personnel, and low cost.

CHAPTER 8 METAL CATALYST RESIDUES IN CARBON NANOTUBES DECREASE THE THERMAL STABILITY OF CARBON NANOTUBE/SILICONE COMPOSITES

8.1 Introduction

CNTs have attracted broad attention from various fields, of which CNT/polymer composites exhibit most promising applications. CNT/polymer composites have many advantages over conventional carbon/polymer composites (e.g. carbon black, diamond, diamond like carbon, graphite and carbon fibers) through improvements in mechanical properties and electrical and thermal conductivity. CNT/polymer composites have formed a new class of superior functional materials for aerospace applications [252], energy storage [253], molecular sensors [254], electronic and optoelectronic devices [255, 256], electromagnetic interference shielding [257], membrane [258] and thermal management [259, 260]. However, as CNT/polymer composites become commercialized, some potential problems need to be addressed, including nano-toxicity [261], the impact on the ecosystem [262] and the reliability- mechanically, chemically and thermally. The present study is focused on the thermal stability of CNT/polymer composite, which is a key factor in determining the reliability of CNT/polymer composites.

Many groups have conducted studies on the thermal stabilities of various CNT/polymer composites. Table 8.1 summarizes some of the representative work. The majority of these studies reported improved thermal stabilities of the CNT/polymer composites compared to pristine polymers, which is not surprising considering the intrinsically good thermal stability of CNTs [263], their network structure [264] and free radical trappping capabilities [248]. However, contradictory results were also presented.

142

For example, Kashiwagi et al. [264, 265] found that both SWNTs and MWNTs significantly enhanced the thermal stability of PMMA so that these CNT/PMMA composites could potentially function as fire retardants, whereas Dervishi et al. [266] and Liu et al. [267] observed decreased thermal stability of MWNT/PMMA composites when the MWNT loading level was large enough. MWNT/atactic PP showed increased stability in N_2 in Yang's study [268], whereas a decreased onset degradation temperature of MWNT/ polypropylene in air and an increased degradation temperature in N_2 was reported by Kashiwagi et al. [269] and Bikiaris et al. [270]. Such discrepancies between these reported results can be attributed to the differences between CNT fillers used by different researchers. One key difference is the metal impurity present in the CNTs. In most cases, metal impurity comes naturally with CNTs as catalysts for CNT synthesis and differs in composition and quantities depending on synthesis and purification process. The impact of the metal impurity on the thermal stability of CNTs based polymer composites has rarely been discussed. In most of the work on CNT/polymer composites, the effect of the metal impurity is not distinct, because of the pretreatment of CNTs via acid purification [271-274] or the low loading of CNTs [255, 264, 265, 269, 275, 276]. In both cases, the concentration of metal nanoparticles in the polymer matrix is too low to result in a significant difference in thermal stability of the composite. While some cases do notice the CNT induced decrease in thermal stabilities of CNT/polymer composites, an explanation for such a phenomenon is lacking. For example, in Dervishi et al.'s work, the CNT fillers in the MWNT/PMMA composites were synthesized by a Fe-Co/CaCO$_3$ catalysis recipe, which may introduce Fe and Co nanoparticles into the composites. Instead of considering the decreased thermal stability as a result of impurities, they

143

attributed it to the formation of agglomerates of CNTs in the composite [266]. Yang et al. [277] proposed that the SWNTs accelerated the thermal degradation of a SWNT/ABS composite by participating in the radical initiation process and called for further investigations into how SWNTs promote the radical initiation. Xu et al. [278] and Kashiwagi et al. [269] hypothesized that the remnant catalysts might play a role in the accelerated thermal degradation of the polymer matrices without providing solid evidence.

In this chapter, we demonstrate that the thermal stability of CNT/silicone composites depends significantly on the metal catalysts that were used for CNT synthesis. CNTs synthesized with cobalt catalysts lead to the accelerated thermal degradation of silicone. Through the analysis of degradation products, we found that the silicone thermally decomposed into cyclic oligomers through a Si-O bond scission in a folded cyclic conformation. Cobalt catalyzes the depolymerization reaction by providing free radicals during degradation, while CNTs can trap some of the free radicals. Based on this degradation mechanism, the role of purification and its efficiency were also discussed. As of now, this is the first analysis specifically intended to elucidate the effect of metal catalyst residues within CNTs on the thermal stability of CNT/polymer composites. Such an analysis provides insight for future research on the thermal stabilities of CNT/polymer composites as well as for possible industrial applications of CNT/polymer composites, primarily in high temperature environments.

Table 8.1 Previous work on thermal stability of CNT/polymer composites

CNTs				Polymer matrix [1]	$T_{D,poly}$ (°C) [2]		$T_{D,comp}$ (°C) [2]				Ref.
Type	Synthesis	Catalyst	Purification		T_i(°C)	T_m(°C)	T_i(°C)	T_m(°C)	CNT %		
MWNT	Vapor grown	-	No	Silicone		468		523	1 wt.%	N_2	[275]
SWNT	HiPco	-	HCl	PMMA (M_w= 100,000)		311		372	0.5 wt.%	Air	[271]
MWNT	Arc-discharge	-	No	PMMA (M_w= 49,000)		320		350	26 wt.%	N_2	[279]
SWNT	HiPco	-	No	PMMA (M_w= 100,000)		365		367	1 wt.%	N_2	[265]
MWNT	CVD[1]	Fe/Co	No	PMMA	330		230		8 wt.%	Air	[266]
SWNT	-	-	No	PMMA (M_w=95,000-150,000)		337		326	50 wt.%	Air	[267]
						388		386		N_2	
MWNT	CVD	Fe	HNO_3	PAN (M_w= 86,000)	268		292		5wt.%	N_2	[272]
CNT	CVD	Fe	No	PANI	230		600		N/A	N_2	[280]
MWNT	CVD	Fe/Ni	HCl	PE		400		420	10 wt.%	N_2	[273]
MWNT	CVD	Fe	No	PP	230		205		2 vol.%	Air	[269]
MWNT	-	-	No	PP (M_w= 41,402)		360		430	5 wt.%	N_2	[268]
SWNT	Laser ablated	Ni/Co	Purified[3]	PI		444[4]		479[4]	1 vol.%	Air	[281]
MWNT	CVD	-	H_2SO_4-HNO_3	Waterborne PU		315		341	2.5 phr	N_2	[274]
SWNT	Arc discharge	Ni/Y	No	PVDF		425		200	49 vol.%	N_2	[278]
SWNT	CoMoCAT™	Co/Mo	HCl & HF	PVA (M_w=150,000)		284		281.2	1 wt.%	N_2	[282]
SWNT	Laser grown	-	Purified[3]	ABS (50% butadiene)		443/623[5]		414/587[5]	10 wt.%	N_2	[277]

1. Abbreviations: PMMA: poly(methyl methacrylate); PAN: polyacrylonitrile; PANI: polyaniline; PE: polyethylene; PP: polypropylene; PU: polyurethane; PVDF: Polyvinylidene fluoride; PVA: polyvinyl alcohol; ABS:Acrylonitrile–butadiene–styrene; CVD : chemical vapor deposition;

2. $T_{D,poly}$: characteristic temperatures of the thermal degradation of the polymer matrices; $T_{D,comp}$: characteristic temperatures of the thermal degradation of the corresponding CNT/polymer composites; T_i: temperatures at which the thermal degradation initiates; T_m: temperatures at which the maximum thermal degradation rate is reached.

3. Purified refers to the cases where authors stated that the CNTs were purified without the description of the purification process.

4. $444^{o}C$ and $479^{o}C$ are the temperatures that 5% weight loss occurred for the polyimide and SWNT/polyimide composite respectively.

5. The thermal degradation of ABS and its composite is a two-step process. The two temperatures correspond to maximum degradation rate in step 1 and step 2.

146

8.2 Experimental

8.2.1 Materials

Six types of MWNTs were used in this study. The abbreviations, product information and the vendors are listed in Table 8.2. Two silicones were selected as polymer matrices. One is a peroxide-curable methyl phenyl silicone gum (SR) provided by Rockbestos-Surprenant Cable Co. The other is Dow Corning HIPEC® Q1-4939 (Q1-4939), a two-part platinum curable polydimethylsiloxane (PDMS). Other materials used include Co (II) acetylacetonate (ACAC), Co (III) ACAC, Fe (II) ACAC, Fe (III) ACAC, Ni (II) ACAC and antioxidant N,N'-diphenyl 1,4-phenylenediamine (DPPD), which were all purchased from Sigma-Aldrich and used as received.

Table 8.2 Product information and vendors of MWNTs

CNTs	Product information				Vendors
	Length (μm)	Dia. (nm)	Purity	Catalyst	
A	10-20	8~15	>95 %	Co	Chengdu Organic chemistry Co., China
B	10-20	>50	95 %	Ni	Chengdu Organic chemistry Co., China
C	0.1-10	10-15,	>90 %	Fe	Sigma-Aldrich, US
D	1-10	10-30	>90 %	Ni-Fe	Sun Nanotech, China
E	5-15	10-20	>98 %	Co	Nanotech Port, China
F	300	~10	N/A	Fe	Synthesized by the authors

8.2.2 Sample Preparation

Composite preparation: Unless otherwise mentioned, the CNTs in CNT/silicone composites were used as received without any purification processes. For CNT/ Q1-4939 composite, CNTs were dispersed in Q1-4939 by ultra-sonication (Sonicator 3000, from

147

Misonix Inc.) for 1 hour and high shear blendering (Talboys model 134-1) for 3 hours. The mixture was then cured in a Teflon mold at 150oC for 1 hour. For the CNT/SR composite, the SR gum was first dissolved in toluene by the high shear blender for 1 hour while the CNTs were dispersed in toluene by ultra-sonication simultaneously. The CNT solution was then poured into the silicone part and mixed in the high shear blender for another 3 hours. The obtained homogenous mixture was then cast in a petri dish and dried under a fume hood for 12 hours. The resulting film was pressed into a Teflon mold and cured for 1.5 hours at 150 °C under 1.6 MPa pressure. Pure silicone matrices were cured following identical procedures.

CNT purification: 1) HNO_3 treatment of CNTs: 5g of the CNTs were mixed with a 250 ml 35% HNO_3 solution and refluxed for 1 hour at 100 °C. The obtained solution was filtered and washed with DI-water. The treated CNTs were then dried under a vacuum for 20 hours at 70 °C before being used. 2) HCl treatment of CNTs: 1g of CNTs were placed in a 500 ml round bottom flask and 200 ml of HCl was added. The mixture was stirred using magnetic stirrer for 2 hrs. The filtration, washing and drying procedures are identical with HNO_3 treated CNTs.

8.2.3 Characterization

TGA (TA Instruments, Model 5000) was used to characterize the thermal stability of the CNTs and all the CNT/silicone composites. In a typical TGA test, approximately 10mg sample was placed in a platinum pan and tested with a ramping rate of 5°C/min from $30^{o}C$ to 800°C in N_2. An isothermal mode in air was also used to mimic the aging process of the composite sample. Samples were heated at $25^{o}C$/min to $210^{o}C$, and held isothermal at $210^{o}C$ for 10-24 hours.

Perkin Elmer Optima 7300DV inductively coupled plasma optical emission spectrometry (ICP-OES) was used to detect the metal catalyst residues in each of the CNT samples. The ICP sample digestion was performed according to ref. [283]. 20 mg of as-received CNTs were placed in a crucible and ashed in a muffle furnace at 550 °C for 4 hours. The ash from each sample was extracted with concentrated nitric acid (1:1) and bath heated at 80 °C for 2 hours to dissolve metal residues. The solution was then centrifuged at 5000 rpm for 30 minutes and 5 ml of the supernatent was collected for ICP-OES analysis. The plasma and auxiliary argon flow rates were 15 and 0.2 L/min, respectively. The nebulizer argon gas flow rate was 0.68 L/min for the glass concentric nebulizer. The forward RF power was 1500 W. Of the 18 scanned elements (Ca, Cd, Co, Cr, Cu, Fe, Mg, Mn, Mo, Ni, Pb, Sb, Se, Sr, Ti, Tl, V, and Zn), only a few elements were found in measurable concentrations in these samples.

The thermal degradation of CNT-A/SR composite was carried out in a glass apparatus (Figure 8.1) isothermally at 210 °C for 24 hours. Liquid nitrogen was used to condense the volatiles and the gas products in a trap tube. The products collected in the trap tube were then dissolved in toluene and analyzed by gas chromatography-mass spectrometry (GC-MS, HP 6890 chromatograph coupled with a Micromass Autospec mass spectroscopy with an Rxi®-5ms column). Chromatograph heating began at 30 °C and was ramped at 15 °C/min to 300 °C. The solvent retention time was 4 minutes. Mass spectroscopy scanned from 900 dalton to 35 dalton with a rate of 0.5 dalton/s.
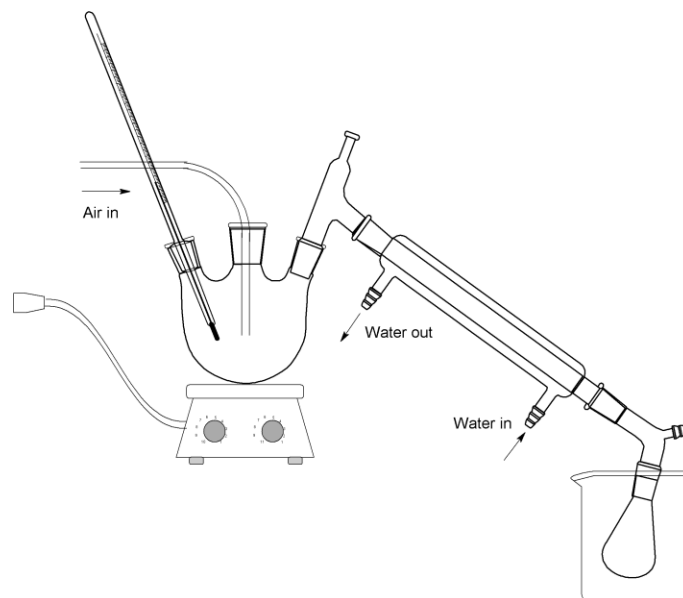
Figure 8.1 CNT-A/SR composite thermal degradation apparatus.

FT-IR (Nicolet, Magna IR 560) with an in-situ heating apparatus was used to investigate the gas products from the thermal degradation of CNT-A/SR composites. An ultrathin composite film was prepared and dried in an oven for 1 hour at 100 ºC before being sandwiched between two KBr pellets. The in-situ heating program was identical with the TGA isothermal mode, ramping from $30^{o}C$ to $210^{o}C$ by $25^{o}C$/min, and isothermally holding at $210^{o}C$ for 24 hours. The spectra were collected every 5 minutes for the first 3 hours and every other hour afterwards. A resolution of 4 cm^{-1} was used over 128 scans. Background spectra were obtained before the first analysis of each sample with only KBr pellets to ensure that there was no contamination.

The CNTs as purchased were imaged by a SEM (LEO 1530) with an accelerating voltage of 5 kV. Surface functional groups of CNTs were characterized by FT-IR and X-ray photoelectron spectroscopy (XPS, Thermo K-Alpha XPS). Raman characterization was carried out using LabRAM ARAMIS, Horiba Jobin Yvon with a 532 nm wavelength laser.

150

8.3 Results and discussion

8.3.1 CNT-induced decrease of thermal stability

Figure 8.2 shows the TGA results of pure SR and CNT-A/SR composites under N2. The pure SR has a degradation peak at 574 ^{o}C. For low loading samples (i.e. less than 3 wt.% CNTs), their weight loss appears more abrupt than that of the pure SR above 500°C. The composites with CNT loadings below 3 wt.% show a degradation peak at 561°C while a shoulder at 517°C begins to emerge. As the loading increases above 3 wt.%, the shoulder begins to protrude and the degradation peak becomes weak. When the filler loading reaches 6 wt.%, the previous degradation peak is replaced by the shoulder that then grows into a broad peak centered at 372°C. Compared to pure SR, 6 wt.% CNT-A shifts the major weight loss temperature region by 200°C lower, leading to a much earlier onset of thermal degradation.
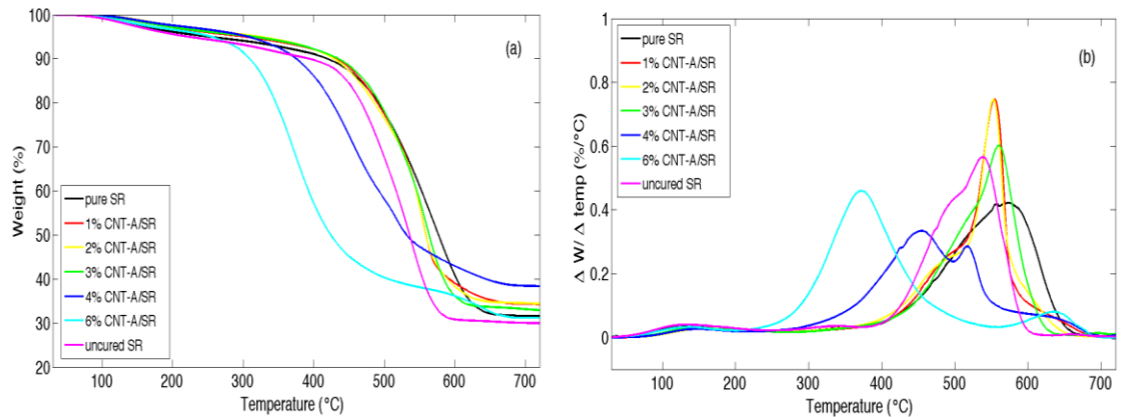
Figure 8.2 TGA (a) and the derivative (b) results of a CNT-A/SR composite at different CNT loadings.

The reduced thermal stability leads to undesirable consequences such as accelerated aging and a shortened lifespan. Figure 8.3 shows the weight loss of all samples held isothermally at 210°C for 10 hours in air to mimic the aging process. The

SR resin loses 5% of its initial weight in the beginning of the aging test, while no further

weight loss is observed afterwards. For the composite with 6 wt.% CNT-A, the weight

decreases linearly to 87.4% of the original weight at the end of the 10-hour aging. In the

case of 9.5 wt.% CNTs, 34.9% of the composite is decomposed within 10 hours.

Therefore, it is seen that increasing the CNT-A loading accelerated the aging of SR

polymer and resulted in a shorter lifetime.
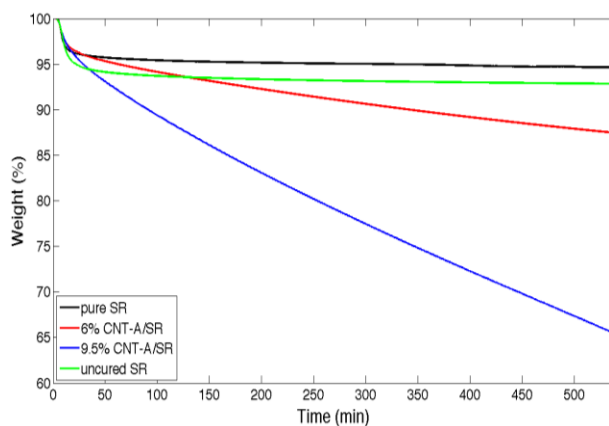
Figure 8.3   Isothermal degradation at 210 oC in air of SR without CNT fillers, SR with 6
wt.% CNT-A, SR with 9.5 wt.% CNT-A and uncured SR.

There are three possibilities for the observed decrease in thermal stability of

CNT/SR composites. The first one is that CNTs or included impurities retard the free

radical polymerization of SR. As a result, SR is not completely cured and may be less

stable than fully cured SR. Secondly, CNTs or their surface functional groups could react

with SR and accelerate the degradation. The third possibility is that the impurities within

CNTs react with SR, where the thermodynamics and kinetics are heavily dependent on

the category and quantities of the impurities.

For the first possibility, it was found that even uncured SR did not show

noticeable weight loss at 210°C (Figure 8.3). Thus the curing level has negligible

contribution to the thermal stability at 210 °C. Moreover, Pt catalyzed PDMS Q1-4939

152

and its CNT composite (CNT-A/Q1-4939 composite) were also analyzed in an isothermal

mode of TGA (Figure 8.4). Although Q1-4939 curing does not involve free radical

reactions, aging acceleration was also observed. Therefore, the decreased thermal

stability is not from the extent of cure of SR.
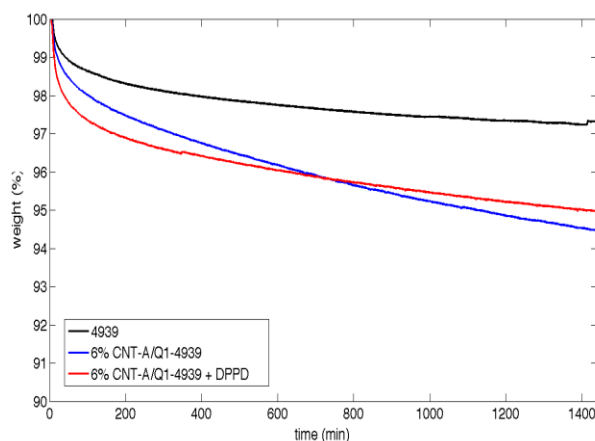
Figure 8.4 Isothermal degradation of pure PDMS Q1-4939, CNT-A/Q1-4939 composite
and CNT-A/Q1-4939 composite with 1 wt.% antioxidant DPPD at 210 oC in air.

To address the second possibility, the thermal stability in N_2 was investigated for

CNT/SR composites with 6wt.% loading of different CNTs. As shown in Figure 8.5,

CNT-A/SR shows much lower thermal stability than other CNT/SR composites. Bikiaris

et al. [270] reported that the functional groups especially the carboxylic acid groups on

the surfaces of CNTs could accelerate the thermal degradation of CNT/PP composites. In

our case, none of the CNTs exhibit obvious peaks corresponding to carboxylic acid

groups at ca. 1700 cm^{-1} in the FTIR spectra (Figure 8.6); moreover, CNT-A is not the

only one with the largest amount of carboxylic acid groups or the one with the most

oxygen containing functional groups according to the XPS results (Figure 8.6, Table 8.3).

Therefore, neither CNTs nor the functional groups on the surface are responsible for the

decreased thermal stability.

153
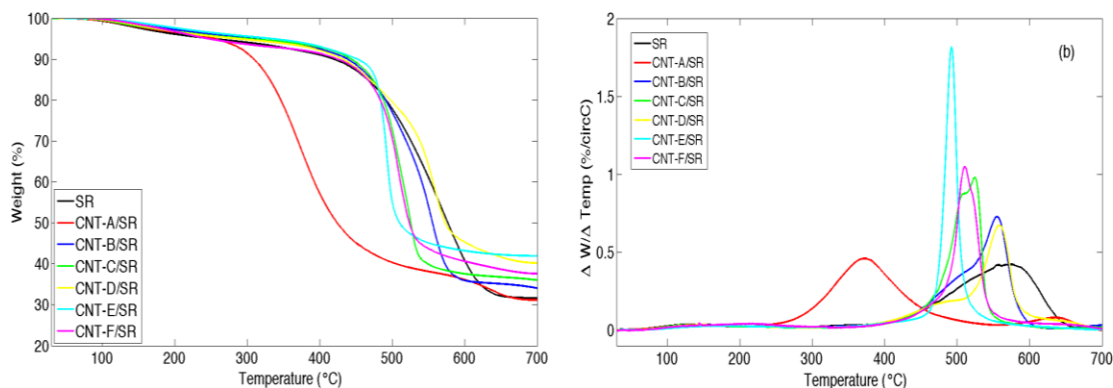
Figure 8.5 TGA results of CNT/SR composites with CNTs from different vendors shown in table 1. All the measurements were performed in N2 where only untreated CNT-A led to the dramatic decrease in the thermal stability of CNT/SR composites.
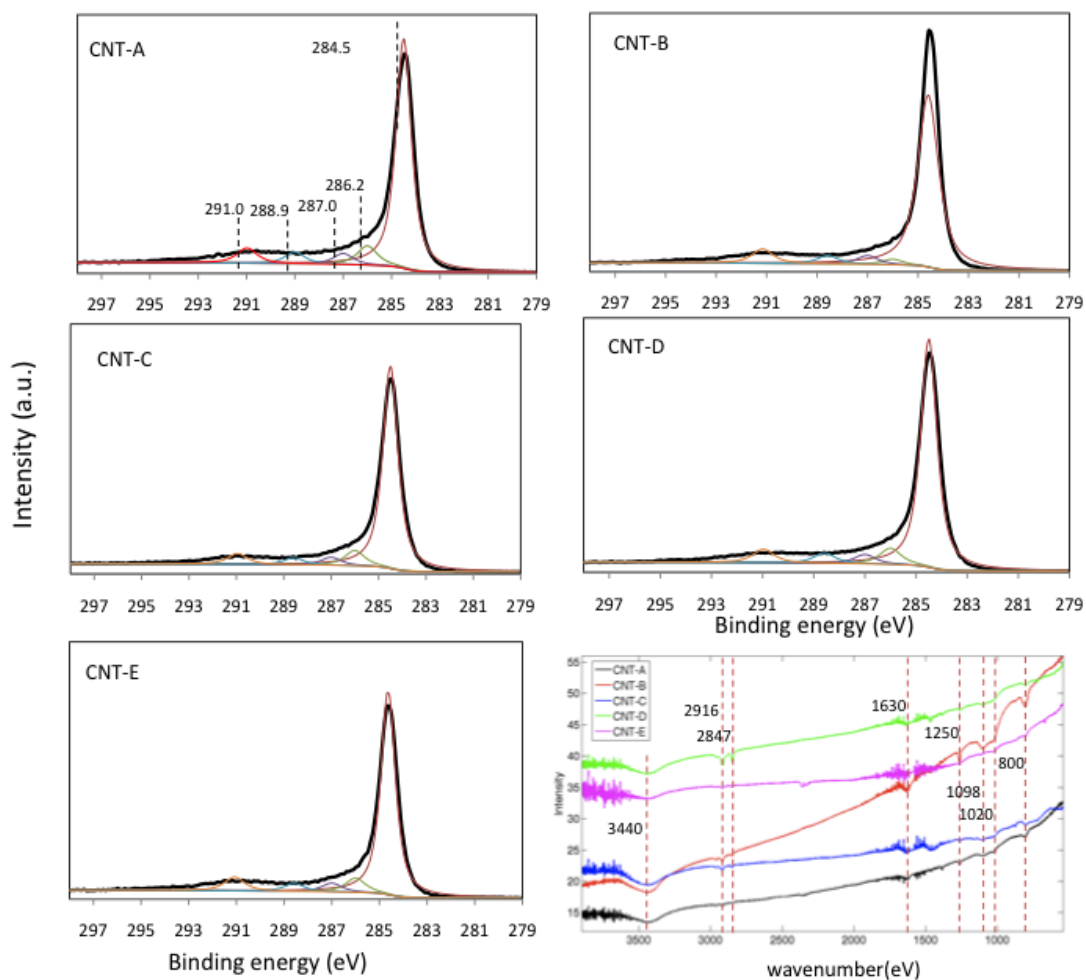
Figure 8.6 High resolution XPS of C1s peak of CNTs A to E and the FTIR of different CNTs. Deconvolution of the C1s peak showed a main peak at 284.5 eV, attributed to the

graphitic structure. The peaks at 286.2, 287.0 and 288.9 eV, correspond to C–OH, C=O, and O=C–OH functional groups, respectively. The π–π^* transition loss peak was detected at 291 eV [284, 285]. For the IR spectra, the peak at 3440, 1630, 1250 and 800 cm-1 correspond to –OH, C-C, C-OH and C-H in the ring, respectively. The peaks at 2916 and 2847 cm-1 signify the existence of -CH3 or -CH2, and the peaks at 1020 and 1098 cm-1 signify the C-O bonding from hydroxyl groups [286].

Table 8.3 The C/O ratio and -COOH content of different CNTs from XPS

	CNT A	CNT B	CNT C	CNT D	CNT E
C/O	35.10	122.41	14.68	24.71	91.59
COOH%	4.71	4.71	3.65	4.69	4.19

For the third possibility, based on SEM images (Figure 8.7) and Raman spectra (Figure 8.8), CNT-D has more amorphous carbon than any of the other CNTs, but does not exhibit any decrease in thermal stability. Therefore, amorphous carbon is not the reason for the accelerated degradation, which leads to an in-depth look at the metal catalysts used for CNT growth. ICP-OES was used to detect the metal content of each CNT sample. The results show that each of the six CNTs was synthesized with different metal catalysts (Figure 8.9 and Table 8.2). Interestingly, the two types of CNTs (CNT-A and CNT-E) that lead to the acceleration of CNT/SR composites are the CNTs synthesized with Co catalyst. CNT-A shows a more pronounced destabilization effect than CNT-E, which may result from the purification process of CNT-E performed by the vendors as evidenced by the higher purification of CNT-E. Considering that only CNT-A and CNT-E lead to the decreased thermal stability of SR composites, we assume that the residues of Co catalysts within CNTs could be one of the major sources for the observed decrease in thermal stability.
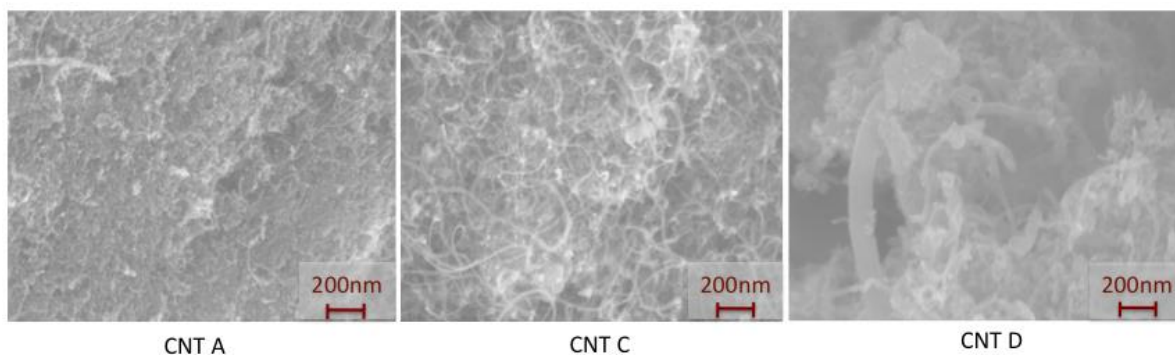
Figure 8.7 SEM images of CNT-A, -C and -D with magnification of 40,000. CNT-D contains more amorphous carbon than CNTs from other vendors.
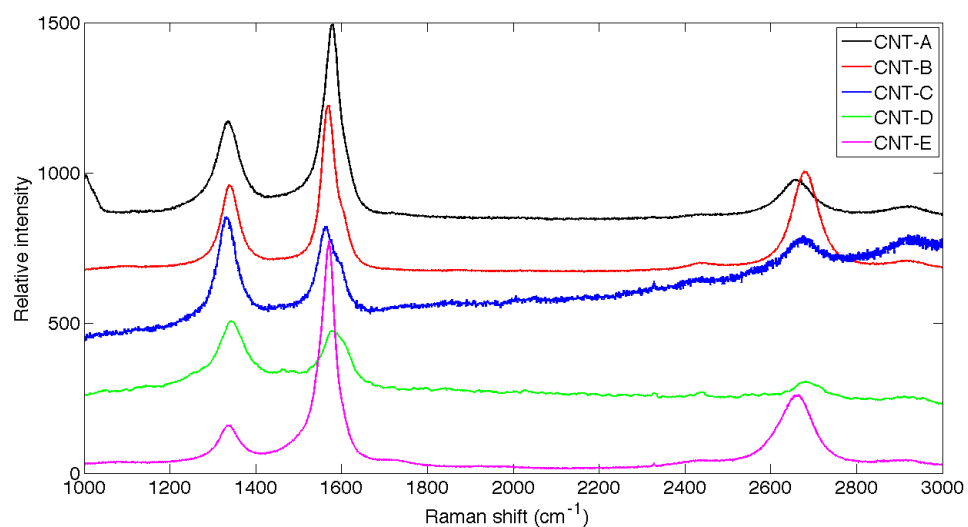
Figure 8.8 Raman spectra of CNTs A to E. Raman scattering is a well-accepted method for evaluating the degree of structural order of MWNTs by using the ratio of the integrated intensity of D band (I_D) at 1334 cm^{-1} to that of G band (I_G) at 1570 cm^{-1}[287]. Among all the CNTs, CNT-C and CNT-D are more defective than others as evidenced by the larger I_D/I_G ratios.
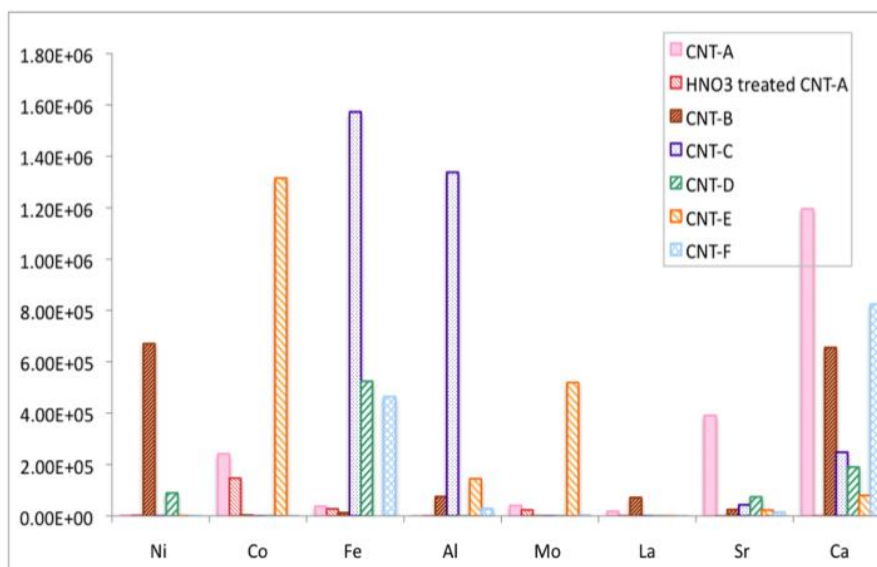
Figure 8.9 ICP-OES results showing the different metal elements in each of the CNT samples. Only elements with considerable concentrations were listed. Notice that the peak intensity here does not represent the exact concentration.

8.3.2 **Mechanism for the decreased thermal stability**

To clarify the role of Co containing CNTs in the thermal degradation of SR, it is necessary to understand the mechanism for SR degradation. Camino et al. showed that PDMS degradation occurred through two competing mechanisms [288]. At 800°C and during rapid heating, degradation occurs through a homolytic Si-C bond scission as the dissociation energy of the Si-C bond (327 kJ/mol) is lower than that of the Si-O bond (452 kJ/mol). The products of PDMS degradation following this mechanism include methane gas and ceramic silicon-oxycarbide (Figure 8.10 (a)). At 400°C and during slow heating, molecular splitting mechanism takes place through the formation of cyclic oligomers (Figure 8.10 (b)). In this case, an intramolecular cyclic transition state is formed. Scission of cyclic dimethylsiloxane is favored in terms of chain flexibility and the assistance of the empty silicon d-orbitals [289, 290]. The products of PDMS degradation following this mechanism are smaller cyclic oligomers, dominantly cyclic

157

trimers (D3). The degradation products are the same in air and in N_2, but in air, the cyclic

siloxanes in gas phase can be further oxidized to CO_2, H_2O and SiO_2.
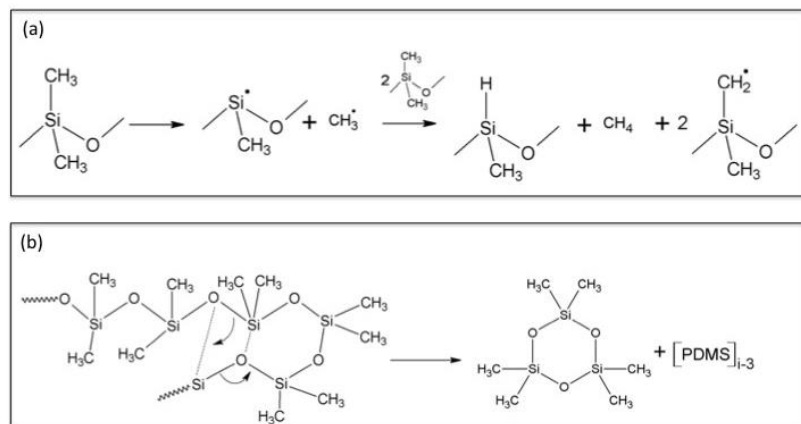
Figure 8.10 PDMS thermal degradation mechanisms. (a) at 800°C and during rapid heating; (b) at 400oC and during slow heating [288].

Figure 8.11 and Table 8.4 show the resulting liquid products from the CNT-A/SR

composite (6 wt.% filler loading) thermally degraded at 210°C in air. Cyclic trimers (D3)

were the most abundant degradation products along with decreasing amounts of tetramer

(D4), pentamer (D5) and hexamer (D6). Because the SR used in this study is a methyl

phenyl siloxane, the degradation products include both cyclic methyl siloxane and cyclic

phenyl siloxanes. The formation of cyclic siloxanes demonstrates that the degradation of

SR in a CNT-A/SR composite obeys the second mechanism. This mechanism is further

supported by the evolution of CO_2 (2350cm^{-1}) and H_2O (3400cm^{-1} and 1600cm^{-1}) in the

in-situ IR measurements (Figure 8.12). The reoccurring strong CO_2 and H_2O peaks from

the beginning of degradation to 80 minutes indicates that the CO_2 and H_2O gas come

from the degradation reaction rather than the desorption from the surface of the

composite.
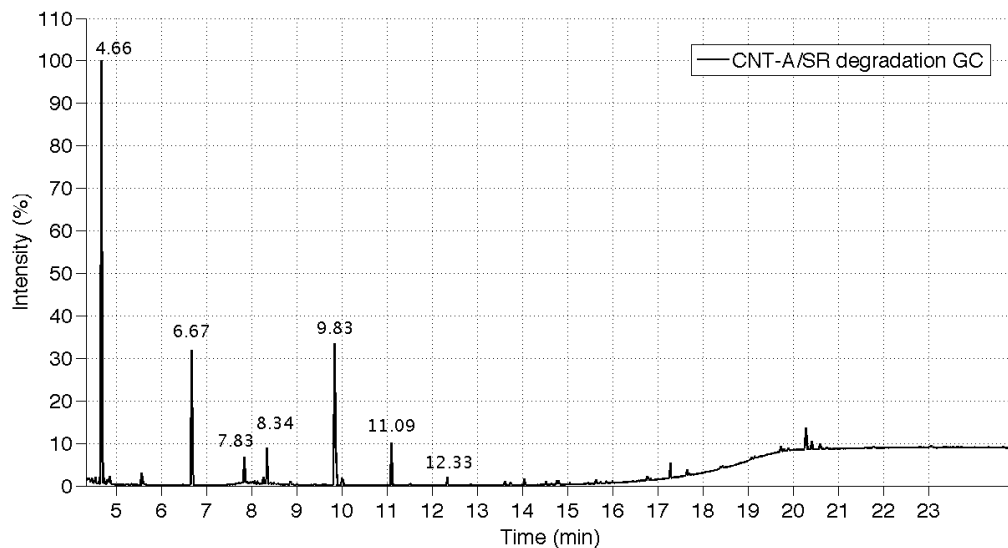
Figure 8.11 Gas chromatogram of the liquidified degradation products from CNT-A/SR composite with 6 wt.% CNT filler loading. The degradation was carried out at 210°C in air for 24 hours.

Table 8.4 Relative amounts of liquid products of CNT-A/SR composite thermal degradation at 210°C in air for 24 hours.
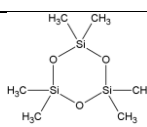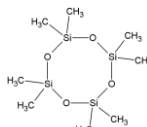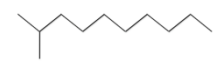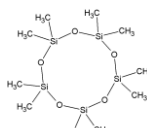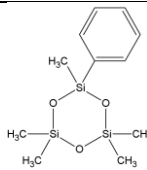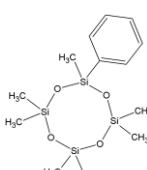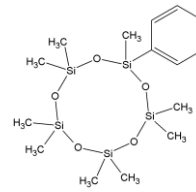
Retention time (min)	Compound	Relative intensity (%)
4.66		100
6.67		31.87
7.83		6.68
8.34		8.9

Table 8.5 Continued

Retention time (min)	Compound	Relative intensity (%)
9.83		33.47
11.09		10.14
12.33		2.00
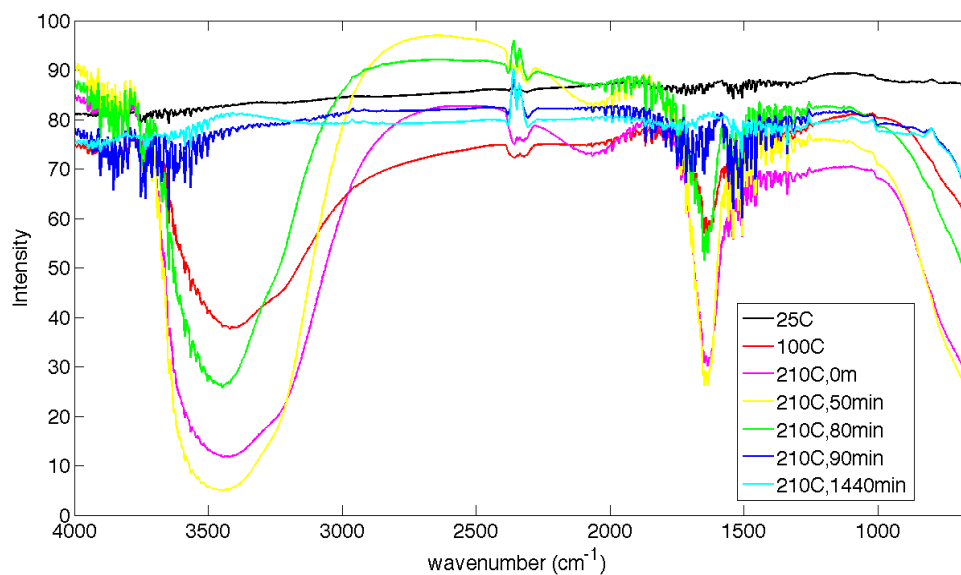
Figure 8.12 The in-situ IR spectra of CNT-A/SR thermal degradation at 210°C for 24 hours. The spectra include the weak signals from CNT-A/SR composite and strong signals from the H_2O and CO_2 products.

Camino et al. compared the thermal degradation of PDMS in both air and N_2 and found that although the degradation mechanism was the same for both cases (i.e. molecule splitting mechanism), the initiation temperature was lower in air than in N_2 [289]. They attributed this difference to the catalytic effect of oxygen through the free radical reaction. Since Co catalyzed thermal degradation of SR also follows the molecule splitting mechanism, it can be assumed that Co residues may also take on a similar role as oxygen to provide large amounts of radicals. Cobalt compounds were reported to accelerate the degradation of polymers and organic compounds such as polypropylene, low-density polyethylene and cyclohexane [291-293] due to their ability to produce radicals by electron transfer in the 3d subshell [291]. Although other transition metals such as Ni and Fe also have the potential to participate in the radical formation reactions, cobalt compounds show the strongest catalytic effect in certain environments [294, 295]. In order to demonstrate that the accelerated degradation is also a free radical reaction, a typical anti-oxidant called DPPD was added into the CNT-A/Q1-4939 composite to scavenge the radicals produced by Co nanoparticles. Q1-4939, a Pt cured silicone was selected to exclude the radical scavenging effect by DPPD on the free radical curing process of peroxide cured SR. As shown in Figure 8.4, incorporating CNT-A into Q1-4939 polymer led to a faster degradation, whereas the addition of DPPD retarded this accelerated degradation. Therefore, Co residues indeed increase the rate of degradation through free radical reactions.

The effect of Co nanoparticles and their composition on the thermal stability of SR was further investigated by looking into the degradation of metal nanoparticle/SR composites. The metal nanoparticle/SR composites were prepared by in-situ

decomposing metal acetylacetonate (ACAC) compound inside SR. Controlling the decomposition atmosphere can produce nanoparticles with different oxidation state. Decomposition in N2 will produce nanoparticles in both metallic and oxide forms [296], while the decomposition in a reducing environment (20 vol.%H_2, 80 vol.% Ar at 300°C for 2 hours) guarantees the nanoparticles in the metallic form [297]. Among the three metal nanoparticles tested, only Co plays a significant role in decreasing the onset degradation temperature of SR in N_2 (Figure 8.13). Both metallic nanoparticles and oxide nanoparticles of Co shows a two-step degradation process. The first degradation peak locates at the same temperature with the degradation peak of CNT-A/SR, i.e. 200oC lower than the pure SR matrix. In comparison, Fe/SR and Ni/SR have only one degradation peak, occurring above 500oC. Comparing the Co nanoparticles/SR composites with and without H2 treatment, the weight loss during the first step of degradation is 6.3% in the former and 31% in the latter. Therefore, only Co shows a significant free radical generating capability in the present system, and the oxide form of Co nanoparticles may be more reactive than the metallic form.

Interestingly, the Co (III) ACAC/HNO$_3$ treated CNT-A/SR three-phase composite shows less weight loss than the Co (III) ACAC/SR or Co (II) ACAC/SR two-phase system in the first step, indicating that CNTs interfered with the free radical reaction. Both density functional theory calculation [298] and experimental studies [248, 299] demonstrated that CNTs could act as free radical scavenger. In our case, some of the free radicals generated by Co species may be trapped by CNTs. As a result, the weight loss due to free radical degradation is reduced in the presence of HNO$_3$ treated CNTs.
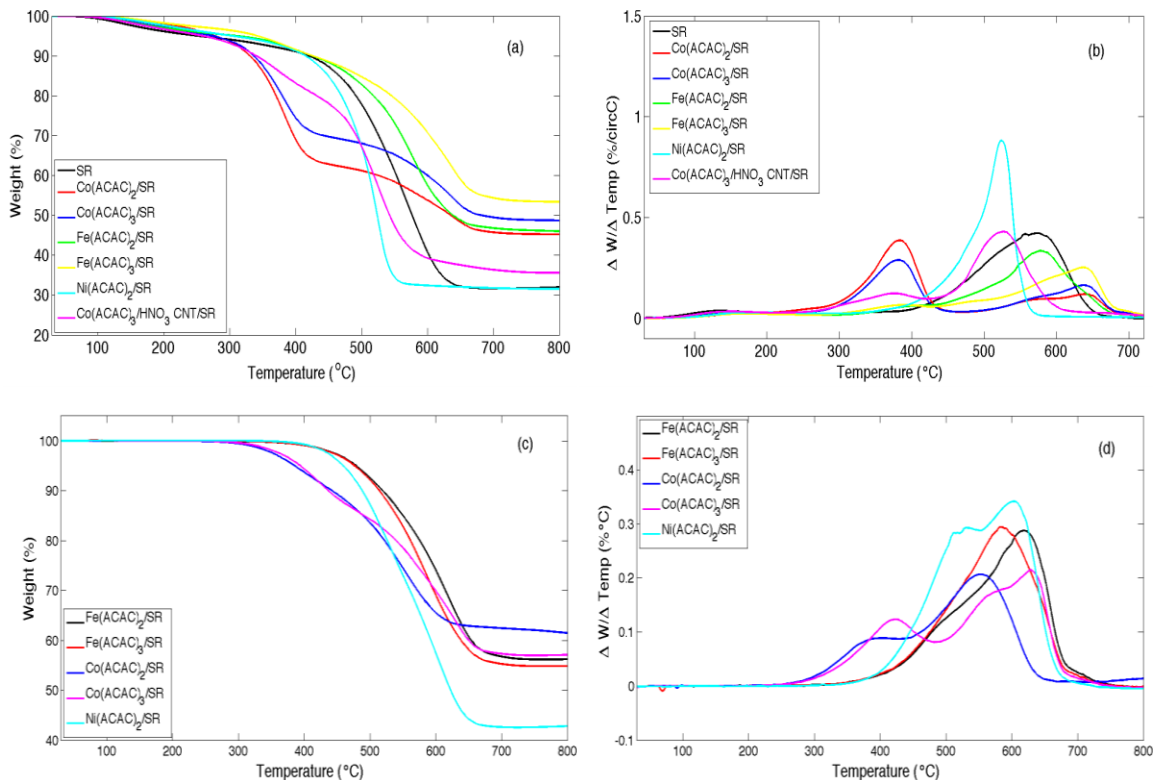
Figure 8.13 Effect of Co, Fe, and Ni nanoparticles on the thermal stability of SR in N_2. (a) (b) Nanoparticles are synthesized by in situ decomposition of corresponding metal ACAC salts in N_2 and are in both metallic and oxide forms. (c) (d) Nanoparticles are synthesized by in situ decomposition of corresponding metal ACAC salts in H_2/Ar and are in metallic form.

8.3.3 **Methods to eliminate accelerated degradation**

One way to avoid the reduced thermal stability of CNT/SR composites is to avoid using Co catalyzed CNTs; however, this would be difficult as Co is a popular catalyst for CNT growth via CVD. A preferential approach then is to remove the Co residues through acid purification of CNTs (Figure 8.9).

Figure 8.15 shows TGA results of acid treated CNT-A/SR composites. HCl-CNT/SR and HNO_3-CNT/SR both show a major degradation peak at 478.7 $^{\circ}$C and 505.2 $^{\circ}$C respectively, which is comparable to the thermal stability of pure SR. However, both of them also show a shoulder peak lower than the pure SR degradation peak. The

163

appearance of the shoulder may result from the introduction of more oxygen-containing functional groups [284]. The FTIR spectra of HCl-CNTs and HNO$_3$-CNTs show a peak at 1740 cm^{-1}, corresponding to the carbonyl groups; whereas the peak is absent in the case of the untreated CNTs (Figure 8.14). On the one hand, these oxygen-containing groups can enhance the free radical scavenging capability of CNTs [298, 300, 301] and thus improve thermal stability; on the other hand, these oxygen containing groups, especially carboxylic groups may accelerate the degradation of the polymer following an acid-catalyzed degradation mechanism as reported by Zeng et al [302] and Bikiaris et al [270]. Therefore, we hypothesize that the degradation peak at a higher temperature represents the enhanced thermal stability by scavenging the free radicals while the shoulder peak at a lower temperature results from the acid-catalyzed degradation of acid treated CNTs.
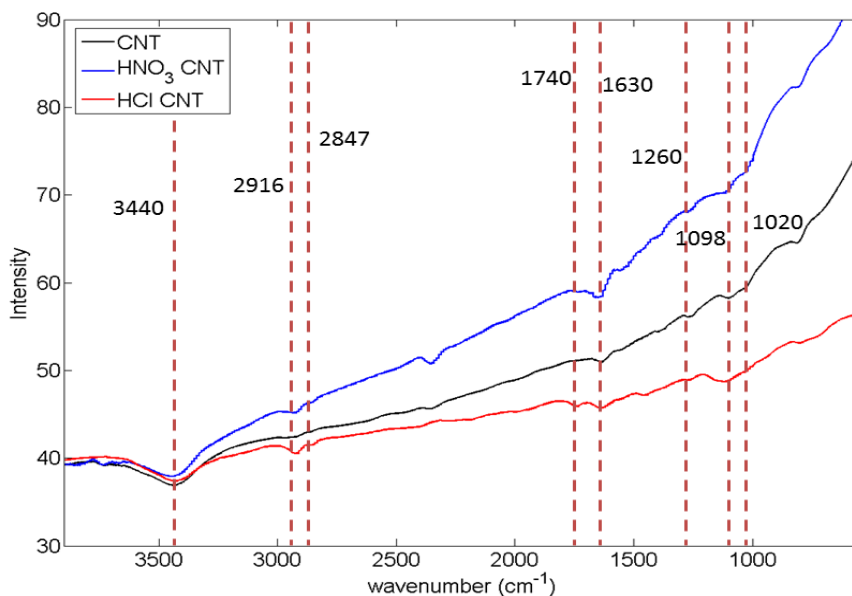
Figure 8.14 FTIR spectra of original and acid treated CNTs. The peak at 3440, 1740, 1630, and 1260 cm^{-1} correspond to –OH, C=O, C-C in graphitic structure, and C-OH, respectively. The peaks at 2916 and 2847 cm^{-1} signify the existence of -CH$_3$ or -CH$_2$, and the peaks at 1020 and 1098 cm^{-1} signify the C-O bonding from hydroxyl groups [286].
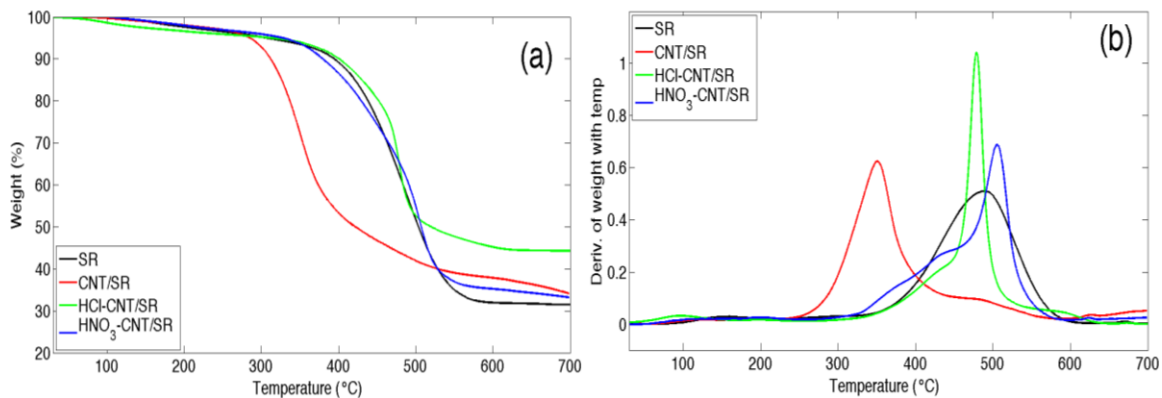
Figure 8.15 (a)TGA results and (b) the derivative of weight loss with temperature of SR, CNT/SR , HCl treated CNT/SR and HNO_3 treated CNT/SR with a ramping rate of $1^oC/min$.

8.4 Conclusions

CNTs synthesized with cobalt catalysts were found to dramatically decrease the thermal stability of silicone in CNT/SR composites, while CNTs synthesized with other metal catalysts did not show expected degradation. The cobalt residues within CNTs accelerate the degradation of silicone through free radical reactions. It is recommended that to gain an increase in CNT/silicone composite stability, another metal catalyst should be used. If that is not possible, further processing CNTs via acid-washing can improve the thermal stability of CNT/silicone composites.

165

CHAPTER 9 CARBON NANOTUBES INHIBIT THE FREE RADICAL CROSS-LINKING OF SILOXANE POLYMERS

9.1 Introduction

Since their discovery in 1991, CNTs have attracted great interest from various fields, the most promising of which is the field of CNT/polymer composites. The exceptional physical and chemical properties of CNTs make them ideal candidates for advanced filler materials in composites. For example, their high electrical conductivity and high aspect ratio can greatly decrease the percolation threshold of conductive plastics [303]. Their massive thermal conductivity may also be exploited to create thermally conductive composites [260]. In addition, their low density, superior Young's modulus [304], and tensile strength [305] can dramatically enhance the mechanical properties of CNT-reinforced composites.

The prerequisite to preparing a CNT/polymer composite for these applications is that the CNTs do not interfere with the polymerization or cross-linking of polymer matrix. For many years, this was simply assumed to be the case, given the graphitic nature of CNTs [306]. However, further studies on CNTs determined that they were not always inert. With a large area of sp^2-hybridized structure and a high electron affinity, CNTs actually exhibit strong reactivity towards free radicals. This unique property has since been used in side-wall functionalization of CNTs [307-310], elongation of polymer lifetime as free radical trapping agents [248], and antioxidant treatment for pathologies [311]. Yet, it is not clear whether this reaction between CNTs and free radicals may affect free radical cross-linking. The present study is aimed at understanding how the structure of CNTs could affect free radical cross-linking in a CNT/polymer composite. A

166

composite of MWCNTs and vinyl-terminated PDMS composite is used as a model

compound.

9.2 Experimental

9.2.1 Materials

Two types of MWCNTs were obtained from Chengdu Organic Chemistry Co.,

China. Both types were 10-20µm long and had purity above 95%. CNT-A had a

diameter of 8-15nm while CNT-B had a diameter of more than 50nm. Graphite 230U was

donated by Asbury Carbons. Wacker® V-20000 (average molecular weight: 48000; vinyl

content: 1.3%) was used as the PDMS matrix with dicumyl peroxide as the cross-linking

initiator. Unless otherwise mentioned, the CNTs in CNT/PDMS composites were used as

received, without any additional purification processes. HNO_3 treatment of CNTs were

performed by mixing 5g CNTs with a 250ml 35% HNO_3 solution and refluxed for

different time at 100^oC. The obtained mixture was filtered and washed with deionized

water. The treated CNTs were then dried under vacuum for 20 hours at 70^oC and denoted

as HNO_3-CNTs.

9.2.2 CNT/PDMS composite preparation

To prepare the CNT/PDMS composite, 2g of PDMS and 0.03g of dicumyl

peroxide were first dissolved together in 20ml toluene, while the CNTs were dispersed in

toluene (8mg/ml) by ultra-sonication (Aquasonic 75HT) for 1 hour. The CNT dispersion

was then poured into the PDMS and mixed by ultra-sonication for an additional 3 hours.

The homogenous mixture was then cast in a petri dish and dried under a fume hood for

24 hours. The resulting dry film was pressed into a Teflon mold and cross-linked at

167

150°C for 1 hour under 1.6MPa pressure. Pure PDMS matrices were cross-linked under an identical procedure to the filled composites.

9.2.3 **Characterization**

Tensile strength and modulus were measured using a typical tensile test setup (Instron microtester 5548). Samples were cut into a dumbbell shape (28.75mm×4.75mm, narrow portion 8.25mm×1.5mm). The testing speed was set at 50mm/min. The same setup was also used to measure the cross-linking density; however, a smaller extension rate of 10mm/min was used to guarantee that the deformation reached equilibrium at any instant of the extension.

Swelling tests were performed by immersing 20mm×5mm×2mm rectangular pieces of PDMS or CNT/PDMS composites in toluene for 5 days to allow thermodynamic equilibrium to be reached. The samples were then taken out of the solvent and placed in the fume hood for 10 days to dry. The weight and dimensions before swelling, after swelling, and after solvent evaporation were measured.

The glass transition temperature of cross-linked CNT/PDMS and pure PDMS was measured by DMA (TA instrument 2890) using the film-tension mold. A 5mm×3mm×2mm film was initially cooled to -150°C using the liquid nitrogen cooling system, and then heated to room temperature at a rate of 5°C/min. The sample was oscillated at a constant frequency of 10Hz with amplitude of 20μm. The DMA Tg is determined to be the intersection of two tangent lines from the storage modulus curve.

Raman spectra of CNTs in the composites were obtained by a LabRAM ARAMIS Raman confocal microscope (HORIBA Jobin Yvon) equipped with a 532nm diode-pumped solid state (DPSS) laser. Si wafer was used as a substrate.

168

The XPS of CNTs was carried out with a Thermo K-Alpha XPS.

9.3 Results and discussion

Free radical reaction is the oldest and one of the most widely-used schemes in preparing PDMS elastomers. Vinyl-terminated PDMS can be cross-linked with a peroxide-based catalyst at elevated temperature via free radical reaction according to the reaction shown in Figure 9.1. The peroxide catalyst decomposes and generates free radicals that can react with vinyl groups and initiate the cross-linking.
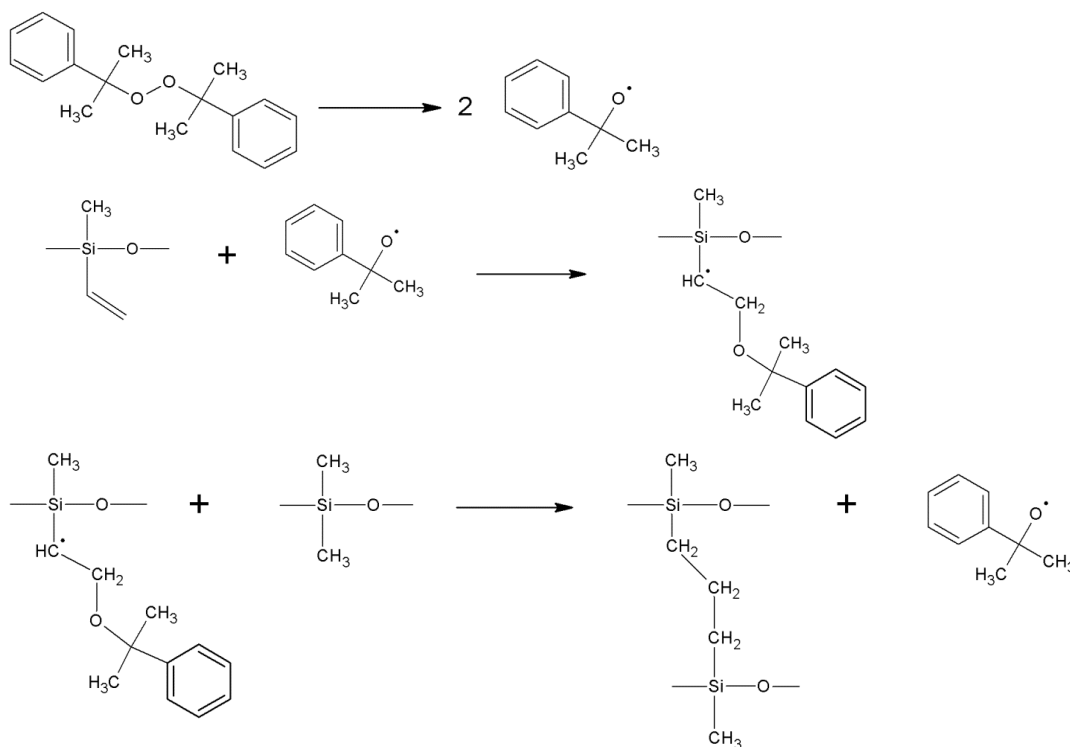
Figure 9.1 Cross-linking mechanism of vinyl-terminated PDMS through free radical reaction.

Carbon-based reinforcements are often added to the elastomers to improve their mechanical properties. CNTs are reported to be more efficient reinforcement than conventional fillers, due to their high aspect ratio and intrinsic mechanical robustness [312]. The Young's modulus and tensile strength of a CNT/PDMS composite usually

increases with increasing loading of CNTs. For CNT-B, it is indeed this case (Figure 9.2

(b)). The tensile strength and Young's modulus increase by 1.5 times and 2.5 times,

respectively, when increasing the CNT loading from 1wt.% to 20wt.%. However, for the

CNT-A/PDMS composite, a totally opposite trend is observed (Figure 9.2(a)); the tensile

strength and Young's modulus decrease with increasing CNT loading. This leads to an

investigation into the possible adverse effects of CNT-A on the cross-linking of PDMS.
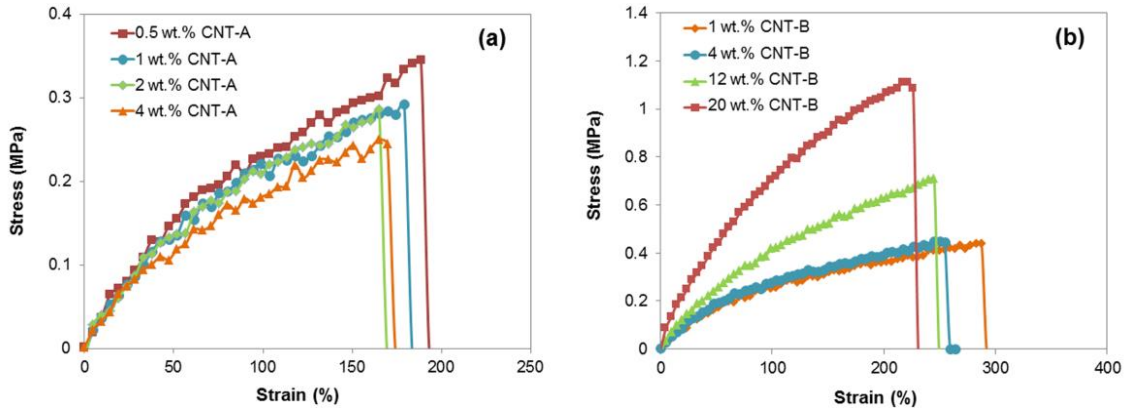
Figure 9.2 Tensile stress-strain curve of (a) CNT-A/PDMS composite, and (b) CNT-B/PDMS composite with various CNT loadings. The concentration of CNTs refers to weight percentage, which is used throughout the whole text.

The cross-linking density of CNT-A/PDMS composites is measured by swelling

test, equilibrium stress-strain measurement, glass transition temperature measurement and

Raman spectroscopy. In a swelling test, CNT-A/PDMS composite samples are immersed

in toluene. The samples absorb toluene and swell, until an equilibrium between the

thermodynamic tendency to swell and the retractive forces from the cross-linked network

is reached. The cross-linking density can be calculated from the swelling phenomenon by

Flory-Rehner equation [313]:

$$N = -\frac{1}{2V_s}\frac{\ln(1-V_r)+V_r+\chi V_r^2}{V_r^{1/3}-V_r/2} \qquad (1)$$

where N is the moles of effective cross-links in a unit volume; V_s and V_r represent the molar volume of toluene and the volume fraction of PDMS in the swollen gel, respectively. χ is the polymer-solvent interaction parameter. For PDMS and toluene, χ is 0.465 and the molar volume of toluene V_s is 106.29 ml/mol [314]. With CNT fillers, the volume fraction of PDMS in swollen gel is given by:

$$Vr = \frac{S_p - \frac{S_e}{(1-\varphi)}(\frac{I-F}{I})}{S_p + S_s\left(\frac{S-F}{I}\right) - S_e\left(\frac{I-F}{I}\right)} \qquad (2)$$

where I is the initial weight, S is the swollen weight, F is the final dry weight, S_p is the initial specific volume of the composite, S_e is the specific volume of the extract, S_s is the specific volume of toluene solvent, and φ is the volume fraction of the filler [315]. The effective cross-linking density of CNT-A/PDMS composites with different CNT loadings is calculated according to Equations (1) and (2) and the results are shown in Figure 9.3(a).
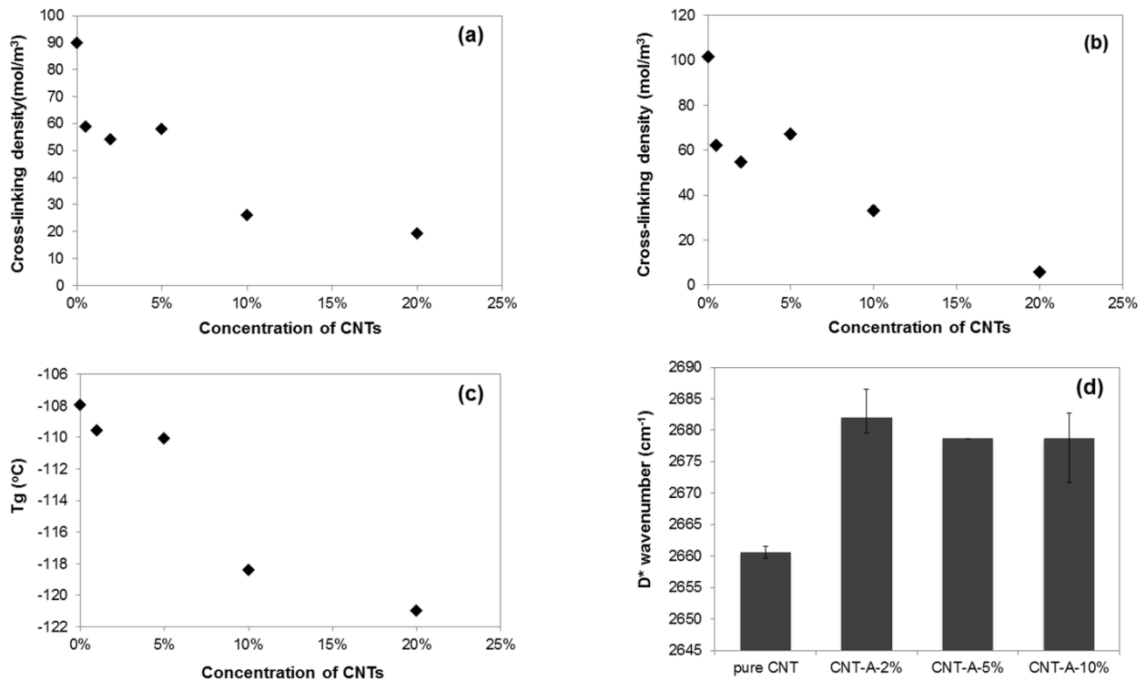
Figure 9.3 Effective cross-linking densities of CNT-A/PDMS composites with different filler loadings determined by (a) swelling test, (b) equilibrium stress-strain

measurements. (c) Glass transition temperature of the CNT-A/PDMS composites as a function of CNT concentration. (d) D* wavenumber in Raman spectra of CNTs in CNT-A/PDMS composites.

In cases where the fillers do not affect the curing process, the measured cross-linking density of the composite will be slightly higher than that of the pure resin. This can be explained by several mechanisms: (1) the fillers can pose steric hindrance to polymer chain movement during swelling; (2) the physical interaction between the fillers and matrix contributes to the total retraction force of the polymer network[316]; and (3) the polymer chain and fillers (especially CNTs) form physical entanglements that restrict the swelling displacement[317]. However, as shown in Figure 9.3(a), the effective cross-linking density of the composites decreases with increase in the amount of filler. Even with 0.5wt.% CNT-A, the cross-linking density decreases 1/3 from 90mol/m^3 to 59mol/m^3. When the CNTs' concentration increases further to 10wt.%, the cross-linking density drops to 26mol/m^3, 1/3 of the original value. This dramatic decrease in the cross-linking density indicates that the carbon fillers may have a negative role on the cross-linking process of a PDMS resin.

Equilibrium stress-strain measurement is another way to determine the cross-linking density from the Mooney-Rivlin equation:

$$\frac{\sigma}{2(\lambda-\lambda^{-2})} = C_1 + \frac{C_2}{\lambda} \qquad\qquad (3)$$

where σ and λ represent the engineering stress and the extension ratio, respectively [313]. C_1 and C_2 are two elastic constants. C_1 is proportional to the effective cross-linking density N_c given by

$$C_1 = N_c RT \qquad\qquad (4)$$

172

where R is the gas constant and T is temperature. Thus a plot of $\frac{\sigma}{2(\lambda-\lambda^{-2})}$ versus $\frac{1}{\lambda}$

can be used to determine the constant C_1 and thus the cross-linking density. To guarantee

that the deformation is reaching equilibrium at any instant, a small extension rate of

10mm/min was used in tensile tests, and only the data approaching the break point was

analyzed. The results are shown in Figure 9.3(b). The values of the cross-linking density

from stress-strain measurements are quite consistent from those of the swelling test. The

cross-linking density drops 1/3 with 0.5wt.% CNT-A, then stays relatively stable from

0.5wt.% to 5wt.% CNTs, likely due to a trade-off between an increase in physical

entanglement and the loss of chemical cross-links. When the CNT loading is above

5wt.%, the cross-linking density continues to drop to 33mol/m^3 and 6mol/m^3 for 10wt.%

loading and 20wt.% loading, respectively.

T_g can be used as an indicator of the cross-linking density, where elastomers with

higher cross-linking density usually have a higher T_g. Here, T_g of CNT/PDMS

composites with different concentrations were measured by DMA and the result is shown

in Figure 9.3(c). For pure PDMS, it has a T_g of -108°C, but with adding CNT-A into the

composite, the T_g decreases monotonically with increasing the CNT-A concentration. T_g

decreases to -110°C, -118 $^{\circ}$C and -121°C after adding 5%, 10% and 20% of CNT-A,

respectively. The decrease in T_g suggests a decreased cross-linking density after adding

CNT-A, which is consistent with results shown in Figure 9.3(a) and Figure 9.3(b).

Raman spectroscopy has also been used to characterize the cross-linking in

CNT/polymer composites. The second-order overtone of the D band, the D* band, is very

sensitive to any perturbation in the load transfer at the interface between the CNTs and

the polymer matrix [318, 319]. Zhao *et al.* took advantage of the Raman shift induced by

173

polymer contraction in the cross-linking process and found a positive correlation between

the D* band up-shift and the cross-linking density[318]. For this study, the D* shifts of

the CNT-A/PDMS composites of different filler loadings were compared (Figure 9.3(d)).

A filler loading as low as 2wt.% will lead to a 22 cm^{-1} up-shift of the D* band, resulting

from the contraction of the PDMS matrix after cross-linking, which imposes a

compression force to the individual CNT. With the increasing CNT concentration, we

observed a down-shift of D* band rather than an up-shift, indicating that the cross-linking

density actually decreases with more CNTs.

All the above results suggest that CNTs may adversely affect the free-radical

cross-linking process of the PDMS matrix. This result is not surprising considering

fullerenes have also been reported to retard the free-radical polymerization reaction of

methyl methacrylate, styrene, vinyl acetate, *etc.*[320-322] The retardation was attributed

to fullerene's strong electron affinity of approximately 2.65eV, and to its ability to

accommodate free radicals by forming stable radical adducts [323, 324].

With a similar sp^2-hybridized structure and even stronger electron affinity than

fullerene [325], CNTs are expected to show a similar spin-trapping capability. As early as

2003, Watts *et al.* proposed that CNTs could act as antioxidants, i.e. radical-trapping

agents, to retard the aging of polystyrene, polyethylene, polypropylene and

poly(vinylidene fluoride) [248]. In addition, intensive studies have been conducted to

modify the CNTs' surface using free radicals [307-310]. Researchers make use of the

addition reaction of radicals with CNT double bonds to graft various functional groups to

the CNTs. These radicals include alkyl radicals and peroxide radicals, indicating that

CNTs can accept a wide range of radicals. The PDMS in this study is cured via a free

174

radical reaction. Therefore, it is reasonable to assume that the decreased cross-linking density of PDMS results from the trapping of free radicals by CNT-A during curing.

However, only some CNTs (such as CNT-A in Figure 9.2) demonstrate this effect, whereas others (such as CNT-B) do not. This raise the question, what structural characteristics in CNTs determine their reactivity towards free radicals?

One possible determining factor is the functionality of CNTs. CNTs contain functional groups either from the synthesis and/or the purification processes. It has been reported that the functional groups, especially hydroxyl and carboxyl groups, increase the free radical trapping activity with respect to pristine CNTs [300, 301]. To demonstrate that the functionality in CNTs may increase the reactivity towards free radicals and decrease the cross-linking density of PDMS, CNT-A was treated with HNO_3 at 100°C for different durations (10mins, 30mins, and 120mins). The XPS results (Table 9.1) show that longer acid treatment time does introduce more oxygen content, i.e. functional groups in CNTs. The effect of the amount of functional groups is evident (Figure 9.4). The cross-linking density decreased dramatically with increasing the acid treatment time. The cross-linking density also decreases with increasing CNT concentration. That is, the cross-linking density is strongly dependent on the total amount of functional groups in the CNTs. For CNTs treated longer than 30mins, the CNT/PDMS cannot cure, even at a low CNT loading of 2wt.% (the composites completely dissolved in toluene during the swelling test). Therefore, functional groups on the CNT surfaces can significantly hinder the free radical polymerization of a PDMS matrix. When preparing CNT/polymer composites, over-functionalizing CNTs during purification should be avoided if they are to be used in polymer matrices that cure by free-radical reactions.

175

Table 9.1 Carbon/oxygen atomic ratio of CNTs measured by XPS

Treatment time (mins)	C/O
CNT-A	39.16
CNT-B	24.71
CNT-A, HNO_3-10min	35.10
CNT-A, HNO_3-30min	22.53
CNT-A, HNO_3-120min	4.99
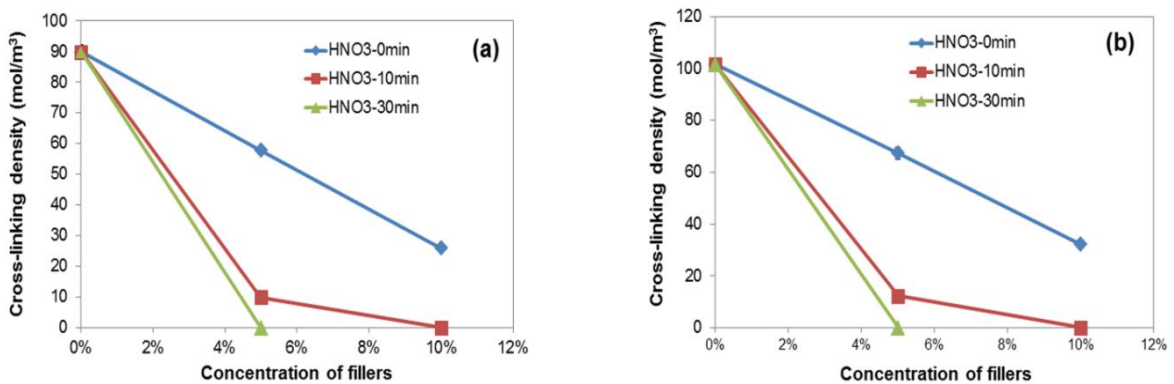
Figure 9.4   Effective cross-linking densities of CNT-A/PDMS composites determined by (a) swelling test and (b) equilibrium stress-strain measurements. The CNT-A is treated with HNO_3 at different durations.

Another possible determining factor is the curvature of the CNTs.[326] Peng *et al*. observed less reactivity of the CNTs with free radicals than that of fullerenes, which was attributed to the smaller curvature of CNT sidewalls built from graphene cylinders [309]. In one study of cyclopolyenes, a high curvature was found to lead to the stabilization of the Lowest Unoccupied Molecular Orbital (LUMO) and an increase in electron affinity [327]. If we regard CNTs as large-area cyclopolyenes, increasing the curvature of the graphene sheet in the CNTs will increase the electron affinity and hence increase the addition reaction rate. In addition, during the study of fullerene's reaction with benzyl radicals, it was found that the curved surface of fullerenes may facilitate the

176

bulky benzyl groups in shielding and stabilizing the radicals [326]. In the present study, three fillers with different curvatures were investigated. CNT-A with a diameter of 8-15nm represents the highest curvature; CNT-B with a diameter of more than 50nm represents the medium-curvature; and graphite represents the lowest, i.e. zero curvature. The cross-linking densities calculated by the swelling tests and stress-strain measurements of PDMS composites with these three fillers are shown in Figure 9.5. As theorized, CNT-A demonstrates the highest reactivity to trap the free radicals and decrease the cross-linking density of PDMS. Graphite has little influence on the cross-linking density due to its zero curvature. CNT-B/PDMS composites show increased cross-linking density when the filler loading increases, indicating that large-diameter CNTs have little effect on the curing of PDMS and the "physical entanglement" between PDMS chains and CNT-B increases the total cross-linking density. Note that the comparison is predicated on the assumption that all parameters other than the diameter are the same for the three fillers. However, in real cases, the functionality cannot be so precisely controlled. XPS results show that CNT-B has a C/O ratio of 24.71 while CNT-A has a C/O ratio of 39.16, indicating that CNT-B may contain more functional groups than CNT-A does. Since CNT-A still shows a more significant reactivity towards free radicals, the determining factor here may be the curvature of CNTs.
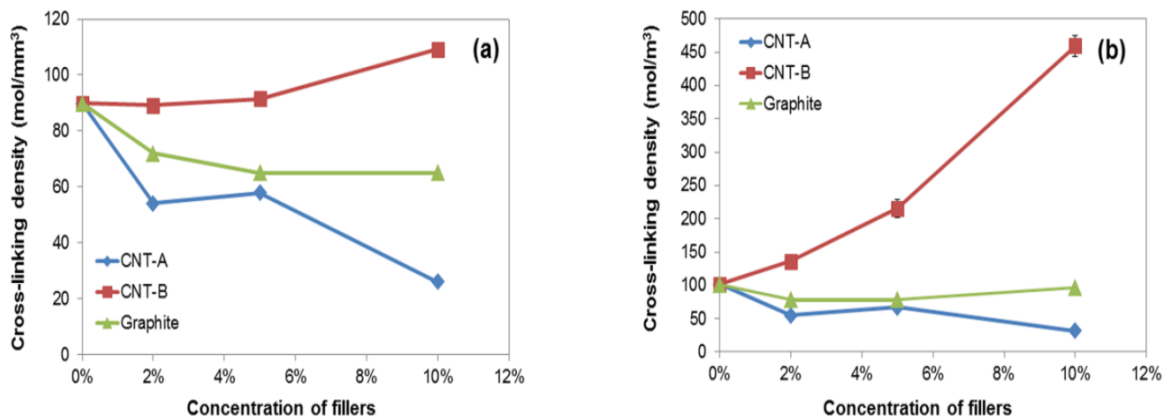
Figure 9.5 Effective cross-linking densities of CNT-A/PDMS, CNT-B/PDMS and graphite/PDMS composites with different filler loadings determined by (a) swelling test and (b) equilibrium stress-strain measurements.

9.4 Conclusion

In conclusion, this study found that CNTs inhibit the curing process of matrix polymers if the polymerization is based on free radical reactions. The inhibition effect is more significant for CNTs with more functional groups and smaller diameters.

CHAPTER 10 AUTOMATIC QUANTIFICATION OF FILLER DISPERSION IN POLYMER COMPOSITES

10.1 Introduction

Filler dispersion plays a critical role in determining various properties of polymer composites, including electrical conductivity [328], dielectric constant [329], heat transfer [330], mechanical strength [312, 331], optical transparency [332], wear resistance [333], *etc.* Uniform filler dispersion has become one of the ultimate goals in the preparation of composites. Although methods to improve filler dispersion have been intensively explored [334-336], it is hard to compare their dispersion quality and thus select the best method due to a deficiency of objective and universal metrics for filler dispersion.

In most prior studies, the dispersion status is characterized by the evaluation of the physical properties of composite materials, including the electrical conductivity, rheology, mechanical properties, *etc.* [334, 337-339] In the meantime, some other dispersion evaluation techniques were also proposed for specific categories of nanocomposites, such as Raman mapping and microscale DMA mapping of carbon nanotube (CNT) based nanocomposites [319, 340]. However, these indirect approaches cannot provide adequate dispersion information because not only filler dispersion but also many other factors could affect the measured properties. For example, in the case of a filled composite with a loading level near the percolation threshold, even if the filler dispersion keeps constant, slight difference in filler loading could lead to orders of magnitude change in the electrical conductivity and viscosity. Therefore, direct

179

assessment of filler dispersion through visualization will be favored in terms of reliable data interpretation.

Direct assessment usually includes three steps. Firstly, images representing the microstructure of composites are captured by microscopes, such as optical microscope, SEM, TEM, *etc.* Secondly, the fillers are identified from the obtained photo images. Thirdly, certain statistical analyses are made to give a numerical value that indicates the level of dispersion. While most of the previous researchers took such a procedure, the bottleneck lies in the correct identification of fillers from the obtained images [341-347]. There are several challenges associated with filler identification from the images.

The first challenge is that many studies neglected the step of filler identification, namely it was often assumed that the positions of the fillers had been obtained, in many cases, manually. Unfortunately, given the large number of fillers that may exist in the image, manually picking them out is an extremely tedious work. Thus it is impossible for such an analysis to be extended to a high throughput scale, which is necessary for more data sets and statistically more robust results. In addition to the time consumption, an even more fundamental problem lies in the subjectivity induced by such a manual tracing process. Therefore, in more recent papers, identification of the fillers is given more weight. For instance, Pegel *et al.* set a threshold for the input image so that pixels in the image with higher intensity values than the threshold are identified as fillers. Based on that, the spatial statistics is computed as an indication of dispersion [348]. Using a similar way to identify the fillers, Sul *et al.* set a global threshold and extract the particles from the original image. After that, the Delaunay triangulation is computed based on which the Lennard-Jones potential is calculated as the dispersion measurement [349]. In the work of

Glaskova et al, the brightness threshold is optimized by the so-called isodata algorithm before subsequent analysis [350]. However, all the above methods take advantage of the strong contrast between fillers and the polymer matrix and set a threshold to separate the fillers from the background. Due to the noise in the imaging devices and spatial difference in electrical conductivity/topography, the images in many cases may display inhomogeneous brightness. Under such scenarios, a single threshold is not sufficient to correctly extract the fillers in the entire image and a more accurate method is needed.

The second challenge is that for high-aspect-ratio fillers, such as CNTs, they exhibit different morphologies from dots to tubes of different lengths, depending on their orientation relative to the observation plane. This complexity of shapes and dimensions increases the difficulties of filler identification. During filler identification, they cannot be simplified as points, as in the case of particulate fillers, because such a simplification will inevitably lose some key information present in the original image, such as orientation.

The present study aims at addressing the above two challenges and presenting an automatic, high-throughput, subjective way to quantify the filler dispersion in composite system. For the first challenge, we present an entire pipeline for the analysis of the filler dispersion with more accurate filler identification and dispersion evaluation processes. In the filler identification step, the images are divided into finite elements and a local comparison in each element is used to separate the fillers from matrix. By doing so, we promote the tolerance of inhomogeneity and noise in the image. With the filler positions obtained, in the dispersion step, the well-developed measurement in probability theory is used to evaluate the (dis)-similarity between two sets of samples. Specifically, the fillers

in the image are considered as realizations of a random variable distributed in the image field of the view. Then, the probability density function (PDF) is estimated and the mathematically rigorously defined "distance" between two PDFs is employed to measure the (dis-) similarity between the filler dispersion under investigation and a uniform distribution. It not only represents a rigorous definition for the dispersion index, but also can reflect the filler size and the aggregation of fillers in the composites, which have rarely been achieved in previous dispersion metrics involving comparison with uniform distribution [343]. For the second challenge (i.e. high-aspect-ratio fillers), we measure the tube-shape characteristics with Hessian matrices for each pixel in the image. With this shape recognition function, the identification of CNTs no longer relies on the brightness assumption, and thus the result is much more accurate.

The developed technique enables convenient quantification of filler dispersion in composites and is of great use to correlate the microstructure of CNT/polymer composites with their processing conditions and properties. Here we used CB/SR composites as the model compounds for composites with particulate fillers. The dispersion efficiency of three commonly used processing methods was compared and the best processing method was identified. CNT/SR composites were used as the model compounds with high-aspect-ratio fillers, the developed filler dispersion method was used to correlate the microstructure of the composites with their electrical properties.

10.2 Experimental

10.2.1 Composite preparation and characterization

10.2.1.1 CB/SR composites preparation

CB/SR composites were used as the model compound with particulate fillers. CB (Vulcan XC72, Cabot) has an aggregate density of 1.8 g/cm^3 and a surface area of 254 m^2/g (tested under N_2). SR resin is a peroxide-curable methyl phenyl silicone gum provided by Rockbestos-Surprenant Cable Co.

Generally there are two strategies to promote dispersion of carbon fillers in a polymer matrix, namely the surface modification of fillers or the optimization of processing conditions [351]. For many industrial applications, chemical modification may be undesirable due to the possible change in the properties or performance of the material. As a result, enhancing dispersion through the processing optimization is preferred. The fabrication processes of carbon/polymer composites can be generally divided into four categories, namely 1) no fluid mixing by shear force, 2) melt mixing through extrusion, 3) dispersion-dissolution-precipitation, where polymers and fillers are dissolved/dispersed in solvents for mixing and then evaporate the solvents, and 4) dispersion reaction, which is applied to liquid monomers with a low viscosity [334].

In the case of the SR used here, three of the above dispersion processes were tested.

1) No-fluid mixing by three roll mill. Dry CB powders were dispersed in SR by shear force provided by three roll mill (Torrey hills technologies LLC). The dispersion level was set by the number of rolling cycles. The initial ten cycles of mixing was used to incorporate all the CB fillers into SR.

183

2) Dispersion-dissolution-precipitation via ultrasonication. The CB fillers were dispersed in toluene for 1 hr under ultrasonication (Misonix 3000) while the SR was dissolved in another beaker with toluene. Then the two solutions were combined and further mixed by ultrasonication for various durations (0-4 hrs). The mixture was then dried under vacuum for 12 hrs before curing.

3) Dispersion-dissolution-precipitation via high shear blending; This method is basically the same with the previous one, except that all the mixing was performed by high shear blending (Talboys laboratory stirrer 104A). Also different time intervals (0-4 hrs) of high shear blending were examined to compare the effect of mixing intensity.

All the samples had a constant filler loading of 15 wt%. In the end, the mixture was pressed into a Teflon mold and cured for 1 hr at 180 $^{\circ}$C under 1.6 MPa pressure.

10.2.1.2 CNT/SR composites preparation

CNT/SR composites with a filler loading of 15 wt% were used as the model compound with high-aspect-ratio fillers. CNTs (Chengdu organic chemicals Co.Ltd) are 10–20 μm by length and 50 nm by diameter. The dry CNTs were dispersed in SR by three roll mill over various times. The dispersion level was set by the number of rolling cycles; the initial ten cycles and analyzed to give the average dispersion/orientation index.

The vertically aligned CNTs (VACNTs) composite was used as an extreme case to test the orientation index. It is prepared by infiltrating the VACNTs with low viscose monomers. The details were described in our previous work [260].

10.2.1.3 <u>Composite characterization</u>

Fractured surfaces of the cured specimens were obtained in liquid nitrogen. Three fractured surfaces per specimen were imaged and analyzed to give the averaged dispersion index. SEM observation was conducted in LEO 1530 FE-SEM with an acceleration voltage of 15kV.

Dynamic mechanical measurements were performed on a DMA (TA instruments 2980) tension mode. Frequency sweep was performed at 50 ^{o}C with a strain of 0.5%.

Samples for electrical measurements were prepared by embedding two Ni coated Cu wires into the composite before curing. Then the electrical resistance was measured by a fluke 289 RMS multimeter after curing. Although the two-point measurement scheme includes the resistance of wires and contacts, this added resistance is negligible compared to the resistance of the composite films.

10.2.2 Filler identification for particulate fillers

Usually, the image is contaminated by the noise from the imaging process. Hence, it is pre-processed to remove the noise by passing through the median filter with a neighborhood size of 3×3. Then, denote the (noise removed) image as $I(x; y) : R^2 \rightarrow R$ and discretely, it can be written as a matrix: $I(i,j)$, where $i = 1, ..., N_x$ and $j = 1, ..., N_y$. Subsequently, the task of filler identification is to obtain a set of points $c_1,...,c_M \subset R^2$, where each c_i represents the coordinates of a single filler element.

Conductive fillers such as CB appear to be bright spots in SEM at high accelerating voltages while the insulative polymer matrix remains dark [352, 353]. Indeed, this is also the insight behind the thresholding technique described previously [348-350]. However, due to the qualities of the sample material, imaging device, or both,

185

often times the brightness of the field is not as homogeneous as expected. In such cases, using a single threshold to determine the filler location would fail. Actually, the brighter intensity of one filler is only relative to its neighboring region. Hence, an adaptive threshold is necessary as the filter marches through the image. That is, the filter takes the input grayscale image I and outputs another image H in which the particle regions are highlighted. Mathematically it is defined as:

$$H(i, j) = \begin{cases} 1, & \text{if } I(i, j) = \max_{(u,v) \in B(i,j)} I(u,v) \\ 0, & \text{otherwise} \end{cases} \tag{1}$$

where $B(i, j)$ is a neighboring region around the position (i, j): $B(i,j) = (x, y; |x-i|<5, |y-j|<5)$.

In the image H, each particle is represented as an island of value 1. But it can be seen in Figure 10.1 that the islands do not always consist of a single point. Indeed, there are some very bright regions in the original image where the image intensity is all saturated. In the segmentation process, each of those regions is considered as a single particle. In order to identify different islands, a distinct label needs to be assigned to each of the islands. To this end, the connected components (CC) are computed in the H image and we denote the total number of CCs as M. Then, the center-of-mass (CoM) for each CC is computed. The M center points $c_1,...,c_M \subset R^2$ are the output of the filler identification process, which are shown in Figure 10.1(c).
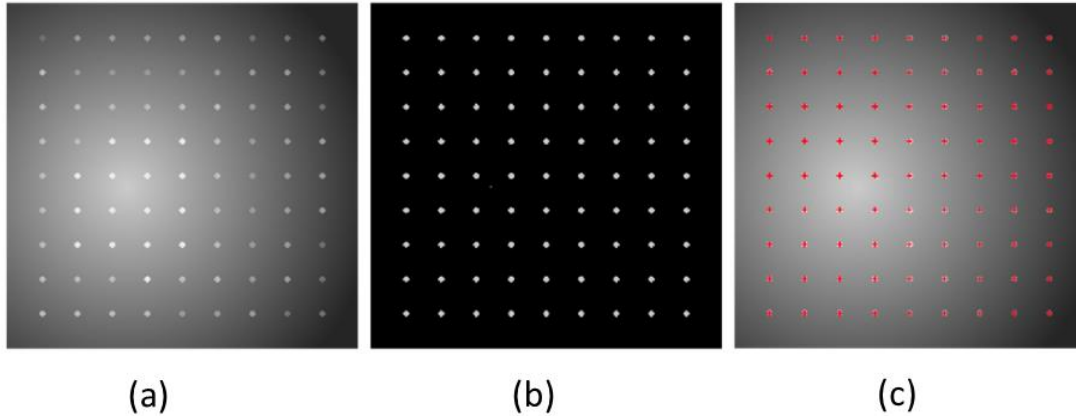
Figure 10.1 (a) the original synthetic image. (b) the binary image of extracted fillers. (c) identified fillers are shown as crosses in the image.

10.2.3 **Filler identification for high-aspect-ratio fillers**

The high-aspect-ratio fillers can be characterized by the Hessian of a gray-scale image. Mathematically, the image intensity can be regarded as a two-dimensional (2D) function $I(x, y)$. Furthermore, near the location (x, y), the function $I(x, y)$ can be written using the Taylor expansion as:

$$I(x+\Delta x, y+\Delta y) = I(x, y) + (\Delta x, \Delta y)\nabla I(x, y) + (\Delta x, \Delta y)H(x, y)\begin{pmatrix} \Delta x \\ \Delta y \end{pmatrix} \tag{2}$$

where $\nabla I(x, y)$ is the image gradient and $H(x, y)$ is the Hessian matrix. In this Taylor expansion, the eigenvalues of $H(x, y)$ at each point reveal the shape of the object around that pixel [354]. This is illustrated in Figure 10.2.

187
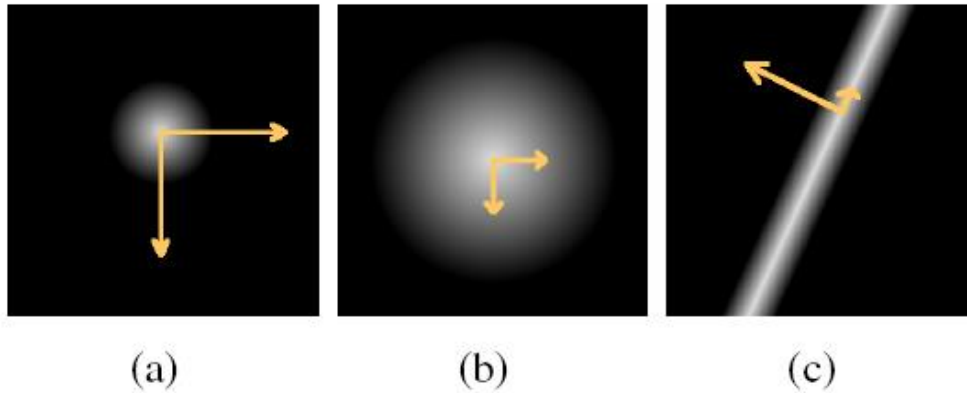
Figure 10.2 The intensity patterns and the eigen vectors of the Hessian matrix. The lengths of the vectors indicate the magnitudes of the eigen values. (a) Small bright blob in the image gives to two large eigen-values. (b) Large bright blob furnishes to two small eigen values. (c) Tubular shape corresponds to one large and one small eigen values.

It can be seen that a tubular object in the image may be characterized via a large eigenvalue and a small eigenvalue of the Hessian matrix, while a spherical shape gives rise to two eigenvalues of similar magnitude. Note that, although in the above examples that the objects are brighter than their surroundings, this discussion can be also applied to the case where objects are darker than the background by simply taking the absolute value of the eigenvalues. With this observation, an indicator function V for the tubular object is defined as:

$$V(x, y) = \exp(-\frac{\alpha\lambda_1^2}{\lambda_2^2})(1 - \exp(-\beta(\lambda_1^2 + \lambda_2^2)))$$

(3)

where λ_1 and λ_2 are the two eigenvalues at the position *(x, y)* with the order $|\lambda_1| \leq |\lambda_2|$. As a result, the closer the function value $V(x, y)$ is to 1, the more likely *(x, y)* is on a tubular shaped object in the image. Therefore, with such processing, the original intensity image *I(x, y)* is converted to a "tube measure image" *V (x, y)*. The filler regions in the image can then be obtained by thresholding the $V(x, y)$ function. In this work, the threshold is fixed at 0.2 for all the images and the performances are consistent.

188

Furthermore, the centerlines of the fillers are extracted by using the morphological thinning operator [355]. Essentially, the regions containing the fillers are 'eroded' until the remaining region has a width of one-pixel. In order to mitigate the variations resulting from the implementation, we use the morphological operation function bwmorph in Matlab®.

After these, the CNTs have been extracted and are represented as an image $B(x, y)$, with pixel values of zero or one. If $B(x, y) = 1$ for the position (x, y), it means at least one filler passing through this point, whereas $B(x, y) = 0$ indicates no filler is passing through.

In the step above, all the fillers in the $B(x, y)$ image have been identified. However, the $B(x, y)$ image only provides the information whether any filler passes through a certain pixel; it does not answer the question regarding which particular filler passes through this pixel location. In order to estimate the dispersion of the CNTs, we first identify each single filler in the $B(x, y)$ image computed above.

To answer this question, for each pixel in $B(x, y)$ with value 1, the 8 neighboring pixels are checked to see if they have value 1. If one neighboring pixel has value 1, then it is grouped with the original pixel as a connected component. This process repeats until no neighboring pixel has the value 1. As a result, all the pixels from the same filler are grouped into one connected component and pixels from different fillers form different connected components. After this step, we obtain an image $L(x, y)$ where pixels belonging to the same filler are marked with a label distinct from all the other fillers. Consequently, if we denote the total number of fillers in the image as M, then the location of the j-th filler in the image is given by pixels: (xi, yi) such that $L(xi, yi) = j$.

189

Consequently, in order to determine the spatial dispersion of the fillers, we take the CoM of each filler as the representative of its spatial location. That is, for the *j-th* filler, its CoM, *(uⱼ , vⱼ)*, is computed as the average position of all the pixel locations with the same label *j*. As a result, we totally have *M* CoMs *(u₁, v₁),…, (uₘ, vₘ)* representing the locations of the *M* fillers.

10.2.4 **Dispersion computation**

After the centers of the fillers having been identified, the fillers in the image are viewed as a random variable in the image field of the view. Specifically, all the center points $c_1,...,c_M \subset R^2$ are treated as *M* samples drawn from a random variable *S*. The more evenly the fillers are distributed, the more such a random variable *S* is similar to the uniform random variable, denoted as *U*. In order to estimate the PDF of *S*, the kernel density estimation method is used. The kernel density estimation is a widely used method to infer the PDF from samples in cases where no prior information of the PDF is available [356]. The PDF is computed as the sum of a series of kernels--usually Gaussian functions. More explicitly, the PDF for *S* is estimated as:

$$f(x) = \frac{1}{M} \sum_{i=1}^{M} \frac{1}{\sqrt{2\pi}\sigma} e^{-\frac{(x-c_i)^2}{2\sigma^2}}$$ (4)

where the standard deviation of the kernel σ is computed with the method proposed in [357].

Then the discrepancy between the PDF obtained and that of the uniform random variable is computed by measuring the L_2 distance between them (In the area of functional analysis, the L_2 distance is one of the most widely used distance for measuring the discrepancy between two functions [358].):

190

$$d(f,g) = \left(\int (f(x) - g(x))^2 \, dx \right)^{\frac{1}{2}} \qquad\qquad (5)$$

where we have *g(x)=1/(area of the image)*, to represent a random variable

uniformly distributed on the image area. While the Euclidean distance defines the

distance between two points apart in space, the above defined L_2 distance gives such a

"distance" between two functions. Many previous analyses investigated certain aspects of

the distribution of the fillers [343, 348, 349, 359], however, either the analysis stops at

providing the distribution histograms which need further human assessment, or the final

dispersion index is computed through some heuristics. Contrastingly, with the L_2 distance,

we give a mathematically more rigorous framework that outputs a single value to

measure the discrepancy between the fillers in the current image with the ideal uniform

distribution. Its capability and benefit will be shown in the next section for both the

synthetic and real images. Intuitively, when centers of the fillers, $c_1,...,c_M$ are distributed

evenly, its corresponding random variable S is more likely to be close to uniform

distribution and thus the L_2 distance d is close to 0. On the contrary, the more non-

uniform the fillers spread, the larger d will be obtained. The MATLAB® code to perform

the above computation can be downloaded from the following website:

http://tinyurl.com/autodispersion.

10.2.5 **Orientation computation for high-aspect-ratio fillers**

In addition to the spatial dispersion, the orientations of high-aspect-ratio fillers

such as CNTs also play an important role in determining various properties of the

composites. In order to estimate the orientation of fillers, we first identify each single

filler in the *B(x; y)* image. This can be achieved from the label image *L(x; y)* computed

191

above. In *L(x; y)*, the pixels in the same filler are given the same label, whereas different fillers have different labels.

Then, for each filler, the pixel locations of this filler are extracted and a line section is fitted to them. Mathematically this is a linear regression problem: denote the points in the *j-th* filler as *{(x$_i$; $_{yi}$) : i = 1,…, Nj}*. Then, we find the slope *k$_j$* and intercept *b$_j$* (the intercept is not used for the orientation estimation) for the *j-th* filler with the minimum fitting error *E$_j$*:

$$E_j(k_j, b_j) = \sum_{i=1}^{N_j} (k_j x_j + b_j - y_j)^2$$

(6)

Then, naturally, the angle *θ$_j$* of this filler is

$$\theta_j = \tan^{-1}(k_j)$$

(7)

After the orientation angle for each filler is computed, we get an array of angles *θ$_i$; i = 1,…, M*. The histogram of the distribution of the *θ$_i$*'s is then computed, which gives the distribution of the filler orientations. This distribution clearly shows which angles the majority of fillers are aligned at. In the meantime, a further step can be performed to give a more quantitative analysis in a similar fashion as those in the dispersion analysis. The different angles of fillers in an image can be viewed as the realizations of a random variable A. By comparing it with a uniform distribution on the range of -90° to 90°, we give a single-valued index for the orientation distribution of the fillers. Again, the closer the obtained orientation index is to zero, the more randomly the fillers are oriented. In contrast, a larger orientation index suggests alignment of fillers in the matrix.

10.3 Results and discussion

10.3.1 Filler identification at inhomogeneous background

Figure 10.3 (a) is a synthetic image with inhomogeneous background and Figure 10.3 (b) shows the fillers extracted by using the local information based adaptive method. As a comparison, the single threshold method is also tested (Figure 10.3 (c) and (d)). As can be observed, it is very difficult, if not impossible, to find a suitable global threshold to characterize all the spots. In Figure 10.3 (c), a global threshold at 150 is able to identify about two thirds of the spots; however a large region around the center region is erroneously included because of the brighter background there. Similarly, a higher threshold at 200 helps differentiate the spots near the center, but misses too many relatively darker spots around the image boundary, as shown in Figure 10.3 (d).

(a)   (b)   (c)   (d)
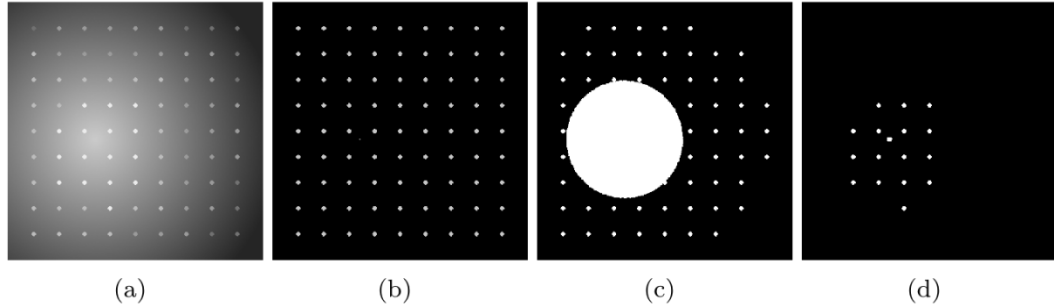
Figure 10.3 An example demonstrating using a local threshold versus a global threshold for extracting filler. (a) the original (synthetic) image. (b) the binary image for extracted fillers using the local threshold. (c) the binary image for extracted fillers using a single threshold at 150. (d) the binary image for extracted fillers using a single threshold at 200.

Since filler identification using a global threshold will probably miss or add some fillers in the image, these artifacts in the identification process will further lead to inaccurate assessment in the dispersion analysis. In Figure 10.4 (a), 1024 particles are uniformly dispersed in the 1000×1000 grid; the corresponding dispersion index is 0.33.

When randomly taking away 10%, 20%, 40% to 60% of the total number of particles, the dispersion index increases almost linearly and the corresponding dispersion index is 0.49, 0.65, 1.05 and 1.38, respectively. Similarly, introducing extra particles will also increase the dispersion index, indicating a non-uniform distribution. Although the effect of missing or adding particles on the ultimate dispersion assessment shown in this example seems trivial when comparing with the effect of real aggregations shown later, this effect can become significant in real cases. This is because in the synthetic images, the removal and addition of particles is still random, whereas missing or adding particles caused by manual counting or by using universal threshold is caused by brightness difference and is probably not random any more.
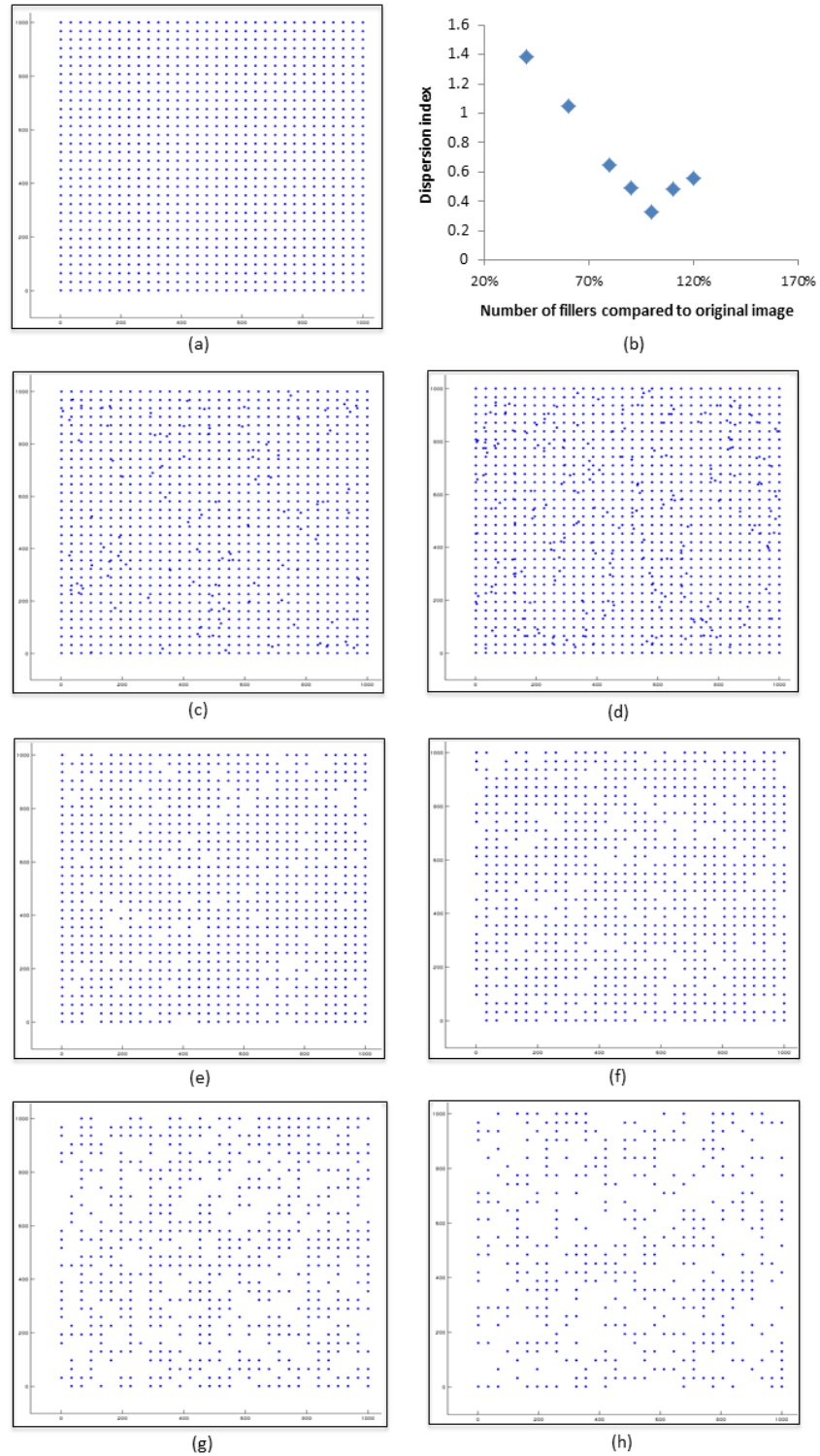
Figure 10.4 (a) The original uniform dispersion is composed of 1024 particles in a 1000×1000 grid. The effect of adding (c) 10%, (d) 20% or missing (e) 10%, (f) 20%, (g) 40%, (h) 60% random particles to the original image. (b) the corresponding dispersion index of each image.

Having illustrated the filler identification for synthetic images, we show an example on a SEM image of CB/SR in Figure 10.5, where CB fillers can be clearly identified even with a non-homogenous background.
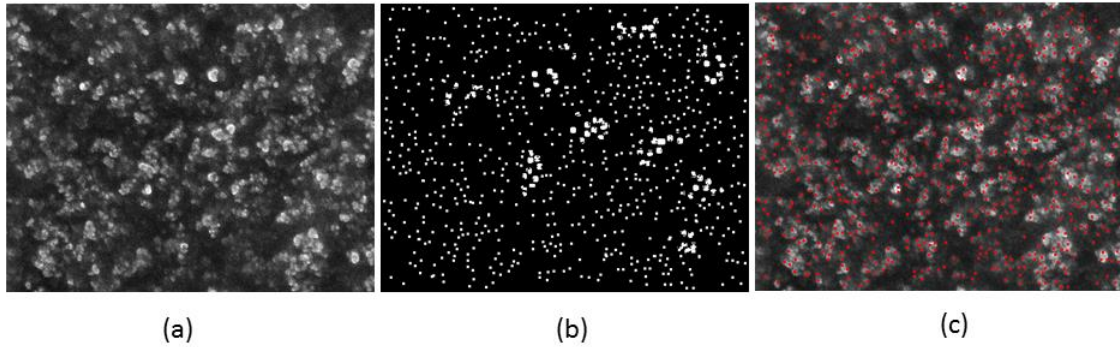
Figure 10.5 Filler identification for CB. (a) original SEM image. (b) the output image H. (c) final extraction result for the centers of fillers (CB).

10.3.2 Synthetic samples with particulate fillers

10.3.2.1 Verification of the present dispersion analysis

To test the developed dispersion assessment method, a series of images were generated to simulate the situation of real images of the polymer composites. Since an ideal dispersion of fillers usually includes both the randomness at both global and local levels, we synthesized three sets of images to represent the effect of dispersion locally (Figure 10.6), globally (Figure 10.7), and a combination of both (Figure 10.8), respectively. In each set, four cases with different levels of filler dispersion are shown. In particular, in order to more faithfully represent the real photos, we made the background of these images with highly inhomogeneous brightness.

In Figure 10.6, the fillers are distributed in a rectangular grid. The differences among Figure 10.6(a), (d), (g) and (j) lie in the degree of the local uniformity. In the middle column, the identified fillers are represented by red markers. Although the

196

background of the images is very inhomogeneous, the synthetic fillers are correctly identified. After that, the right column shows the estimated PDFs obtained from the identified fillers. Such density functions are then compared with the uniform distribution to determine the level of dispersion. Similar experiments are conducted to show the effect of dispersion globally in Figure 10.7 and a more general case in Figure 10.8. Figure 10.9 shows the quantified results of all the 12 cases that the dispersion indices increase monotonically as the dispersion gradually gets worse. The dispersion index can provide sensitive response to the dispersion status of fillers at both local and global levels, while the failure of random dispersion in both levels can give rise to an even larger dispersion index. The results are consistent with visual assessment, confirming its applicability to composites with different dispersion states.
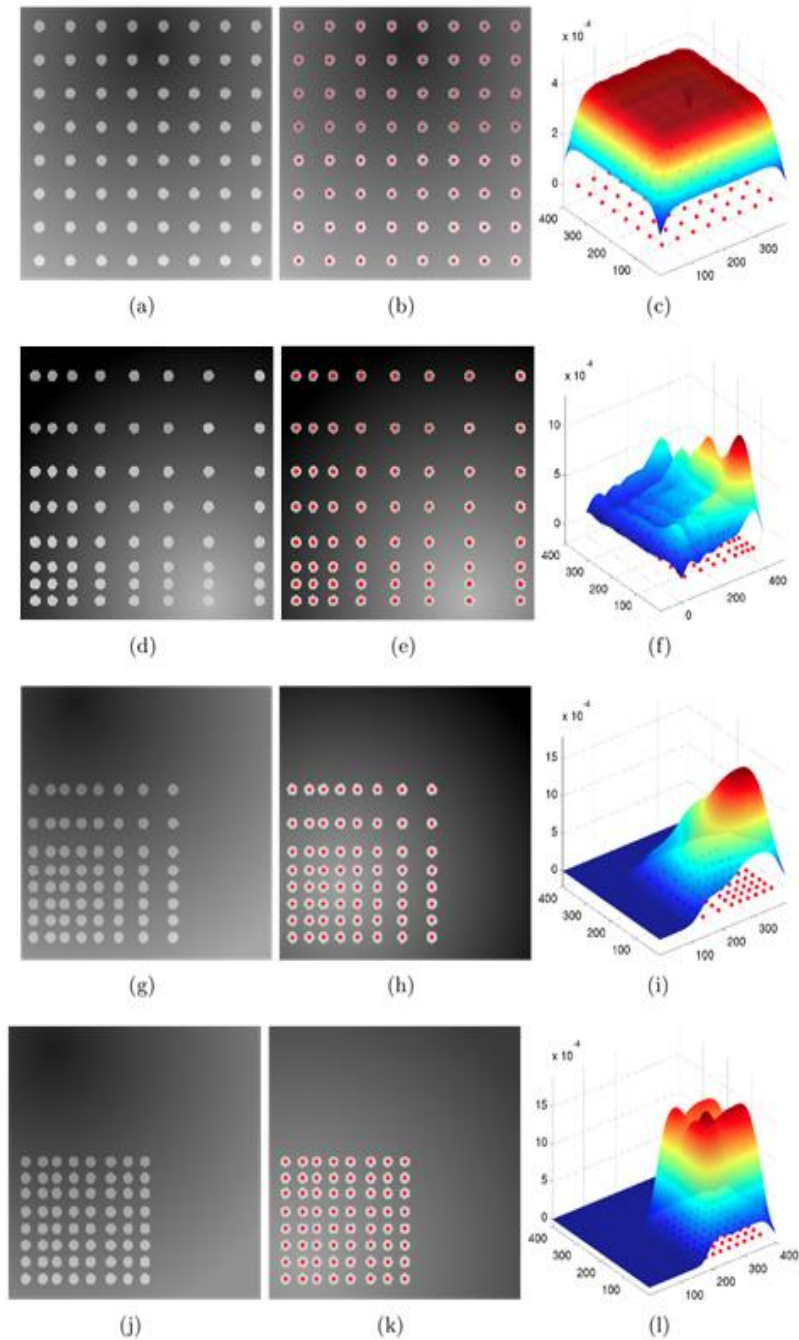
Figure 10.6 The first set of synthetic images, illustrating the effect of local dispersion. The left column (a,d,g,j) shows four synthetic images. In the middle column (b,e,h,k), the fillers are identified and are represented as red markers. The right column (c,f,i,l) shows the estimated PDFs obtained from the identified fillers, which is to be compared with uniform density function to assess the dispersion. From the top row to the bottom row, the dispersion is getting worse locally.
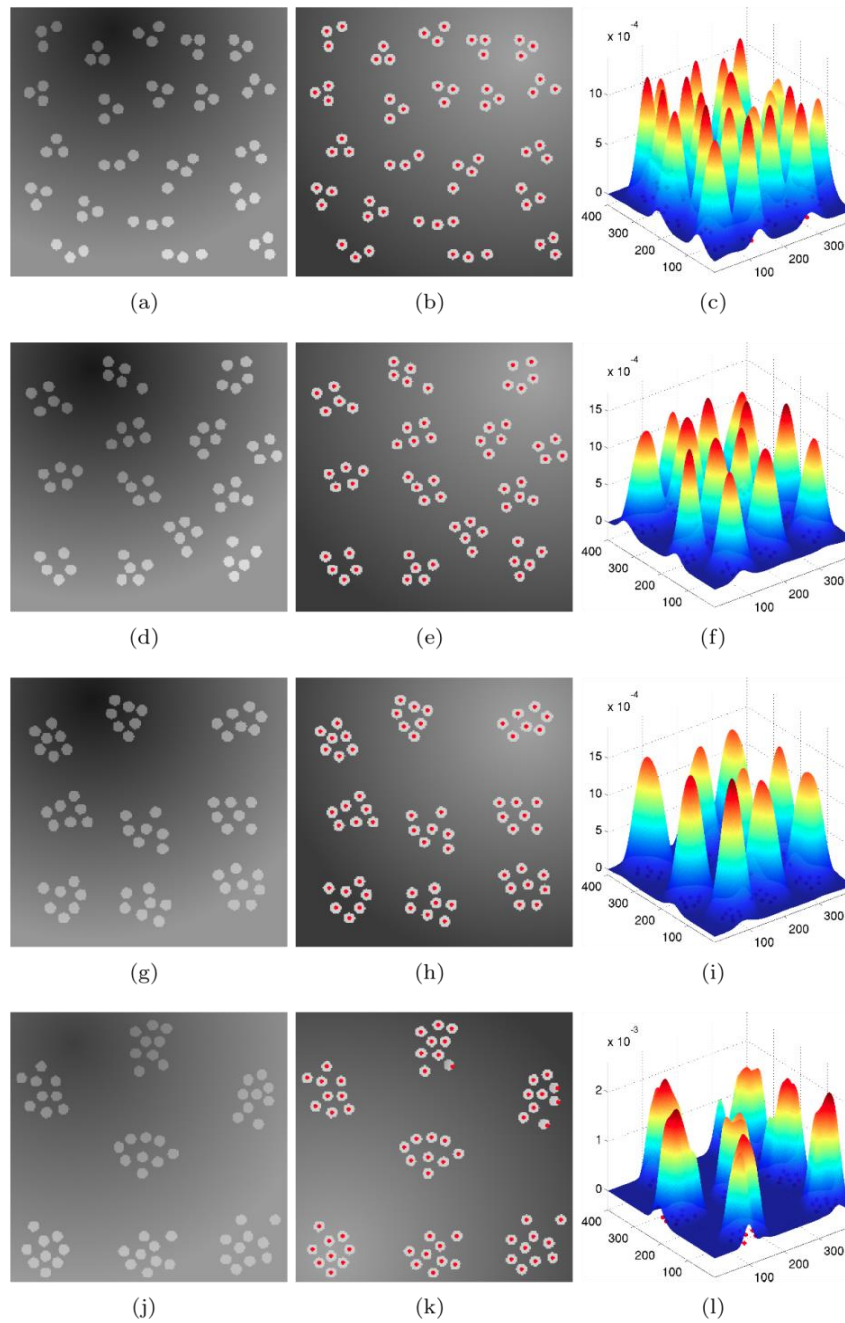
Figure 10.7 The second set of synthetic images, illustrating the effect of global dispersion. The left column (a,d,g,j) shows four synthetic images. In the middle column (b,e,h,k), the fillers are identified and are represented as red markers. The right column (c,f,i,l) shows the estimated PDFs obtained from the identified fillers. From the top row to the bottom row, the dispersion is getting worse globally.

199
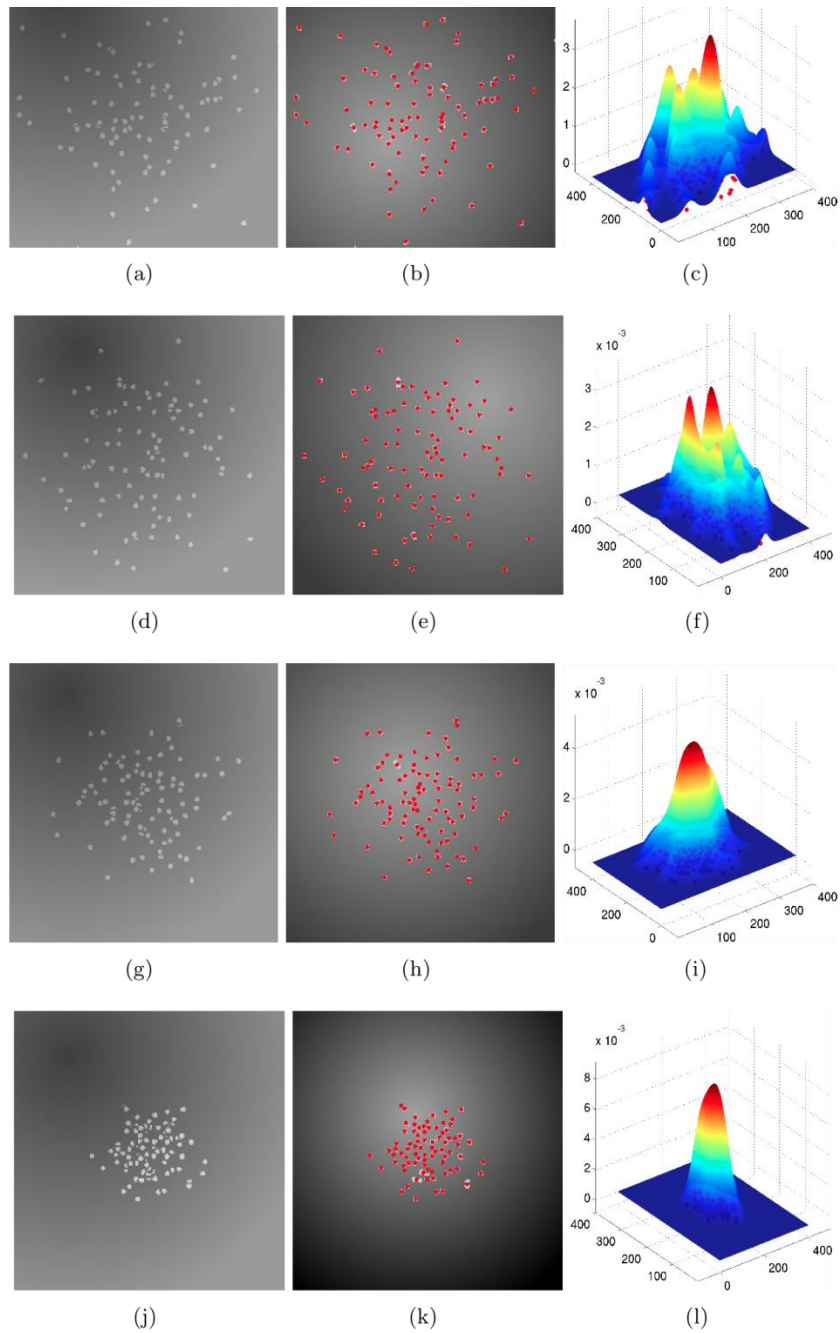
Figure 10.8 The third set of testing images, illustrating the effects of the combination of local and global dispersion. The left column (a,d,g,j) shows four synthetic images. In the middle column (b,e,h,k), the fillers are identified and are represented as red markers. The right column (c,f,i,l) shows the estimated PDFs obtained from the identified fillers.

200
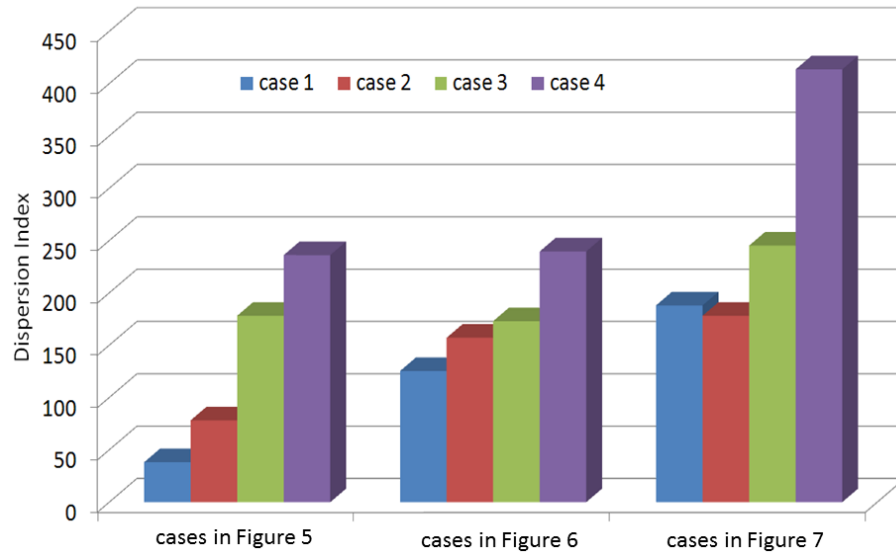
Figure 10.9 Dispersion measurements for all the 12 cases in Figure 10.6, Figure 10.7 and Figure 10.8.

10.3.2.2 Sensitivity to particle size

One of the drawbacks of many previously developed filler dispersion analyses is that they are unable to identify the effect of particle size, because these methods are established on the comparison of sample images against a "uniform distribution" that is independent of any measurement of the density of dispersion [343]. This limits their application in predicting the mechanical properties of composites, which is very sensitive to the particle size [312]; Moreover, these methods would also be incompetent to provide the information of the agglomeration of the particles. To solve this problem, Burris et al. utilized the distance between neighboring particles as the computation metric [343]. In a constant filler loading, the smaller particle size means larger numbers of particles (i.e. larger density of particles) and thus a smaller interparticle distance. In our case, since we are using the PDF, the smaller particle size will directly be reflected in the density of particles. That is, our method is able to recognize the difference of particle size. To illustrate this, two images (Figure 10.10 (a) and (d)) with an identical filler loading but

201

different particle sizes are compared. Although both the cases display a perfectly uniform

distribution, larger particles form individual density peaks in the PDF while smaller

particles construct a more flat and continuous PDF. Therefore, the obtained dispersion

index is 56.74 of larger particles and 16.27 for smaller particles, indicating a better

"dispersion" in the case of smaller particle sizes. This will correspond to the real case that

breaking up agglomerates during processing renders a smaller particle size and better

dispersion.
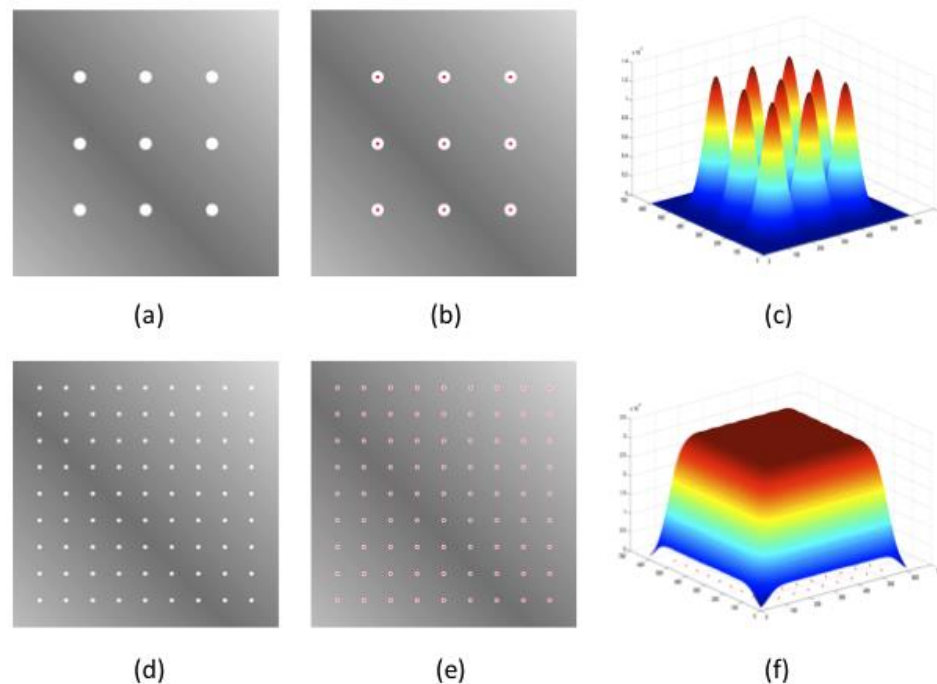
Figure 10.10 Effect of particle size on the dispersion index. The two synthetic images (a)
and (d) have the same filler loading but different filler size. The filler size in (d) is 1/3 of
that in (a). The middle column (b, e) shows the identified fillers in each image and the
right column (c, f) shows the PDF of fillers in each image, respectively.

10.3.3 Synthetic samples with high-aspect-ratio fillers

Figure 10.11 shows the results of the proposed method applied to synthetic

images. Four synthetic images are generated to represent four different situations: (1)

uniform dispersion and alignment (Figure 10.11 (a)); (2) uniform dispersion and random

202

orientation (Figure 10.11 (e)); (3) non-uniform dispersion and alignment (Figure 10.11 (i)); (4) non-uniform dispersion and random orientation (Figure 10.11 (m)). Specifically, in Figure 10.11 (a) and (e), the fillers are placed on a uniform grid whereas in Figure 10.11 (i) and (m), the fillers are made to concentrate in the top-left 2/3 corner. On the other hand, the orientations of the fillers in Figure 10.11 (a) and (i) are controlled to be normally distributed around 30° with a standard deviation of 10°. In contrast, the filler orientations in Figure 10.11 (f) and (n) are uniformly distributed from -60° to 60°. In all of the cases, the intensity of the background is simulated to vary gradually to mimic the inhomogeneous background present in real images. The method identifies the fillers in the synthetic images, which are shown in red color in the second column. As can be seen, in spite of severe background inhomogeneity, all the fillers can be correctly identified. The third column shows the dispersion density function with the dispersion indices on the top-right corner. From this, it is verified that the dispersion index correctly characterizes the spatial dispersion of the fillers. That is, the more uniformly the fillers are distributed, the smaller the dispersion index is. Finally, in the fourth column, the distribution of the filler orientations and their orientation indices are displayed. The alignment can be easily identified by the much larger orientation index.
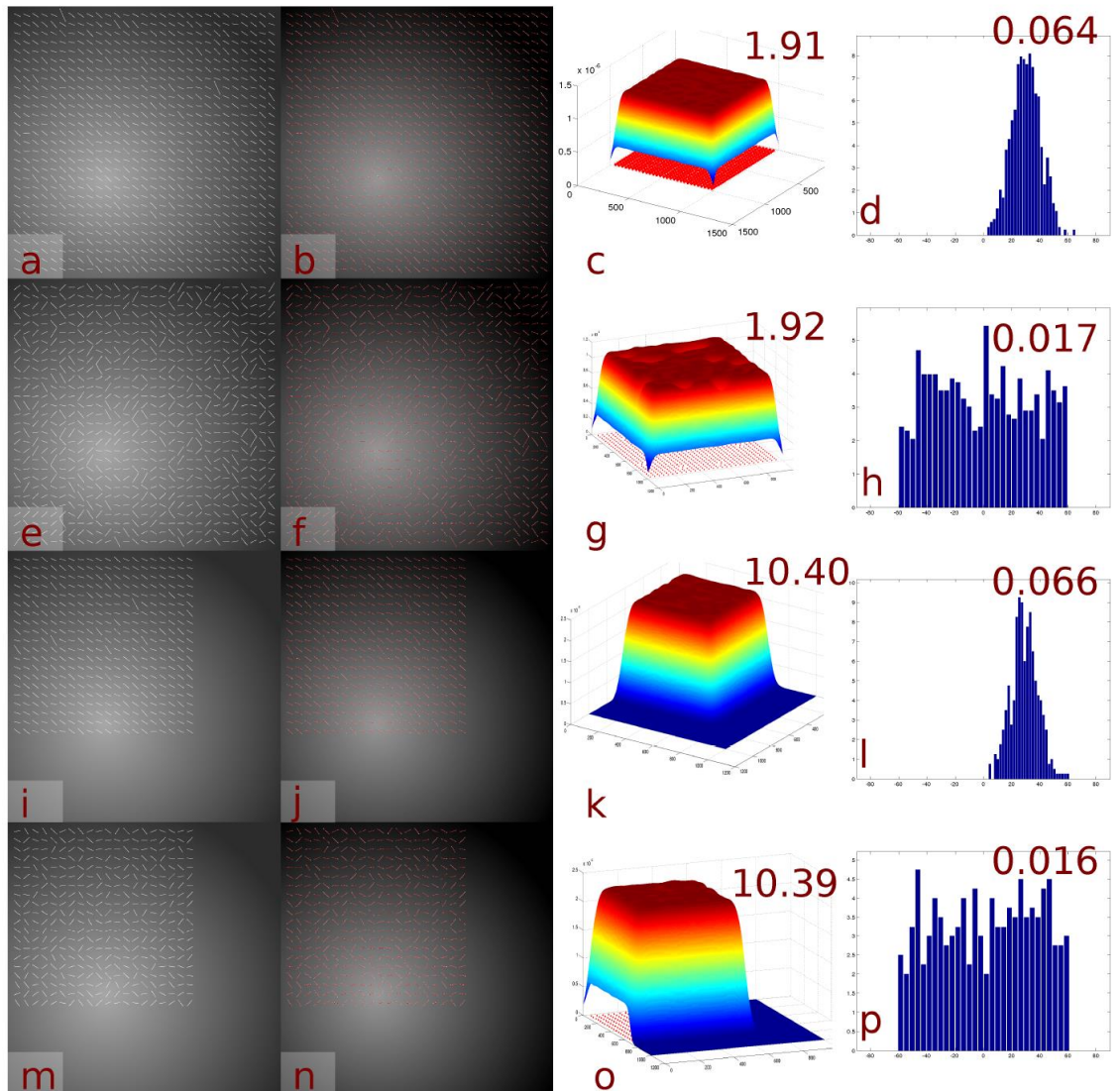
Figure 10.11 Test on synthetic images. First column: four synthetic images. Second column: identified CNTs in red. Third column: CNT dispersion density functions and the dispersion index. Fourth column: the CNT orientation distribution and orientation index. See text for detail.

10.3.4 **Application to real composite systems – CB/SR composites**

Besides the synthetic images, CB/SR is used as a model compound to validate the developed dispersion assessment method. With the help of the dispersion index, we aim at selecting the best processing methods among the three and also elucidate the dispersion

204

as a function of mixing intensity. In the meanwhile, the mechanical properties of all samples are measured to correlate with the dispersion index.

Figure 10.12 shows the typical cross-sections of the samples processed by three-roll mill at different mixing intensities. Compared to the simplified synthetic images, it is even more difficult to manually pick out all the CB fillers from these real images. Thus it is necessary to utilize the automatic filler identification and dispersion analysis for the real cases. The dispersion indices obtained from the developed method are shown in Figure 10.13. For all three processing methods, there is a general trend that the dispersion index decreases with a longer mixing time. This is intuitively understandable since a longer mixing time would result in better filler dispersion. A comparison among the three mixing methods clearly shows that the sequence of dispersion efficiency is ultrasonication > three-roll mill > high shear blending. The dispersion index of ultrasonication for 0 hour is lower than any roll mill or high shear blending samples, suggesting that even without any further mixing after combining CB and dissolved SR together, the pre-dispersion of CB in solvent is already efficient enough to give a good dispersion in the final composite. In contrast, high shear blending is not able to break down CB aggregate in solvent in the premixing stage, therefore fails to obtain a good dispersion of the composite. In the case of three-roll mill, the breakdown process is facilitated by the large shear force during roll milling as well as the gel formation in the interface between SR and CB [360]. Hence, the dispersion efficiency of three-roll mill is better than that of high shear blending but inferior to that of ultrasonication.

The storage modulus at a frequency of 0.01 Hz and 50 ^{o}C well corresponds to the dispersion index results (Figure 10.14). Because ultrasonication is able to break down the

205

aggregation of CB and leads to a good dispersion, the storage modulus of ultrasonicated samples is almost 50% higher than those made by the other two methods. For each individual processing method, a slight increase can be observed of high shear blending samples and three-roll mill samples in the first 400 cycles, while this trend is not very obvious for the ultrasonication samples. The sudden drop of storage modulus after 400 rolling cycles in the three-roll mill processing probably results from the degradation of polymer chains of the fierce mechanical mastication [361].

Overall, the ultrasonication shows the best dispersion and thus the best mechanical properties among the three processing methods. The dispersion indices can well represent the efficiencies in dispersion and can also be used to predict the mechanical properties of nanocomposites when no interfering factors such as polymer degradation exist.
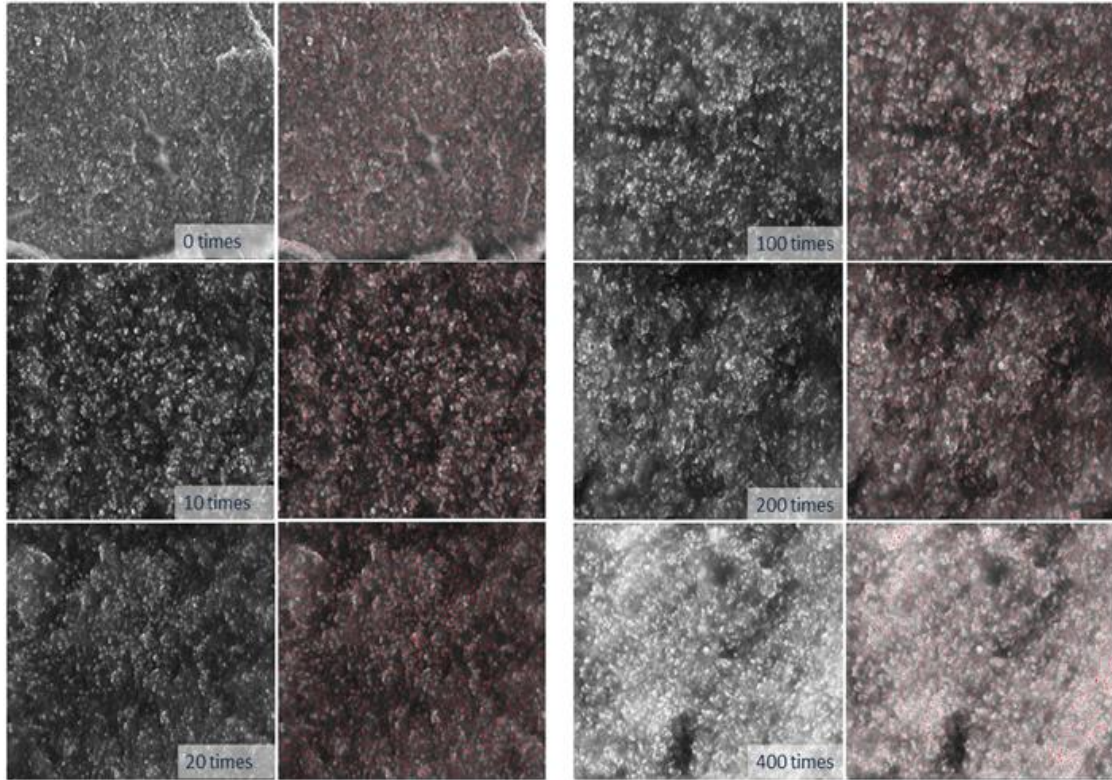
Figure 10.12 The images before and after filler identification of the samples processed by three roll milling. The inset textboxes show the number of cycles that the composites pass through the roll mill.
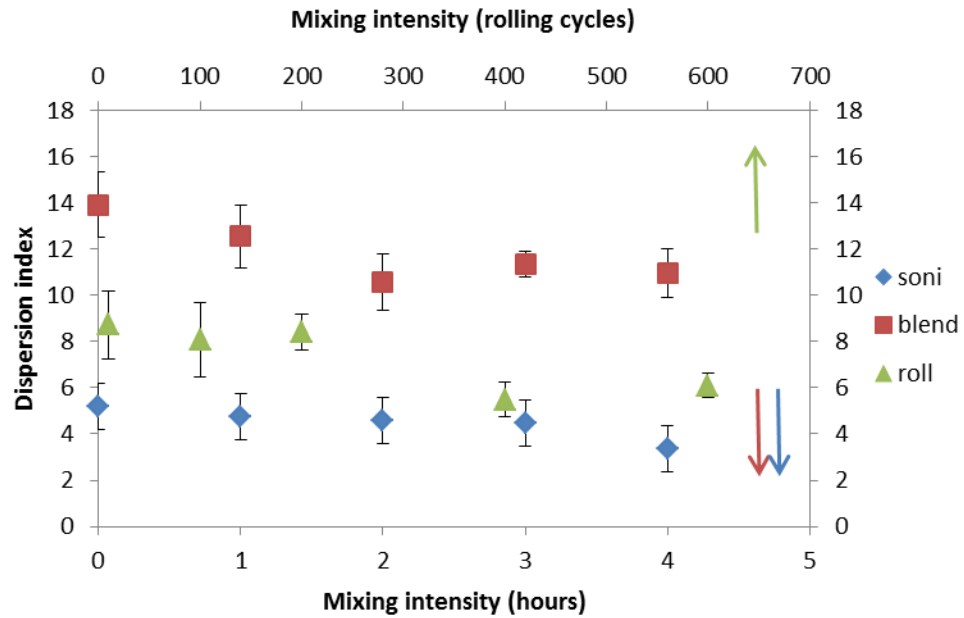
Figure 10.13 The computed dispersion index of samples processed by different methods and at different mixing intensity.
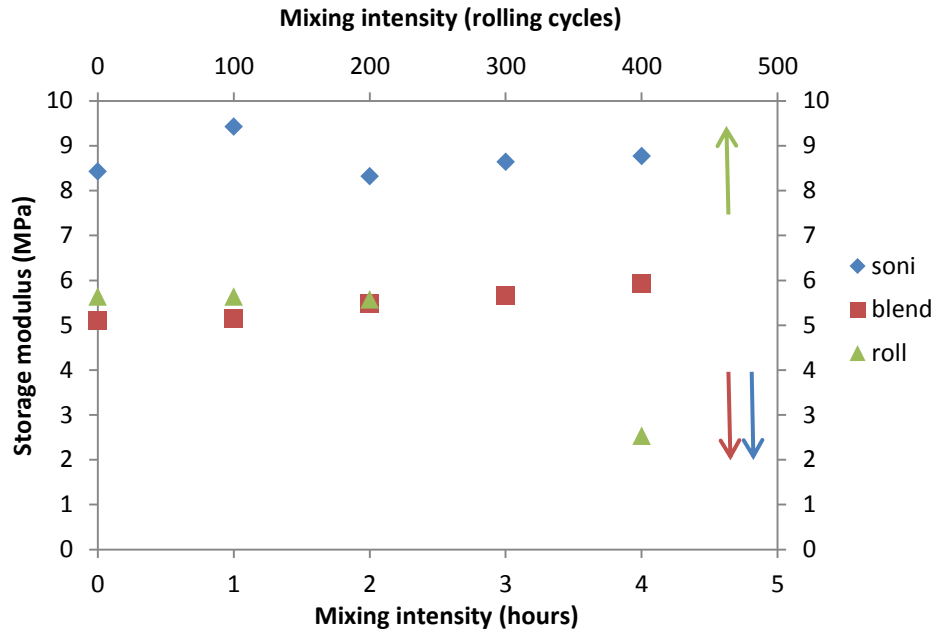
Figure 10.14 The storage modulus of samples processed by different methods and at different mixing intensity.

10.3.5 **Application to real composite systems – CNT/SR composites**

10.3.5.1 <u>Verification of the present dispersion and orientation analysis</u>

In addition to synthetic images, the proposed technique was applied to a total of 81 SEM images of model compounds. These images include compounds prepared with different conditions and observed at different magnifications. As shown in Figure 10.15, the CNTs are extracted from the images and marked as red threads. The figures show that our method works robustly for various magnifications from 7k to 20k.
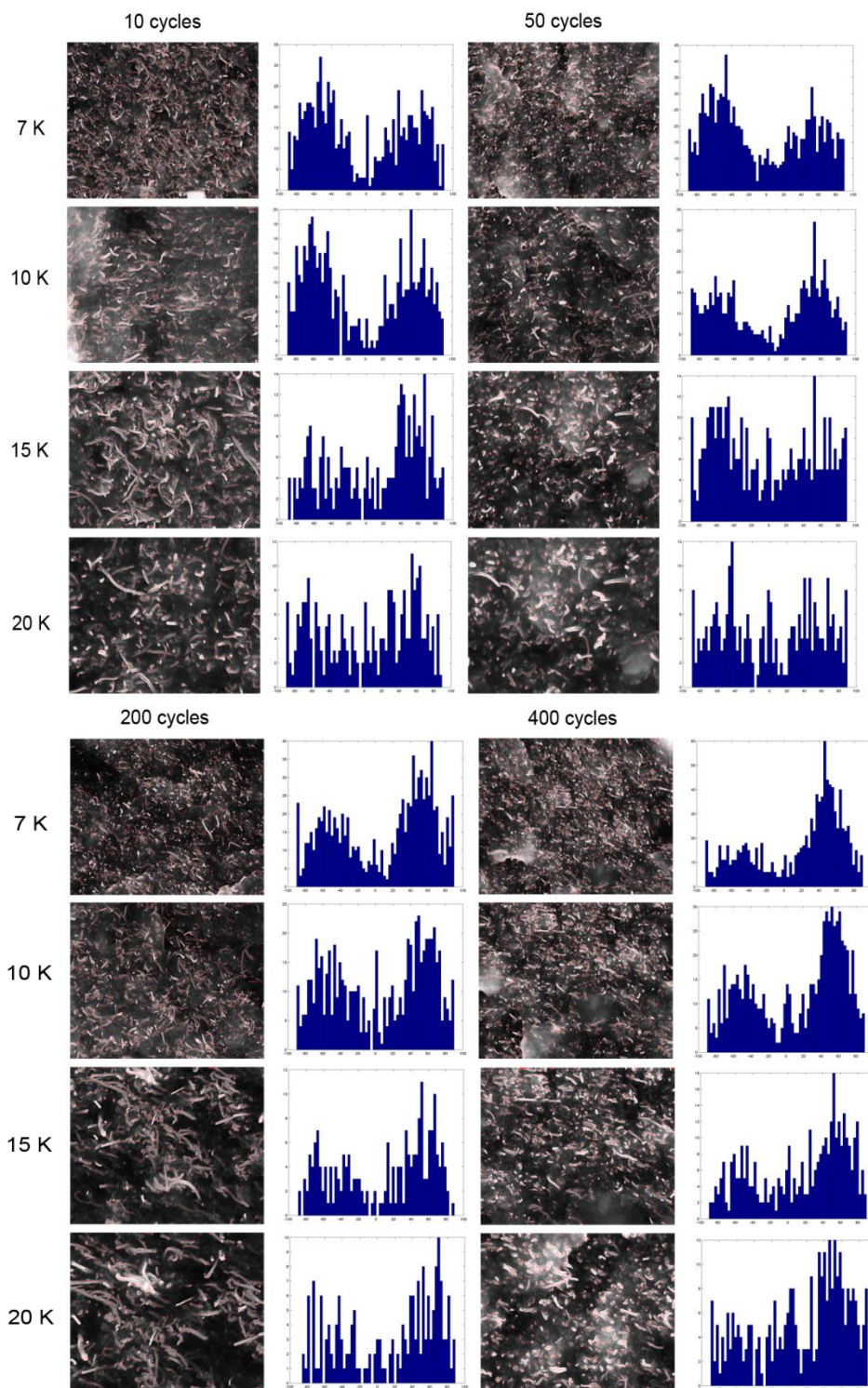
Figure 10.15 The extraction of the CNT in the SEM images of model compounds prepared at various mixing intensity. The red threads in the images indicate the CNT identified by the proposed algorithm. The identification algorithm works well for various magnifications from 7K to 20K.

To test the accuracy of the dispersion analysis, the images of one well-dispersed composite sample (Figure 10.16(a)) and one barely dispersed sample (Figure 10.16 (d)) were analyzed using the proposed dispersion index. Despite the same filler concentration, in Figure 10.16 (d), the CNTs were seriously agglomerated, leaving some blank polymer part; in contrast, the good dispersion in Figure 10.16 (a) was illustrated by the even dispersion of CNTs over the whole field of view. The calculated dispersion index of Figure 10.16 (a) is 5.32 while the dispersion index of Figure 10.16 (d) is 15.70, which agrees well with the visual observation. Therefore, the dispersion index reasonably represents real dispersion situations.
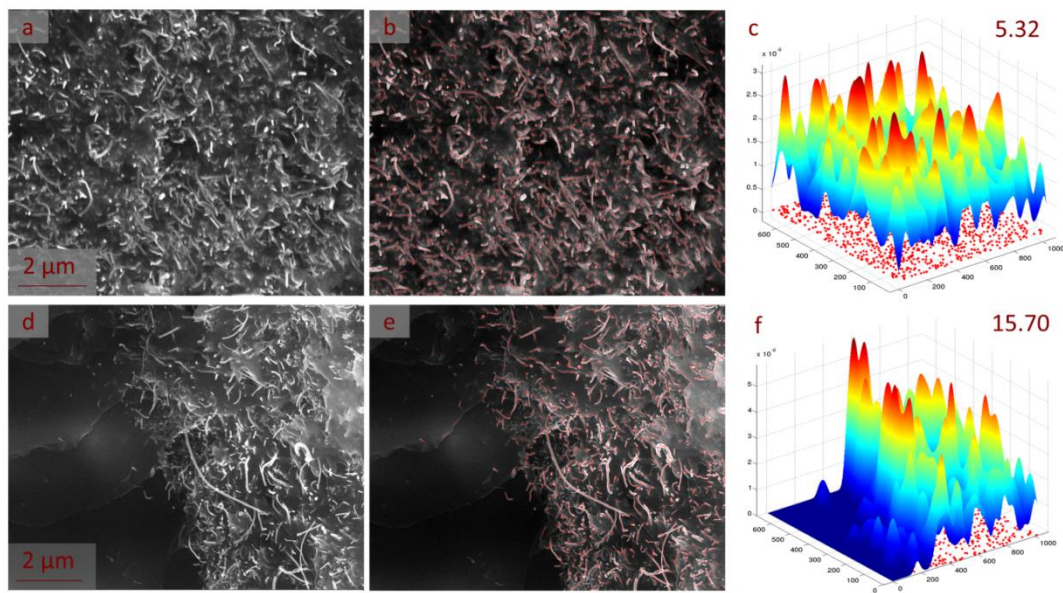
Figure 10.16 Validation of the dispersion analysis by comparing the dispersion of two CNT/SR composites. (a) The original image of a well-mixed sample. (b) Identification of the CNTs in the image of (a). (c) The PDF of the image in (a). The inserted number is the calculated dispersion index. (d) The original image of a barely dispersed sample. (e) Identification of CNTs in the image of (d). (f) The PDF of the image in (d). The inserted numbers represent the dispersion index.

Similarly to the dispersion analysis verification, two extreme cases of orientation, namely a VACNT-based composite and a random CNT-based composite were used to

show the effectiveness of the orientation index. Figure 10.17 shows the images of the two

samples and the histogram of their statistic distribution at different directions. The

calculated orientation of VACNT based is 0.065 and that of the random CNT-based

composite is 0.04. The VACNT orientation index is much larger than the random CNTs,

which well represents the orientations of the two samples.
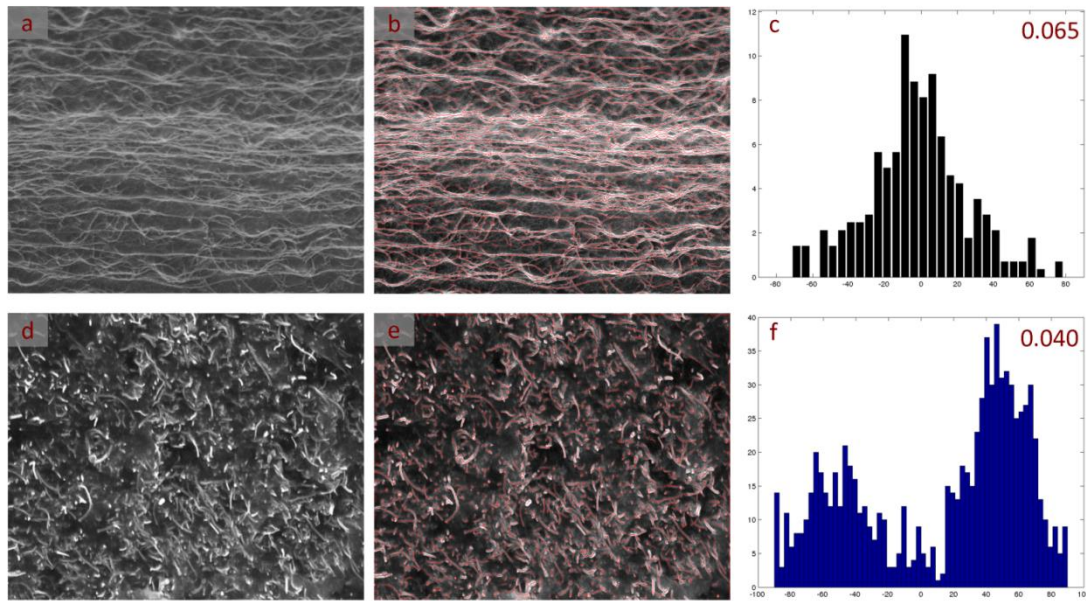
Figure 10.17 Validation of the orientation analysis by comparing the dispersion of two
CNT/SR composites. (a) The original image of a VACNT/SR sample. (b) Identification
of the CNTs in the image of (a). (c) The histogram of the orientation distribution of
image in (a). The inserted number is the calculated orientation index. (d) The original
image of a random CNT/SR sample. (e) Identification of CNTs in the image of (d). (f)
The PDF of the image in (d). The inserted number is the calculated the dispersion index.

10.3.5.2 <u>Structure-properties relationship of the model compounds</u>

After validating the proposed dispersion and orientation methodology, we now

consider a model compound prepared with different mixing intensities.

Figure 10.18(a) shows the calculated dispersion indices as a function of rolling

intensity. A significant decrease of dispersion index occurs in the first five rolling cycles,

indicating a substantial improvement of dispersion at the beginning. Further rolling did

not show a significant effect, as the slightly increased dispersion index may result from the statistical fluctuation of data. A final dispersion index as low as 6.78 can be achieved after intensive mixing of 400 rolling cycles. The general trend of a decreasing dispersion index with mixing agrees with our/common observation that a longer mixing time would result in better filler dispersion. A detailed analysis of the decreasing rate determines that 5–10 rolling cycles are enough for a good dispersion, which makes it possible to avoid the damage to the polymer chain or CNT fillers induced by fierce mechanical manipulation.
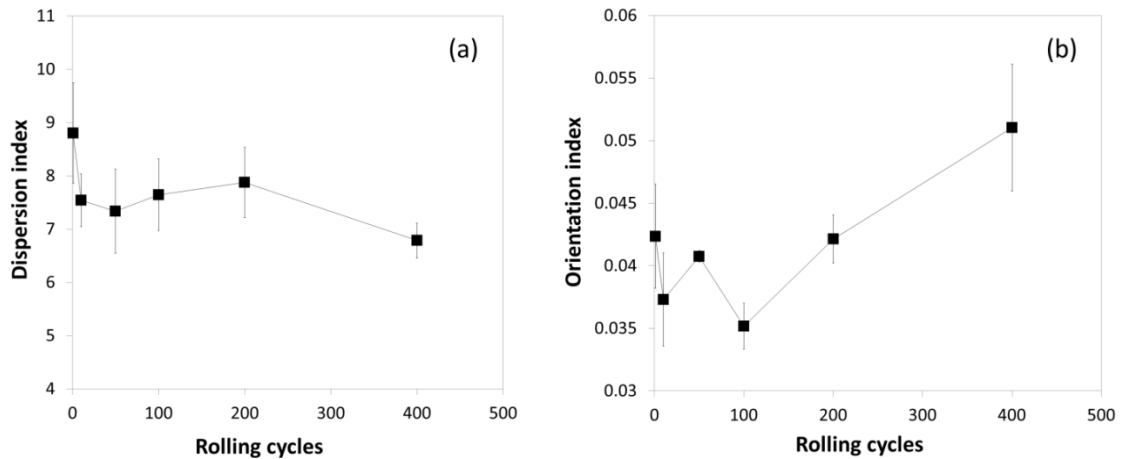
Figure 10.18   The calculated (a) dispersion indices and (b) orientation indices of CNT/SR composites prepared at different rolling cycles.

Due to the insufficient filler identification technique, only a few previous studies are able to characterize both the CNT dispersion and orientation analysis [348]. In our algorithm, the orientation index can be obtained simultaneously with the dispersion index, as shown in Figure 10.18(b). The first 5 rolling cycles also contribute to the randomization of orientation of CNTs, as indicated by the decreased orientation index. However, after 100 cycles, the substantial increase in the orientation index was observed,

suggesting the alignment of CNTs by the strong and consistent shear force from the roll milling.

After the dispersion and orientation indices of samples prepared with various mixing intensities are obtained, they may be used to predict the properties of the obtained composites. In the present study, the electrical properties were measured as an example.

Due to the high-aspect-ratio and possible alignment in the premixing stage, all the obtained composites show anisotropic properties. As shown in Figure 10.19, the resistivity measured in direction 1 is at least one order of magnitude smaller than the resistivity measured in direction 2. Therefore, direction 1 is more likely the direction in which the CNTs are aligned. The resistivity ratio further decreases with rolling cycles, especially after 100 cycles. This may result from the CNT alignment by shear forces during rolling as demonstrated by the orientation index analysis [362]. In addition, it is found that the standard deviation of resistivity ratio decreases with rolling cycles: the standard deviation is 0.04 without rolling while after 50 cycles, it is lower than 0.004. It is assumed that a better dispersion by intensive mixing is one important contributor to the reduced deviation. According to the dispersion index analysis, the dispersion improves with longer mixing time. A better dispersion quality could enhance the reproducibility and reduce the variation between parallel specimens. Therefore, after 50 cycles, the standard deviation is dramatically reduced. Above all, using the proposed image analysis technique, one can fully disclose the distribution and morphology of CNT fillers in the composites, which will be very useful to explain and predict various properties of the composites.

213
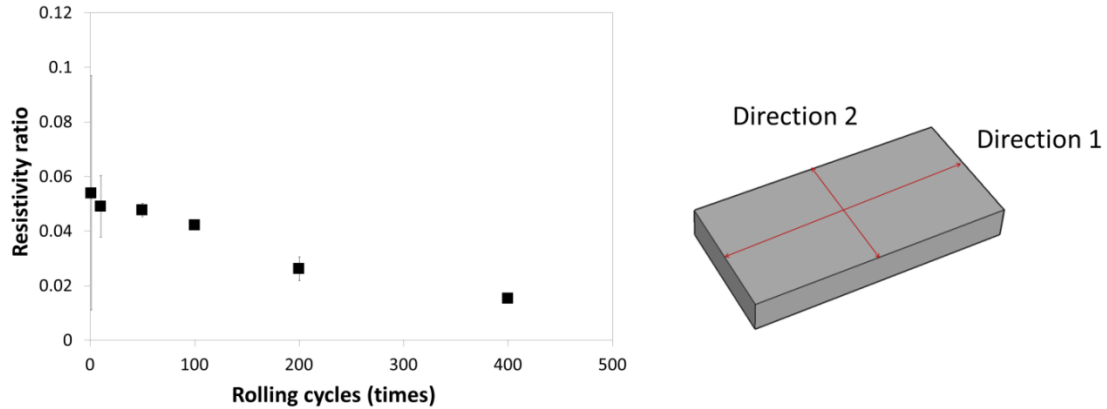
Figure 10.19 The ratio of the resistivity measured at direction 1 over the resistivity measured at direction 2.

10.3.5.3 Discussion on the CNT orientation.

Sometimes CNTs exhibit wavy or curved shape in the composite. This can be seen in both the original images and the detected CNTs in Figure 10.15 to Figure 10.17. However, during the quantitative correlation between orientation of CNTs and the material properties, one has to define a certain value to represent the orientation of the curved CNT. To solve this problem, in this work we use the line fitting technique which find the 'major axis direction' of the curved CNT, the distribution of which has been correlated with the rolling cycles and electrical properties. Nevertheless, it is also realized that in some cases the 'major axis direction' may have some limitations. For example, it was found that the reinforcement in CNT/rubber composites is strongly dependent on the persistence length; i.e., the more straight shape CNTs exhibit, the higher the persistence length and the better reinforcement [363]. When we use the major axis direction to represent each CNT in the orientation analysis, we lose the information of how tortuous the CNTs are. Therefore, we are unable to correlate the mechanical properties change

214

induced by the persistence length evolution with the current dispersion and orientation analysis.

One possible solution to this problem is to further utilize the wellness of the fitting: when finding the major direction using line fitting, we can measure the wellness of such fitting. The more tortuous a CNT is, the worse it can be fit by a line. Therefore, by measuring quantities such as R^2 coefficients, such wellness can be estimated. Consequently, for those highly tortuous CNTs, either a scheme similar to [363] can be adopted by cutting the CNTs to smaller but more linear section; or we can use higher order polynomial to model the shapes of the CNTs. Evidently, such analysis will lose the concept of 'orientation'. Therefore, a combination of the orientation analysis and the tortuousness of CNTs is preferred for problems such as the reinforcement of CNT/polymer composites.

10.4 Conclusion

A quantitative and automatic analysis has been developed in the current study to estimate the dispersion of fillers in polymer composites. The importance of automatic filler identification is stressed and a local threshold is used to separate the fillers from the background in order to eliminate the interference from inhomogeneous background. The dispersion metric is based on the distance between the PDF function of the sample image and the PDF of uniformity. This metric can not only represent the distribution status of the fillers but also reflect the filler size, as demonstrated by a series of synthetic images. Application of the method to the model composite also shows that it can accurately predict the dispersion and mechanical properties of model composites. This method is applicable to different scales of filler reinforced composites.

CHAPTER 11 FUTURE WORK

11.1 Silver nanowire-based electrically conductive adhesives to reduce filler loading

In Chapter 2, we successfully increased the electrical conductivity of silver flake-based ECAs by one order of magnitude (10^5 S/cm) without sacrificing their processibility. Based on our understanding of the surface chemistry of the silver flakes, we were able to chemically reduce the insulating lubricant on the flakes to silver nanoparticles during epoxy curing; this was achieved by either adding a small amount of reducing agent to the epoxy matrix. Furthermore, we found that these nanoparticles can sinter with each other and form metallurgical bonds during the curing of the polymer matrix, further increasing the conductivity.

However, the silver flake-based ECAs studied previously generally require high filler loadings (~80wt.% or ~30vol.%) for optimum performance. The high loading increases the overall density, weight and of course the total cost of the composite.

From classical percolation theory, the percolation threshold and the electrical conductivity of conductor-filled composites is significantly dependent on the filler shape. Computational studies have shown that fillers with high aspect ratios can dramatically decrease the percolation threshold and thus increase the conductivity at lower loadings [364]. In addition, some recent studies also experimentally demonstrate the potential of using silver nanowires (AgNWs) to decrease the percolation threshold [159, 364-366]

Although extensive evidence has verified the effectiveness of replacing Ag particles with AgNWs to decrease the percolation threshold, there is a paucity of information concerning AgNW-based ECAs that can achieve conductivity at 10^5 S/cm levels. This likely results from two main factors.

216

First, the aggregation of AgNWs poses significant difficulties in dispersing large amounts of AgNWs into a polymer matrix. The high surface area and high aspect-ratio of AgNWs cause them to have a tendency to aggregate. Moreover, AgNWs are hydrophilic while epoxy resins are hydrophobic. The polarity difference further promotes the aggregation of AgNWs even after they are mixed into epoxy matrix [367]. To solve this problem, prior studies conducted surface treatments with silane coupling agents on AgNWs to increase the compatibility between AgNWs and epoxy [367]. However, it is not clear if these surface treatments would detract from the conductivity and mechanical properties of ECAs.

The second challenge is the large contact resistance between silver nanowires. Some studies attributed the contact resistance to the loose contact between Ag NWs [368-371]; in other examinations, polyvinylpyrrolidone (PVP) layers, which are used to coat the AgNWs for directional growth and dispersion during AgNWs synthesis [372, 373], are considered as the main culprit behind an increased contact resistance between NWs [374-377] (Figure 11.1). As a result, researchers are apt to partially remove the PVP layers before mixing them into an epoxy matrix, because PVP seriously inhibits electron conduction in the ECAs. However, complete removal leads to the segregation of the AgNWs even during pretreatment processes, and these segregated AgNWs cannot be redispersed again. Therefore, prior studies have been focused on a subsequent step to remove the PVP layers and sinter the AgNWs after mixing into the epoxy matrix. These treatments include high temperature and long-duration thermal annealing (200-350$^{\text{o}}$C) [376, 377], applying extra pressure [369-371], and burning PVP under high intensity light [375]. Although these may be functional treatments for pure AgNWs, they may lose their

efficiency in the ECA composites due to the composites' limited heat transfer (for heat treatment), micro-scale load transfer (for pressure treatment) and light transmittance (for intense light treatment).

In Chapter 2-6, we have developed a comprehensive procedure to guarantee both the facile processbility and elevated conductivity of silver flake-based ECAs. In this procedure, silver flakes are lubricated with long-chain fatty acids so that the flakes can be well dispersed in the polymer matrix even at 80 wt.% loading. The lubricant layers may then be easily removed during epoxy curing via the iodination of silver flakes or the addition of reducing agents, such as ethylene glycol to the epoxy matrix.

This process will be modified and applied to the AgNW-based ECAs, which is very promising to solve both of the challenges mentioned above. We propose to gradually replace PVP with long-chain fatty acid by washing the as-synthesized Ag NWs with long-chain fatty acid ethanol solutions. PVP is highly soluble in ethanol, and hence washing with ethanol was demonstrated to be a most efficient way to remove PVP from Ag NWs [374]. At the same time, carboxylate groups can form strong coordination bonds with the silver surfaces [378-380]. In our previous studies, even immersing silver particles in a fatty acid ethanol solution can coat a fatty acid layer on the silver surface. By washing the as-synthesized AgNWs with fatty acid ethanol solution, a silver-fatty acid layer will form immediately after the PVP is removed. This lubrication process provide three obvious advantages: 1) The removal of PVP is accompanied by the coating with fatty acid, which supports homogeneous dispersion of the AgNWs and thus eliminates aggregation concerns [137, 381]; 2) The fatty acid layer contains a long alkane chain, which makes the surface hydrophobic and thus compatible with the hydrophobic

epoxy resin. In this way, the role of this layer is similar to that of the silane treatment of

AgNWs in the aforementioned study [367]; 3) The fatty acid layer has much lower

thermal decomposition temperature than that of PVP, which is a considerable advantage

for the sintering of AgNWs during ECA curing (Figure 11.1). PVP, as a polymeric

surfactant, has a thermal decomposition temperature around $400^{\circ}C$, and moreover the

PVP adsorbed on the surface of the Ag could be even more stable according to previous

studies [382, 383]. On the contrary, fatty acids have thermal decomposition temperatures

of approximately $200^{\circ}C$ (though this value may change with the chain length and specific

structure) [135, 140]. More importantly, our previous work shows that the iodination

treatment and addition of ethylene glycol could even decrease the surfactant

decomposition and sintering temperature to below $150^{\circ}C$ (i.e. the curing temperature of

the current epoxy matrix). With the coating of fatty acid to AgNWs, we can perform the

in-situ reduction of silver fatty acid layer to silver nanoparticles to achieve the increased

conductivity as demonstrated previously.
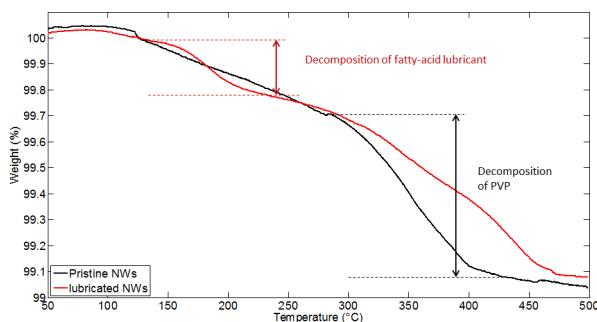
Figure 11.1 TGA of commercially available Ag NWs (black) and NWs treated with stearic acid (red). The pristine NWs have a degradation peak around $390^{\circ}C$ due to the decomposition of PVP layer, while lubricated NWs show a degradation peak below $200^{\circ}C$ due to the decomposition of lubricant.

The surface treatment of AgNWs will be characterized with Raman spectroscopy

and TGA. The processsilibity of the composite will be characterized by measuring the

viscosity of the AgNWs in epoxy at room temperature. The decomposition of fatty acid and nanoparticle sintering will be observed by SEM before and after curing, and the electrical conductivity will be measured to determine whether the method is applicable to the AgNWs system. The concentration of fatty acid, treatment time, and curing conditions will be varied to achieve the best conductivity.

11.2 Using silver dendrites for stretchable ECAs

In Chapter 6, we introduced using 2-D silver flakes as fillers in stretchable ECAs to mitigate the dependence of tunneling distance on the applied strain, because the shortest interparticle distance will not change if the local displacement of fillers is in the same plane with flakes. The tunneling distance will only increase when separating the flakes in the direction perpendicular to the flakes themselves. Therefore, we see a lessened dependence on applied strain with the increasing "dimensionality" of the filler particles. Drawing from this conclusion, we propose to use the 3-D dendritic structures, which have high aspect ratio branches in every direction, so that a low tunneling distance is maintained regardless of the deformation direction (Figure 11.2).
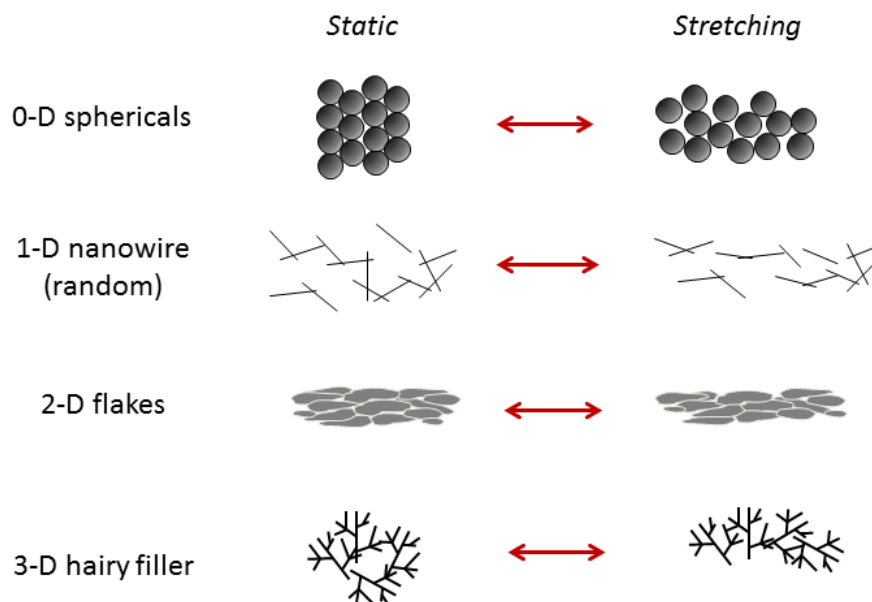
Figure 11.2 Schematic illustration of fillers with different shapes under lateral extension.

Figure 11.3 shows the preliminary results of silver nanosphere-, silver nanoflake- and silver dendrite-filled stretchable ECA at the same filler loading [384]. Here commercial PDMS, Sylgard® 184 was used as the ECA resin while silver nanospheres, silver nanoflakes were obtained from Ferro and used as received. The silver dendrites were synthesized according to previous report [385]. For the 0-D spherical particles, the resistance increases exponentially with strain, as expected from the above analysis. The resistance increases by two orders of magnitudes within 20% elongation and becomes insulating after reaching 30% elongation. Moreover, it is found that the resistance change follows the relation $R_c \propto s.\exp(s)$ within 20% elongation as shown by the fitting curve in Figure 11.3. After 20%, this resistance increases dramatically, indicating that after this point the inter-particle distance may be out of the range of electronic tunneling. For the 2-D flake-filled silo-ECA, the resistance increased at a much lower rate than that of sphere-filled silo-ECAs. The resistance increase remains within 5 times its original value, even at strains as large as 80%. This relatively small change in resistance may result from the

221

fact that most of the displacement occurs as sliding between overlapping flakes, which will not greatly affect the inter-particle distance and leads to little resistance change. For the dendrite-filled silo-ECAs, the resistance decreases with strain when the strain is below 30%. One possible explanation is that extension in one direction would lead to shrinkage in the other two directions; such shrinkage may compact the dendrites and produce more contact points than the ones lost due to extension. However, further work is needed to confidently elucidate the reason for the resistance drop. At strains greater than 30%, the resistance gradually increases, yet the total resistance change from the original value is still below 0, meaning that the resistance does not increase at all under stretching. The comparison in Figure 11.3 demonstrates the feasibility of the suggested work. It is important to note that the dendrites shown here are 2-D branched structures with a length of 5-10μm and aspect ratio of 100. The resistance could be maintained at even larger strains when using 3-D branched structures and when the length of dendrites and the aspect ratio of the branches are optimized.
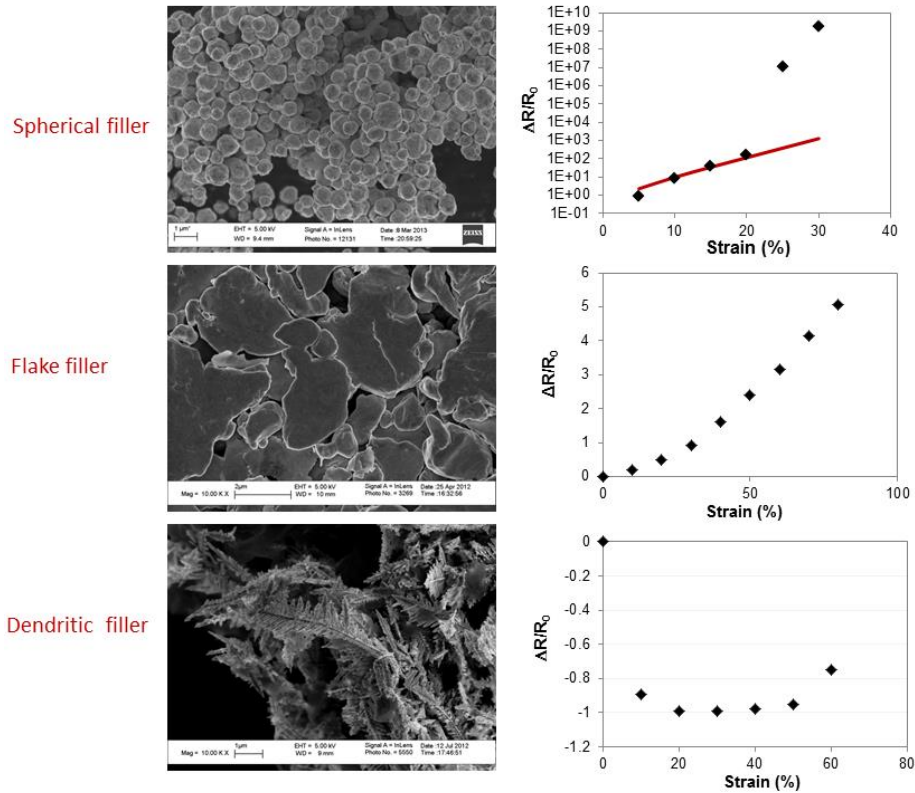
Figure 11.3 Electrical resistance change under stretching for silo-ECA (right) and the SEM images corresponding to the fillers of different shapes (left).

11.3 Application of stretchable silo-ECAs for 3D electrically small antenna

Modern mobile electronics are striving for miniaturization and increased functionality. Considering that antenna is probably the largest component in a typical wireless device, design and fabrication of so called electrically small antennas (ESAs) has attracted enormous attention.

An antenna is considered as an ESA when ka<0.5, where k=$2\pi/\lambda$ is the free space wavenumber and a is the minimum radius of a sphere that circumscribes the antenna. Unlike the other electronic components, decreasing the size of an antenna may sacrifice its performances including the gain, efficiency, system range and bandwidth. A majority of efforts on ESA studies are focused on improving the efficiency and bandwidth as much as possible while shrinking the size; however, there is a fundamental restriction on

223

the maximum achievable bandwidth. The bandwidth of ESA is inversely proportional to the radiation quality factor Q (which is defined as the ratio of energy stored to energy radiated) and as the dimension decreases below a wavelength, the minimum attainable Q rapidly increases following the equation below, a phenomenon commonly referred to as Chu's limit [386-388]:

$$Q_{Chu} = \eta_{eff}(\frac{1}{(\kappa a)^3} + \frac{1}{\kappa a}) \quad (1)$$

where η_{eff} is the radiation efficiency. One approach to overcome the problem of narrow bandwidth is to optimize the use of the volume that the antenna occupies within the Chu-sphere. A 3-D spherical antenna covers the entire surface of the Chu-sphere, and thus providing a very efficient way to minimize the Q-value. Hemispherical helix antennas can achieve a similar efficiency with spherical antenna and reduce the interference from the surrounding coupling structures due to the presence of a ground plane, so it has been demonstrated with good performance as ESAs [389].

While the research on 3D ESA design has been reported for decades, most of those designs are fabricated by manually bending wires into desired shapes [390-392], which is inaccurate, tedious and time-consuming. Recent advances in materials science have enabled a series of new fabrication methods. Adams *et al.* reported conformal printing of silver nano-ink onto contoured 3D surfaces [393]. This method can provide accurate patterns but the process is still slow and cannot support large scale fabrication. Bhattacharya *et al.* printed antennas onto a flexible printed circuit board using conventional photolighography, and then deform the circuit board into desired shape [394]. Yet a potential concern is that the metallic line may crack during the mechanical deformation. Toriz-Garcia *et al.* used holographic photolithography to achieve 3D

patterning, but this method needs expensive instrument and clean room environment [395]. Pfeiffer *et al.* introduced direct pattern transfer onto a 3D surface by a conformal polymer stamp, but the transfer process relies on forming a cold-welded bond between the stamp and substrate, which requires extremely clean and smooth surface of the substrate [396]. Also the metal conductor may delaminate from the substrate.

Considering the limitations of above methods, Jobs *et al.* introduced the fabrication methods to build stretchable antennas to construct a 3D antenna [397]. Basically, a planar liquid alloy filled microfluidic antenna is built first and then is inflated into a hemisphere 3D antenna. They also demonstrate that the central frequency of the so-built antenna can be tuned by the height, i.e. inflation extent.

In chapter 6, we successfully demonstrated stretchable antennas could be built by embedding silo-ECAs in pure silicone elastomer substrates. Compared to liquid metal-based antennas, the ECA-based ones have many advantages, including: 1). ECAs have a wide operation temperature window. In contrast to the liquid metal alloy that can only be operated at room temperature and above (e.g. eutectic GaIn alloy, $T_m \sim 15.5^{\circ}C$ [212]), silicone-ECA based RF devices can be used in extreme environment ($T_g < -100\,^{\circ}C$, $T_d > 400\,^{\circ}C$). 2). ECA can be co-cured with the silicone substrate, the strong interfacial bonding between the conductor and substrate eliminate the delamination issue and leakage of liquid metal alloy. 3) Soft lithography technique can enable large scale production and fine pitch.

Here, we can extend the fabrication method of stretchable antennas with ECA as conductors to build 3D ESAs. The process is shown in Figure 11.4. The pattern is first formed on a silicon chip using conventional lithography. Silicone prepolymers are

225

applied onto the silicon chip and get cured to form the patterned substrate. ECAs are

dispensed into the cavity in the silicone substrate and get cured. Then the planar pattern is

inflated to form the hemisphere 3D antenna.
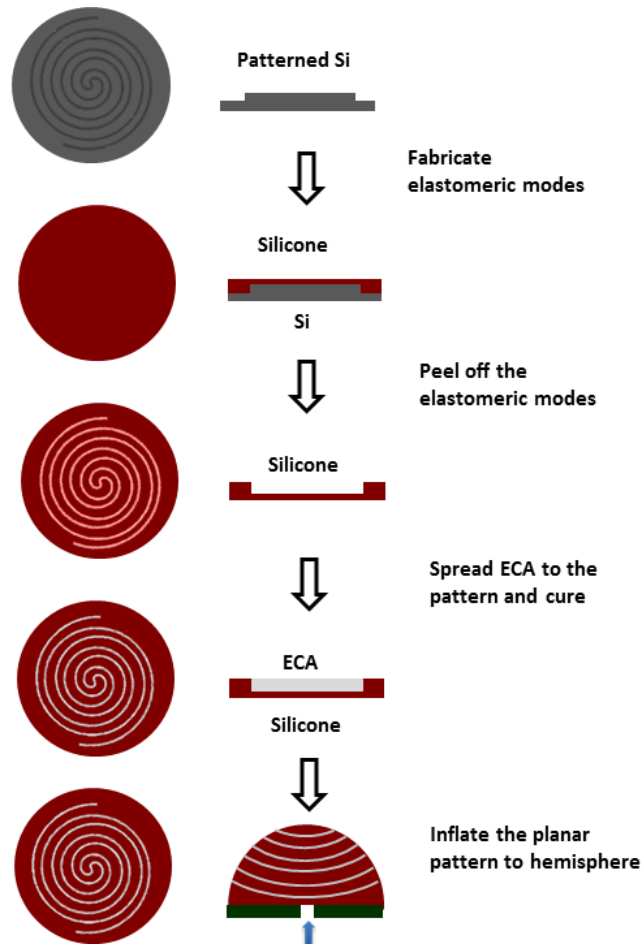
Figure 11.4 The fabrication method of 3D ESA by silicone ECAs.

In addition to the advantages listed above, using ECAs and soft-lithography

fabrication method solve some fundamental problems that cannot be achieved previously,

including 1) enable large-scale, fast fabrication; 2) the excellent conductivity of ECA and

easily tunable thickness of ECA conductive microstrips can make it easy for impedance

matching; 3) the high resolution of fidelity of soft-lithography can print more conductive

microstrips with smaller microstrip width. More conductive microstrips allows a more

226

complete filling of the shpereical volume and thus a low Q[393]; while narrower strips could enhance the reflection coefficient [395].

After the antenna is fabricated, its reflection coefficient, tunable range, input impedance and resonance frequency will be measured by a vector network analyzer. The radiation pattern will be measured in an anechoic chamber and compared with the simulation results. Antenna's radiation efficiency will be measured by the wheeler cap method and the gain comparison method [394, 398]. The radiation quality factor Q will also be obtained by the measured input impedance according to the equation [399]

$$Q(\omega_0) = \frac{\omega_0}{2R_0} \left| \frac{dz(\omega_0)}{d\omega} \right| \quad (2)$$

Where ω_0 is the resonant frequency of the antenna, R_0 is the input resistance and $\frac{dz(\omega_0)}{d\omega}$ is the frequency derivative of the input impedance evaluated at the resonant frequency.

11.4 Graphene-based conductive composites with ultra-low percolation threshold

In Chapter 7-10, we discussed the CNT or CB-based conductive composites. As another important member in carbon family, graphene can provide many benefits as fillers in the composites as well. The outstanding properties of graphene, especially the high thermal conductivity (~5000 $Wm^{-1}K^{-1}$)[400], large surface area (2630 m^2/g, calculated value)[401], and excellent mechanical properties (Young's modules ~1100GPa)[402] have great potential to produce composites with exceptional thermal/mechanical/chemical properties.

Integration of single layer graphene into macroscopic three dimensional structures is essential to achieve high performance of graphene based composites.

227

Compared with graphene/polymer composites made of randomly-dispersed graphene, a pre-formed graphene network infiltrated with polymer resin would dramatically decrease the percolation threshold and have much higher electrical and thermal conductivity with equivalent loading. There have been great interests to fabricate 3-D graphene structure, such as Langmuir–Blodgett films [403], porous carbon films [404], hydrogels [405], graphene foams [406] with chemically modified graphene. However, the graphene used here are mostly reduced graphene, which has inferior thermal and electrical conductivity compared to intrinsic graphene. There are also efforts to develop 3D graphene by CVD methods [407]. Basically, a 3D metal template (usually Ni foam) was used as growth substrate for 3D graphene. However, CVD method cannot be used for large-scale cost-effective growth.

Here we propose a new idea to form 3D graphene, which can also be extended to other 2D materials such as BN, MoS et al. The scheme is shown in Figure 11.5. Graphene or other 2D materials can be obtained by liquid exfoliation [408-410]. Polymer latex solution or silica solution was added to the graphene solution. The polymer microspheres or silica spheres serve as templates for graphene assembly. The solvents are removed by either filtration or evaporation. The concentration of graphene increases and graphene could no longer to disperse in solvents. They tend to aggregate and attach to the surface of polymer spheres. After the complete removal of solvents, the spheres are coated with a layer of graphene. The microspheres themselves also self-assembled and packed into a densely packed HCP structure. The graphene coating on the spheres also packed together, forming a network structure. Then polymer resins, such as epoxy or silicone is filtrated to form a composites.

228

The composites prepared with this method would have the similar structure with CVD grew-3D graphene, but with much facile preparation and it can be extended to other 2D materials.
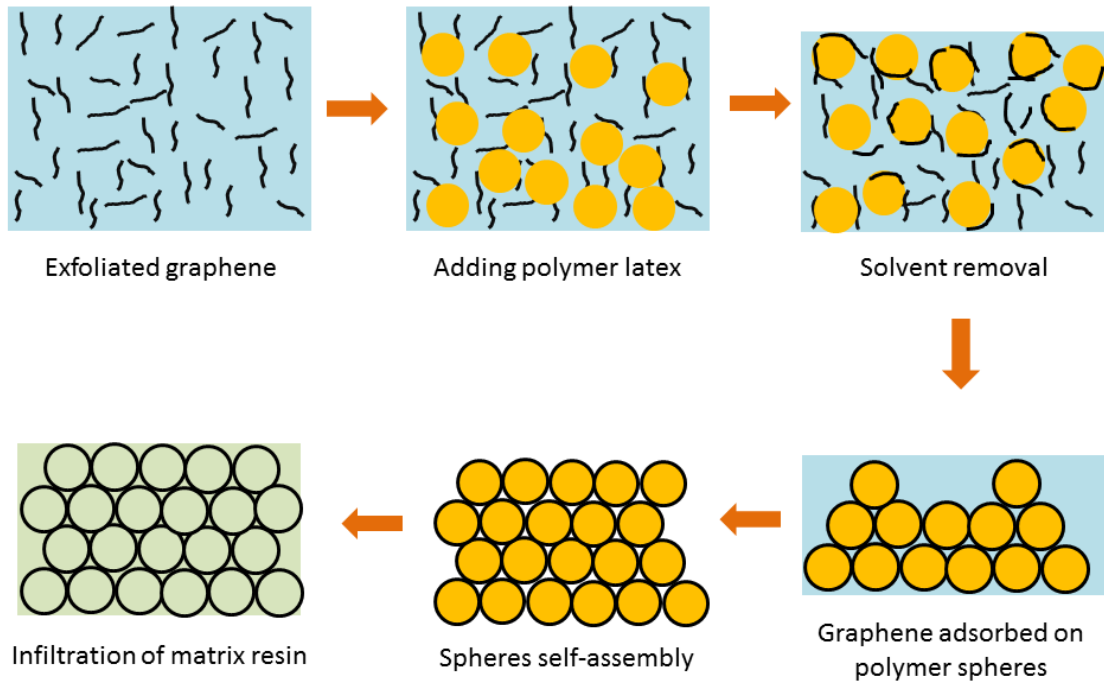
Figure 11.5 Preparing 3D graphene/polymer composites by assembly of graphene on spherical particles.

APPENDIX A

CALCULATION ON MINIMUM THICKNESS TO ELIMINATE DLO EFFECT

A.1 DLO effect

When air surrounds the insulation system during aging, oxygen will dissolve in the insulation materials. Aging consumes the dissolved oxygen via oxidation reactions. If these reactions occur faster than diffusion processes from the surrounding air, the concentration of oxygen in the polymer interior will be reduced from its equilibrium value to lower or even non-existent levels. This effect can lead to diffusion-limited oxidation (DLO) effects, where the rate of oxidation is reduced or eliminated in such regions. The importance of DLO effects depends upon the material, its geometry (thickness) and its aging environment. It is critical to note that for most insulation systems, DLO effects will likely be unimportant under the slow oxidation conditions occurring for ambient aging. In such instances, equilibrium oxidation should occur uniformly across the entire cross-section of the polymer materials. But for short-term accelerated aging in laboratory conditions, DLO may occur. If we assume DLO effects are negligible when the integrated oxidation across a sample cross-section is greater than 90% of what it would be for a homogeneously oxidized material, the following expression gives the maximum sample thickness that guarantees 90% oxidation.

$$L_{90} \approx 2 \left[\frac{pP_{Ox}}{\phi} \right]^{0.5} \qquad (1) \quad [411]$$

The partial pressure of oxygen p surrounding the sample is 15.96 cmHg and the oxygen permeability coefficient P_{ox} and the oxygen consumption rate Φ are determined by the polymer in use.

A.2. EPDM

A.2.1 EPDM oxygen consumption rate calculation

Oxygen consumption rate of EPDM at different temperatures were reported before [412]. The reported data (shown in black in Table 1) are used to calculate the activation energy of the oxidative thermal degradation. The activation energy is 112 kJ/mol below 111°C, and 75 kJ above 111°C. The oxygen consumption rate at 25°C, 100°C and 200°C are then calculated from the Arrhenius equation (shown in red in Table 1).

Table 1 EPDM oxygen consumption rate calculation according to Arrhenius equation

T(^{o}C)	T(K)	-1/(RT)	Ln(Φ)	Φ (mol/g/s)
160	433	-0.00028	-21.23	6.00E-10
140	413	-0.00029	-22.62	1.50E-10
125	398	-0.00030	-23.54	6.00E-11
111	384	-0.00031	-25.33	1.00E-11
200	473	-0.00025	-18.49	9.31E-09
111	384	-0.00031	-25.33	1.00E-11
96	369	-0.00033	-26.02	5.00E-12
80	353	-0.00034	-27.22	1.50E-12
52	325	-0.00037	-29.53	1.50E-13
100	373	-0.00032	-25.89	5.67E-12
25	298	-0.00040	-32.00	1.27E-14

A.2.2 EPDM oxygen permeability coefficient calculation

Oxygen permeability coefficient data are obtained from Ref. [244, 411] and summarize in Table 2.

Table 2 EPDM oxygen permeability coefficients

T (^{o}C)	P_{ox} (cc STP/cm-s-cm-Hg)
200	6.00E-08
100	1.90E-08
25	2.00E-09

A.2.3 Maximum sample thickness for EPDM

The maximum sample thickness L_{90} at 25 ^{o}C, 100 ^{o}C and 200 ^{o}C can be then calculated from equation 1 and it is summarized in Table 3.

Table 3 Maximum sample thickness for EPDM at different temperatures

T (^{o}C)	Φ (mol/g/s)	P_{ox} (ccSTP/cm-s-cm-Hg)	L_{90} (mm)
200	9.31481E-09	6.00E-08	3.58E+01
100	5.67472E-12	1.90E-08	8.17E+02
25	1.26843E-14	2.00E-09	5.61E+03

A.3 Epoxy

If Φ and P_{ox} both obey the Arrhenius equation with the respective activation energies E_{ox} (thermal oxidation) and E_D (diffusion), the L_{90} must vary with the temperature according to

$$L_{90} = (L_{90})_0 \exp[\frac{1}{2}\frac{E_{ox} - E_D}{RT}] \qquad (2)$$

Eox and ED is 99 kJ/mol and 10.4 kJ/mol, respectively, according to Ref.[413]. The experimental obtained L_{90} at 200°C is 22 μm [413]. The L_{90} at 100°C and 25°C can then be calculated according to Equation 2.

$$(L_{90})_{200\,^oC} = (L_{90})_0 \exp[\frac{99000 - 10400}{2 \times 8.314 \times 473.15}] = 22\,\mu m$$

$$(L_{90})_{100\,^oC} = (L_{90})_0 \exp[\frac{99000 - 10400}{2 \times 8.314 \times 373.15}] = 20.45 \times (L_{90})_{200\,^oC} = 450\,\mu m$$

$$(L_{90})_{25\,^oC} = (L_{90})_0 \exp[\frac{99000 - 10400}{2 \times 8.314 \times 298.15}] = 742.44 \times (L_{90})_{200\,^oC} = 16.33\,\mu m$$

Table 4 Maximum sample thickness for epoxy at different temperatures

T (^{o}C)	L_{90} (mm)
200	0.022
100	0.45
25	16.33

A.4. Summary

It is to be noted that all the oxidation rates and the diffusion rates, along with their

activation energies are obtained from references, which may be different with the

materials we used in the present study. However, it can provide a general idea that a

sample thickness of 300 μm would be probably be thin enough for EPDM-based sensors

to avoid DLO. But in the case of epoxy-based sensors at current aging temperatures, there

may be some oxygen diffusion issue, which may affect the accuracy of the epoxy-based

sensors.

APPENDIX B

AUTHOR'S PUBLICATIONS

B.1 Journal Publications

1. Z. Li, K.S. Moon, Y. Yao, S. Wilkins, and C.P. Wong. "*Carbon nanotubes inhibit the free radical cross-linking of siloxane polymers*". J. Appli. Polym. Sci., In print.

2. Z. Li, K. Hansen, Y. Yao, Y. Ma, K. S. Moon and C.P. Wong. "*Conduction development mechanism of silicone-based electrically conductive adhesives*". J. Mater. Chem. C, 1: 4368-4374, 2013.

3. Z. Li, K. S. Moon, K. Hansen, L. Morato, K. Watkins, and C.P. Wong. "CNT/polymer nano-composites: sensing the thermal aging conditions of electrical insulation components ". Carbon, 65: 71-79, 2013.

4. Z. Li, R. Zhang, K.S. Moon, Y. Liu, K. Hansen, and C.P. Wong. "*Highly conductive, flexible polyurethane-based adhesives for flexible and printed electronics* ". Adv. Funct. Mater., 23 (11): 1459–1465, 2013.

5. Y. Gao, Z. Li, Z. Lin, L. Zhu, A. Tannenbaum, S. Bouix and C.P. Wong. "*Automated dispersion and orientation analysis for carbon nanotube reinforced polymer composites* ". Nanotechnology, 23 (43): 435706-435715, 2012.

6. Z. Li, Y. Gao, K.S. Moon, Y. Yao, A. Tannenbaum, and C.P. Wong. "*Automatic quantification of filler dispersion in polymer composites*". Polymer, 25(2): 99-107, 2012.

7. Z. Li, S. J. Wilkins, K. S. Moon, and C.P. Wong. "*Carbon nanotube/polymer nanocomposites: improved or reduced thermal stabilities?*" Mater. Sci. Forum, 722: 77, 2012.

8. Z. Li, W. Lin, K. S. Moon, S. J. Wilkins, Y. Yao, K. Watkins, L. Morato, and C.P.Wong. *"Metal catalyst residues in carbon nanotubes decrease the thermal stability of carbon nanotube/ silicone composites "*. Carbon, 49(13): 4138-4148, 2011.

9. Z. Li, Y. Yao, Z. Lin , K. S. Moon, W. Lin, and C.P. Wong. *"Ultrafast, dry microwave synthesis of graphene sheets"*. J. Mater. Chem., 20: 4781-4783, 2010.

10. Z. Lin, Z. Li, K.S. Moon, Y. Fang, Y. Yao, L. Li , and C.P. Wong. "Robust vertically aligned carbon nanotube-carbon fiber paper hybrid as versatile electrodes for supercapacitors and capacitive deionization". Carbon, 63: 547–553, 2013.

11. Y. Yao, <u>Z.Li</u>, and C.P. Wong. "*Quality control of vertically aligned carbon nanotubes grown by chemical vapor deposition*", IEEE Trans. Compon. Packag. Manuf. Technol., 3 (11): 1804-1810, 2013

12. Y. Yao, Z. Lin, <u>Z. Li</u>, X. Song, K. S. Moon, and C.P. Wong. *"Large-scale production of two-dimensional nanosheets"*. J. Mater. Chem., 22: 13494-13499, 2012.

13. Z. Lin, T. Le, X. Song, Y. Yao, <u>Z. Li</u> , K.S. Moon, M. Tentzeris, and C.P. Wong. "*Preparation of water-based carbon nanotube inks and application in the inkjet printing of carbon* ". J. Electron. Packaging, 98 (9):1601-1609, 2012.

14. Z. Lin, Y. Liu, Y. Yao, O. J. Hildreth, <u>Z. Li</u>, K.S. Moon, and C.P. Wong. *"Superior Capacitance of Functionalized Graphene"*. J. Phys. Chem. C, 115(14): 7120-7125, 2011.

15. Y. Yao, <u>Z. Li</u>, Z. Lin, K. S. Moon, J. Agar, and C.P. Wong. *"Controlled growth of multi-layer, few-layer, and single-layer graphene on metal substrates"*. J. Phys. Chem. C, 115(13): 5232–5238, 2011

16. Z. Lin, Y. Yao, <u>Z. Li</u>, K. S. Moon, and C. P. Wong. *"Recent progress in facile preparation of graphene"*. ECS Trans., 37 (1): 115-119, 2011

17. Z. Lin, Y. Yao, <u>Z. Li</u>, Y. Liu , Z. Li, and C.P. Wong. *"Solvent-assisted thermal reduction of graphite oxide"*. J. Phys. Chem. C, 114(35): 14819–14825, 2010

B.2 Conference Proceedings

18. <u>Z. Li</u>, L. Li, K.S. Moon, F. Cai, J. Papapolymerous, and C.P. Wong, "*Stretchable RF devices via high-throughput, high-definability soft-lithography fabrication*", 63rd IEEE ECTC, Las Vegas, NV, 2013.

19. <u>Z. Li</u>, K. Hansen, K.S. Moon, and C.P. Wong, "*Shape engineering of the fillers in stretchable, electrically conductive adhesives: its effect on percolation and conductivity change during stretching*", 63rd IEEE ECTC, Las Vegas, NV, 2013.

20. <u>Z. Li</u>, R. Zhang, Y. Ma, K.S. Moon, and C.P. Wong, "*Enhance the electrical conductivity of electrically conductive adhesives by in-situ generation of metal nanoparticles.* " 2013 ICOLSE, Seattle, WA, 2013.

21. <u>Z. Li</u>, Y. Gao, K.S. Moon, A. Tannenbaum, and C.P. Wong. *"Nano filler dispersion in polymer composites for electronic packaging"*. 62nd IEEE ECTC, San Diego, CA, 2012.

22. <u>Z. Li</u>, R. Zhang; Y. Liu, T. Le, and C.P. Wong. *"Highly conductive, flexible, bio-compatible poly-urethane based isotropic conductive adhesives for flexible*

electronics". 62nd IEEE ECTC, San Diego, CA, 2012.

23. Z. Li, K.S. Moon, S.W. Kim, and C.P. Wong. "Enhancement of dielectric strength and processibility of high dielectric constant Al nanocomposite by organic molecule treatment". 61st IEEE ECTC, Orlando, Fl, 2011.

24. Z. Lin, Z. Li,1 K.S. Moon and C.P. Wong. "Capacitive Deionization of Water Coolant Using Hybrid Carbon Electrodes for High Power Electronic Applications". 64th IEEE ECTC, Orlando, Fl, 2014.

25. J. Gakkestad, Z. Li, T. Helland, and C.P. Wong. "Thermo-Mechanical Properties of Isotropic Conductive Adhesive Filled with Metallized Polymer Spheres." 15th IEEE EPTC, Singapore, 2013.

26. F. Cai, Z. Li, J. Agar, C.P. Wong, and J. Papapolymerou. *"Novel stretchable electrically conductive composites for tunable RF devices".* IEEE MTT-S International, Montreal, QC, Canada, 2012

27. Z. Lin, Y. Liu, Y. Yao, O.J Hildreth, Z. Li, K.S. Moon, J.C. Agar, and C.P. Wong. "Surface engineering of graphene for high performance supercapacitors". 61st IEEE ECTC, Orlando, Fl, 2011.

28. K. S. Moon, D. Staiculescu, S. Kim, Z. Li, H. Chan, V. Sundaram, R. Tummala, and C.P. Wong. "Adhesion and RF Properties of Electrically Conductive Adhesives". 60th IEEE ECTC, Las Vegas, NV, 2010.

29. K.S. Moon, Z. Li, Y. Yao, Z. Lin, Q. Liang, J.C. Agar, M. Song, M. Liu, and C.P. Wong. "Graphene for ultracapacitors". 60th IEEE ECTC, Las Vegas, NV, 2010.

APPENDIX C

VITA

Zhuo Li was born in Yidu, Hubei Province in China. She received a B.S. in Environmental Science from Tongji University, Shanghai, China in 2007 and a M.S. in Biological Systems Engineering from Virginia Tech, Blacksburg, Virginia in 2009 before coming to Georgia Tech to pursue a Ph.D. in Materials Science and Engineering under the supervision of Professor C.P.Wong in 2009. Her primary research interests lies in functional polymer composites. When she is not working on research, Ms. Li enjoys hiking, playing badminton, cooking and Chinese history.

REFERENCES

1. Tummala, R.R., E.J. Rymaszewski, and A.G. Klopfenstein, *microelectronics packaging handbook*1997: Springer.
2. Li, Z., et al., *Highly Conductive, Flexible, Polyurethane-Based Adhesives for Flexible and Printed Electronics.* Advanced Functional Materials, 2013. **23**(11): p. 1459-1465.
3. Yang, C., et al., *Investigation of a Biocompatible Polyurethane-Based Isotropically Conductive Adhesive for UHF RFID Tag Antennas.* Journal of Electronic Materials, 2011. **40**(1): p. 78-84.
4. Lutz, M.A. and R.L. Cole. *Flexible silicone adhesive with high electrical conductivity*. in *The 39th Electronic Components and Technology Conference, IEEE*. 1989.
5. Agar, J.C., et al. *Novel PDMS(silicone)-in-PDMS(silicone): Low cost flexible electronics without metallization*. in *The 60th Electronic Components and Technology Conference, IEEE*. 2010.
6. Li, Z., et al., *The conduction development mechanism of silicone-based electrically conductive adhesives.* Journal of Materials Chemistry C, 2013. **1**(28): p. 4368-4374.
7. Lu, D. and C.P. Wong, *Joining electroconductive materials with electroconductive adhesive containing epoxide-modified polyurethane*, 2004, Google Patents.
8. Daoqiang, L. and C.P. Wong, *High performance conductive adhesives.* Electronics Packaging Manufacturing, IEEE Transactions on, 1999. **22**(4): p. 324-330.
9. Ma, R., et al., *Carbon-Nanotube/Silver Networks in Nitrile Butadiene Rubber for Highly Conductive Flexible Adhesives.* Adv. Mater., 2012. **24**(25): p. 3344-3349.
10. Pujol, J.M., et al., *Electroconductive adhesives: Comparison of three different polymer matrices. Epoxy, polyimide, and silicone.* Journal of Adhesion, 1989. **27**: p. 213-229.
11. Lutz, M.A. and R.L. Cole, *High performance electrically conductive adhesives.* Hybrid Circuits, 1990. **23**: p. 27-30.
12. Liu, J., *Reliability of Surface-mounted Anisotropically Conductive Adhesive Joints.* Circuit World, 1993. **19** (4): p. 4-15.
13. Kim, S.-C. and Y.-H. Kim, *Review paper: Flip chip bonding with anisotropic conductive film (ACF) and nonconductive adhesive (NCA).* Current Applied Physics, 2013. **13, Supplement 2**(0): p. S14-S25.
14. Zonghe, L. and L. Johan, *Anisotropically conductive adhesive flip-chip bonding on rigid and flexible printed circuit substrates.* Components, Packaging, and Manufacturing Technology, Part B: Advanced Packaging, IEEE Transactions on, 1996. **19**(3): p. 644-660.
15. Wichmann, M.H.G., et al., *Piezoresistive response of epoxy composites with carbon nanoparticles under tensile load.* Physical Review B, 2009. **80**(24).

16. Iwama, S. and T. Sahashi, *Sintering of ultrafine metal powders. I. Coalescence growth stage of gold and silver.* Japanese Journal of Applied Physics, 1980. **19**(6): p. 1039-44.

17. Simmons, J.G., *Generalized Formula for the Electric Tunnel Effect between Similar Electrodes Separated by a Thin Insulating Film.* Journal of Applied Physics, 1963. **34**(6): p. 1793-1803.

18. Simmons, J.G., *Electric Tunnel Effect between Dissimilar Electrodes Separated by a Thin Insulating Film.* Journal of Applied Physics, 1963. **34**(9): p. 2581-2590.

19. Simmons, J.G., *Low-Voltage Current-Voltage Relationship of Tunnel Junctions.* Journal of Applied Physics, 1963. **34**(1): p. 238-239.

20. Simmons, J.G. and G.J. Unterkofler, *Potential Barrier Shape Determination in Tunnel Junctions.* Journal of Applied Physics, 1963. **34**(6): p. 1828-1830.

21. Yuanming, C., et al. *Compaction uniformity and environmental adaptability of printed RFID antenna.* in *Anti-Counterfeiting Security and Identification in Communication (ASID), 2010 International Conference on.* 2010.

22. Leung, S.Y.Y. and D.C.C. Lam, *Geometric and compaction dependence of printed polymer-based RFID tag antenna performance.* Ieee Transactions on Electronics Packaging Manufacturing, 2008. **31**(2): p. 120-125.

23. Lu, D., Q.K. Tong, and C.P. Wong, *Conductivity mechanisms of isotropic conductive adhesives (ICAs).* IEEE Trans. Compon. Packag. Technol., 1999. **22**(3): p. 223-227.

24. Lu, D. and C.P. Wong, *Effects of shrinkage on conductivity of isotropic conductive adhesives.* International Journal of Adhesion and Adhesives, 2000. **20**(3): p. 189-193.

25. Lu, D., Q.K. Tong, and C.P. Wong, *A study of lubricants on silver flakes for microelectronics conductive adhesives.* Components and Packaging Technologies, IEEE Transactions on, 1999. **22**(3): p. 365-371.

26. Lu, D. and C. Wong, *Characterization of Silver Flake Lubricants.* J. Therm. Anal. Calorim., 2000. **59**(3): p. 729-740.

27. Lu, D. and C. Wong, *Thermal Decomposition of Silver Flake Lubricants.* J. Therm. Anal. Calorim., 2000. **61**(1): p. 3-12.

28. Zhang, R., et al., *Fast Preparation of Printable Highly Conductive Polymer Nanocomposites by Thermal Decomposition of Silver Carboxylate and Sintering of Silver Nanoparticles.* ACS Appl. Mater. Interfaces 2010. **2**(9): p. 2637-2645.

29. Yi, L., et al. *Conductivity improvement of isotropic conductive adhesives with short-chain dicarboxylic acids.* in *Electronic Components and Technology Conference, 2004. Proceedings. 54th.* 2004.

30. Yi, L., et al. *Development of isotropic conductive adhesives with improved conductivity.* in *Advanced Packaging Materials: Processes, Properties and Interfaces, 2004. Proceedings. 9th International Symposium on.* 2004.

31. Yi, L., M. Kyoung-Sik, and C.P. Wong, *Electrical property improvement of electrically conductive adhesives through in-situ replacement by short-chain difunctional acids.* Components and Packaging Technologies, IEEE Transactions on, 2006. **29**(1): p. 173-178.

32.   Ye, L., et al., *Effect of Ag particle size on electrical conductivity of isotropically conductive adhesives.* IEEE Transactions on Electronics Packaging Manufacturing, 1999. **22**(4): p. 299-302.

33.   Kotthaus, S., et al., *Study of isotropically conductive bondings filled with aggregates of nano-sized Ag-particles.* IEEE Transactions on Components, Packaging, and Manufacturing Technology, Part A, 1997. **20**(1): p. 15-20.

34.   Lee, H.-H., K.-S. Chou, and Z.-W. Shih, *Effect of nano-sized silver particles on the resistivity of polymeric conductive adhesives.* International Journal of Adhesion and Adhesives, 2005. **25**(5): p. 437-441.

35.   Jiang, H., et al., *Surface Functionalized Silver Nanoparticles for Ultrahigh Conductive Polymer Composites.* Chem. Mater., 2006. **18**(13): p. 2969-2973.

36.   Jiang, H.J., et al., *Conductivity enhancement of nano silver-filled conductive adhesives by particle surface functionalization.* Journal of Electronic Materials, 2005. **34**(11): p. 1432-1439.

37.   Zhang, R.W., et al., *Preparation of highly conductive polymer nanocomposites by low temperature sintering of silver nanoparticles.* Journal of Materials Chemistry, 2010. **20**(10): p. 2018-2023.

38.   Ko, S.H., et al., *Air stable high resolution organic transistors by selective laser sintering of ink-jet printed metal nanoparticles.* Applied Physics Letters, 2007. **90**(14): p. 141103-3.

39.   Aminuzzaman, M., A. Watanabe, and T. Miyashita, *Direct writing of conductive silver micropatterns on flexible polyimide film by laser-induced pyrolysis of silver nanoparticle-dispersed film.* Journal of Nanoparticle Research, 2010. **12**(3): p. 931-938.

40.   Aminuzzaman, M., A. Watanabe, and T. Miyashita, *Fabrication of conductive silver micropatterns on an organic–inorganic hybrid film by laser direct writing.* Thin Solid Films, 2009. **517**(20): p. 5935-5939.

41.   Galagan, Y., et al., *Photonic sintering of inkjet printed current collecting grids for organic solar cell applications.* Organic Electronics, 2013. **14**(1): p. 38-46.

42.   Kim, H.-S., et al., *Intense pulsed light sintering of copper nanoink for printed electronics.* Applied Physics A, 2009. **97**(4): p. 791-798.

43.   Tobjörk, D., et al., *IR-sintering of ink-jet printed metal-nanoparticles on paper.* Thin Solid Films, 2012. **520**(7): p. 2949-2955.

44.   Mark, L.A., et al., *Electrical sintering of nanoparticle structures.* Nanotechnology, 2008. **19**(17): p. 175201.

45.   Perelaer, J., B.J. de Gans, and U.S. Schubert, *Ink-jet Printing and Microwave Sintering of Conductive Silver Tracks.* Advanced Materials, 2006. **18**(16): p. 2101-2104.

46.   Perelaer, J., et al., *Microwave Flash Sintering of Inkjet-Printed Silver Tracks on Polymer Substrates.* Advanced Materials, 2009. **21**(47): p. 4830-4834.

47.   Reinhold, I., et al., *Argon plasma sintering of inkjet printed silver tracks on polymer substrates.* Journal of Materials Chemistry, 2009. **19**(21): p. 3384-3388.

48.   Wakuda, D., K. Keun-Soo, and K. Suganuma, *Room-Temperature Sintering Process of Ag Nanoparticle Paste.* Components and Packaging Technologies, IEEE Transactions on, 2009. **32**(3): p. 627-632.

49.   Wakuda, D., M. Hatamura, and K. Suganuma, *Novel method for room temperature sintering of Ag nanoparticle paste in air.* Chemical Physics Letters, 2007. **441**(4–6): p. 305-308.

50.   Mark, A., et al., *Substrate-facilitated nanoparticle sintering and component interconnection procedure.* Nanotechnology, 2010. **21**(47): p. 475204.

51.   Coutts, M.J., et al., *Rapid and Controllable Sintering of Gold Nanoparticle Inks at Room Temperature Using a Chemical Agent.* The Journal of Physical Chemistry C, 2009. **113**(4): p. 1325-1328.

52.   Grouchko, M., et al., *Conductive Inks with a "Built-In" Mechanism That Enables Sintering at Room Temperature.* ACS Nano, 2011. **5**(4): p. 3354-3359.

53.   Long, Y., et al., *Rapid sintering of silver nanoparticles in an electrolyte solution at room temperature and its application to fabricate conductive silver films using polydopamine as adhesive layers.* Journal of Materials Chemistry, 2011. **21**(13): p. 4875-4881.

54.   Magdassi, S., et al., *Triggering the Sintering of Silver Nanoparticles at Room Temperature.* ACS Nano, 2010. **4**(4): p. 1943-1948.

55.   Lu, D. and C.P. Wong, *Characterization of silver flake lubricants.* Journal of Thermal Analysis and Calorimetry, 2000. **59**(3): p. 729-740.

56.   Lu, D., Q.K. Tong, and C.P. Wong, *A study of lubricants on silver flakes for microelectronics conductive adhesives.* IEEE Transactions on Components and Packaging Technologies, 1999. **22**(3): p. 365-371.

57.   Yamamoto, M., Y. Kashiwagi, and M. Nakamoto, *Size-Controlled Synthesis of Monodispersed Silver Nanoparticles Capped by Long-Chain Alkyl Carboxylates from Silver Carboxylate and Tertiary Amine.* Langmuir, 2006. **22**(20): p. 8581-8586.

58.   Yang, C., et al., *Water-Based Isotropically Conductive Adhesives: Towards Green and Low-Cost Flexible Electronics.* Adv. Funct. Mater., 2011. **21**(23): p. 4582-4588.

59.   Yi, L., et al., *Enhancement of Electrical Properties of Electrically Conductive Adhesives (ECAs) by Using Novel Aldehydes.* Components and Packaging Technologies, IEEE Transactions on, 2006. **29**(4): p. 758-763.

60.   Li, Z., et al., *Highly Conductive, Flexible, Polyurethane-Based Adhesives for Flexible and Printed Electronics.* Advanced Functional Materials, 2012: p. n/a-n/a.

61.   Zhang, R., et al., *A simple, low-cost approach to prepare flexible highly conductive polymer composites by in situ reduction of silver carboxylate for flexible electronic applications.* Compos. Sci. Technol., 2011. **71**(4): p. 528-534.

62.   Yang, C., et al., *Silver Surface Iodination for Enhancing the Conductivity of Conductive Composites.* Advanced Functional Materials, 2010. **20**(16): p. 2580-2587.

63.   Chung, D.D.L., *Electromagnetic interference shielding effectiveness of carbon materials.* Carbon, 2001. **39**(2): p. 279-285.

64.   Al-Saleh, M.H. and U. Sundararaj, *Electromagnetic interference shielding mechanisms of CNT/polymer composites.* Carbon, 2009. **47**(7): p. 1738-1746.

65. Wu, J. and D.D.L. Chung, *Improving colloidal graphite for electromagnetic interference shielding using 0.1 µm diameter carbon filaments.* Carbon, 2003. **41**(6): p. 1313-1315.

66. Annadurai, P., A.K. Mallick, and D.K. Tripathy, *Studies on microwave shielding materials based on ferrite- and carbon black-filled EPDM rubber in the X-band frequency.* Journal of Applied Polymer Science, 2002. **83**(1): p. 145-150.

67. Yang, Y., et al., *Conductive Carbon Nanofiber–Polymer Foam Structures.* Advanced Materials, 2005. **17**(16): p. 1999-2003.

68. Yang, Y., et al., *A Comparative Study of EMI Shielding Properties of Carbon Nanofiber and Multi-Walled Carbon Nanotube Filled Polymer Composites.* Journal of Nanoscience and Nanotechnology, 2005. **5**(6): p. 927-931.

69. Li, N., et al., *Electromagnetic interference (EMI) shielding of single-walled carbon nanotube epoxy composites.* Nano Lett, 2006. **6**(6): p. 1141-5.

70. Huang, Y., et al., *The influence of single-walled carbon nanotube structure on the electromagnetic interference shielding efficiency of its epoxy composites.* Carbon, 2007. **45**(8): p. 1614-1621.

71. Liu, Z., et al., *Reflection and absorption contributions to the electromagnetic interference shielding of single-walled carbon nanotube/polyurethane composites.* Carbon, 2007. **45**(4): p. 821-827.

72. Yang, Y., et al., *Novel Carbon Nanotube−Polystyrene Foam Composites for Electromagnetic Interference Shielding.* Nano Letters, 2005. **5**(11): p. 2131-2134.

73. Kim, H.M., et al., *Charge transport properties of composites of multiwalled carbon nanotube with metal catalyst and polymer: application to electromagnetic interference shielding.* Current Applied Physics, 2004. **4**(6): p. 577-580.

74. Kim, H.M., et al., *Electrical conductivity and electromagnetic interference shielding of multiwalled carbon nanotube composites containing Fe catalyst.* Applied Physics Letters, 2004. **84**(4): p. 589-591.

75. Zhang, C.-S., et al., *Electromagnetic interference shielding effect of nanocomposites with carbon nanotube and shape memory polymer.* Composites Science and Technology, 2007. **67**(14): p. 2973-2980.

76. Wang, Y. and X. Jing, *Intrinsically conducting polymers for electromagnetic interference shielding.* Polymers for Advanced Technologies, 2005. **16**(4): p. 344-351.

77. Ma, C.-C.M., et al., *Preparation and electromagnetic interference shielding characteristics of novel carbon-nanotube/siloxane/poly-(urea urethane) nanocomposites.* Journal of Polymer Science Part B: Polymer Physics, 2005. **43**(4): p. 345-358.

78. Liang, J., et al., *Electromagnetic interference shielding of graphene/epoxy composites.* Carbon, 2009. **47**(3): p. 922-925.

79. Zhang, H.-B., et al., *Tough Graphene−Polymer Microcellular Foams for Electromagnetic Interference Shielding.* ACS Applied Materials & Interfaces, 2011. **3**(3): p. 918-924.

80. Eswaraiah, V., V. Sankaranarayanan, and S. Ramaprabhu, *Functionalized Graphene–PVDF Foam Composites for EMI Shielding.* Macromolecular Materials and Engineering, 2011. **296**(10): p. 894-898.

81. Yan, D.-X., et al., *Efficient electromagnetic interference shielding of lightweight graphene/polystyrene composite.* Journal of Materials Chemistry, 2012. **22**(36): p. 18772-18774.

82. Bai, X., Y. Zhai, and Y. Zhang, *Green Approach To Prepare Graphene-Based Composites with High Microwave Absorption Capacity.* The Journal of Physical Chemistry C, 2011. **115**(23): p. 11673-11677.

83. Bingqing, Y., et al., *Comparison of electromagnetic interference shielding properties between single-wall carbon nanotube and graphene sheet/polyaniline composites.* Journal of Physics D: Applied Physics, 2012. **45**(23): p. 235108.

84. Leterrier, Y., et al., *Mechanical integrity of transparent conductive oxide films for flexible polymer-based displays.* Thin Solid Films, 2004. **460**(1–2): p. 156-166.

85. De, S., et al., *Transparent, Flexible, and Highly Conductive Thin Films Based on Polymer−Nanotube Composites.* ACS Nano, 2009. **3**(3): p. 714-720.

86. Kuilla, T., et al., *Recent advances in graphene based polymer composites.* Progress in Polymer Science, 2010. **35**(11): p. 1350-1375.

87. Lyons, P.E., et al., *The relationship between network morphology and conductivity in nanotube films.* Journal of Applied Physics, 2008. **104**(4): p. -.

88. Geng, H.-Z., et al., *Absorption spectroscopy of surfactant-dispersed carbon nanotube film: Modulation of electronic structures.* Chemical Physics Letters, 2008. **455**(4–6): p. 275-278.

89. Guang-Feng, W., T. Xiao-Ming, and W. Rong-Xin, *Flexible organic light-emitting diodes with a polymeric nanocomposite anode.* Nanotechnology, 2008. **19**(14): p. 145201.

90. Wang, W., et al., *Metallic Single-Walled Carbon Nanotubes for Conductive Nanocomposites.* Journal of the American Chemical Society, 2008. **130**(4): p. 1415-1419.

91. Ham, H.T., et al., *PEDOT-PSS/singlewall carbon nanotubes composites.* Polymer Engineering & Science, 2008. **48**(1): p. 1-10.

92. Mustonen, T., et al., *Inkjet printing of transparent and conductive patterns of single-walled carbon nanotubes and PEDOT-PSS composites.* physica status solidi (b), 2007. **244**(11): p. 4336-4340.

93. Moon, J.S., et al., *Transparent conductive film based on carbon nanotubes and PEDOT composites.* Diamond and Related Materials, 2005. **14**(11–12): p. 1882-1887.

94. Carroll, D.L., R. Czerw, and S. Webster, *Polymer–nanotube composites for transparent, conducting thin films.* Synthetic Metals, 2005. **155**(3): p. 694-697.

95. Blighe, F.M., et al., *Observation of Percolation-like Scaling – Far from the Percolation Threshold – in High Volume Fraction, High Conductivity Polymer-Nanotube Composite Films.* Advanced Materials, 2007. **19**(24): p. 4443-4447.

96. Park, C., et al., *Dispersion of single wall carbon nanotubes by in situ polymerization under sonication.* Chemical Physics Letters, 2002. **364**(3–4): p. 303-308.

97. Wei, C., et al., *Multifunctional Chemical Vapor Sensors of Aligned Carbon Nanotube and Polymer Composites.* Journal of the American Chemical Society, 2006. **128**(5): p. 1412-1413.

243

98.   Zhang, B., et al., *Preparation and characterization of gas-sensitive composites from multi-walled carbon nanotubes/polystyrene.* Sensors and Actuators B: Chemical, 2005. **109**(2): p. 323-328.

99.   Hargsoon, Y., et al., *Passive wireless sensors using electrical transition of carbon nanotube junctions in polymer matrix.* Smart Materials and Structures, 2006. **15**(1): p. S14.

100.   Weber, I. and P. Schwartz, *Monitoring bending fatigue in carbon-fibre/epoxy composite strands: a comparison between mechanical and resistance techniques.* Composites Science and Technology, 2001. **61**(6): p. 849-853.

101.   Schulte, K. and C. Baron, *Load and failure analyses of CFRP laminates by means of electrical resistivity measurements.* Composites Science and Technology, 1989. **36**(1): p. 63-76.

102.   Kupke, M., K. Schulte, and R. Schüler, *Non-destructive testing of FRP by d.c. and a.c. electrical methods.* Composites Science and Technology, 2001. **61**(6): p. 837-847.

103.   Schueler, R., S.P. Joshi, and K. Schulte, *Damage detection in CFRP by electrical conductivity mapping.* Composites Science and Technology, 2001. **61**(6): p. 921-930.

104.   Inpil, K., et al., *A carbon nanotube strain sensor for structural health monitoring.* Smart Materials and Structures, 2006. **15**(3): p. 737.

105.   Zhang, W., J. Suhr, and N. Koratkar, *Carbon Nanotube/Polycarbonate Composites as Multifunctional Strain Sensors.* Journal of Nanoscience and Nanotechnology, 2006. **6**(4): p. 960-964.

106.   Prasad, D., et al., *Nanotube film based on single-wall carbon nanotubes for strain sensing.* Nanotechnology, 2004. **15**(3): p. 379.

107.   Lee, D.Y., et al., *Ionic polymer-metal composite bending actuator loaded with multi-walled carbon nanotubes.* Sensors and Actuators, A: Physical, 2007. **133**(1): p. 117-127.

108.   Landi, B.J., et al., *Development and characterization of single wall carbon nanotube-Nafion composite actuators.* Materials Science and Engineering B: Solid-State Materials for Advanced Technology, 2005. **116**(3 SPEC.ISS.): p. 359-362.

109.   Li, C., E.T. Thostenson, and T.-W. Chou, *Sensors and actuators based on carbon nanotubes and their composites: A review.* Composites Science and Technology, 2008. **68**(6): p. 1227-1249.

110.   Zhang, S., et al., *Microstructure and electromechanical properties of carbon nanotube/ poly(vinylidene fluoride-trifluoroethylene-chlorofluoroethylene) composites.* Advanced Materials, 2005. **17**(15): p. 1897-1901.

111.   Yun, Y.H., et al., J. Intell. Mater. Syst. Struct., 2006. **17**: p. 191.

112.   Yun, Y.H., et al., *Development of novel single-wall carbon nanotube-epoxy composite ply actuators.* Smart Materials and Structures, 2005. **14**(6): p. 1526-1532.

113.   Courty, S., et al., *Nematic elastomers with aligned carbon nanotubes: New electromechanical actuators.* Europhysics Letters, 2003. **64**(5): p. 654-660.

114.   Wang, S., et al., *Thermal Expansion of Graphene Composites.* Macromolecules, 2009. **42**(14): p. 5251-5255.

115. Xu, Y., G. Ray, and B. Abdel-Magid, *Thermal behavior of single-walled carbon nanotube polymer–matrix composites.* Composites Part A: Applied Science and Manufacturing, 2006. **37**(1): p. 114-121.

116. Biercuk, M.J., et al., *Carbon nanotube composites for thermal management.* Applied Physics Letters, 2002. **80**(15): p. 2767-2769.

117. Huang, H., et al., *Aligned Carbon Nanotube Composite Films for Thermal Management.* Advanced Materials, 2005. **17**(13): p. 1652-1656.

118. Shahil, K.M.F. and A.A. Balandin, *Graphene–Multilayer Graphene Nanocomposites as Highly Efficient Thermal Interface Materials.* Nano Letters, 2012. **12**(2): p. 861-867.

119. Yu, A., et al., *Graphite Nanoplatelet−Epoxy Composite Thermal Interface Materials.* The Journal of Physical Chemistry C, 2007. **111**(21): p. 7565-7569.

120. Yu, A., et al., *Effect of single-walled carbon nanotube purity on the thermal conductivity of carbon nanotube-based composites.* Applied Physics Letters, 2006. **89**(13): p. -.

121. Wang, S., et al., *Dispersion and thermal conductivity of carbon nanotube composites.* Carbon, 2009. **47**(1): p. 53-57.

122. Nan, C.-W., et al., *Interface effect on thermal conductivity of carbon nanotube composites.* Applied Physics Letters, 2004. **85**(16): p. 3549-3551.

123. Peng, C., et al., *Carbon nanotube and conducting polymer composites for supercapacitors.* Progress in Natural Science-Materials International, 2008. **18**(7): p. 777-788.

124. Sun, Y.Q. and G.Q. Shi, *Graphene/polymer composites for energy applications.* Journal of Polymer Science Part B-Polymer Physics, 2013. **51**(4): p. 231-253.

125. Li, Y. and C.P. Wong, *Recent advances of conductive adhesives as a lead-free alternative in electronic packaging: Materials, processing, reliability and applications.* Materials Science and Engineering: R: Reports, 2006. **51**(1–3): p. 1-35.

126. Li, Y., K.-s. Moon, and C.P. Wong, *Electronics Without Lead.* Science, 2005. **308**(5727): p. 1419-1420.

127. Lu, D. and C.P. Wong, *A study of contact resistance of conductive adhesives based on anhydride-cured epoxy systems.* IEEE Trans. Compon. Packag. Technol., 2000. **23**(3): p. 440-446.

128. Li, Y., et al., *High performance electrically conductive adhesives (ECAs) modified with novel aldehydes.* 55th Electronic Components & Technology Conference, Vols 1 and 2, 2005 Proceedings, 2005: p. 1648-1652.

129. Greer, J.R. and R.A. Street, *Thermal cure effects on electrical performance of nanoparticle silver inks.* Acta Materialia, 2007. **55**(18): p. 6345-6349.

130. Coutts, M.J., et al., *Rapid and Controllable Sintering of Gold Nanoparticle Inks at Room Temperature Using a Chemical Agent.* Journal of Physical Chemistry C, 2009. **113**(4): p. 1325-1328.

131. Moskovits, M. and J.S. Suh, *Conformation of mono- and dicarboxylic acids adsorbed on silver surfaces.* J. Am. Chem. Soc., 1985. **107**(24): p. 6826-6829.

132. Yamamoto, S., K. Fujiwara, and H. Watarai, *Surface-enhanced Raman scattering from oleate-stabilized silver colloids at a liquid/liquid interface.* Analytical Sciences, 2004. **20**(9): p. 1347-1352.

133. Adamson, A.W. and A.P. Gast, *Physical chemistry of surfaces*1997: Wiley.

134. Giles, J.K. and C.S. Salmon, *CLXXIX.-The properties of some silver organosols.* Journal of the Chemical Society, Transactions, 1923. **123**(0): p. 1597-1608.

135. Nagasawa, H., et al., *Physical Characteristics of Stabilized Silver Nanoparticles Formed Using a New Thermal-Decomposition Method.* physica status solidi (a), 2002. **191**(1): p. 67-76.

136. Young, R.P., *Infrared spectroscopic studies of adsorption and catalysis. Part 3. Carboxylic acids and their derivatives adsorbed on silica.* Canadian Journal of Chemistry, 1969. **47**(12): p. 2237-2247.

137. Wang, W., X. Chen, and S. Efrima, *Silver Nanoparticles Capped by Long-Chain Unsaturated Carboxylates.* The Journal of Physical Chemistry B, 1999. **103**(34): p. 7238-7246.

138. Fields, E.K. and S. Meyerson, *Thermal and photochemical decomposition of silver carboxylates.* The Journal of Organic Chemistry, 1976. **41**(6): p. 916-920.

139. Judd, M.D., B.A. Plunkett, and M.I. Pope, *The thermal decomposition of calcium, sodium, silver and copper(II) acetates.* Journal of thermal analysis, 1974. **6**(5): p. 555-563.

140. Yang, N., K. Aoki, and H. Nagasawa, *Thermal Metallization of Silver Stearate-Coated Nanoparticles Owing to the Destruction of the Shell Structure.* The Journal of Physical Chemistry B, 2004. **108**(39): p. 15027-15032.

141. Uvarov, N.F., et al., *Conductivity of long-chain silver carboxylates and their thermal decomposition products.* Solid State Ionics, 1998. **107**(1–2): p. 31-40.

142. Rao, C.R.K. and D.C. Trivedi, *Biphasic synthesis of fatty acids stabilized silver nanoparticles: Role of experimental conditions on particle size.* Materials Chemistry and Physics, 2006. **99**(2–3): p. 354-360.

143. Flores, M., et al., *Efficient impact resistance improvement of epoxy/anhydride thermosets by adding hyperbranched polyesters partially modified with undecenoyl chains.* Polymer, 2012. **53**(23): p. 5232-5241.

144. Flores, M., et al., *Novel epoxy-anhydride thermosets modified with a hyperbranched polyester as toughness enhancer. I. Kinetics study.* Thermochimica Acta, 2012. **544**(0): p. 17-26.

145. Levita, G., et al., *Crosslink density and fracture toughness of epoxy resins.* Journal of Materials Science, 1991. **26**(9): p. 2348-2352.

146. Ramkumar, S.M., H. Venugopalan, and K. Khanna. *Novel anisotropic conductive adhesive for 3D stacking and lead-free PCB packaging - A review*. in *Electronic Components and Technology Conference (ECTC), 2011 IEEE 61st*. 2011.

147. Watanabe, I., et al. *Recent advances of interconnection technologies using anisotropic conductive films in flat panel display applications*. in *Advanced Packaging Materials: Processes, Properties and Interfaces, 2004. Proceedings. 9th International Symposium on*. 2004.

148. Matsuda, K. and I. Watanabe. *Recent progress toward anisotropic conductive films in flat panel display and semiconductor packaging applications*. in *High Density Microsystem Design and Packaging and Component Failure Analysis, 2004. HDP '04. Proceeding of the Sixth IEEE CPMT Conference on*. 2004.

149. Basavanhally, N.R., et al. *Direct chip interconnect with adhesive-connector films*. in *Electronic Components and Technology Conference, 1992. Proceedings., 42nd*. 1992.

150. Yim, M., et al., *Highly reliable flip-chip-on-flex package using multilayered anisotropic conductive film.* Journal of Electronic Materials, 2004. **33**(1): p. 76-82.

151. Un-Byoung, K. and Y.-H. Kim, *A new COG technique using low temperature solder bumps for LCD driver IC packaging applications.* Components and Packaging Technologies, IEEE Transactions on, 2004. **27**(2): p. 253-258.

152. Jin, S., et al., *New, Z-direction anisotropically conductive composites.* Journal of Applied Physics, 1988. **64**(10): p. 6008-6010.

153. Jin, S., et al., *Anisotropically conductive polymer films with a uniform dispersion of particles.* Components, Hybrids, and Manufacturing Technology, IEEE Transactions on, 1993. **16**(8): p. 972-977.

154. Jin, S., T.H. Tiefel, and R. Wolfe, *Directionally-conductive, optically-transparent composites by magnetic alignment.* Magnetics, IEEE Transactions on, 1992. **28**(5): p. 2211-2213.

155. Moon, S. and W.J. Chappell, *Novel Three-Dimensional Packaging Approaches Using Magnetically Aligned Anisotropic Conductive Adhesive for Microwave Applications.* Ieee Transactions on Microwave Theory and Techniques, 2010. **58**(12): p. 3815-3823.

156. Moon, S., S.K. Khanna, and W.J. Chappell, *Multilayer Silicon RF System-in-Package Technique Using Magnetically Aligned Anisotropic Conductive Adhesive.* 2009 Ieee/Mtt-S International Microwave Symposium, Vols 1-3, 2009: p. 797-800.

157. Moon, S., et al., *Magnetically Aligned Anisotropic Conductive Adhesive for Microwave Applications.* Ieee Transactions on Microwave Theory and Techniques, 2008. **56**(12): p. 2942-2949.

158. Sancaktar, E. and N. Dilsiz, *Anisotropic alignment of nickel particles in a magnetic field for electronically conductive adhesives applications.* Journal of Adhesion Science and Technology, 1997. **11**(2): p. 155-166.

159. De, S., et al., *Silver Nanowire Networks as Flexible, Transparent, Conducting Films: Extremely High DC to Optical Conductivity Ratios.* ACS Nano, 2009. **3**(7): p. 1767-1774.

160. Park, S.-I., et al., *Printed Assemblies of Inorganic Light-Emitting Diodes for Deformable and Semitransparent Displays.* Science, 2009. **325**(5943): p. 977-981.

161. Russo, A., et al., *Pen-on-Paper Flexible Electronics.* Adv. Mater., 2011. **23**(30): p. 3426-+.

162. Sekitani, T., et al., *Organic Nonvolatile Memory Transistors for Flexible Sensor Arrays.* Science, 2009. **326**(5959): p. 1516-1519.

163. Han, L., et al., *Ultraflexible amorphous silicon transistors made with a resilient insulator.* Applied Physics Letters, 2010. **96**(4).

164. Takei, K., et al., *Nanowire active-matrix circuitry for low-voltage macroscale artificial skin.* Nat Mater, 2010. **9**(10): p. 821-826.

165.   Fan, Z., et al., *Three-dimensional nanopillar-array photovoltaics on low-cost and flexible substrates.* Nat. Mater., 2009. **8**(8): p. 648-653.

166.   Yoon, J., et al., *Ultrathin silicon solar microcells for semitransparent, mechanically flexible and microconcentrator module designs.* Nat. Mater., 2008. **7**(11): p. 907-915.

167.   Hu, L., et al., *Thin, Flexible Secondary Li-Ion Paper Batteries.* ACS Nano, 2010. **4**(10): p. 5843-5848.

168.   Hu, L., et al., *Highly conductive paper for energy-storage devices.* Proc. Nat. Acad. Sci. USA 2009. **106**(51): p. 21490-21494.

169.   LeMieux, M.C. and Z.N. Bao, *FLEXIBLE ELECTRONICS Stretching our imagination.* Nat. Nanotechnol., 2008. **3**(10): p. 585-586.

170.   Rogers, J.A., T. Someya, and Y. Huang, *Materials and Mechanics for Stretchable Electronics.* Science, 2010. **327**(5973): p. 1603-1607.

171.   Lacour, S.P., et al., *Stretchable Interconnects for Elastic Electronic Surfaces.* Proc. IEEE 2005. **93**(8): p. 1459-1467.

172.   Gates, B.D., *Flexible Electronics.* Science, 2009. **323**(5921): p. 1566-1567.

173.   Hu, X., et al., *Stretchable Inorganic-Semiconductor Electronic Systems.* Adv. Mater., 2011. **23**(26): p. 2933-2936.

174.   Kim, D.-H. and J.A. Rogers, *Stretchable Electronics: Materials Strategies and Devices.* Adv. Mater., 2008. **20**(24): p. 4887-4892.

175.   Lee, J., et al., *Stretchable GaAs Photovoltaics with Designs That Enable High Areal Coverage.* Adv. Mater., 2011. **23**(8): p. 986-991.

176.   Sun, Y., et al., *Controlled buckling of semiconductor nanoribbons for stretchable electronics.* Nat Nano, 2006. **1**(3): p. 201-207.

177.   Li, T., et al., *Stretchability of thin metal films on elastomer substrates.* Appl. Phys. Lett. , 2004. **85**(16): p. 3435-3437.

178.   Lacour, S.P., et al., *Stretchable gold conductors on elastomeric substrates.* Appl. Phys. Lett. , 2003. **82**(15): p. 2404-2406.

179.   Ahn, B.Y., et al., *Omnidirectional Printing of Flexible, Stretchable, and Spanning Silver Microelectrodes.* Science, 2009. **323**(5921): p. 1590-1593.

180.   Lee, H.M., et al., *A Novel Solution-Stamping Process for Preparation of a Highly Conductive Aluminum Thin Film.* Adv. Mater., 2011. **23**(46): p. 5524-+.

181.   Garcia, A., et al., *Localized Ligand Induced Electroless Plating (LIEP) Process for the Fabrication of Copper Patterns Onto Flexible Polymer Substrates.* Adv. Funct. Mater., 2011. **21**(11): p. 2096-2102.

182.   Cong, H. and T. Pan, *Photopatternable Conductive PDMS Materials for Microfabrication.* Adv. Funct. Mater., 2008. **18**(13): p. 1912-1921.

183.   Chun, K.-Y., et al., *Highly conductive, printable and stretchable composite films of carbon nanotubes and silver.* Nat Nano, 2010. **5**(12): p. 853-857.

184.   Kahraman, R., M. Sunar, and B. Yilbas, *Influence of adhesive thickness and filler content on the mechanical performance of aluminum single-lap joints bonded with aluminum powder filled epoxy adhesive.* J. Mater. Process. Technol., 2008. **205**(1-3): p. 183-189.

185.   Lu, D. and C.P. Wong, *Effects of shrinkage on conductivity of isotropic conductive adhesives.* Int. J. Adhes. Adhes., 2000. **20**(3): p. 189-193.

248

186.   Popa, M., et al., *Stable silver colloidal dispersions using short chain polyethylene glycol.* Colloids Surf., A 2007. **303**(3): p. 184-190.

187.   Luo, L.B., et al., *Large-scale fabrication of flexible silver/cross-linked poly(vinyl alcohol) coaxial nanocables by a facile solution approach.* J Am Chem Soc 2005. **127**(9): p. 2822-2823.

188.   Park, S.-I., et al., *Theoretical and Experimental Studies of Bending of Inorganic Electronic Materials on Plastic Substrates.* Advanced Functional Materials, 2008. **18**(18): p. 2673-2684.

189.   McDonald, J.C. and G.M. Whitesides, *Poly(dimethylsiloxane) as a material for fabricating microfluidic devices.* Accounts of Chemical Research, 2002. **35**(7): p. 491-499.

190.   Cai, D. and A. Neyer, *Cost-effective and reliable sealing method for PDMS (PolyDiMethylSiloxane)-based microfluidic devices with various substrates.* Microfluidics and Nanofluidics, 2010. **9**(4): p. 855-864.

191.   Niu, X.Z., et al., *Characterizing and Patterning of PDMS-Based Conducting Composites.* Advanced Materials, 2007. **19**(18): p. 2682-2686.

192.   Zhang, Q., et al., *In-situ synthesis of poly(dimethylsiloxane)-gold nanoparticles composite films and its application in microfluidic systems.* Lab on a Chip, 2008. **8**(2): p. 352-357.

193.   F.Cai, et al. *Novel Stretchable Electrically Conductive Composites for Tunable RF Devices*. in *Microwave Symposium Digest (MTT), 2012 IEEE MTT-S International*. 2012.

194.   Agar, J., et al. *Electrically conductive silicone nano-composites for stretchable RF devices*. in *Microwave Symposium Digest (MTT), 2011 IEEE MTT-S International*. 2011.

195.   Xu, F. and Y. Zhu, *Highly Conductive and Stretchable Silver Nanowire Conductors.* Advanced Materials, 2012: p. n/a-n/a.

196.   Hailin, C. and P. Tingrui. *Microfabrication of conductive PDMS on flexible substrates for biomedical applications*. in *Nano/Micro Engineered and Molecular Systems, 2009. NEMS 2009. 4th IEEE International Conference on*. 2009.

197.   Sivaramakrishnan, S., et al., *Controlled insulator-to-metal transformation in printable polymer composites with nanometal clusters.* Nature Materials, 2007. **6**(2): p. 149-155.

198.   Klosterman, D., L. Li, and J.E. Morris, *Materials characterization, conduction development, and curing effects on reliability of isotropically conductive adhesives.* Ieee Transactions on Components Packaging and Manufacturing Technology Part A, 1998. **21**(1): p. 23-31.

199.   Li, L. and J.E. Morris, *Electrical conduction models for isotropically conductive adhesive joints.* Ieee Transactions on Components Packaging and Manufacturing Technology Part A, 1997. **20**(1): p. 3-8.

200.   Yu, Z., et al., *Highly Flexible Silver Nanowire Electrodes for Shape-Memory Polymer Light-Emitting Diodes.* Advanced Materials, 2011. **23**(5): p. 664-668.

201.   Simpson, T.R.E., B. Parbhoo, and J.L. Keddie, *The dependence of the rate of crosslinking in poly(dimethyl siloxane) on the thickness of coatings.* Polymer, 2003. **44**(17): p. 4829-4838.

202. Goyal, A., et al., *In situ Synthesis of Metal Nanoparticle Embedded Free Standing Multifunctional PDMS Films.* Macromolecular Rapid Communications, 2009. **30**(13): p. 1116-1122.

203. Smith, A.L., ed. *The analytical chemistry of silicones*. Chemical analysis, a series of monographs on analytical chemistry and its applications, ed. J.D. Winefordner and I.M. Kolthoff. Vol. 112. 1991, John Wiley & sons, Inc. 324-328.

204. Capozzi, C.A., L.D. Pye, and R.A. Condrate Sr, *Vibrational spectral/structural changes from the hydrolysis/polycondensation of methyl-modified silicates. I. comparisons for single monomer condensates.* Materials Letters, 1992. **15**(1–2): p. 130-136.

205. Gatzoulis, L. and I. Iakovidis, *Wearable and Portable eHealth Systems.* Engineering in Medicine and Biology Magazine, IEEE, 2007. **26**(5): p. 51-56.

206. Kim, D.-H., et al., *Dissolvable films of silk fibroin for ultrathin conformal bio-integrated electronics.* Nat Mater, 2010. **9**(6): p. 511-517.

207. Fan, C., et al. *Novel stretchable electrically conductive composites for tunable RF devices*. in *Microwave Symposium Digest (MTT), 2012 IEEE MTT-S International*. 2012.

208. Verma, A., et al. *6 GHz microstrip patch antennas with PEDOT and polypyrrole conducting polymers*. in *Electromagnetics in Advanced Applications (ICEAA), 2010 International Conference on*. 2010.

209. Kaufmann, T., et al., *Efficiency of a Compact Elliptical Planar Ultra-Wideband Antenna Based on Conductive Polymers.* International Journal of Antennas and Propagation, 2012.

210. Bayram, Y., et al., *E-Textile Conductors and Polymer Composites for Conformal Lightweight Antennas.* Ieee Transactions on Antennas and Propagation, 2010. **58**(8): p. 2732-2736.

211. Dickey, M.D., et al., *Eutectic Gallium-Indium (EGaIn): A Liquid Metal Alloy for the Formation of Stable Structures in Microchannels at Room Temperature.* Advanced Functional Materials, 2008. **18**(7): p. 1097-1104.

212. Kubo, M., et al., *Stretchable Microfluidic Radiofrequency Antennas.* Advanced Materials, 2010. **22**(25): p. 2749-2752.

213. Kaufmann, T., et al., *Efficiency of a Compact Elliptical Planar Ultra-Wideband Antenna Based on Conductive Polymers.* International Journal of Antennas and Propagation, 2012. **2012**: p. 11.

214. Johansson, L., et al., *Surface acoustic wave induced particle manipulation in a PDMS channel—principle concepts for continuous flow applications.* Biomedical Microdevices, 2012. **14**(2): p. 279-289.

215. Sekitani, T., et al., *A Rubberlike Stretchable Active Matrix Using Elastic Conductors.* Science, 2008. **321**(5895): p. 1468-1472.

216. Sekitani, T., et al., *Stretchable active-matrix organic light-emitting diode display using printable elastic conductors.* Nat Mater, 2009. **8**(6): p. 494-499.

217. Li, Y. and H. Shimizu, *Toward a Stretchable, Elastic, and Electrically Conductive Nanocomposite: Morphology and Properties of Poly[styrene-b-(ethylene-co-butylene)-b-styrene]/Multiwalled Carbon Nanotube Composites Fabricated by High-Shear Processing.* Macromolecules, 2009. **42**(7): p. 2587-2593.

218. Shin, M.K., et al., *Elastomeric Conductive Composites Based on Carbon Nanotube Forests.* Advanced Materials, 2010. **22**(24): p. 2663-2667.

219. Liu, K., et al., *Cross-Stacked Superaligned Carbon Nanotube Films for Transparent and Stretchable Conductors.* Advanced Functional Materials, 2011. **21**(14): p. 2721-2728.

220. Kim, K.H., M. Vural, and M.F. Islam, *Single-Walled Carbon Nanotube Aerogel-Based Elastic Conductors.* Advanced Materials, 2011. **23**(25): p. 2865-2869.

221. Hansen, T.S., et al., *Highly Stretchable and Conductive Polymer Material Made from Poly(3,4-ethylenedioxythiophene) and Polyurethane Elastomers.* Advanced Functional Materials, 2007. **17**(16): p. 3069-3073.

222. Xu, F., et al., *Wavy Ribbons of Carbon Nanotubes for Stretchable Conductors.* Advanced Functional Materials, 2012. **22**(6): p. 1279-1283.

223. Zhang, Y., et al., *Polymer-Embedded Carbon Nanotube Ribbons for Stretchable Conductors.* Advanced Materials, 2010. **22**(28): p. 3027-3031.

224. Vosgueritchian, M., D.J. Lipomi, and Z. Bao, *Highly Conductive and Transparent PEDOT:PSS Films with a Fluorosurfactant for Stretchable and Flexible Transparent Electrodes.* Advanced Functional Materials, 2012. **22**(2): p. 421-428.

225. Kost, J., A. Foux, and M. Narkis, *Quantitative model relating electrical resistance, strain, and time for carbon black loaded silicone rubber.* Polymer Engineering & Science, 1994. **34**(21): p. 1628-1634.

226. Wack, P.E., R.L. Anthony, and E. Guth, *Electrical Conductivity of GR-S and Natural Rubber Stocks Loaded with Shawinigan and R-40 Blacks.* Journal of Applied Physics, 1947. **18**(5): p. 456-469.

227. Park, M., H. Kim, and J.P. Youngblood, *Strain-dependent electrical resistance of multi-walled carbon nanotube/polymer composite films.* Nanotechnology, 2008. **19**(5).

228. Zhang, X.W., et al., *Time dependence of piezoresistance for the conductor-filled polymer composites.* Journal of Polymer Science Part B-Polymer Physics, 2000. **38**(21): p. 2739-2749.

229. Taya, M., W.J. Kim, and K. Ono, *Piezoresistivity of a short fiber/elastomer matrix composite.* Mechanics of Materials, 1998. **28**(1–4): p. 53-59.

230. Kim, Y., et al., *Stretchable nanoparticle conductors with self-organized conductive pathways.* Nature, 2013. **advance online publication**.

231. *Report of Large Motor Reliability Survey of Industrial and Commercial Installations .1.* Ieee Transactions on Industry Applications, 1985. **21**(4): p. 853-864.

232. *IEEE Guide for Designing Multistress Aging Tests of Electrical Insulation in a Radiation Environment.* IEEE Std 775-1993, 1993.

233. Anandakumaran, K., W. Seidl, and P.V. Castaldo, *Condition assessment of cable insulation systems in operating nuclear power plants.* Dielectrics and Electrical Insulation, IEEE Transactions on, 1999. **6**(3): p. 376-384.

234. Mattson, B., et al., *Novel techniques used to assess the ageing of carbon-black-filled materials.* Polymer Degradation and Stability, 1993. **41**(2): p. 211-221.

235. Wise, J., K.T. Gillen, and R.L. Clough, *Quantitative model for the time development of diffusion-limited oxidation profiles.* Polymer, 1997. **38**(8): p. 1929-1944.

236. Anandakumaran, K. and D.J. Stonkus, *Assessment of oxidative thermal degradation of crosslinked polyethylene and ethylene propylene rubber cable insulation.* Polymer Engineering & Science, 1992. **32**(18): p. 1386-1393.

237. Assink, R.A., K.T. Gillen, and B. Sanderson, *Monitoring the degradation of a thermally aged EPDM terpolymer by 1H NMR relaxation measurements of solvent swelled samples.* Polymer, 2002. **43**(4): p. 1349-1355.

238. Harris, D.J., R.A. Assink, and K.T. Gillen, *1H T2-NMR monitoring of crosslinked polyolefin aging.* Journal of Applied Polymer Science, 2003. **90**(9): p. 2578-2582.

239. Gillen, K.T., R.L. Clough, and N.J. Dhooge, *Density profiling of polymers.* Polymer, 1986. **27**(2): p. 225-232.

240. Mason, L.R. and A.B. Reynolds, *Standardization of oxidation induction time testing used in life assessment of polymeric electric cables.* Journal of Applied Polymer Science, 1997. **66**(9): p. 1691-1702.

241. Sun, Y., et al., *An electrical approach to monitor wire and cable thermal oxidation aging condition based on carbon black filled conductive polymer composite.* Journal of Applied Polymer Science, 2004. **93**(2): p. 513-520.

242. Sun, Y., et al., *Electrical approach to monitor the thermal oxidation aging of carbon black filled ethylene propylene rubber.* Polymer Degradation and Stability, 2004. **86**(2): p. 209-215.

243. Li, Z., et al., *Automatic quantification of filler dispersion in polymer composites.* Polymer, 2012. **53**(7): p. 1571-1580.

244. Celina, M. and K.T. Gillen, *Oxygen Permeability Measurements on Elastomers at Temperatures up to 225 ¬ ∞C.* Macromolecules, 2005. **38**(7): p. 2754-2763.

245. Last, B.J. and D.J. Thouless, *Percolation Theory and Electrical Conductivity.* Physical Review Letters, 1971. **27**(25): p. 1719.

246. Pochiraju, K.V., G.P. Tandon, and G.A. Schoeppner, *Evolution of stress and deformations in high-temperature polymer matrix composites during thermo-oxidative aging.* Mechanics of Time-Dependent Materials, 2008. **12**(1): p. 45-68.

247. Stauffer, D. and D. Aharony, *Introduction to Percolation Theory*1994, London, U.K.: Taylor & Francis.

248. Watts, P.C.P., et al., *Carbon nanotubes as polymer antioxidants.* J Mater Chem, 2003. **13**(3): p. 491-495.

249. Wise, J., K.T. Gillen, and R.L. Clough, *An Ultrasensitive Technique for Testing the Arrhenius Extrapolation Assumption for Thermally Aged Elastomers.* Polymer Degradation and Stability, 1995. **49**(3): p. 403-418.

250. Li, Z., et al., *Metal catalyst residues in carbon nanotubes decrease the thermal stability of carbon nanotube/silicone composites.* Carbon, 2011. **49**(13): p. 4138-4148.

251. *IEEE Recommended Practice for Thermal Evaluation of Insulation Systems for Alternating-Current Electric Machinery Employing Form-Wound Preinsulated Stator Coils for Machines Rated 6900 V and Below.* IEEE Std 275-1992, 1992: p. 0_1.

252. Chae, H.G. and S. Kumar, *Making strong fibers.* Science, 2008. **319**(5865): p. 908-909.

253. Zhou, C.F., et al., *Functionalized single wall carbon nanotubes treated with pyrrole for electrochemical supercapacitor membranes.* Chem Mater, 2005. **17**(8): p. 1997-2002.

254. Wei, C., et al., *Multifunctional chemical vapor sensors of aligned carbon nanotube and polymer composites.* J Am Chem Soc, 2006. **128**(5): p. 1412-1413.

255. Ounaies, Z., et al., *Electrical properties of single wall carbon nanotube reinforced polyimide composites.* Compos Sci Technol 2003. **63**(11): p. 1637-1646.

256. Peng, H., *Aligned carbon nanotube/polymer composite films with robust flexibility, high transparency, and excellent conductivity.* J Am Chem Soc, 2007. **130**(1): p. 42-43.

257. Li, N., et al., *Electromagnetic interference (EMI) shielding of single-walled carbon nanotube epoxy composites.* Nano Lett, 2006. **6**(6): p. 1141-1145.

258. Ismail, A.F., et al., *Transport and separation properties of carbon nanotube-mixed matrix membrane.* Sep Purif Technol 2009. **70**(1): p. 12-26.

259. Huang, H., et al., *Aligned carbon nanotube composite films for thermal management.* Adv Mater, 2005. **17**(13): p. 1652-1656.

260. Lin, W., K.S. Moon, and C.P. Wong, *A combined process of in situ functionalization and microwave treatment to achieve ultrasmall thermal expansion of aligned carbon nanotube-polymer nanocomposites: toward applications as thermal interface materials.* Adv Mater, 2009. **21**(23): p. 2421-2424.

261. Warheit, D.B., *What is currently known about the health risks related to carbon nanotube exposures?* Carbon, 2006. **44**(6): p. 1064-1069.

262. Kang, S., M.S. Mauter, and M. Elimelech, *Microbial cytotoxicity of carbon-based nanomaterials: implications for river water and wastewater effluent.* Environ Sci Technol, 2009. **43**(7): p. 2648-2653.

263. Thostenson, E.T., C. Li, and T.-W. Chou, *Nanocomposites in context.* Compos Sci Technol, 2005. **65**(3-4): p. 491-516.

264. Kashiwagi, T., et al., *Nanoparticle networks reduce the flammability of polymer nanocomposites.* Nat Mater, 2005. **4**(12): p. 928-933.

265. Kashiwagi, T., et al., *Flammability properties of polymer nanocomposites with single-walled carbon nanotubes: effects of nanotube dispersion and concentration.* Polymer, 2005. **46**(2): p. 471-481.

266. Dervishi, E., et al. *Electrical and thermal properties of carbon nanotube polymer composite films.* in *Mater. Res. Soc. 2007 Spring meeting, Symp. EE.* 2007. Warrendale (Pennsylvania. USA): Materials Research Society.

267. Liu, J., et al., *Processing and properties of carbon nanotube/poly(methyl methacrylate) composite films.* J Appl Polym Sci 2009. **112**(1): p. 142-156.

268. Yang, J., et al., *Morphology, thermal stability, and dynamic mechanical properties of atactic polypropylene/carbon nanotube composites.* J Appl Polym Sci, 2005. **98**(3): p. 1087-1091.

269. Kashiwagi, T., et al., *Thermal degradation and flammability properties of poly(propylene)/carbon nanotube composites.* Macromol Rapid Comm 2002. **23**(13): p. 761-765.

270. Bikiaris, D., et al., *Effect of acid treated multi-walled carbon nanotubes on the mechanical, permeability, thermal properties and thermo-oxidative stability of isotactic polypropylene.* Polym Degrad Stabil, 2008. **93**(5): p. 952-967.

271. Du, F., J.E. Fischer, and K.I. Winey, *Coagulation method for preparing single-walled carbon nanotube/poly(methyl methacrylate) composites and their modulus, electrical conductivity, and thermal stability.* J Polym Sci Pol Phys 2003. **41**(24): p. 3333-3338.

272. Ge, J.J., et al., *Assembly of well-aligned multiwalled carbon nanotubes in confined polyacrylonitrile environments: electrospun composite nanofiber sheets.* J Am Chem Soc, 2004. **126**(48): p. 15754-15761.

273. McNally, T., et al., *Polyethylene multiwalled carbon nanotube composites.* Polymer, 2005. **46**(19): p. 8222-8232.

274. Kuan, H.-C., et al., *Synthesis, thermal, mechanical and rheological properties of multiwall carbon nanotube/waterborne polyurethane nanocomposite.* Compos Sci Technol, 2005. **65**(11-12): p. 1703-1710.

275. Verdejo, R., et al., *Physical properties of silicone foams filled with carbon nanotubes and functionalized graphene sheets.* Eur Polym J 2008. **44**(9): p. 2790-2797.

276. Gao, J., et al., *Continuous spinning of a single-walled carbon nanotube-nylon composite fiber.* J Am Chem Soc, 2005. **127**(11): p. 3847-3854.

277. Yang, S., et al., *Thermal analysis of an acrylonitrile-butadiene-styrene/SWNT composite.* Polym Degrad Stabil 2004. **83**(3): p. 383-388.

278. Xu, Y., G. Ray, and B. Abdel-Magid, *Thermal behavior of single-walled carbon nanotube polymer-matrix composites.* Compos Part A-Appl S 2006. **37**(1): p. 114-121.

279. Jin, Z., et al., *Dynamic mechanical behavior of melt-processed multi-walled carbon nanotube/poly(methyl methacrylate) composites.* Chem Phys Lett, 2001. **337**(1-3): p. 43-47.

280. Feng, W., et al., *Well-aligned polyaniline/carbon-nanotube composite films grown by in-situ aniline polymerization.* Carbon, 2003. **41**(8): p. 1551-1557.

281. Park, C., et al., *Dispersion of single wall carbon nanotubes by in situ polymerization under sonication.* Chem Phys Lett, 2002. **364**(3-4): p. 303-308.

282. Probst, O., et al., *Nucleation of polyvinyl alcohol crystallization by single-walled carbon nanotubes.* Polymer, 2004. **45**(13): p. 4437-4443.

283. Ge, C.C., et al., *Quantitative analysis of metal impurities in carbon nanotubes: efficacy of different pretreatment protocols for ICPMS spectroscopy.* Anal Chem, 2008. **80**(24): p. 9426-9434.

284. Datsyuk, V., et al., *Chemical oxidation of multiwalled carbon nanotubes.* Carbon, 2008. **46**(6): p. 833-840.

285. Lin, Z., et al., *Solvent-Assisted Thermal Reduction of Graphite Oxide.* J Phys Chem C, 2010. **114**(35): p. 14819-14825.

286. Lin, W., et al., *Self-assembled monolayer-assisted chemical transfer of in situ functionalized carbon nanotubes.* J Am Chem Soc, 2008. **130**(30): p. 9636-9637.

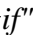287. Lin, W., et al., *Microwave Makes Carbon Nanotubes less Defective.* Acs Nano, 2010. **In press**.

288. Camino, G., S.M. Lomakin, and M. Lageard, *Thermal polydimethylsiloxane degradation. Part 2. The degradation mechanisms.* Polymer, 2002. **43**(7): p. 2011-2015.

289. Camino, G., S.M. Lomakin, and M. Lazzari, *Polydimethylsiloxane thermal degradation - Part 1. Kinetic aspects.* Polymer, 2001. **42**(6): p. 2395-2402.

290. Zhang, J., S.Y. Feng, and Q.Y. Ma, *Kinetics of the thermal degradation and thermal stability of conductive silicone rubber filled with conductive carbon black.* J Appl Polym Sci, 2003. **89**(6): p. 1548-1554.

291. Roy, P.K., et al., *Effect of benzil and cobalt stearate on the aging of low-density polyethylene films.* Polym Degrad Stabil, 2005. **90**(3): p. 577-585.

292. Perkas, N., et al., *Oxidation of cyclohexane with nanostructured amorphous catalysts under mild conditions.* Appl Catal A-Gen, 2001. **209**(1-2): p. 125-130.

293. Osawa, Z., *Role of metals and metal-deactivators in polymer degradation.* Polym Degrad Stabil, 1988. **20**(3-4): p. 203-236.

294. Anipsitakis, G.P., E. Stathatos, and D.D. Dionysiou, *Heterogeneous activation of oxone using Co3O4.* J Phys Chem B, 2005. **109**(27): p. 13052-13055.

295. Anipsitakis, G.P. and D.D. Dionysiou, *Radical generation by the interaction of transition metals with common oxidants.* Environ Sci Technol, 2004. **38**(13): p. 3705-3712.

296. Lupo, F., R. Kamalakaran, and A. Gulino, *Viable route for cobalt oxide-carbon nanocomposites.* J Phys Chem C, 2009. **113**(35): p. 15533-15537.

297. Goyal, A., et al., *In situ synthesis of catalytic metal nanoparticle-PDMS membranes by thermal decomposition process.* Compos Sci Technol, 2011. **71**(2): p. 129-133.

298. Galano, A., *Carbon nanotubes as free-radical scavengers.* J Phys Chem C, 2008. **112**(24): p. 8922-8927.

299. Fenoglio, I., et al., *Reactivity of carbon nanotubes: Free radical generation or scavenging activity?* Free Radical Bio Med, 2006. **40**(7): p. 1227-1233.

300. Francisco-Marquez, M., A. Galano, and A. Martinez, *On the Free Radical Scavenging Capability of Carboxylated Single-Walled Carbon Nanotubes.* J Phys Chem C, 2010. **114**(14): p. 6363-6370.

301. Martnez, A., M. Francisco-Marquez, and A. Galano, *Effect of Different Functional Groups on the Free Radical Scavenging Capability of Single-Walled Carbon Nanotubes.* J Phys Chem C, 2010. **114**(35): p. 14734-14739.

302. Zeng, Y., et al., *Effects of Carbon Nanotubes on Processing Stability of Polyoxymethylene in Melting-Mixing Process.* J Phys Chem C, 2007. **111**(37): p. 13945-13950.

303. Kilbride, B.E., et al., *Experimental observation of scaling laws for alternating current and direct current conductivity in polymer-carbon nanotube composite thin films.* Journal of Applied Physics, 2002. **92**(7): p. 4024-4030.

304. Wong, E.W., P.E. Sheehan, and C.M. Lieber, *Nanobeam mechanics: Elasticity, strength, and toughness of nanorods and nanotubes.* Science, 1997. **277**(5334): p. 1971-1975.

305. Yu, M.F., et al., *Strength and breaking mechanism of multiwalled carbon nanotubes under tensile load.* Science, 2000. **287**(5453): p. 637-640.

306.   Bottini, M., et al., *Multi-walled carbon nanotubes induce T lymphocyte apoptosis.* Toxicology Letters, 2006. **160**(2): p. 121-126.

307.   Peng, H., et al., *Sidewall functionalization of single-walled carbon nanotubes with organic peroxides.* Chem Comm, 2003(3): p. 362-363.

308.   Ying, Y., et al., *Functionalization of Carbon Nanotubes by Free Radicals.* Org Lett, 2003. **5**(9): p. 1471-1473.

309.   Peng, H., et al., *Sidewall Carboxylic Acid Functionalization of Single-Walled Carbon Nanotubes.* J Am Chem Soc 2003. **125**(49): p. 15174-15182.

310.   McIntosh, D., V.N. Khabashesku, and E.V. Barrera, *Benzoyl Peroxide Initiated In Situ Functionalization, Processing, and Mechanical Properties of Single-Walled Carbon Nanotube‚àíPolypropylene Composite Fibers.* J Phys Chem C, 2007. **111**(4): p. 1592-1600.

311.   Marcano, D.C., et al., *Design of Poly(ethylene Glycol)-Functionalized Hydrophilic Carbon Clusters for Targeted Therapy of Cerebrovascular Dysfunction in Mild Traumatic Brain Injury.* Journal of Neurotrauma, 2013. **30**(9): p. 789-796.

312.   Coleman, J.N., et al., *Small but strong: A review of the mechanical properties of carbon nanotube-polymer composites.* Carbon, 2006. **44**(9): p. 1624-1652.

313.   Hamed, G.R., *Materials and Compounds*, in *Engineering with Rubber—How to Design Rubber Component*, A.N.Gent, Editor 1992, Hanser: New York.

314.   Treloar, L.R.G., *The physics of rubber elasticity*. 3 ed2005, Oxford: Clarendon Press.

315.   Chien, A., et al., *Characterization of radiation-induced aging in silica-reinforced polysiloxane composites.* Radiat Phys Chem, 2000. **59**(5-6): p. 493-500.

316.   Maxwell, R.S., et al., *The effects of γ-radiation on the thermal, mechanical, and segmental dynamics of a silica filled, room temperature vulcanized polysiloxane rubber.* Polym Degrad Stabil, 2003. **80**(3): p. 443-450.

317.   Verge, P., et al., *Investigation on the dispersion of carbon nanotubes in nitrile butadiene rubber: Role of polymer-to-filler grafting reaction.* Compos Sci Technol, 2010. **70**(10): p. 1453-1459.

318.   Zhao, Q., R. Tannenbaum, and K.I. Jacob, *Carbon nanotubes as Raman sensors of vulcanization in natural rubber.* Carbon, 2006. **44**(9): p. 1740-1745.

319.   Linton, D., et al., *The importance of chain connectivity in the formation of non-covalent interactions between polymers and single-walled carbon nanotubes and its impact on dispersion.* Soft Matter, 2010. **6**(12): p. 2801-2814.

320.   Kirkwood, K., D. Stewart, and C.T. Imrie, *Role of C60 in the free radical polymerization of methyl methacrylate.* J Polym Sci Pol Chem, 1997. **35**(15): p. 3323-3325.

321.   Chen, Y. and K.-C. Lin, *Radical polymerization of styrene in the presence of C60.* J Polym Sci Pol Chem, 1999. **37**(15): p. 2969-2975.

322.   Seno, M., M. Maeda, and T. Sato, *Effect of fullerene on radical polymerization of vinyl acetate.* J Polym Sci Pol Chem, 2000. **38**(14): p. 2572-2578.

323.   Liu, J., et al., *Fullerene Pipes.* Science, 1998. **280**(5367): p. 1253-1256.

324.   Morton, J.R., et al., *ESR studies of the reaction of alkyl radicals with fullerene (C60).* J Phys Chem C 1992. **96**(9): p. 3576-3578.

325. Buonocore, F., et al., *Ab initio calculations of electron affinity and ionization potential of carbon nanotubes.* Nanotechnology, 2008. **19**(2): p. 025711.

326. KRUSIC, P.J., et al., *Radical Reactions of C60.* Science, 1991. **254**(5035): p. 1183-1185.

327. Sola, M., J. Mestres, and M. Duran, *Molecular Size and Pyramidalization: Two Keys for Understanding the Reactivity of Fullerenes.* J Phys Chem C 1995. **99**(27): p. 10752-10758.

328. Sumita, M., et al., *Dispersion of fillers and the electrical conductivity of polymer blends filled with carbon black.* Polym. Bull., 1991. **25**(2): p. 265-271.

329. Xu, J. and C.P. Wong, *Characterization and properties of an organic–inorganic dielectric nanocomposite for embedded decoupling capacitor applications.* Composites Part A, 2007. **38**(1): p. 13-19.

330. Le, H., et al., *Effect of filler dispersion degree on the Joule heating stimulated recovery behaviour of nanocomposites.* J. Mater. Sci., 2010. **45**(21): p. 5851-5859.

331. Montes, H., et al., *Particles in model filled rubber: Dispersion and mechanical properties.* Eur. Phys. J. E, 2010. **31**(3): p. 263-268.

332. Pu, Z., et al., *Effects of Dispersion and Aggregation of Silica in the Reinforcement of Poly(methyl acrylate) Elastomers.* Chem. Mater., 1997. **9**(11): p. 2442-2447.

333. Dasari, A., et al., *Clay exfoliation and organic modification on wear of nylon 6 nanocomposites processed by different routes.* Compos. Sci. Technol. , 2005. **65**(15-16): p. 2314-2328.

334. Grady, B.P., *Recent Developments Concerning the Dispersion of Carbon Nanotubes in Polymers.* Macromol. Rapid Commun. , 2010. **31**(3): p. 247-257.

335. Supova, M., G.S. Martynkova, and K. Barabaszova, *Effect of Nanofillers Dispersion in Polymer Matrices: A Review.* Sci. Adv. Mater., 2011. **3**(1): p. 1-25.

336. Moniruzzaman, M. and K.I. Winey, *Polymer nanocomposites containing carbon nanotubes.* Macromolecules, 2006. **39**(16): p. 5194-5205.

337. Lim, S.W., et al., *Glass Beads-Assisted Fine Dispersion of Multiwalled Carbon Nanotube in Silicone Matrix.* Macromol. Res., 2010. **18**(8): p. 766-771.

338. Ha, H., S.C. Kim, and K. Ha, *Effect of Molecular Weight of Polymer Matrix on the Dispersion of MWNTs in HDPE/MWNT and PC/MWNT Composites.* Macromol. Res., 2010. **18**(5): p. 512-518.

339. Schroder, A., L. Briquel, and M. Sawe, *Effect of MWCNT-Dispersion in NBR-Compounds.* KGK-Kautsch. Gummi Kunstst., 2011. **64**(1-2): p. 42-47.

340. Gershon, A.L., et al., *Nanomechanical characterization of dispersion and its effects in nano-enhanced polymers and polymer composites.* J. Mater. Sci., 2010. **45**(23): p. 6353-6364.

341. Ciecierska, E., A. Boczkowska, and K. Kurzydlowski, *Quantitative description of the spatial dispersion of carbon nanotubes in polymeric matrix.* J. Mater. Sci., 2010. **45**(9): p. 2305-2310.

342. Kashiwagi, T., et al., *Relationship between dispersion metric and properties of PMMA/SWNT nanocomposites.* Polymer, 2007. **48**(16): p. 4855-4866.

343. Khare, H.S. and D.L. Burris, *A quantitative method for measuring nanocomposite dispersion.* Polymer, 2010. **51**(3): p. 719-729.

344. Liang, J.Z., *Evaluation of dispersion of nano-CaCO3 particles in polypropylene matrix based on fractal method.* Composites Part A, 2007. **38**(6): p. 1502-1506.
345. Liang, J.Z. and R.K.Y. Li, *Measurement of dispersion of glass beads in PP matrix.* J. Reinf. Plast. Compos., 2001. **20**(8): p. 630-638.
346. Mills, S.L., et al., *An Improved Method for the Dispersion Assessment of Flame Retardant Filler/Polymer Systems Based on the Multifractal Analysis of SEM Images.* Macromol. Mater. Eng. , 2004. **289**(10): p. 864-871.
347. Mills, S.L., et al., *Prediction of Mechanical Properties Following the Dispersion Assessment of Flame Retardant Filler/Polymer Composites Based on the Multifractal Analysis of SEM Images.* J. Macromol. Sci., Part B: Phys. , 2005. **44**(6): p. 1137-1151.
348. Pegel, S., et al., *Spatial statistics of carbon nanotube polymer composites.* Polymer, 2009. **50**(9): p. 2123-2132.
349. Sul, I.H., J.R. Youn, and Y.S. Song, *Quantitative dispersion evaluation of carbon nanotubes using a new analysis protocol.* Carbon, 2011. **49**(4): p. 1473-1478.
350. Glaskova, T., et al., *Method of quantitative analysis of filler dispersion in composite systems with spherical inclusions.* Compos. Sci. Technol. , 2011. **71**(13): p. 1543-1549.
351. Grossiord, N., et al., *Toolbox for Dispersing Carbon Nanotubes into Polymers To Get Conductive Nanocomposites.* Chem. Mater. , 2006. **18**(5): p. 1089-1099.
352. Kovacs, J.Z., et al., *Analyzing the quality of carbon nanotube dispersions in polymers using scanning electron microscopy.* Carbon, 2007. **45**(6): p. 1279-1288.
353. Peter, T.L. and et al., *A quantitative assessment of carbon nanotube dispersion in polymer matrices.* Nanotechnology, 2009. **20**(32): p. 325708.
354. Frangi, A., et al. *Multiscale vessel enhancement filtering*. in *The 1st International Conference on Medical Image Computing and Computer-Assisted Intervention* 1998. Cambridge, MA.
355. Lam, L., S.W. Lee, and C.Y. Suen, *Thinning methodologies-a comprehensive survey.* IEEE Trans. Pattern Anal. Mach. Intell., 1992. **14**: p. 869-885.
356. Duda, R.O., P.E. Hart, and D.G. Stork, *Pattern classification*2001: Wiley.
357. Botev, Z.I., J.F. Grotowski, and D.P. Kroese, *Kernel density estimation via diffusion* Ann. Stat., 2010. **38**(5): p. 2916-2957.
358. Kreyszig, E., *Introductory functional analysis with applications*1989: Wiley.
359. Zhu, Y., et al., *Statistical analysis of particle dispersion in a PE/TiO2 nanocomposite film.* Compos. Struct. , 2010. **92**(9): p. 2203-2207.
360. Karásek, L. and M. Sumita, *Characterization of dispersion state of filler and polymer-filler interactions in rubber-carbon black composites.* J. Mater. Sci. , 1996. **31**(2): p. 281-289.
361. Watson, W.F., *Combination of Rubber and Carbon Black on Cold Milling.* Ind. Eng. Chem., 1955. **47**(6): p. 1281-1286.
362. Xu, J., et al., *Shear Modulated Percolation in Carbon Nanotube Composites.* The Journal of Physical Chemistry B, 2006. **110**(25): p. 12289-12292.
363. Deng, F., et al., *Elucidation of the Reinforcing Mechanism in Carbon Nanotube/Rubber Nanocomposites.* ACS Nano, 2011. **5**(5): p. 3858-3866.

364.   White, S.I., et al., *Electrical Percolation Behavior in Silver Nanowire–Polystyrene Composites: Simulation and Experiment.* Advanced Functional Materials, 2010. **20**(16): p. 2709-2716.

365.   Gelves, G.A., et al., *Low Electrical Percolation Threshold of Silver and Copper Nanowires in Polystyrene Composites.* Advanced Functional Materials, 2006. **16**(18): p. 2423-2430.

366.   Wu, H.P., et al., *High conductivity of isotropic conductive adhesives filled with silver nanowires.* International Journal of Adhesion and Adhesives, 2006. **26**(8): p. 617-621.

367.   Yu, Y.-H., et al., *Morphology, Electrical, and Rheological Properties of Silane-Modified Silver Nanowire/Polymer Composites.* Macromolecular Materials and Engineering, 2010. **295**(11): p. 1017-1024.

368.   Zhu, R., et al., *Fused Silver Nanowires with Metal Oxide Nanoparticles and Organic Polymers for Highly Transparent Conductors.* ACS Nano, 2011. **5**(12): p. 9877-9882.

369.   Gaynor, W., et al., *Smooth Nanowire/Polymer Composite Transparent Electrodes.* Advanced Materials, 2011. **23**(26): p. 2905-+.

370.   Gaynor, W., J.Y. Lee, and P. Peumans, *Fully Solution-Processed Inverted Polymer Solar Cells with Laminated Nanowire Electrodes.* ACS Nano, 2010. **4**(1): p. 30-34.

371.   Lee, J.Y., et al., *Semitransparent Organic Photovoltaic Cells with Laminated Top Electrode.* Nano Letters, 2010. **10**(4): p. 1276-1279.

372.   Sun, Y., et al., *Uniform Silver Nanowires Synthesis by Reducing AgNO3 with Ethylene Glycol in the Presence of Seeds and Poly(Vinyl Pyrrolidone).* Chemistry of Materials, 2002. **14**(11): p. 4736-4745.

373.   Sun, Y., et al., *Polyol Synthesis of Uniform Silver Nanowires: A Plausible Growth Mechanism and the Supporting Evidence.* Nano Letters, 2003. **3**(7): p. 955-960.

374.   Zhang, Z.X., X.Y. Chen, and F. Xiao, *The Sintering Behavior of Electrically Conductive Adhesives Filled with Surface Modified Silver Nanowires.* Journal of Adhesion Science and Technology, 2011. **25**(13): p. 1465-1480.

375.   Jiu, J., et al., *Strongly adhesive and flexible transparent silver nanowire conductive films fabricated with a high-intensity pulsed light technique.* Journal of Materials Chemistry, 2012. **22**(44): p. 23561-23567.

376.   Lee, J.Y., et al., *Solution-processed metal nanowire mesh transparent electrodes.* Nano Letters, 2008. **8**(2): p. 689-692.

377.   Hu, L.B., et al., *Scalable Coating and Properties of Transparent, Flexible, Silver Nanowire Electrodes.* ACS Nano, 2010. **4**(5): p. 2955-2963.

378.   Olson, L.P., et al., *The Simple Yet Elusive Crystal Structure of Silver Acetate and the Role of the Ag−Ag Bond in the Formation of Silver Nanoparticles during the Thermally Induced Reduction of Silver Carboxylates.* Chemistry of Materials, 2006. **18**(6): p. 1667-1674.

379.   Binnemans, K., et al., *Structure and Mesomorphism of Silver Alkanoates.* Chemistry of Materials, 2004. **16**(10): p. 2021-2027.

380.   Lee, S.J., et al., *Structure and Thermal Behavior of a Layered Silver Carboxylate.* The Journal of Physical Chemistry B, 2002. **106**(11): p. 2892-2900.

381. Aoki, K., et al., *Charge-Transfer Reactions of Silver Stearate-Coated Nanoparticles in Suspensions.* Langmuir, 2003. **19**(23): p. 9904-9909.

382. Carotenuto, G., *Synthesis and characterization of poly(N-vinylpyrrolidone) filled by monodispersed silver clusters with controlled size.* Applied Organometallic Chemistry, 2001. **15**(5): p. 344-351.

383. Du, Y.K., et al., *Thermal decomposition behaviors of PVP coated on platinum nanoparticles.* Journal of Applied Polymer Science, 2006. **99**(1): p. 23-26.

384. Zhuo, L., et al. *Shape engineering of the fillers in stretchable, electrically conductive adhesives: Its effect on percolation and conductivity change during stretching.* in *Electronic Components and Technology Conference (ECTC), 2013 IEEE 63rd.* 2013.

385. You, H.J., et al., *Size Effect on Nanoparticle-Mediated Silver Crystal Growth.* Crystal Growth & Design, 2011. **11**(12): p. 5449-5456.

386. McLean, J.S., *A re-examination of the fundamental limits on the radiation Q of electrically small antennas.* Antennas and Propagation, IEEE Transactions on, 1996. **44**(5): p. 672.

387. Thal, H.L., *New Radiation <img src="/images/tex/228.gif" alt="Q"> Limits for Spherical Wire Antennas.* Antennas and Propagation, IEEE Transactions on, 2006. **54**(10): p. 2757-2763.

388. Chu, L.J., *Physical Limitations of Omni‐Directional Antennas.* Journal of Applied Physics, 1948. **19**(12): p. 1163-1175.

389. Best, S.R. *The performance properties of an electrically small folded spherical helix antenna.* in *Antennas and Propagation Society International Symposium, 2002. IEEE.* 2002.

390. Best, S.R., *A discussion on the properties of electrically small self-resonant wire antennas.* Antennas and Propagation Magazine, IEEE, 2004. **46**(6): p. 9-22.

391. Best, S.R. and D.L. Hanna, *A Performance Comparison of Fundamental Small-Antenna Designs.* Antennas and Propagation Magazine, IEEE, 2010. **52**(1): p. 47-70.

392. Kim, O.S., *Low-Q Electrically Small Spherical Magnetic Dipole Antennas.* Antennas and Propagation, IEEE Transactions on, 2010. **58**(7): p. 2210-2217.

393. Adams, J.J., et al., *Conformal Printing of Electrically Small Antennas on Three-Dimensional Surfaces.* Advanced Materials, 2011. **23**(11): p. 1335-1340.

394. Bhattacharya, R., et al., *Organic LED Pixel Array on a Dome.* Proceedings of the IEEE, 2005. **93**(7): p. 1273-1280.

395. Toriz-Garcia, J.J., et al., *Fabrication of a 3D electrically small antenna using holographic photolithography.* Journal of Micromechanics and Microengineering, 2013. **23**(5): p. 055010.

396. Pfeiffer, C., et al., *Direct Transfer Patterning of Electrically Small Antennas onto Three-Dimensionally Contoured Substrates.* Advanced Materials, 2012. **24**(9): p. 1166-1170.

397. Jobs, M., et al., *A Tunable Spherical Cap Microfluidic Electrically Small Antenna.* Small, 2013. **9**(19): p. 3230-3234.

398. Geissler, M., et al. *An improved method for measuring the radiation efficiency of mobile devices.* in *Antennas and Propagation Society International Symposium, 2003. IEEE.* 2003.

399. Yaghjian, A.D. and S.R. Best, *Impedance, bandwidth, and Q of antennas.* Antennas and Propagation, IEEE Transactions on, 2005. **53**(4): p. 1298-1324.

400. Balandin, A.A., et al., *Superior thermal conductivity of single-layer graphene.* Nano Letters, 2008. **8**(3): p. 902-907.

401. Stoller, M.D., et al., *Graphene-Based Ultracapacitors.* Nano Letters, 2008. **8**(10): p. 3498-3502.

402. Lee, C., et al., *Measurement of the elastic properties and intrinsic strength of monolayer graphene.* Science, 2008. **321**(5887): p. 385-388.

403. Li, X.L., et al., *Highly conducting graphene sheets and Langmuir-Blodgett films.* Nature Nanotechnology, 2008. **3**(9): p. 538-542.

404. Lee, S.H., et al., *Three-Dimensional Self-Assembly of Graphene Oxide Platelets into Mechanically Flexible Macroporous Carbon Films.* Angewandte Chemie-International Edition, 2010. **49**(52): p. 10084-10088.

405. Xu, Y., et al., *Self-Assembled Graphene Hydrogel via a One-Step Hydrothermal Process.* Acs Nano, 2010.

406. Qiu, L., et al., *Biomimetic superelastic graphene-based cellular monoliths.* Nat Commun, 2012. **3**: p. 1241.

407. Chen, Z., et al., *Three-dimensional flexible and conductive interconnected graphene networks grown by chemical vapour deposition.* Nat Mater, 2011. **10**(6): p. 424-428.

408. Coleman, J.N., et al., *Two-Dimensional Nanosheets Produced by Liquid Exfoliation of Layered Materials.* Science, 2011. **331**(6017): p. 568-571.

409. Hernandez, Y., et al., *High-yield production of graphene by liquid-phase exfoliation of graphite.* Nat Nano, 2008. **3**(9): p. 563-568.

410. Coleman, J.N., *Liquid Exfoliation of Defect-Free Graphene.* Accounts of Chemical Research, 2012. **46**(1): p. 14-22.

411. Gillen, K.T., R.A. Assink, and R. Bernstein, *Nuclear Energy Plant Optimization (NEPO) Final Report on Aging and Condition Monitoring of Low-Voltage Cable Materials*, in *SAND2005-7331*2005, Sandia National Lab.

412. Gillen, K.T. and M. Celina, *The wear-out approach for predicting the remaining lifetime of materials.* Polymer Degradation and Stability, 2000. **71**(1): p. 15-30.

413. Damian, C., E. Espuche, and M. Escoubes, *Influence of three ageing types (thermal oxidation, radiochemical and hydrolytic ageing) on the structure and gas transport properties of epoxy-amine networks.* Polymer Degradation and Stability, 2001. **72**(3): p. 447-458.